

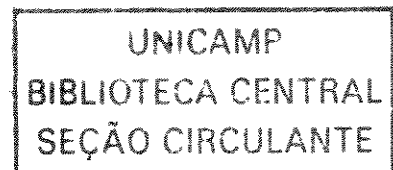
ESTE EXEMPLAR CORRESPONDE A REDAÇÃO FINAL DA
TESE DEFENDIDA POR *Lázaro Valentim Donadon*
E APROVADA PELA
COMISSÃO JULGADORA EM *30/08/2002*
José Roberto de França Arruda
ORIENTADOR

UNIVERSIDADE ESTADUAL DE CAMPINAS
FACULDADE DE ENGENHARIA MECÂNICA
COMISSÃO DE PÓS-GRADUAÇÃO EM ENGENHARIA MECÂNICA

Análise Teórica e Experimental de Estratégias de Controle Ativo de Ruído

Autor: **Lázaro Valentim Donadon**
Orientador: José Roberto de França Arruda

01/03



**UNIVERSIDADE ESTADUAL DE CAMPINAS
FACULDADE DE ENGENHARIA MECÂNICA
COMISSÃO DE PÓS-GRADUAÇÃO EM ENGENHARIA MECÂNICA
DEPARTAMENTO DE MECÂNICA COMPUTACIONAL**

Análise Teórica e Experimental de Estratégias de Controle Ativo de Ruído

Autor: Lázaro Valentim Donadon

Orientador: José Roberto de França Arruda

**Curso: Engenharia Mecânica
Área de Concentração: Projetos Mecânicos**

Tese de doutorado apresentada à comissão de Pós Graduação da Faculdade de Engenharia Mecânica, como requisito para a obtenção do título de Doutor em Engenharia Mecânica.

Campinas, 2002
S.P. – Brasil

UNIDADE	80
Nº CHAMADA	UNICAMP
	D 714a
V	EX
TOMBO BCI	53209
PROC.	124103
C	<input type="checkbox"/>
D	<input checked="" type="checkbox"/>
PREÇO	R\$ 11,00
DATA	17/10/03
Nº CPD	

CM00182144-B

B ID 287893

FICHA CATALOGRÁFICA ELABORADA PELA
BIBLIOTECA DA ÁREA DE ENGENHARIA - BAE - UNICAMP

Donadon, Lázaro Valentim
D714a Análise teórica e experimental de estratégias de controle
ativo de ruído / Lázaro Valentim Donadon. --Campinas, SP:
[s.n.], 2002.

Orientador: José Roberto de França Arruda.
Tese (doutorado) - Universidade Estadual de Campinas,
Faculdade de Engenharia Mecânica.

1. Som - Intensidade. 2. Vibração. 3. Controle de ruído.
4. Guias de ondas. I. Arruda, José Roberto de França. II.
Universidade Estadual de Campinas. Faculdade de Engenharia
Mecânica. III. Título.

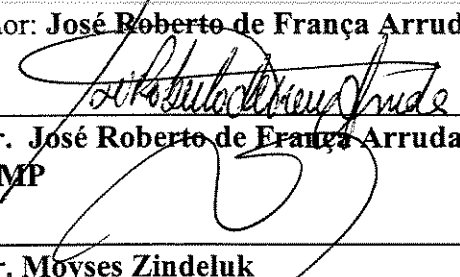
UNIVERSIDADE ESTADUAL DE CAMPINAS
FACULDADE DE ENGENHARIA MECÂNICA
COMISSÃO DE PÓS-GRADUAÇÃO EM ENGENHARIA MECÂNICA
DEPARTAMENTO DE MECÂNICA COMPUTACIONAL

TESE DE DOUTORADO

**Análise Teórica e Experimental de Estratégias
de Controle Ativo de Ruído**

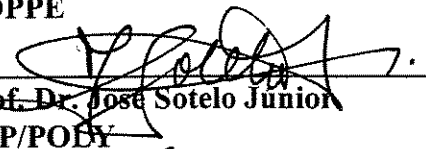
Autor: **Lázaro Valentim Donadon**

Orientador: **José Roberto de França Arruda**

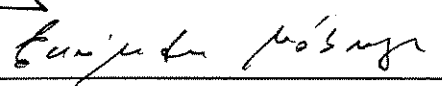


Prof. Dr. José Roberto de França Arruda
UNICAMP

Prof. Dr. Moyses Zindeluk
COPPE



Prof. Dr. José Sotelo Junior
USP/POBY



Prof. Dr. Eurípedes Guilherme de Oliveira Nóbrega
UNICAMP



Prof. Dr. José Maria Campos dos Santos
UNICAMP

Campinas, 30 de agosto de 2002

Dedicatória:

Dedico este trabalho aos meus queridos pais Lazinho Donadon e Maria Aparecida Sotana Donadon pelo apoio dado nas horas mais difíceis, e aos meus queridos padrinhos Adelino Fernandes e Albertina dos Anjos Fernandes (em memória).

Agradecimentos

Este trabalho não poderia ser terminado sem a ajuda de diversas pessoas às quais presto minha homenagem:

Ao meu orientador José Roberto de França Arruda. Acredito que orientar é mais do que mostrar os caminhos a serem seguidos, é ser companheiro e amigo, é dar apoio quando necessário e ao mesmo tempo cobrar quando o trabalho não estiver bom. Orientar é tudo isso e muito mais que até me fogem as palavras. Então fica aqui registrado o quanto sou grato por ter recebido a orientação deste valoroso professor.

Aos meus companheiros de trabalho, Belisário, Khaled, Eder Lima, Fuganholi e muitos outros, que, agora no final desta jornada, posso realmente chamá-los de amigos. As horas passadas juntas foram maravilhosas, as discussões, os cafés, e até mesmo, os papos furados mas que, de uma forma ou de outra, tornaram muito mais agradável o nosso ambiente de trabalho.

A todos os professores que me passaram os seus conhecimentos através de longas horas de aulas, mas não posso deixar de agradecer em especial ao meu orientador de mestrado Eurípedes G.O. Nóbrega, que me iniciou como um pesquisador.

Agradeço também à CAPES, ao CNPq pela bolsa de estudo, pela FAPESP pelo apoio financeiro referente ao projeto 1998/06248-2, que tornaram possível a execução esta tese.

Por fim, agradeço a Deus e àquele que me protege lá em cima. Talvez um dia irei descobrir quem ele realmente é.

Um dos discípulos de Confúcio chegou até ele e disse,
- *Mestre, o que acha disto:*

*“Uma libélula rubra,
tirai-lhe as asas,
uma pimenta.”*

Confúcio pensou e disse,
- Que tal:

*“Uma pimenta,
colocai-lhe asas,
uma libélula rubra.”*

E concluiu dizendo que as pessoas têm uma tendência a serem pessimistas e sempre dizem que o copo com água até a metade está meio vazio, porque não dizer que o copo está meio cheio, que é uma idéia mais otimista. Assim, devemos sempre ser otimistas, o pensamento positivo já é meio caminho andado.

Resumo

Donadon, Lázaro Valentim, *Análise Teórica e Experimental de Estratégias de Controle Ativo de Ruído*, Campinas,: Faculdade de Engenharia Mecânica, Universidade Estadual de Campinas, 2002. 260 p. Tese (Doutorado)

Este trabalho descreve a aplicação de métodos de controle ativo de ruído utilizando uma abordagem de filtragem adaptativa na configuração avanço, onde o objetivo é a observação do comportamento energético do sistema controlado. Os métodos de controle ativo testados foram o Filtered-X LMS no domínio do tempo e da frequência e o ASIC (método de controle de intensidade sonora ativa) desenvolvido e implementado no domínio da frequência.

Este trabalho está dividido em duas partes principais. Na primeira parte, os métodos de controle ativo foram testados em um ambiente acústico unidimensional constituído por um duto na forma de “T” com duas fontes acústicas. O modelo teórico do guia de ondas unidimensional foi desenvolvido utilizando o método dos elementos espectrais para o caso acústico. Neste experimento foram testadas as técnicas de medidas de intensidade sonora, potência radiada e sensores de velocidade de partícula. Os resultados teóricos e experimentais mostraram que o método dos elementos espectrais pode ser utilizado com sucesso para prever os fenômenos acústicos, e que não ocorrem diferenças significativas entre os métodos de controle ativo mesmo quando foram alteradas as funções de custo (troca dos sensores de pressão por sensores de velocidade de partícula).

Na segunda parte, o algoritmo Filtered-X LMS no domínio do tempo foi implementado em um cilindro com o intuito de atenuar o ruído interno quando este é gerado pela casca cilíndrica ou por uma fonte sonora externa à cavidade. Os esquemas de controle ativo testados foram o controle de vibração (AVC) e o controle ativo de ruído via atuação estrutural (ASAC).

Demonstrou-se experimentalmente que, se o ruído interno é gerado pela vibração da casca cilíndrica, o melhor desempenho é atingido pelo controle de vibração, enquanto que, se o ruído é gerado por uma fonte externa, o controle ativo de ruído via atuação estrutural é a melhor alternativa.

Palavras Chave

Controle ativo, vibração, ruído, intensidade sonora, atuação estrutural, fluxo de potência, guia de ondas unidimensional, fuselagem aeronáutica.

Abstract

Donadon, Lázaro Valentim, *Analytical and Experimental Analysis of Active Noise Control Strategies*, Campinas,: Faculdade de Engenharia Mecânica, Universidade Estadual de Campinas, 2002. 260 p. Ph.D. Dissertation (Doctorate)

This work describes applications of the active noise control techniques using adaptive feedforward filtering theory, where the objective is to analyze energetic behavior of the controlled system. The active noise control methods employed are the normalized filtered-X LMS in the time and frequency domain and the Active Sound Intensity Controller (ASIC), which is developed and implemented in the frequency domain.

This thesis is divided in two main parts. In the first part, the active noise control methods are applied in an one-dimensional waveguide constituted by a T-shaped duct with two acoustic sources. The one-dimensional waveguide was modeled by the Spectral Element Method (SEM). In this experiment, the measurements include the sound intensity, the radiated acoustic power, and the particle velocity. The theoretical and experimental results show that the spectral element method can be used successfully to predict the acoustic phenomena in one-dimensional waveguides. Besides, there is no significant difference when different active noise control strategies are implemented, even when the cost functions were changed (the change in the error sensor type means a change in the cost function).

In the second part, the normalized filtered-X LMS in the time domain is applied to attenuate the interior noise in a cylindrical cavity. The adaptive control schemes implemented were the Active Control of Vibration (AVC) and the Active Structural Acoustic Control (ASAC). Results

obtained when the primary noise is generated by mechanically exciting the cylindrical shell and by using an external acoustical source are compared. It is shown that if the interior noise is generated by shaking the cylindrical shell, it is better to apply the AVC scheme, while if the interior noise is generated by an external acoustical source it is better to apply the ASAC scheme.

Key Words

Active noise and vibration control, sound intensity control, active structural acoustic control, power flow, one-dimensional waveguide, aircraft fuselage.

Summary

FIGURE LIST	VIII
TABLE LIST	XV
NOMENCLATURE	XVII

CAPÍTULO 1 (PORTUGUÊS) : INTRODUÇÃO1

1.1 CONFIGURAÇÕES BÁSICAS DE UM SISTEMA DE CONTROLE ATIVO	2
1.2 ESQUEMAS DE CONTROLE ATIVO	4
1.3 ALGORITMOS DE CONTROLE ATIVO	4
1.4 CONTROLE ATIVO UTILIZANDO TEORIA DE FILTRAGEM ADAPTATIVA	6
1.5 TIPOS DE ATUADORES E SENSORES	6
1.6 IMPORTÂNCIA DA ANÁLISE ENERGÉTICA	9
1.7 OBJETIVOS DESTA TESE	10
1.8 ORGANIZAÇÃO DA TESE	11

CHAPTER 1 (ENGLISH) : INTRODUCTION12

1.1 BASIC CONFIGURATIONS OF AN ACTIVE CONTROL SYSTEM.....	13
1.2 ACTIVE CONTROL SCHEMES / ESQUEMAS DE CONTROLE ATIVO.....	15
1.3 ACTIVE CONTROL ALGORITHM	15
1.4 ACTIVE CONTROL USING ADAPTIVE FILTERING THEORY	16
1.5 SENSOR AND ACTUATOR TYPES	17
1.6 ENERGETIC ANALYSIS IMPORTANCE	19
1.7 OBJECTIVES OF THE PH.D. DISSERTATION	20
1.8 PHD DISSERTATION ORGANIZATION	21

CAPÍTULO 2 (PORTUGUÊS) : REVISÃO BIBLIOGRÁFICA.....23

2.1	ALGORITMOS ADAPTATIVOS PARA CONTROLE ATIVO DE RUÍDO	23
2.2	MELHORIAS E TENDÊNCIAS	24
2.3	ALTERANDO A FUNÇÃO DE CUSTO	25
2.4	APLICAÇÃO EM GUIA DE ONDAS UNIDIMENSIONAIS	27
2.5	APLICAÇÕES NO CONTROLE DE RUÍDO RADIADO PARA O INTERIOR DE CAVIDADES.....	29
2.6	ERROS NAS MEDIDAS DE INTENSIDADE	31
2.7	ERROS NOS MÉTODOS DE CONTROLE ATIVO.....	33

CHAPTER 2 (ENGLISH) : BIBLIOGRAPHY REVIEW34

2.1	ACTIVE NOISE CONTROL ADAPTIVE ALGORITHMS.....	34
2.2	IMPROVEMENTS AND TRENDS	35
2.3	CHANGING THE COST FUNCTION	36
2.4	APPLICATION TO ONE-DIMENSIONAL ACOUSTIC WAVEGUIDES	38
2.5	ACTIVE NOISE CONTROL OF THE SOUND RADIATED TO CAVITIES	40
2.6	ERRORS IN THE INTENSITY MEASUREMENT	42
2.7	ERRORS IN THE ACTIVE CONTROL METHODS	43

CHAPTER 3 : BASIC CONCEPTS IN ACOUSTICS45

3.1	PRESSURE AND VELOCITY EQUATIONS.....	45
3.2	ACOUSTIC INTENSITY	48
3.3	PARTICLE VELOCITY USING P-P APPROACH.....	50
3.4	ACOUSTIC INTENSITY USING P-P APPROACH	51
3.5	ACOUSTIC IMPEDANCE	52
3.6	SOURCES IN ACOUSTIC FIELDS	53
3.7	ACOUSTIC POWER INTRODUCED BY VIBRATING SOURCES.....	53
3.8	EXPERIMENTAL MEASUREMENTS OF THE ACOUSTICAL PROPERTIES	54

CHAPTER 4 : ACTIVE CONTROL METHODS.....57

4.1 OPTIMAL SOLUTIONS..... 58

4.1.1 *Optimal solution for the secondary source base upon controlling the acoustic potential energy density* 59

4.1.2 *Optimal solution for the secondary source based upon controlling the acoustic kinetic energy density* 60

4.1.3 *Optimal solution for the secondary source based upon controlling the acoustic total energy density* 61

4.1.4 *Optimal solution for the secondary source based upon controlling the acoustic active intensity*..... 62

4.1.5 *Optimal solution for the secondary source based upon controlling the acoustic reactive intensity* 63

4.1.6 *Optimal solution for the secondary source based upon controlling the acoustic power radiated by two sources*..... 65

4.1.7 *Summary and observations about the optimal solutions* 66

4.1.8 *Optimal solution using two microphones to estimate the particle velocity* 68

4.2 ADAPTIVE CONTROL METHODS 72

4.2.1 *Adaptive control method based upon controlling the potential energy density*..... 73

4.2.2 *Adaptive control method based upon controlling the kinetic energy density*..... 74

4.2.3 *Adaptive control method based upon controlling the acoustic energy density* 75

4.2.4 *Adaptive control method based upon controlling the acoustic active intensity using the P-U approach* 76

4.2.5 *Adaptive control method based upon controlling the active intensity using the P-P approach*..... 77

4.2.6 *Summary of the adaptive control methods* 79

4.2.7 *Optimal solution*..... 80

CHAPTER 5 : ACTIVE NOISE CONTROL IN ENCLOSED SPACE82

5.1 ACTIVE NOISE CONTROL IN ACOUSTIC ROOMS 82

5.1.1 *Experimental set up*..... 83

5.1.2 *Identification of the secondary source* 84

5.1.3 *Implementation of the controller in real time*..... 86

5.1.4 *Conclusion* 89

5.2 ACTIVE NOISE CONTROL OF THE ENGINE IN THE CABIN OF A VEHICLE 89

5.2.1 *Conclusion* 92

5.3 GENERAL CONCLUSION 92

CHAPTER 6 : ACTIVE NOISE CONTROL APPLIED TO ONE-DIMENSIONAL WAVEGUIDE.....	93
6.1 SPECTRAL ELEMENT METHOD FOR ONE-DIMENSIONAL ACOUSTIC WAVEGUIDES	93
6.1.1 <i>Element Matrix</i>	94
6.1.2 <i>Throw-off element</i>	96
6.1.3 <i>Imposing boundary conditions</i>	97
6.1.4 <i>Wave component</i>	97
6.1.5 <i>T-Duct Example one</i>	99
6.1.6 <i>Testing a particle velocity sensor</i>	103
6.2 THEORETICAL MODEL OF A DUCT WITH TWO ACOUSTIC SOURCES	106
6.2.1 <i>Primary source transfer functions</i>	108
6.2.2 <i>Secondary source transfer functions</i>	109
6.3 ANALYTICAL RESULTS USING THE OPTIMAL SOLUTION TO THE SECONDARY SOURCE	111
6.3.1 <i>Optimal Control Volume Velocity Q_s</i>	112
6.3.2 <i>Pressure and velocity fields with optimal secondary source</i>	113
6.3.3 <i>Acoustical impedance with optimal secondary source</i>	116
6.3.4 <i>Total energy in the duct with optimal secondary source</i>	117
6.3.5 <i>The Intensity with optimal secondary source</i>	118
6.3.6 <i>The radiated acoustic power from the sources with optimal secondary source</i>	119
6.3.7 <i>Conclusions</i>	121
6.4 APPLYING THE ADAPTIVE CONTROL METHODS IN A T-DUCT EXPERIMENTALLY.....	122
6.4.1 <i>Experimental measurements of the acoustical properties</i>	124
6.4.2 <i>Testing the error sensors</i>	127
6.4.3 <i>Off-line control analyses</i>	130
6.4.4 <i>Performance of the ASIC under phase mismatch in the error sensors</i>	133
6.4.5 <i>Energetic analysis</i>	136
6.4.6 <i>Conclusions</i>	140
6.5 GENERAL CONCLUSIONS	141

CHAPTER 7 : ACTIVE CONTROL OF THE SOUND RADIATED INTO CYLINDRICAL ACOUSTIC CAVITIES USING STRUCTURAL ACTUATORS.142

7.1	EXPERIMENTAL SET UP TO THE CYLINDRICAL CAVITY	144
7.2	MODAL ANALYSIS USING STRUCTURAL DISTURBANCE.....	148
7.2.1	<i>Structural Modal Analysis</i>	148
7.2.2	<i>Vibro-acoustic Modal Analysis</i>	152
7.2.3	<i>Conclusion</i>	156
7.3	EXPERIMENTAL SET UP FOR CONTROL APPLICATIONS.....	158
7.4	COMPARISON BETWEEN THE ASAC AND AVC METHODS FOR STRUCTURAL DISTURBANCES.....	159
7.4.1	<i>Identification of the secondary path</i>	163
7.4.2	<i>Theoretical comparison of multiple error-sensing strategies for a single frequency</i>	164
7.4.3	<i>Other possible control schemes</i>	168
7.4.4	<i>Theoretical comparison of single channel controlled for narrow band excitation</i>	169
7.4.5	<i>Experimental comparison of single channel control at a single frequency</i>	175
7.4.6	<i>Experimental comparison of single channel control for narrow band random disturbance</i>	177
7.4.7	<i>Conclusion</i>	180
7.5	COMPARISON BETWEEN THE ASAC AND AVC METHODS FOR ACOUSTIC DISTURBANCES.....	180
7.5.1	<i>Identification of the secondary path</i>	182
7.5.2	<i>Experimental comparison of single channel for tonal perturbation at 216 Hz</i>	183
7.5.3	<i>Conclusion</i>	185
7.6	GENERAL CONCLUSIONS	186

CAPÍTULO 8 (PORTUGUÊS) : CONCLUSÃO187

8.1	CONTROLE ATIVO DE RUÍDO EM GUIAS DE ONDAS UNIDIMENSIONAIS	187
8.2	CONTROLE DE VIBRAÇÃO E RUÍDO EM CILINDROS	189
8.3	SUGESTÕES DE TRABALHOS FUTUROS	190
8.4	PUBLICAÇÕES GERADAS POR ESTA TESE	191

CHAPTER 8 (ENGLISH) : CONCLUSION192

8.1 ACTIVE NOISE CONTROL IN ONE-DIMENSIONAL ACOUSTIC WAVEGUIDES.....	192
8.2 ACTIVE NOISE AND VIBRATION CONTROL IN CYLINDERS	194
8.3 SUGGESTIONS TO FUTURE RESEARCHES	195
8.4 PUBLICATION ARISING FROM THIS THESIS.....	196

REFERENCES197

APPENDIX A : DERIVATION OF COMPLEX VARIABLES201

A.1 BASIC DEFINITIONS.....	201
A.2 CASE I.....	203
A.3 CASE II.....	206
A.4 CASE III.....	209
A.5 SUMMARY	211
A.6 OTHER USUAL RELATIONS FOR COMPLEX NUMBERS	212
A.7 APPLICATION TO COST FUNCTIONS	212

APPENDIX B : MATLAB/SIMULINK PROGRAMS213

B.1 FILTERED-X LMS IN THE TIME DOMAIN	213
B.2 FILTERED-X LMS ESTIMATOR	215
B.3 FREQUENCY DOMAIN CONTROLLERS	216
<i>B.3.1 Filtered-X LMS in the frequency domain.....</i>	<i>217</i>
<i>B.3.2 ASIC using P-U approach.....</i>	<i>219</i>
<i>B.3.3 ASIC using the P-P approach</i>	<i>220</i>
<i>B.3.4 Stating the real time implementation</i>	<i>221</i>
<i>B.3.5 Program to load the dSPACE 1102 control board.....</i>	<i>222</i>
B.4 MATLAB CONTROLLERS	223
B.5 IMPLEMENTATION TO THE SPECTRAL ELEMENT METHOD TO ACOUSTIC CASES.....	227

APPENDIX C : MODAL PARAMETER IDENTIFICATION AND EXTRACTION FROM FRFS	231
C.1 LEAST MEAN SQUARE AS PARAMETER ESTIMATOR.....	232
C.2 EIGENSYSTEM REALIZATION ALGORITHM.....	234
C.3 ORTHOGONAL CHEBYCHEFF POLYNOMIALS METHOD	237
 APPENDIX D : LEAST MEAN SQUARE ALGORITHM.....	 240
D.1 INTRODUCTION TO THE ADAPTIVE FILTERING THEORY.....	240
D.2 MEAN-SQUARE ERROR.....	242
D.3 METHOD OF STEEPEST DESCENT	246
D.4 LMS ALGORITHM.....	247
D.4.1 Performance analysis.....	248
D.4.2 Normalized LMS algorithm.....	250
D.5 FILTERED-X LMS ALGORITHM	251
D.5.1 Convergence analysis	253
D.5.2 Normalization.....	255
D.6 NORMALIZED FILTERED-X LMS ALGORITHM IN THE FREQUENCY DOMAIN	255
 APPENDIX E : LIST OF THE EQUIPMENT.....	 258
E.1 EQUIPMENT USED IN THE ONE-DIMENSIONAL ACOUSTIC WAVEGUIDE.....	259
E.2 EQUIPMENT USED IN THE CYLINDRICAL SHELL	260

Figure List

FIGURA 1.1: ESQUEMA TÍPICO DE UM SISTEMA DE CONTROLE ATIVO DE RUÍDO.....	3
FIGURE 1.1: TYPICAL SCHEME OF AN ACTIVE NOISE CONTROL SYSTEM	14
FIGURE 3.1: COMPARISON BETWEEN THE “-” INSTANTANEOUS INTENSITY, $I(t)$, “...” ACTIVE INTENSITY, I_a , “-.-” REACTIVE INTENSITY, I_r , AND THE “---” TOTAL INTENSITY, $I_t = I_a + \sqrt{I_a^2 + I_r^2}$	49
FIGURE 5.1: MICROPHONE ARRAY IN THE ACOUSTIC CHAMBER.....	83
FIGURE 5.2: DETAIL OF (A) THE MICROPHONE ARRAY AND (B) THE PRIMARY AND SECONDARY SOURCES	84
FIGURE 5.3: DEVICES USED IN THE EXPERIMENTAL SET UP – 3 POWER AMPLIFIERS, 2 ANALOG FILTERS, 1 FUNCTION GENERATOR, 1 OSCILLOSCOPE, 1 SIGNAL CONDITIONING UNIT, 1 DSP CONTROL BOARD AND 1 SPECTRAL ANALYZER.....	84
FIGURE 5.4: BLOCK DIAGRAM OF THE IDENTIFICATION OF THE SECONDARY PATH	85
FIGURE 5.5: SECONDARY PATH FIR WEIGHTS IDENTIFIED IN THE LOW REVERBERANT ROOM.....	85
FIGURE 5.6: BLOCK DIAGRAM OF THE CONTROL IMPLEMENTATION.....	86
FIGURE 5.7: SOUND PRESSURE LEVEL MEASURED WITH THE MICROPHONE ARRAY AT (A) 270 Hz AND (B) 540 Hz. -○- NO CONTROL, -+- CONTROLLED	87
FIGURE 5.8: SOUND PRESSURE LEVEL IN THE ROOM MEASURED IN OCTAVES BY THE MICROPHONE AT POSITION (A) 15 CM, (B) 30 CM, (C) 45 CM, AND (D) 60 CM FROM THE ERROR SENSOR. -■- NO CONTROL, -□- CONTROLLED.	87
FIGURE 5.9: RESULTS ACQUIRED WITH THE ERROR SENSOR. (A) SPL IN OCTAVES, MEASURED BY A SPECTRAL ANALYZER; (B) SIGNAL ACQUIRED WITH THE DSPACE 1102 CONTROL BOARD.....	88
FIGURE 5.10: COMPARISON OF THE AUTO-SPECTRUM OF THE ERROR SENSOR. (A) NO CONTROL, (B) CONTROLLED.....	89
FIGURE 5.11: LOCALIZATION OF (A) THE MICROPHONE, (B) THE SECONDARY SOURCE IN THE VEHICLE CABIN.....	90
FIGURE 5.12: TIME-FREQUENCY SPECTRA OF THE SIGNALS ACQUIRED FROM THE DRIVER POSITION OBTAINED WITH THE SLIDING SHORT TIME FOURIER TRANSFORM TECHNIQUE (A) NO CONTROL, (B) CONTROLLED, AND (C) CONTROLLED AND EDITED.	91

FIGURE 6.1: ERRORS DUE TO THE FINITE DIFFERENCE APPROXIMATION IN: (A) PARTICLE VELOCITY, (B) ACTIVE INTENSITY.	99
FIGURE 6.2: EXPERIMENTAL SETUP FOR THE T-DUCT. UNITS IN CENTIMETERS.....	100
FIGURE 6.3: SEM MODEL OF THE T-DUCT. UNITS IN CENTIMETERS.	100
FIGURE 6.4: COMPARISON BETWEEN THE THEORETICAL AND EXPERIMENTAL IMPEDANCES IN THE T DUCT AT: (A) POSITION 2, (B) POSITION 3, (C) POSITION 4, (D) POSITION 5, (E) POSITION 6, (F) POSITION 8, (G) POSITION 9. “-” EXPERIMENTAL, “....” THEORETICAL. UNITS IN PA/V.	102
FIGURE 6.5: EXPERIMENTAL SETUP TO THE STRAIGHT DUCT. UNITS IN CENTIMETERS.....	103
FIGURE 6.6: TRANSFER IMPEDANCES FOR THE MICROPHONES LOCATED AT (A) POSITION 1, (B) POSITION 2, AND (C) POSITION 3. “-” EXPERIMENTAL, “....” THEORETICAL. UNITS IN DB REF. 1 PA/(M/S).	104
FIGURE 6.7: COMPARISON BETWEEN THE SEM, THE PARTICLE VELOCITY SENSOR, AND THE TWO MICROPHONES TECHNIQUE TO MEASURE THE (A) TRANSFER PARTICLE VELOCITY, (B) ACTIVE INTENSITY. -O- SEM APPROACH, -+- PARTICLE VELOCITY SENSOR, -□- P-P APPROACH.	105
FIGURE 6.8: ERRORS ARISING FROM THE FINITE DIFFERENCE APPROXIMATION IN THE STRAIGHT DUCT IN (A) PARTICLE VELOCITY, (B) ACTIVE INTENSITY.	105
FIGURE 6.9: COMPARISON BETWEEN THE PARTICLE VELOCITY PREDICTED BY THE SEM MODEL, AND BY PARTICLE VELOCITY SENSOR AND BY THE TWO-MICROPHONE TECHNIQUE CORRECTED WITH THE SEM INTERPOLATION FUNCTION. -O- SEM APPROACH, -+- PARTICLE VELOCITY SENSOR, -√- P-P APPROACH CORRECTED.	106
FIGURE 6.10. DIAGRAM OF THE IDEAL DUCT	107
FIGURE 6.11. THE OPTIMAL VOLUME VELOCITY “SAME RESULT PRODUCED BY THE THREE CONTROL STRATEGIES”	113
FIGURE 6.12. PRESSURE FIELD IN THE DUCT: (A) AT POSITION $x = L/4$; (B) AT THE ERROR SENSOR POSITION. -O- P_p ; -+- P_s ; *- P_t . $P_{REF} = 20 \mu\text{PA}$	115
FIGURE 6.13. PARTICLE VELOCITY FIELD IN THE DUCT: (A) AT POSITION $x = L/4$; (B) AT THE ERROR SENSOR POSITION. -O- U_p ; -+- U_s , AND *- U_t . $u_{ref} = P_{ref} / \rho_0 c$	115
FIGURE 6.14. THEORETICAL IMPEDANCE AT THE PRIMARY SOURCE POSITION. -O- Z_p ; *- Z_t , -+- IMPEDANCE OF A DUCT WITH $L/2$ AND $Z_R \rightarrow 0$. $Z_{REF} = 1 \text{ PA/(M/S)}$	117
FIGURE 6.15. TOTAL ENERGY DENSITY BEFORE AND AFTER THE CONTROL ACTION: (A) UPSTREAM (B) DOWNSTREAM. -O- PRIMARY SOURCE ACTING ALONE; -+- SECONDARY SOURCE ACTING ALONE WITH OPTIMAL VOLUME VELOCITY Q_s , *- SOUCES ACTING (CONTROL ON). $E_{REF} = 1 \text{ J}$	117
FIGURE 6.16. ACTIVE INTENSITY BEFORE AND AFTER THE CONTROL ACTION. THE MEASUREMENT POINT WAS AT 0,05 M BEFORE AND 0,05 M PAST THE SECONDARY SOURCE: (A) UPSTREAM (B) DOWNSTREAM. - O- PRIMARY SOURCE ACTING ALONE; -+- SECONDARY SOURCE ACTING ALONE WITH OPTIMAL VOLUME VELOCITY Q_s , AND *- IS THE SOUCES ACTING (CONTROL ON). $I_{REF} = 10^{-12} \text{ W/M}^2$	118
FIGURE 6.17. REACTIVE INTENSITY BEFORE AND AFTER THE CONTROL ACTION: (A) UPSTREAM (B) DOWNSTREAM. -O- PRIMARY SOURCE ACTING ALONE; -+- SECONDARY SOURCE ACTING ALONE WITH OPTIMAL VOLUME VELOCITY Q_s , AND *- SOUCES ACTING (CONTROL ON). $I_{REF} = 10^{-12} \text{ W/M}^2$	119
FIGURE 6.18. ACOUSTIC POWER RADIATED BY THE PRIMARY AND SECONDARY SOURCES: (A) SOURCES ACTING ONE AT A TIME, (B) SOURCES ACTING SIMULTANEOUSLY. -O- PRIMARY SOURCE; -+- SECONDARY SOURCE WITH OPTIMAL VOLUME VELOCITY Q_s . $W_{REF} = 10^{-12} \text{ W}$	120
FIGURE 6.19. ACOUSTIC POWER STORED (REACTIVE) BY THE PRIMARY AND SECONDARY SOURCES: (A) SOURCES ACTING ONE AT A TIME, (B) SOURCES ACTING SIMULTANEOUSLY. -O- PRIMARY SOURCE; -+- SECONDARY SOURCE WITH OPTIMAL VOLUME VELOCITY Q_s . $W_{REF} = 10^{-12} \text{ W}$	120
FIGURE 6.20: POSITION OF SENSORS AND ACTUATORS IN THE DUCT. LENGTHS ARE IN CENTIMETERS	122

FIGURE 6.21: EXPERIMENTAL SETUP DETAIL WITH THE ERROR SENSORS 5, 6 AND 7.....	123
FIGURE 6.22: BLOCK DIAGRAM OF THE EXCITATION SYSTEM	124
FIGURE 6.23: BLOCK DIAGRAM OF THE CONTROL SIGNAL	124
FIGURE 6.24: PHASE MISMATCH BETWEEN THE TWO MICROPHONE PAIRS. -O- 1 ST SENSOR PAIR; -+- 2 ND SENSOR PAIR.....	128
FIGURE 6.25: FREQUENCY RESPONSE FUNCTIONS (FRFs) OF THE SENSOR PAIRS. (A) 1 ST MICROPHONE PAIR (B) 2 ND MICROPHONE PAIR. -O- Z_{P5} ; -+- Z_{P7} ; -* Z_{S5} ; -□- Z_{S7}	128
FIGURE 6.26: COMPARISON OF THE 1 ST AND 2 ND SENSOR PAIRS. (A) THEORETICAL OPTIMAL CONTROL LAW OF THE ASIC-PP; (B) DENOMINATOR OF THE ASIC-PP. -O- 1 ST SENSOR PAIR; -+- 2 ND SENSOR PAIR.	129
FIGURE 6.27: SOUND INTENSITY PHASE OF THE ERROR SENSORS. -O- 1 ST SENSOR PAIR; -+- 2 ND SENSOR PAIR.	130
FIGURE 6.28: FREQUENCY RESPONSE FUNCTIONS (FRFs) BETWEEN THE SOURCES AND THE ERROR SENSORS IN THE PRESENCE OF THE RECONSTRUCTION FILTER. (A) ERROR SENSORS AT POSITIONS 5 AND 7, -O- Z_{P5} ; -+- Z_{P7} ; -* Z_{S5} ; -□- Z_{S7} ; (B) ERROR SENSORS AT POSITION 6. -O- Z_{P6} ; -+- Y_{P6} ; -* Z_{S6} ; -□- Y_{S6}	131
FIGURE 6.29: ANALYSIS OF THE ERROR SENSOR TO THE ASIC-PU CONTROLLER. (A) DENOMINATOR OF THE ASIC-PU; (B) PHASE OF THE SOUND INTENSITY.....	131
FIGURE 6.30: ANALYSIS OF THE ERROR SENSOR TO THE ASIC-PP CONTROLLER. (A) DENOMINATOR OF ASIC-PP; (B) PHASE OF THE SOUND INTENSITY.....	132
FIGURE 6.31: OPTIMAL VOLUME VELOCITY OF THE SECONDARY SOURCE. -O- LMS-P; -+- LMS-U; -* ASIC-PP; -□- ASIC-PU.....	133
FIGURE 6.32: OPTIMAL VOLUME VELOCITY OF THE SECONDARY SOURCE WITH $\pm 10^\circ$ PHASE MISMATCH BETWEEN THE ERROR SENSORS DURING THE IDENTIFICATION PROCESS. (A) ASIC-PU; (B) ASIC-PP. -O- WITHOUT ERROR PHASE; -+- $+10^\circ$ PHASE; -* -10° PHASE.....	134
FIGURE 6.33: DENOMINATOR OF THE ASIC WITH $\pm 10^\circ$ PHASE MISMATCH BETWEEN THE ERROR SENSOR PAIR. (A) DENOMINATOR OF THE ASIC-PU; (B) DENOMINATOR OF THE ASIC-PP. -O- WITHOUT ERROR PHASE; -+- $+10^\circ$ PHASE; -* -10° PHASE.....	134
FIGURE 6.34: OPTIMAL VOLUME VELOCITY OF THE SECONDARY SOURCE WITH $\pm 10^\circ$ PHASE MISMATCH BETWEEN THE IDENTIFICATION AND CONTROL PROCESS. (A) ASIC-PU; (B) ASIC-PP. -O- WITHOUT ERROR PHASE; -+- $+10^\circ$ PHASE; -* -10° PHASE.....	135
FIGURE 6.35: CHANGE IN THE EXPERIMENTAL VOLUME VELOCITY OF THE PRIMARY SOURCE CAUSED BY THE CONTROLLER. -O- LMS-P; -+- LMS-U; -* ASIC-PP; -□- ASIC-PU.....	137
FIGURE 6.36: ATTENUATION IN THE RADIATED ACOUSTIC POWER W_R . (A) PRIMARY SOURCE POWER ATTENUATION; (B) POWER RADIATED BY THE SECONDARY SOURCE RELATIVE TO THE POWER RADIATED BY THE PRIMARY SOURCE ALONE. -O- LMS-P; -+- LMS-U; -* ASIC-PP; -□- ASIC-PU.....	138
FIGURE 6.37: ATTENUATION IN THE ACTIVE INTENSITY I_A MEASURED (A) BETWEEN THE ERROR SENSORS AT POSITIONS 2 AND 3, (B) BETWEEN THE ERROR SENSORS AT POSITIONS 8 AND 9. -O- LMS-P; -+- LMS-U; -* ASIC-PP; -□- ASIC-PU.....	139
FIGURE 6.38: ATTENUATION IN THE POTENTIAL ENERGY DENSITY E_p MEASURED AT (A) POSITION 2, (B) POSITION 8. -O- LMS-P; -+- LMS-U; -* ASIC-PP; -□- ASIC-PU.....	140
FIGURE 7.1: EXPERIMENTAL SET UP OF THE CYLINDER.....	144
FIGURE 7.2: COVER DETAILS: FOAM WEDGES AND RUBBER RING	145

FIGURE 7.3: ACTUATORS AND SENSORS USED IN THE EXPERIMENT. (A) PZT; (B) VELOCITY SENSOR; (C) ACCELEROMETERS.....	145
FIGURE 7.4: SCHEMATIC DIAGRAM TO THE POSITION OF THE ACTUATORS AND SENSORS ALONG THE CYLINDER.....	146
FIGURE 7.5: ACTUATOR POSITIONS IN THE CYLINDRICAL PLANE. (A) SHAKER POSITION; (B) PZT POSITIONS.....	146
FIGURE 7.6: SENSOR ARRANGEMENT IN THE SEMI-CIRCLE IN THE CYLINDER – DIMENSIONS IN CENTIMETERS; WHERE • INDICATE THE ACCELEROMETER POSITIONS AND ■ INDICATE THE MICROPHONE POSITIONS.....	147
FIGURE 7.7: SENSORS USED IN EXPERIMENTAL SET UP. (A) ACCELEROMETER ARRAY, (B) MICROPHONE ARRAY AND VELOCITY SENSOR.	147
FIGURE 7.8: TYPICAL STRUCTURAL FREQUENCY RESPONSES ACQUIRED FOR THE ACCELEROMETER ARRAY. (A) USING AS REFERENCE THE SIGNAL FROM THE FORCE TRANSDUCER; (B) USING AS REFERENCE THE ELECTRIC SIGNAL SENT TO THE SHAKER; (C) USING AS REFERENCE THE ELECTRIC SIGNAL SENT TO THE PZT. UNITS: DB RELATIVE TO (A) 1 M/S ² /N; (B) AND (C) 10 M/S ² /V.....	149
FIGURE 7.9: NARROW-BAND STRUCTURAL FREQUENCY RESPONSES ACQUIRED FROM THE ACCELEROMETER ARRAY. (A) USING AS REFERENCE THE SIGNAL FROM THE FORCE TRANSDUCER; (B) USING AS REFERENCE THE ELECTRIC SIGNAL SENT TO THE SHAKER; (C) USING AS REFERENCE THE ELECTRIC SIGNAL SENT TO THE PZT SET. COLORMAP UNITS ARE IN DB RELATIVE TO (A) 1 M/S ² /N, (B) AND (C) 10 M/S ² /V.	149
FIGURE 7.10: COMPARISON BETWEEN THE ANALYTICAL 10 TH MODE SHAPE OF THE CYLINDRICAL SHELL WITH: (A) THE ODS MEASURED AT 216 Hz, (B) THE IDENTIFIED MODE SHAPE (TABLE 7.1). --- THEORETICAL MODE SHAPE; -o- EXPERIMENTAL USING THE FORCE TRANSDUCER AS REFERENCE; -+ - EXPERIMENTAL USING THE ELECTRICAL SIGNAL SENT TO THE SHAKER AS REFERENCE; -* - EXPERIMENTAL USING THE ELECTRICAL SIGNAL SENT TO THE PZT PATCHES AS REFERENCE.	152
FIGURE 7.11: FIRST CIRCUMFERENTIAL ANALYTICAL MODE SHAPE OF A CYLINDRICAL CAVITY.....	153
FIGURE 7.12: TYPICAL ACOUSTIC FREQUENCY RESPONSE FUNCTIONS FOR THE MICROPHONE ARRAY. (A) USING AS REFERENCE THE SIGNAL FROM THE FORCE TRANSDUCER; (B) USING AS REFERENCE THE ELECTRIC SIGNAL SENT TO THE SHAKER; (C) USING AS REFERENCE THE ELECTRIC SIGNAL SENT TO THE PZT PATCHES. UNITS: DB RELATIVE TO (A) 0.1 PA/N; (B) AND (C) 1 PA/V.	154
FIGURE 7.13: NARROW BAND FREQUENCY RESPONSE FUNCTIONS FOR THE MICROPHONE ARRAY IN THE LINE NUMBER 9. (A) USING AS REFERENCE THE SIGNAL FROM THE FORCE TRANSDUCER; (B) USING AS REFERENCE THE ELECTRIC SIGNAL SENT TO THE SHAKER; (C) USING AS REFERENCE THE ELECTRIC SIGNAL SENT TO THE PZT PATCHES. COLORMAP UNITS IN DB RELATIVE TO (A) 0.1 PA/N, (B) AND (C) 1 PA/V.....	154
FIGURE 7.14: AMPLITUDE OF THE ACOUSTIC FIELD AT 216 Hz FOR THE MICROPHONE ARRAY. (A) USING AS REFERENCE THE SIGNAL FROM THE FORCE TRANSDUCER; (B) USING AS REFERENCE THE ELECTRIC SIGNAL SENT TO THE SHAKER; (C) USING AS REFERENCE THE ELECTRIC SIGNAL SENT TO THE PZT PATCHES. UNITS ARE IN (A) PA/KGF, (B) AND (C) PA/V.....	155
FIGURE 7.15: TWO TIME INSTANTS FROM THE ANIMATION OF THE ODS IN THE FREQUENCY OF 216 Hz USING AS REFERENCE THE SIGNAL FROM THE FORCE TRANSDUCER. (A) MICROPHONE ARRAY FORMED BY THE MICROPHONE AT POSITION 1 (NEAR THE WALL), (B) MICROPHONE ARRAY FORMED BY THE MICROPHONE AT POSITION 4 (NEAR THE CENTER).	156
FIGURE 7.16: CONTROL SIGNAL GENERATION PATH FROM THE dSPACE 1102 CONTROL BOARD TO THE STRUCTURE	158
FIGURE 7.17: DIAGRAM OF THE SHAKER AND THE ERROR SENSORS TO CONTROL THE STRUCTURAL DISTURBANCE.....	159
FIGURE 7.18: DIAGRAM OF THE DRIVER AND THE ERROR SENSORS USED TO CONTROL THE ACOUSTIC DISTURBANCE.....	159

FIGURE 7.19: ERROR SENSOR PLACEMENT ON THE CYLINDRICAL SHELL CAVITY FOR THE STRUCTURAL DISTURBANCE EXPERIMENT. WHERE --●-- REPRESENT THE ACCELEROMETER POSITIONS, --○-- REPRESENT THE MICROPHONE POSITIONS, AND --*-- REPRESENT THE VELOCITY SENSOR POSITION.....	160
FIGURE 7.20: FREQUENCY RESPONSE FUNCTIONS MEASURED AT THE SENSORS INDICATED IN FIGURE 7.19. (A) BETWEEN THE ACCELEROMETERS AND THE SHAKER, (B) BETWEEN THE ACCELEROMETERS AND THE PZT PATCHES, (C) BETWEEN THE MICROPHONES AND THE SHAKER, (D) BETWEEN THE MICROPHONES AND THE PZT PATCHES, (E) BETWEEN THE VELOCITY SENSOR AND THE SHAKER, (F) BETWEEN THE VELOCITY SENSOR AND THE PZT PATCHES.	161
FIGURE 7.21: FREQUENCY RESPONSE FUNCTIONS OF THE ACCELEROMETER ARRAY USING AS REFERENCE THE (A) SHAKER, AND (B) PZT PATCHES. COLORMAP UNITS IN $M/S^2/V$	162
FIGURE 7.22: FREQUENCY RESPONSE FUNCTIONS FOR THE MICROPHONE ARRAY USING AS REFERENCE THE (A) SHAKER, AND (B) PZT PATCHES. COLORMAP UNITS IN Pa/V	163
FIGURE 7.23: COMPARISON BETWEEN THE MEASURED FRFs AND THE FRFs ESTIMATED USING ERA. (A) RELATIVE TO THE ACCELEROMETER AT POSITION 4; (B) TO THE MICROPHONE AT POSITION 1; (C) TO THE PARTICLE VELOCITY SENSOR. “-” MEASURED FRFs, “-” FRFs RECONSTRUCTED USING THE IDENTIFIED POLES.....	164
FIGURE 7.24: ATTENUATION IN THE ENERGY WHEN ONE ERROR SENSOR IS APPLIED. USING (A) ACCELEROMETERS, AND (B) MICROPHONES AS ERROR SENSORS. ATTENUATION IN THE -O- STRUCTURAL KINETIC ENERGY, AND +- ACOUSTIC POTENTIAL ENERGY.....	165
FIGURE 7.25: ATTENUATION IN THE ENERGY WHEN TWO ERROR SENSORS ARE APPLIED. USING (A) ACCELEROMETERS, AND (B) MICROPHONES AS ERROR SENSORS. ATTENUATION IN THE -O- STRUCTURAL KINETIC ENERGY, AND +- ACOUSTIC POTENTIAL ENERGY.....	165
FIGURE 7.26: ATTENUATION IN THE ENERGY WHEN THREE ERROR SENSORS ARE APPLIED. USING (A) ACCELEROMETERS, AND (B) MICROPHONES AS ERROR SENSORS. ATTENUATION IN THE -O- STRUCTURAL KINETIC ENERGY, AND +- ACOUSTIC POTENTIAL ENERGY.....	166
FIGURE 7.27: ATTENUATION IN THE ENERGY WHEN FOUR ERROR SENSORS ARE APPLIED. USING (A) ACCELEROMETERS, AND (B) MICROPHONES AS ERROR SENSORS. ATTENUATION IN THE -O- STRUCTURAL KINETIC ENERGY, AND +- ACOUSTIC POTENTIAL ENERGY.....	168
FIGURE 7.28: ATTENUATION IN THE ENERGY WHEN THE ASIC IS IMPLEMENTED. USING (A) ACCELEROMETERS, AND (B) MICROPHONES AS ERROR SENSORS. ATTENUATION IN THE -O- STRUCTURAL KINETIC ENERGY, AND +- ACOUSTIC POTENTIAL ENERGY.....	169
FIGURE 7.29: OPTIMAL CONTROL SIGNAL GENERATED USING THE THREE ERROR-SENSING STRATEGIES. USING AS ERROR SENSOR THE +- ACCELEROMETER AT POSITION 4; -* MICROPHONE AT POSITION 1; -□ VELOCITY SENSOR.	170
FIGURE 7.30: FREQUENCY RESPONSE FUNCTIONS MEASURED AT THE SENSORS INDICATED IN FIGURE 7.19 TO NARROW BAND. (A) BETWEEN THE ACCELEROMETERS AND THE SHAKER, (B) BETWEEN THE ACCELEROMETERS AND THE PZT PATCHES, (C) BETWEEN THE MICROPHONES AND THE SHAKER, (D) BETWEEN THE MICROPHONES AND THE PZT PATCHES, (E) BETWEEN THE VELOCITY SENSOR AND THE SHAKER, (F) BETWEEN THE VELOCITY SENSOR AND THE PZT PATCHES. -O- INDICATES THE FRFs USED TO CALCULATE THE OPTIMAL SOLUTION TO THE SECONDARY SOURCE	171
FIGURE 7.31: ATTENUATION IN THE (A) KINETIC ENERGY AND (B) POTENTIAL ENERGY. USING AS ERROR SENSOR THE +- ACCELEROMETER AT POSITION 4; -* MICROPHONE AT POSITION 1; -□ VELOCITY SENSOR.....	172
FIGURE 7.32: SYSTEM RESPONSE WHEN THE OPTIMAL CONTROL SIGNAL IS APPLIED AT THE FREQUENCY OF 216 HZ MEASURED WITH (A) ACCELEROMETERS, AND (B) MICROPHONES. -O- NO CONTROL AND CONTROLLED USING AS ERROR SENSOR THE +- ACCELEROMETER AT POSITION 4; -* MICROPHONE AT POSITION 1; -□ PARTICLE VELOCITY SENSOR.....	174

FIGURE 7.33: SYSTEM RESPONSE WHEN THE OPTIMAL CONTROL LAW IS APPLIED TO THE FREQUENCY OF 210 HZ IN THE (A) ACCELEROMETERS, AND (B) MICROPHONES. -O- NO CONTROL AND CONTROLLED USING AS ERROR SENSOR THE +- ACCELEROMETER AT POSITION 4; -* -MICROPHONE AT POSITION 1; -◇- VELOCITY SENSOR.	174
FIGURE 7.34: EXPERIMENTAL RESPONSES TO THE ADAPTIVE CONTROL USING ONE ERROR SENSING AT 216 HZ MEASURED WITH (A) ACCELEROMETERS AND (B) MICROPHONES; -O- NO CONTROL AND CONTROLLED USING AS ERROR SENSOR THE +- ACCELEROMETER AT POSITION 4; -* -MICROPHONE AT POSITION 1; -◇- VELOCITY SENSOR.	175
FIGURE 7.35: DIGITAL SIGNALS ACQUIRED WITH THE CONTROL BOARD BEFORE AND AFTER THE CONTROL APPLICATION – (A) SIGNAL FROM ACCELEROMETER AT POSITION 4; (B) SIGNAL FROM THE MICROPHONE AT POSITION 1; (C) SIGNAL FROM THE VELOCITY SENSOR; “—” CONTROL OFF, “—” CONTROL ON.....	176
FIGURE 7.36: CONTROL SIGNAL GENERATED WITH THE CONTROL BOARD. USING AS ERROR SENSOR THE +- ACCELEROMETER, -* - MICROPHONE, AND -◇- VELOCITY SENSOR.	176
FIGURE 7.37: ATTENUATION IN THE (A) STRUCTURAL KINETIC ENERGY AND (B) ACOUSTIC POTENTIAL ENERGY. USING AS ERROR SENSOR THE +- ACCELEROMETER AT POSITION 4; -* - MICROPHONE AT POSITION 1; -◇- VELOCITY SENSOR.	177
FIGURE 7.38: NORMALIZED STRUCTURAL RESPONSE. (A) NO CONTROL AND CONTROLLED USING AS THE ERROR SENSOR: (B) THE ACCELEROMETER AT POSITION 4, (C) THE MICROPHONE AT POSITION 1, AND (D) THE PARTICLE VELOCITY. COLORMAP UNITS IN $M/S^2/V$	178
FIGURE 7.39: NORMALIZED ACOUSTIC FIELD RESPONSE. (A) NO CONTROL AND CONTROLLED USING AS THE ERROR SENSOR, (B) THE ACCELEROMETER AT POSITION 4, (C) THE MICROPHONE AT POSITION 1, AND (D) THE PARTICLE VELOCITY. COLORMAP UNITS IN Pa/V	179
FIGURE 7.40: POSITION OF THE ERROR SENSORS UNDER ACOUSTIC DISTURBANCES.....	181
FIGURE 7.41: FREQUENCY RESPONSE FUNCTIONS MEASURED IN THE ERROR SENSORS USING AS REFERENCE THE ELECTRICAL SIGNAL SENT TO THE PZT PATCHES; -O- ACCELEROMETER; +- MICROPHONE; -* - VELOCITY SENSOR.	181
FIGURE 7.42: COMPARISON BETWEEN THE MEASURED FRFS AND THE ESTIMATED BY THE ERA. (A) FOR THE ACCELEROMETER; (B) FOR THE MICROPHONE AT POSITION 1; (C) FOR THE VELOCITY SENSOR; — MEASURED FRFS, --- FRFS RECONSTRUCTED USING THE IDENTIFIED POLES.....	182
FIGURE 7.43: IMPEDANCE MEASURED BY THE MICROPHONE ARRAY. -O- NO CONTROL AND CONTROLLED USING THE +- ACCELEROMETER; -* -MICROPHONE; -◇- PARTICLE VELOCITY SENSOR.	183
FIGURE 7.44: DIGITAL SIGNALS ACQUIRED WITH THE CONTROL BOARD BEFORE AND AFTER THE CONTROL APPLICATION. (A) SIGNAL FROM ACCELEROMETER AT POSITION 4; (B) SIGNAL FROM THE MICROPHONE AT POSITION 1; (C) SIGNAL FROM THE VELOCITY SENSOR; “—” CONTROL OFF; — CONTROL ON.....	184
FIGURE 7.45: CONTROL SIGNAL CAPTURED FROM THE CONTROL BOARD IN DISTINCT INSTANT TIMES DURING THE CONTROL APPLICATION. WHERE WAS IMPLEMENTED USING AS ERROR SENSOR THE +- ACCELEROMETER, -* - MICROPHONE, AND -◇- VELOCITY SENSOR.	185
FIGURE B.1: MAIN BLOCK OF THE NORMALIZED FILTERED-X LMS CONTROLLER IN THE TIME DOMAIN.....	213
FIGURE B.2: BLOCK OF THE NORMALIZED FILTERED-X LMS ALGORITHM.	214
FIGURE B.3: BLOCK DIAGRAM OF THE SECONDARY PATH	214
FIGURE B.4: PROGRAM “COCKPIT” TO CONTROL THE REAL TIME IMPLEMENTATION.	215
FIGURE B.5: MAIN BLOCK DIAGRAM TO THE FILTERED-X LMS AS AN ESTIMATOR.	215
FIGURE B.6: EXPANSION OF THE BLOCK NAMED ESTIMATOR nLMS IN FIGURE B.5.....	216

FIGURE B.7: BLOCKS TO IMPLEMENT THE FFT, EXPANSION OF THE BLOCK “TIME->FREQ”	216
FIGURE B.8: BLOCKS TO IMPLEMENT THE IFFT, EXPANSION OF THE BLOCK “FEQ->TIME”	216
FIGURE B.9: EXPANSION OF THE BLOCK “GROUP”	217
FIGURE B.10: BLOCK DIAGRAM OF THE FILTERED-X LMS IN THE FREQUENCY DOMAIN CONTROLLER	217
FIGURE B.11: EXPANSION OF THE BLOCK “FREQUENCY-DOMAIN FILTERED-X LMS CONTROLLER”	218
FIGURE B.12: EXPANSION OF THE BLOCK “FREQUENCY-DOMAIN FILTERED-X LMS ALGORITHM”	218
FIGURE B.13: EXPANSION OF THE BLOCK “NORMALIZATION” TO LMS	218
FIGURE B.14: BLOCK DIAGRAM OF THE ASIC-PU CONTROLLER	219
FIGURE B.15: EXPANSION OF THE BLOCK “ASIC-PU CONTROLLER”	219
FIGURE B.16: EXPANSION OF THE BLOCK “ASIC-PU ALGORITHM”	219
FIGURE B.17: EXPANSION OF THE BLOCK “NORMALIZATION – ASIC-PU”	220
FIGURE B.18: BLOCK DIAGRAM OF THE ASIC-PP CONTROLLER	220
FIGURE B.19: EXPANSION OF THE BLOCK “ASIC-PP CONTROLLER”	220
FIGURE B.20: EXPANSION OF THE BLOCK “ASIC-PP ALGORITHM”	221
FIGURE B.21: EXPANSION OF THE BLOCK “NORMALIZATION – ASIC-PP”	221
FIGURE B.22: INITIAL DATA FROM THE ASIC-PP	222
FIGURE B.23: GRAPHIC INTERFACE DEVELOPED IN COCKPIT 1.0 TO DRIVE THE CONTROLLERS IN REAL TIME	222
FIGURE C.1: BLOCK DIAGRAM OF THE LEAST MEAN SQUARE ALGORITHM AS AN ESTIMATOR	233
FIGURE D.1: DETAILED STRUCTURE OF THE TRANSVERSAL FILTER	241
FIGURE D.2: BLOCK DIAGRAM OF THE ADAPTIVE TRANSVERSAL FILTER	242
FIGURE D.3: PORTION OF A TWO-DIMENSIONAL QUADRATIC PERFORMANCE SURFACE	244
FIGURE D.4: SCHEMATIC REPRESENTATION OF AN ACTIVE NOISE CONTROL SYSTEM TO 1-ERROR SENSOR, 1- PRIMARY SOURCE AND 1-SECONDARY SOURCE	252
FIGURE D.5: BLOCK DIAGRAM OF THE FILTERED-X LMS ALGORITHM APPLIED TO ACTIVE NOISE CONTROL SYSTEMS	252

Table List

TABELA 1.1: ESQUEMAS DE CONTROLE E OS TIPOS DE ATUADORES E SENSORES UTILIZADOS.....	4
TABELA 1.2: TIPOS DE ATUADORES E OS ESQUEMAS DE CONTROLE MAIS COMUMENTE UTILIZADOS EM APLICAÇÕES DE CONTROLE ATIVO.....	7
TABELA 1.3: TIPOS DE SENSORES E OS ESQUEMAS DE CONTROLE ATIVO.....	8
TABLE 1.1: CONTROL SCHEMES AND THE KIND OF ACTUATORS AND SENSORS USED.	15
TABLE 1.2: ACTUATORS TYPE AND THE CONTROL SCHEMES GENERALLY USED IN ACTIVE CONTROL APPLICATIONS	17
TABLE 1.3: SENSORS TYPE AND THE ACTIVE CONTROL SCHEMES	19
<hr/>	
TABLE 3.1: FOURIER SERIES AND FOURIER TRANSFORM PROPERTIES	47
TABLE 4.1: OPTIMAL SOLUTIONS FOR THE VOLUME VELOCITY OF THE SECONDARY SOURCES.....	67
TABLE 4.2: OPTIMAL SOLUTIONS FOR THE VOLUME VELOCITY OF THE SECONDARY SOURCE FOR ONE ERROR SENSOR, ONE PRIMARY SOURCE AND ONE SECONDARY.	68
TABLE 4.3: OPTIMAL SOLUTION FOR THE VOLUME VELOCITY OF THE SECONDARY SOURCES USING THE P-P APPROACH TO ESTIMATE THE PARTICLE VELOCITY.....	72
TABLE 4.4: SUMMARY OF THE ADAPTIVE CONTROL METHODS.....	79
TABLE 7.1: RESULTS OF THE STRUCTURAL MODAL ANALYSIS.	150
TABLE 7.2: NATURAL FREQUENCY OF A CYLINDRICAL SHELL OF INFINITE LENGTH, WITH $E = 70\text{GPa}$, $\nu = 0.3$, R $= 0.48\text{ m}$, $H = 0.0021\text{ m}$ AND $\rho = 2800\text{ KG/M}^3$	151
TABLE 7.3: THEORETICAL NATURAL FREQUENCY OF A CLOSED CYLINDRICAL ACOUSTIC CAVITY.....	153
TABLE 7.4: RESULTS OF THE VIBRO-ACOUSTIC MODAL ANALYSIS.	155
TABLE 7.5: RESULTS OF THE SYSTEM IDENTIFICATION FOR THE CONTROL OF THE STRUCTURAL DISTURBANCES	164
TABLE 7.6: ERROR SENSOR SETS.....	167
TABLE 7.7: RESULTS OF THE SYSTEM IDENTIFICATION FOR THE CONTROL OF THE ACOUSTIC DISTURBANCES.	182

TABLE A.1: SUMMARY OF THE GRADIENT RELATIONS	211
TABLE B 1: VALUE OF THE GAINS TO THE SECONDARY PATH BLOCK	214
TABLE E.1: EQUIPMENT USED IN THE ONE-DIMENSIONAL ACOUSTIC WAVEGUIDE.....	259
TABLE E 2 : EQUIPMENT USED IN THE CYLINDRICAL SHELL.....	260

Nomenclature

Latin Letters

a – Radius of a circular duct	[m]
f – Frequency	[Hz]
i – Imaginary number - $\sqrt{-1}$	
u – Particle velocity	[m/s]
E_P – Acoustic potential energy density	[J]
E_K – Acoustic kinetic energy density	[J]
E_T – Acoustic total energy density	[J]
G – Power spectral density	
I – Sound intensity	[W/m ²]
K – Wavenumber	[1/m]
P – Sound pressure	[Pa]
Q – Volume velocity of acoustic sources	[(m/s)/m ³]
U – Volume velocity	[(m/s)/m ³]
Y – Particle velocity transfer function	[(m/s)/(m/s)]
Z – Acoustic Impedance	[Pa/(m/s)]

.....

Græek Letters

α, β - constants

δ - distance between two microphones [m]

ϕ - phase angle

λ - Wavelength [m]

μ - Step size

ρ_0 - air density [kg/m³]

ω - angular frequency [rad/s]

∇ - Gradient operator

∇^2 - Laplacian operator

.....

Superscripts

* - Conjugate

H - Hermitian

.....

Subscripts

a - Relative to propagation

s - Relative to the secondary source

p - Relative to primary source

r - Relative to storage

rad - relative to the radiation

.....

Abbreviations

ANC – Active Noise Control
ASAC – Active Structural Acoustic Control
ASIC – Active Sound/Structural Intensity Control
AVC – Active Vibration Control
LMS – Least Mean Square
PZT – Piezoelectric actuator/sensor
SEM – Spectral Element Method
IL – Intensity Level
SPL – Sound Pressure Level

Symbols

..... \Re - Real part of a complex number

..... \Im - Imaginary part of a complex number

.....

Capítulo 1 (Português)

Introdução

Controle ativo é um método de atenuação de distúrbios indesejados através do uso de fontes controláveis capazes de atuar no sistema eliminando estes distúrbios através da introdução de energia ou potência. Refere-se aqui ao controle ativo em contraposição aos sistemas passivos onde o controle é feito sem que se injetem potência ou energia no sistema a ser controlado.

Os sistemas de controle ativo são aplicados principalmente quando os controles passivos não atendem aos requisitos especificados de atenuação ou não apresentam uma solução adequada para o problema. De modo geral, a faixa de frequência do distúrbio a ser controlado especifica que tipo de controle, passivo ou ativo, deve ser usado. Em altas frequências os mecanismos de dissipação de energia interna dos materiais são geralmente efetivos e o controle passivo apresenta bons resultados. Já em baixas frequências torna-se muito difícil atenuar significativamente as perturbações de forma passiva, sendo indicado o uso do controle ativo.

Implementações adequadas de sistemas de controle ativo requerem um conhecimento detalhado tanto do sistema de controle quanto do sistema físico a ser controlado. Este conhecimento visa dar entendimento das capacidades e limitações dos sistemas de controle. Os princípios físicos envolvendo controle ativo podem ser encontrados com maiores detalhes em Elliott (2001), o qual sugere que a implementação adequada de um sistema de controle deve seguir os seguintes passos fundamentais,

1. *Análise do sistema físico utilizando modelos analíticos simplificados*, assim, pode-se estabelecer o desempenho esperado do sistema de controle ativo para a aplicação em questão;
2. *Cálculo do desempenho ótimo para várias estratégias de controle*, visa demonstrar analiticamente quais as possíveis estratégias de controle que podem ser implementadas com sucesso;
3. *Simulação de diferentes estratégias de controle utilizando dados do sistema real*, esta etapa estabelece precisamente qual a melhor estratégia de controle a ser implementada;
4. *Implementação da melhor estratégia de controle em tempo real*.

Os passos acima demonstram que o conhecimento das capacidades dos sistemas de controle ativo e das características físicas do problema são de vital importância na implementação de um sistema de controle ativo bem sucedido.

1.1 Configurações básicas de um sistema de controle ativo

Os sistemas de controle ativo são constituídos basicamente por processadores de controle, atuadores e sensores. Os atuadores podem ser separados em fontes primárias e secundárias, Hansen e Snyder (1997). As fontes primárias são todas as fontes responsáveis pela introdução da perturbação ou distúrbio no sistema físico. As fontes secundárias são fontes introduzidas artificialmente no sistema físico e visam eliminar os distúrbios provenientes das fontes primárias. Os sensores são os mecanismos responsáveis pela medição dos níveis de distúrbio presente no sistema físico. Um esquema básico de um sistema de controle ativo, neste caso controle ativo de ruído, para o caso de uma fonte primária, uma fonte secundária e um sensor de erro, conhecido como 1-1-1, Kuo e Morgan (1996), pode ser observado na Figura 1.1.

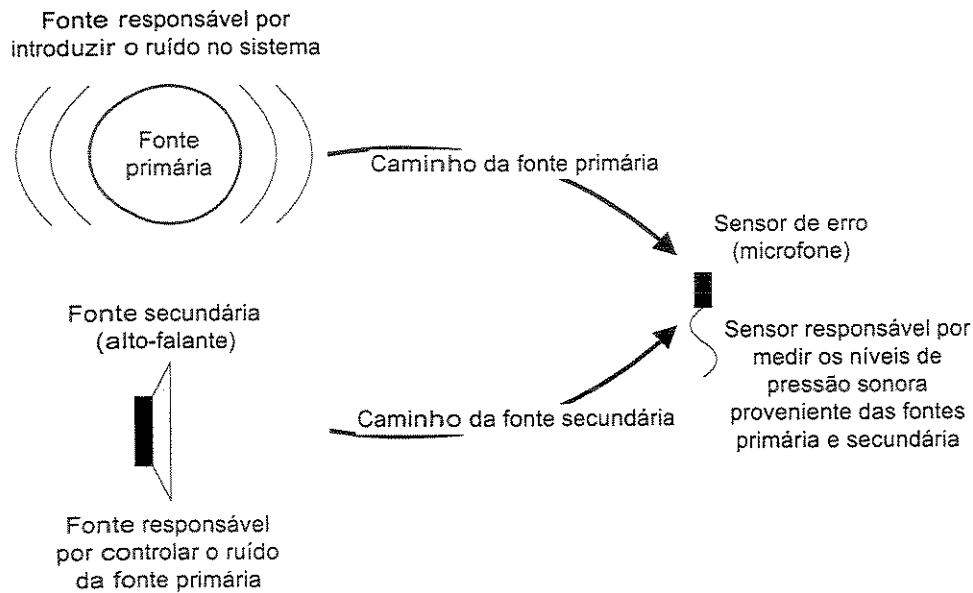


Figura 1.1: Esquema típico de um sistema de controle ativo de ruído

Além dos atuadores e sensores, há o método de controle, que é responsável pela geração dos sinais de controle, conhecidos como lei de controle, enviados às fontes secundárias. Os métodos de controle são caracterizados por uma função objetivo ou função de custo, a qual oferece ao método de controle informações sobre o que do sistema físico deve ser alterado.

A escolha da função de custo a ser implementada depende do tipo de atuação desejada e da posição e tipo de sensores e atuadores. Porém, a principal informação para a definição de qual função de custo deve ser utilizada vem do próprio sistema físico em que será implementado o sistema de controle, significando que uma análise prévia do sistema representa um dos primeiros passos para a implementação de um sistema de controle eficaz.

Desta forma, a escolha e a localização dos atuadores e sensores bem como a escolha do método de controle e de sua função custo são fatores decisivos na implementação de um sistema de controle que apresente desempenho satisfatório.

1.2 Esquemas de controle ativo

Dependendo das posições dos atuadores e sensores, o sistema de controle ativo recebe denominações diferentes. As mais comuns são as técnicas conhecidas como Controle Ativo de Vibração - AVC (“Active Vibration Control”), Fuller et al. (1996), Controle Ativo de Ruído - ANC (“Active Noise Control”), Elliott e Nelson (1992) e Controle Ativo de Ruído utilizando atuadores Estruturais - ASAC (“Active Structural Acoustic Control”), Fuller e Jones (1987) e Snyder e Hansen (1991). As diferenças entre os três esquemas de controle podem ser observadas na Tabela 1.1. Onde observa-se que a diferença entre ASAC e AVC é o tipo de sensor utilizado, enquanto que entre ANC e ASAC é o tipo de atuador empregado.

Tabela 1.1: Esquemas de controle e os tipos de atuadores e sensores utilizados.

Esquemas de Controle	Tipo de Atuador	Tipo de Sensor
ANC	Acústico	Acústico
ASAC	Estrutural	Acústico
AVC	Estrutural	Estrutural

À primeira vista, os esquemas de controle são muito similares; porém, os resultados obtidos e a sua utilização são diferentes. O AVC é recomendado para controle ativo de vibração, enquanto que o ANC é recomendado para controle ativo de ruído e o ASAC é recomendado para aplicações onde o objetivo é controlar o som radiado de uma estrutura vibrando. Assim, a escolha adequada do esquema de controle a ser implementado apresenta grande influência no desempenho final do sistema de controle ativo.

1.3 Algoritmos de controle ativo

Os algoritmos de controle ativo são os métodos responsáveis pelos cálculos envolvidos na obtenção das leis de controle que devem ser enviadas às fontes secundárias. Os algoritmos de controle ativo podem utilizar informações provenientes dos sensores de erro (por exemplo, em sistema de controle em realimentação), do conhecimento prévio do sistema físico (por exemplo,

da função de transferência entre a fonte secundária e o sensor de erro), do objetivo a ser atingido (função de custo) e do distúrbio introduzido pela fonte primária (conhecido como sinal de referência, utilizado em sistema de controle em avanço), entre outras.

Os algoritmos de controle ativo mais utilizados em ANC, ASAC e AVC são baseados na teoria de filtragem adaptativa na configuração de avanço ("feedforward"), Elliott e Nelson (1992), Kuo e Morgan (1996), Widrow e Steins (1985). A filtragem adaptativa é utilizada principalmente devido às características de pequenas variações que as plantas, em particular acústicas, sofrem; assim, os sistemas de controle ativo podem adaptar-se a elas sem comprometer o desempenho global. A utilização de um sistema em avanço torna possível cancelar apenas as perturbações que estão correlacionadas com uma dada referência. Porém, apresentam o inconveniente de necessitarem de uma referência do distúrbio, que em alguns casos não está disponível. Além disso, a filtragem adaptativa requer usualmente sofisticadas placas de controle de processamento digital, conhecidas como DSP ("Digital signal processing") para a implementação do algoritmo adaptativo de controle, Kuo e Morgan (1996).

Os algoritmos de controle ativo são baseados em ajustar um conjunto de pesos de acordo com uma lei de adaptação a fim de atingir uma determinada função de custo. Esta função de custo pode ser a energia potencial, a energia cinética ou a energia total de um sistema acústico ou vibracional. Recentemente foram incluídas as funções de custo baseadas em controle de intensidade ativa, reativa ou total. Desta forma, estes algoritmos de controle ativo visam controlar a energia contida ou que se propaga em um sistema físico.

Como consequência, uma análise cautelosa do sistema permite encontrar adequadamente qual função de custo deve ser implementada, e esta pode ser escolhida segundo condições energéticas tais como condições de ondas estacionárias e/ou propagantes e direção do fluxo de energia.

1.4 Controle ativo utilizando teoria de filtragem adaptativa

O objetivo não é iniciar uma discussão sobre qual o tipo de controle ativo mais adequado a ser implementado, mas dar alguns dos fundamentos sobre a escolha do método que será utilizado. Implementações sobre diferentes tipos de controladores podem ser encontradas em Elliott e Nelson (1992), Kuo e Morgan (1996) e Snyder e Hansen (1997).

De modo geral, ambientes acústicos sofrem pequenas alterações de impedância ao longo do tempo ocasionadas por aberturas de portas e janelas, posições das pessoas no ambiente acústico e outros tipos de intrusões. Além disso, os distúrbios acústicos são, de maneira geral, conhecidos, isto é, é possível identificar as fontes geradoras do ruído no ambiente acústico.

Assim, na maioria dos casos, a aplicação de controle ativo de ruído em ambientes significa controlar um sistema que pode variar ao longo do tempo e é possível obter uma referência do distúrbio. Um método de controle ativo adequado a estas características é o conhecido Filtered-X LMS, que é um método de controle baseado em filtragem adaptativa utilizando um controle em avanço. Características de convergência do método de controle podem ser achadas no apêndice D.

Contudo, metodologias de controle em realimentação, tais como controle ótimo, controle robusto, entre outras, podem ser utilizadas dependendo das características do sistema de controle, como variações das plantas envolvidas no processo, posição dos atuadores e sensores, tempo de atuação, estacionaridade da perturbação, etc.

1.5 Tipos de Atuadores e sensores

Os atuadores e sensores utilizados em controle ativo são dos mais variados tipos; sua escolha freqüentemente está relacionada com o tipo de esquema adotado e com o sistema em que será implementado.

Porém, de maneira geral, os atuadores podem ser do tipo excitadores eletrodinâmicos (“shakers”), atuadores piezelétricos (PZT¹), Lima Jr (1999), e alto-falantes. A aplicação dos atuadores em função do esquema de controle é encontrada na Tabela 1.2.

Tabela 1.2: Tipos de atuadores e os esquemas de controle mais comumente utilizados em aplicações de controle ativo

Tipo de controlador	Tipo de atuação	Tipo de atuador
AVC, ASAC	Estrutural	Excitador eletrodinâmico
AVC, ASAC	Estrutural	Atuador piezelétrico
ANC	Acústica	Alto-falante

Os excitadores eletrodinâmicos são utilizados como atuadores estruturais impondo deslocamento, velocidade, aceleração ou força. Podem ser do tipo inercial ou por molas; os inerciais apresentam a facilidade de não necessitarem de uma base de apoio e serem diretamente fixados em qualquer parte da estrutura; já os por mola necessitam de uma base externa para dar apoio à atuação. A simplicidade de uso e sua fácil fixação tornaram os excitadores eletrodinâmicos os atuadores estruturais mais típicos; porém, apresentam porte relativamente grande se comparado aos atuadores piezelétricos, sendo geralmente inviáveis em aplicações de controle ativo de estruturas.

Os atuadores piezelétricos são utilizados como atuadores estruturais e são constituídos por materiais cerâmicos que transformam voltagem em deformação (e vice-versa) e são fixados por meio de cola adesiva diretamente na estrutura, Lima Jr. (1999). São de fácil aplicação e apresentam bom desempenho. Porém, sua atuação é de baixa potência e normalmente requerem grande amplificação da voltagem para atingir um nível adequado de atuação para aplicações em sistemas de controle ativo. Além disso, o seu processo de fabricação pode limitar sua aplicação a estruturas planas ou com um determinado raio de curvatura máximo. Entretanto, são menores, mais leves e mais baratos em relação aos excitadores eletrodinâmicos, desta forma, são mais adequados como atuadores em sistemas de controle ativo.

¹ Titanato Zirconato de Chumbo (PZT): cerâmica piezelétrica utilizada como atuador ou sensor.

Os alto-falantes são utilizados como atuadores acústicos e são classificados quanto à sua faixa de frequência de atuação sendo basicamente divididos em “sub-woofer”, “woofer”, e “tweeter”, para baixa, média e alta frequência, respectivamente, além dos “horn drivers” para altas potências.

Assim como os atuadores, os sensores dependem do esquema de controle e do tipo de sistema em que será aplicado. Podem-se destacar os acelerômetros, sensores piezelétricos, Lima Jr. (1999), vibrômetros laser Doppler, microfones, sensores de velocidade de partícula, Bree et al. (1996, 1999) e Eerden et al. (1998), sondas de intensidade, Fahy (1995), sensores em filme PVDF². A aplicação dos sensores em cada esquema de controle é encontrada na Tabela 1.3.

Tabela 1.3: Tipos de sensores e os esquemas de controle ativo

Tipos de sensor	Tipos de esquema	Tipos de medida
Acelerômetros	AVC	Aceleração
Sensores piezelétricos	AVC	Deformação
Vibrômetros laser	AVC	Velocidade e deslocamento
Filmes PVDF	AVC	Deformação
Microfones	ANC, ASAC	Pressão
Sensores de velocidade	ANC, ASAC	Velocidade
Sondas de intensidade	ANC, ASAC	Intensidade

Os acelerômetros são os sensores mais comumente utilizados para o esquema AVC, por serem pequenos, fáceis de serem instalados e de custo relativamente baixo. Os sensores piezelétricos são do mesmo tipo que os atuadores, já que servem tanto como atuadores como sensores. Os vibrômetros laser são equipamentos caros para serem implementados em sistemas de controle ativo; porém, podem ser utilizados em seu desenvolvimento, já que são de fácil manuseio e apresentam excelentes resultados práticos. Os microfones são os mais comuns sensores para o esquema ANC e ASAC; porém, nos últimos anos os sensores de velocidade de

² Fluorido de Polivinilideno (PVDF): filme plástico piezelétrico.

partícula e as sondas de intensidade têm ganhado notoriedade devido ao uso crescente de funções de custo que envolvem fluxo de energia.

Como pode ser observado, os atuadores e sensores utilizados em sistemas de controle ativo apresentam um grande variedade de tipos e de aplicações, permitindo a implementação das mais variadas formas de controle ativo. Por si só, a escolha dos atuadores e sensores é um passo importante para a implementação adequada de um sistema de controle ativo que atenda às necessidades estabelecidas em projeto.

1.6 Importância da análise energética

Com a análise energética de sistemas ativamente controlados têm-se informações indispensáveis ao entendimento da forma de funcionamento do sistema, isto é, a introdução de fontes secundárias em um sistema causa alterações nos padrões de distribuição energética no sistema; assim, um entendimento profundo permite ao projetista identificar possíveis posições onde os atuadores e sensores afetam o sistema de uma forma benéfica, isto é, diminuindo o nível de energia global do sistema, Elliott (2001).

Diferentemente de variáveis como deslocamento, velocidade e aceleração, que são quantidades de primeira ordem, as variáveis energéticas como energia potencial e cinética são quantidades de segunda ordem. São quantidades conservativas, mais fáceis de serem usadas para o desenvolvimento de modelos analíticos, Fahy (2001). Além disso, para médias e altas frequências a abordagem energética constitui uma das principais ferramentas de modelagem e análise, Arruda (2001), e possui a capacidade de fornecer funções de custo quadráticas em termos dos sinais que devem ser enviados às fontes secundárias, Qiu e Hansen (1998) e Elliott e Nelson (1992).

A forma mais interessante de controle energético consiste em evitar que as fontes primárias introduzam energia ou potência ao sistema, reduzindo assim a energia presente. Outra possibilidade é evitar que a energia de uma determinada parte do sistema propague, restringindo, assim, a distribuição de energia a uma determinada região do sistema. Finalmente, podem ser

criados sorvedouros de energia, que podem diminuir a energia do sistema; porém, neste caso o sistema continua tendo um grande fluxo de energia proveniente das fontes de distúrbio em direção ao sorvedouro.

1.7 Objetivos desta tese

O objetivo central deste trabalho é a comparação das funções de custo envolvendo energia ou a propagação de energia em sistemas de controle ativo de ruído. As funções de custo comparadas são a densidade de energia potencial, densidade de energia cinética e a intensidade ativa, todas implementadas no domínio da frequência, tanto na análise teórica quanto experimental. Os sistemas de controle ativo de ruído serão implementados em um ambiente unidimensional (guia de onda) para a verificação do comportamento energético de sistema ativamente controlado envolvendo as diferentes funções de custo. O ambiente unidimensional é modelado utilizando o método dos elementos espectrais, Doyle (1997), aplicado ao caso acústico a fim de obter analiticamente o desempenho dos métodos de controle ativo e o comportamento energético do sistema. Como consequência, será verificado experimentalmente o desempenho dos métodos de controle ativo de ruído fazendo uma ponte entre a implementação teórica e experimental para explicar as possíveis diferenças entre os resultados.

É feita a comparação dos três esquemas de controle ativo - ANC, AVC e ASAC - na atenuação de ruído e da vibração em cilindros, isto é, na atenuação da vibração da casca cilíndrica e na atenuação do ruído radiado para o interior da cavidade, sendo o sistema sujeito à excitação estrutural e acústica. Para entender os fenômenos envolvidos, é feita a análise modal estrutural e acústica para verificar as interações fluido/estrutura existentes. Utilizando o resultado da análise modal, uma investigação analítica é desenvolvida comparando os resultados obtidos utilizando os diversos esquemas de controle ativo. A implementação dos esquemas de controle ativo em tempo real é realizada a fim de verificar as possíveis diferenças entre as funções de custo envolvidas no processo de controle ativo.

1.8 Organização da tese

Esta tese está assim dividida:

- Capítulo 1: Uma visão geral de sistemas de controle ativo e de sua implementação é feita visando dar entendimento de sua complexidade.
- Capítulo 2: Uma revisão bibliográfica dos principais trabalhos e avanços científicos é apresentado.
- Capítulo 3: Este capítulo fornece uma visão geral das propriedades acústicas e das equações básicas para o desenvolvimento dos métodos de controle ativo.
- Capítulo 4: Os métodos de controle ativo são desenvolvidos, juntamente com suas soluções ótimas para as velocidades de volume das fontes secundárias em função das velocidades de volume das fontes primárias e das funções de transferência envolvidas no processo. Além disso, os métodos de controle utilizando filtragem adaptativa para as diversas funções de custo são deduzidos.
- Capítulo 5: Uma aplicação simples de controle ativo de ruído em veículos é descrita.
- Capítulo 6: Descreve-se o método dos elementos espectrais para o caso acústico unidimensional, sendo verificado experimentalmente através de dois exemplos simples. É feita uma análise teórica de um sistema de controle ativo em cavidades e, finalmente, a implementação dos métodos de controle ativo em tempo real é feita para uma comparação teórico/experimental.
- Capítulo 7: É realizada a verificação dos esquemas de controle ativo aplicados em um cilindro, onde é aplicada uma análise modal estrutural e acústica para fornecer os fundamentos necessários para a implementação em tempo real dos esquemas de controle ativo.
- Capítulo 8: São apresentadas as conclusões gerais desta tese.
- Capítulo 9: Bibliografia utilizada nesta tese.
- Apêndice A: São demonstradas as derivações das funções complexas utilizadas para equacionar os algoritmos de controle ativo.
- Apêndice B: Os programas necessários para a implementação dos algoritmos de controle em tempo real são apresentados.
- Apêndice C: Uma revisão dos métodos de estimação de parâmetros utilizados é dada.
- Apêndice D: Uma revisão geral do algoritmo Least Mean Square é apresentada.

Chapter 1 (English)

Introduction

Active control is a method of attenuation of unwanted disturbances with the use of controllable sources that are capable of acting in the system to abate the effect of the disturbances with the introduction of energy or power. The active control distinguishes itself from passive techniques, where the control is performed without the addition of energy or power in the system to be controlled.

Active control systems are mainly applied when passive controllers do not achieve the project requirements or are not a good solution to the problem. Generally, the frequency range of the disturbances to be controlled dictates the kind of control - passive or active - should be used. At high frequencies, the internal energy dissipation mechanisms of the materials are generally effective and passive control achieves better results. At low frequencies, it is very difficult to attenuate the disturbances using passive devices and, in this case, it is better to use active control.

Adequate implementations of active control systems require a detailed knowledge of both the control system and the physical system to be controlled. This knowledge gives understanding about the capability and possible limitations of the control systems. The physical and mathematical principles involved in the active control of sound can be found with more detail in Elliott (2001), who suggests that a suitable implementation of a control system should follow these fundamental steps,

1. *Analysis of the physical system using simplified analytical models*; thus, it is possible to determine the expected performance of the active control system to be implemented;
2. *Calculation of the optimum performance using different control strategies under ideal control conditions*; thus, it is possible to know the best control strategies to be implemented successfully;
3. *Simulation of different control strategies using data from the physical system that is to be controlled*; this step shows precisely what control strategy should be implemented;
4. And, finally, *the implementation of a real-time controller and testing of the system under all conditions to ensure that its behavior is as predicted*.

The above steps demonstrate that the knowledge of the controller and the physical characteristics of the problem are very important in the successful implementation of an active control system.

1.1 Basic configurations of an active control system

Active control systems consist basically of a control processor, actuators and sensors. The actuators can be divided into primary and secondary sources, Hansen and Snyder (1997). The primary sources are the sources responsible for introducing the perturbation or the disturbance in the physical system. The secondary sources are the sources introduced artificially in the physical system to attenuate the disturbance from the primary sources. The error sensors are responsible for measuring the disturbance level present in the physical system. A basic scheme of an active control system, in this case the active noise control system, for the case of one primary source, one secondary source, and one error sensor, known as 1-1-1, Kuo and Morgan (1996), can be observed in Figure 1.1.

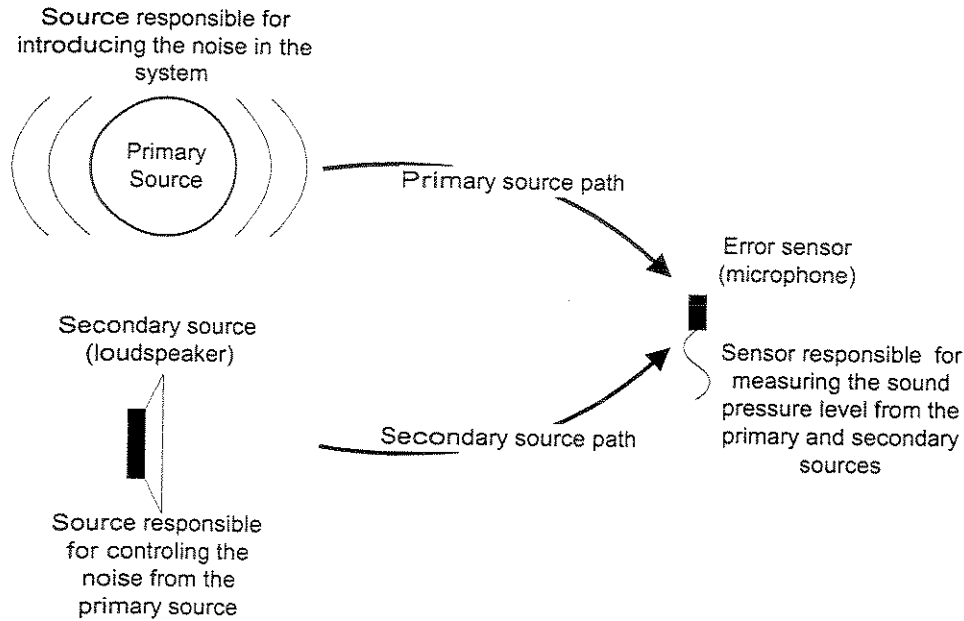


Figure 1.1: Typical scheme of an active noise control system

Besides the actuators and sensors, there is the control processor, which is responsible for the generation of the control signals, known as the control law, sent to the secondary sources. Control methods are characterized by an objective function or cost function, which offers to the control method information about what should be minimized in the physical system.

The choice of the cost function that should be implemented depends on the kind of desired actuation and the kind of actuator and sensor used. However, the main information to define what cost function should be used comes from the physical system where the controller will be implemented, which means that the previous analysis of the physical system represents one of the first steps to implement an active control system efficiently.

In short, the choice and the location of the actuators and sensors as well as the choice of the control method and its cost function are decisive factors in the implementation of an active control system that aims at achieve a desired performance.

1.2 Active control schemes / Esquemas de controle ativo

Depending on the actuator and sensor positions, the active control systems receive different terminology. The most used techniques are the AVC (Active Vibration Control), Fuller et al. (1996), the ANC (Active Noise Control), Elliott e Nelson (1992), and the ASAC (Active Structural Acoustic Control), Fuller and Jones (1987) and Snyder and Hansen (1991). The difference between the schemes can be observed in the Table 1.1. Where it can be observed that while the difference between ASAC and AVC is the type of sensor, the difference between ANC and ASAC is the type of actuator.

Table 1.1: Control schemes and the kind of actuators and sensors used.

Control scheme	Actuator type	Sensor type
ANC	Acoustic	Acoustic
ASAC	Structural	Acoustic
AVC	Structural	Structural

The control schemes are very similar. However, the final results and their utilization may be very different. The AVC is recommended to control vibration, the ANC is recommended to control noise, and the ASAC is recommended in applications where the objective is to control the radiated sound by a vibrating structure. Thus, the adequate choice of the control scheme to be implemented has great influence upon the performance of the active control system.

1.3 Active control algorithm

The active control algorithms are the methods responsible for the calculations involved in the generation of the control law, i.e., of the signals that should be sent to the secondary sources. The active control algorithms use the information from the error sensors, the previous knowledge of the physical system (i.e., the transfer function between the secondary source and the error sensor), the objective to be achieved (the cost function), and from the disturbance introduced by

the primary source (so-called reference signal, which is used in feedforward control systems), and others.

The most used active control algorithms in ANC, ASAC, and AVC schemes are based upon the feedforward adaptive filtering theory, Elliott and Nelson (1992), Kuo and Morgan (1996), Widrow and Steins (1985). The adaptive filtering theory is mainly used due small variations of the paths, in particular the acoustic paths. Thus, the active control systems can adapt to small variations without degrading the global system performance. Besides, the use of the feedforward system makes it possible to cancel the disturbance correlated to the reference signal. It should be mentioned that a good reference from the disturbance is necessary and that, in some cases, this reference is not available. Furthermore, the adaptive filtering systems require sophisticate signal processing control boards, known as DSP (Digital Signal Processing) for the implementation of the adaptive algorithm, Kuo e Morgan (1996).

The active control algorithms are based upon adjusting a set of weights following an adaptation law to minimize a given cost function, which can be the potential energy, the kinetic energy or the total energy of an acoustic or vibrating system. Recently, function such as the active, the reactive, and the total intensity were included as cost functions. Thus, these active control algorithms control the stored or the propagating energy in the physical system.

As a consequence, a careful analysis of the system allows to adequately find what cost function should be implemented, which can be chosen according to energetic conditions such as the stationary or the propagating waves and the energy flux direction.

1.4 Active control using adaptive filtering theory

The objective here is not starting a discussion about what the type of active control is best to be implemented, but to give some information about the choice of the method that will be used. Implementations of different controller types can be found in Elliott and Nelson (1992), Kuo and Morgan (1996), and Snyder and Hansen (1997).

The majority of acoustic fields suffer small impedance changes in time, which are caused by door and window openings, the number and the position of people present in the acoustic field, etc. Moreover, the acoustic disturbances are, in general, known, i.e., it is possible to identify the sources that are generating the noise in the field.

Thus, in the majority of the cases, the application of active noise control in acoustic fields means to apply the control in a time-variant system and it is possible to obtain a reference of the disturbance. An active control method that uses these characteristics is known as the Filtered-X LMS. It is a control method based on the adaptive filtering theory using a feedforward scheme. Characteristics of convergence of the control method can be found in appendix D.

However, other feedback control methodologies, such as optimal control, robust control, and others, can be used depending on the characteristics of the system, e.g., variations of the plants in the control process, actuator and sensor position, time to act, stationarity of the disturbance, etc.

1.5 Sensor and actuator types

The actuators and sensors used in active control are of varied types and applications. Their choice is frequently related to the type of control scheme and the type of physical system where the implementation is performed.

However, in a general way, the actuators can be electrodynamic exciters (shakers), piezoelectric actuators (PZT), Lima Jr (1999), and loudspeakers. The function and the schemes where the actuators are employed are shown in the Table 1.2.

Table 1.2: Actuators type and the control schemes generally used in active control applications

Controller type	Actuation type	Actuator type
AVC, ASAC	Structural	Electrodynamics actuator
AVC, ASAC	Structural	Piezoelectric actuator
ANC	Acoustic	loudspeaker

The electrodynamic exciters are used as structural actuators imposing displacement, velocity, acceleration or force. They can be inertial or by spring. While the inertial ones have the facility of not needing an external foundation and being directly attached to any part of the structure, the spring ones need a foundation to give support to the actuation. Their simplicity of use and their easy attachment made them the most typical structural actuators. However, their relatively large weight if compared with piezoelectric actuators and the need for an external attachment make them unsuitable for active control.

Piezoelectric actuators are used as structural actuators and consist of a ceramic patch that transforms voltage in deformation (and vice-versa), they can be attached using glue directly on the structure, Lima Jr. (1999). They are easily applicable and show good performance. However, they deliver relatively small forces, and need a power amplifier to achieve a desired performance in active control systems. Besides, the fabrication process can limit its application to plane structures or structures with small curvatures. They are much lighter and cheaper than the electrodynamic exciters. Thus, they are more adequate in active control applications.

Loudspeakers are used as acoustic actuators and are classified in relation to the frequency band of actuation, and are basically divided in “sub-woofer”, “woofer” and “tweeter”, for low, middle, and high frequencies, respectively, besides the “horn drivers” used for high power amplifications.

As with the actuators, the choice of the sensors depends on the control scheme and the physical system in which the sensor is applied. Among the most widely used are accelerometers, piezoelectric sensors, Lima Jr. (1999), laser Doppler vibrometers, microphones, particle velocity sensors, Bree et al. (1996, 1999) and Eerden et al. (1998), intensity probes, Fahy (1995), PVDF film sensors. The sensors used in each control scheme is shown in Table 1 3.

Table 1 3: Sensors type and the active control schemes

Sensors type	Scheme type	Measurement type
Accelerometers	AVC	Acceleration
Piezoelectric Sensors	AVC	Deformation
Laser Vibrometers	AVC	Velocity e displacement
PVDF films	AVC	Deformation
Microphones	ANC, ASAC	Pressure
Velocity sensors	ANC, ASAC	Velocity
Intensity Probes	ANC, ASAC	Intensity

Accelerometers are the most commonly used sensors in AVC schemes, because they are of relatively small size, easy to be installed and of low cost. The piezoelectric sensors are of the same type of the piezoelectric actuators, which means that they can be used either as sensors or as actuators. The laser Doppler vibrometer can be used in the development phase of active control systems, since they are easy to be used and shown excellent performance; however, they are too expensive to be used permanently in a control system. The microphones are the most common sensors in ANC and ASAC schemes, although recently the particle velocity sensors and the intensity probes have gained notoriety due to the increased number of alternative cost functions they provide, mainly sound intensity.

As it can be noticed, there are a great variety of actuators and sensors that can be used in active control systems, allowing the implementation of a wide variety of active control systems. Therefore, the choice of the actuators and sensors is one important step to an adequate implementation of an active control system.

1.6 Energetic Analysis importance

It is possible to obtain useful information about the way a system operates with the energetic analysis of the actively controlled systems. The introduction of secondary sources in the system cause significant changes in the energy distribution pattern. Thus, a complete comprehension allows identifying possible locations were the positioning of actuators and

sensors affect in a beneficial way the system performance, e.g., attenuating the overall energy level of the system, Elliott (2001).

Differently from the variables as displacement, velocity or acceleration, which are primary order quantities, the energetic variables as the potential and kinetic energy, are second order quantities. They are conservative quantities, easier to be used for the development of analytical models, Fahy (2001). Moreover, in the middle and high frequency range, energetic analysis constitute the main tool for modeling, Arruda (2001). Besides, this approach is capable of supplying quadratic cost functions in terms of the signals that must be sent to the secondary sources, Qiu and Hansen (1998) and Elliott and Nelson (1992).

The most interesting form of energetic control consists of preventing that the primary sources introduce energy, thus reducing the overall energy present in the system. Another possibility is to prevent that the energy of one specific part of the system to propagate, thus, restricting the energetic distribution in one determined region of the system. Finally, energy sinks can be created, that can decrease the energy of the system; however, in that case the system continues to have a great energy flow from the primary sources towards the sinks.

1.7 Objectives of the Ph.D. dissertation

The aim of this Ph.D. dissertation is the comparison of several cost functions involving energy or the energy flow in active noise control systems. The compared cost functions are the potential energy density, the kinetic energy density and the active intensity, all of them implemented in the frequency domain, and the analyses are performed experimentally and theoretically. The active noise control systems will be implemented in a one-dimensional acoustic waveguide to verify the energy behavior of an actively controlled system involving different cost functions. The one-dimensional acoustic waveguide is modeled using the spectral element method, Doyle (1997), applied to the acoustic case in order to obtain analytically the performance of the active control methods and the energetic behavior of the acoustic system. In the sequence, the active noise control method performance is verified experimentally and a link between the

theoretical and the experimental implementation is also shown in order to explain the differences between the results.

These active control schemes - ANC, AVC and ASAC - are compared in the attenuation of the noise and vibration in cylinders, i.e., in the attenuation of the cylindrical shell vibration and in the attenuation of the noise radiated to the cylindrical shell cavity, under the structural and acoustic disturbance. In order to understand the phenomena involved, the structural and acoustical modal analysis is made to verify the fluid-structure interaction. Using the results of the modal analysis, an analytical investigation is performed to compare the results obtained using the active control schemes. The active control schemes are implemented in real time to verify the possible differences between the cost functions involved in the process of the active control.

1.8 PhD dissertation Organization

This PhD dissertation is divided as follows:

-
- Chapter 1: An overview of the active control systems and their implementation shows the complexity involved in the process of implementing the active control.
 - Chapter 2: A review of the main works and scientific advances in the field is presented.
 - Chapter 3: This chapter supplies a general vision of the acoustic properties and the basic equations involved in the development of the active control methods.
 - Chapter 4: The active control methods as well as the optimal solutions for the volume velocity of the secondary sources as a function of the volume velocity of the primary sources are developed. Moreover, the active control methods using adaptive filtering theory for several cost functions are deduced.
 - Chapter 5: A simple application of active noise control in vehicles is described.
 - Chapter 6: The spectral element method applied to one-dimensional acoustic waveguides is described. The method is verified experimentally using two simple examples. A theoretical analysis of an active control system in a one-dimensional acoustic waveguide is made and, finally, the active control method is implemented in real time where a theoretical and experimental comparison is made.
 - Chapter 7: The implementation of an active control schemes in a cylinder is performed, where a structural and acoustical modal analysis is applied to supply the necessary foundation to the implementation of real time active control schemes.
 - Chapter 8: The general conclusions of this thesis are presented.

Chapter 9: Bibliography used in this thesis.

Appendix: The derivations of the complex functions used in the development of the active control algorithms are demonstrated.

Appendix B: The programs developed for the implementation of the active control algorithms in real time are presented.

Appendix C: An overview of parameter identification algorithm is given.

Appendix D: An overview of the algorithm Least Mean Square method is presented.

Capítulo 2 (Português)

Revisão Bibliográfica

Para projetar um sistema de controle ativo de ruído e/ou vibração utilizando conceitos de filtragem adaptativa, deve-se estar ciente de sua complexidade, isto é, o número de variáveis a serem controladas em função do objetivo final desejado. Os sistemas de controle ativo na configuração de avanço utilizando filtragem adaptativa, em sua grande maioria, são desenvolvidos a partir da metodologia LMS (“Least Mean Square”), Widrow e Steins (1985).

O mais importante dos métodos de controle ativo utilizando a teoria de filtragem adaptativa é o filtered-X LMS no domínio do tempo, o qual é relativamente simples se comparado a outros métodos de controle (controle robusto ou ótimo, por exemplo). Além disso, é de fácil implementação e apresenta desempenho satisfatório em aplicações simples, particularmente naquelas onde a fonte de ruído apresenta apenas uma frequência (controle tonal) ou a frequência fundamental e suas harmônicas.

2.1 Algoritmos adaptativos para controle ativo de ruído

Os trabalhos aplicados em controle ativo de ruído, seja para o esquema ANC ou para o ASAC, possuem como base algoritmos utilizando filtragem adaptativa. Podem ser implementados no domínio do tempo ou frequência e utilizam diversas funções de custo.

O primeiro trabalho utilizando filtragem adaptativa aplicado ao controle ativo de ruído foi realizado por Burges (1981). Nele foi aplicado o algoritmo LMS, utilizado originalmente para

cancelamento de eco em telecomunicações. O sistema de controle ativo foi configurado de tal forma que o sensor de erro foi posicionado após as fontes primária e secundária e em uma localização adequada para medir a maior amplitude de sinal possível. Ele mostrou que, se o sistema de dutos funciona como guia de ondas onde apenas ondas planas propagam, o problema de controle ativo de ruído em dutos pode ser resolvido. Porém, se o ponto de controle for entre as fontes ou se o sistema de controle for implementado em cavidades, onde há modos de ordem superior (acima da frequência de corte para ondas planas), o sistema de controle proposto por Burges (1981) precisa ser melhorado a fim de ampliar a área de atenuação do ruído. A primeira resposta a esta necessidade veio com Elliott et al. (1987), onde foi testado e implementado o mesmo algoritmo utilizado por Burges (1981), só que utilizando múltiplos sensores de erro. Elliott e Nelson (1992) propuseram o *filtered-X LMS* multicanal, onde podem ser utilizados para múltiplos sensores de erro, múltiplas fontes secundárias e para múltiplas referências.

2.2 Melhorias e tendências

O método de controle ativo utilizado por Elliott e Nelson (1992), quando é aplicado ao controle ativo de ruído em banda larga (admite-se como banda larga uma ampla faixa de frequências onde há contribuição de vários modos do sistema a ser controlado ativamente), apresenta algumas dificuldades de convergência pelo fato do método não ser normalizado e por trabalhar no domínio do tempo. Quando o método não é normalizado, o fator de passo deve atender a requisitos de convergência baseados nos autovalores da matriz de autocorrelação da referência filtrada, Kuo e Morgan (1996). Mais detalhes podem ser obtido no Apêndice D.

O método de Elliott e Nelson (1992) é baseado no algoritmo de otimização de máximo descenso (*steepest descent*), onde o erro quadrático médio é aproximado pelo erro quadrático instantâneo. Pode-se aproximar a matriz de autocorrelação da referência filtrada pelo seu valor instantâneo e o método de ajuste baseado no máximo descenso pode ser substituído pelo algoritmo auto-ortogonalizável, como mostrado por Cowan (1987). Esta normalização permite que o fator de passo do método de controle esteja contido entre 0 e 1. Isto facilita encontrar o fator de passo mais adequado para toda a faixa de frequências em que o sistema de controle será

implementado. Outras formas de normalização podem ser encontradas em Kuo e Morgan (1996) e Haykin (1996).

Outra alteração que pode ser implementada é a transformação para o domínio da frequência. Os métodos adaptativos no domínio da frequência podem ser encontrados em Shynk (1992) e foram aplicados ao controle ativo de ruído por Shen e Spanias (1996). As vantagens da implementação no domínio da frequência são muitas, entre elas podem-se destacar a precisão, a velocidade de adaptação e, principalmente, a possibilidade de adaptar cada frequência independentemente, Shen e Spanias (1996). Porém, transformadas e anti-transformadas rápidas de Fourier (FFTs e IFFTs) necessitam ser processadas em tempo real e esta operação acaba reduzindo a faixa de frequência em que o método de controle pode ser empregado.

Cabell e Fuller (1999) introduziram uma alternativa ao algoritmo filtered-X LMS multicanal através da decomposição em valores singulares matriz de transferência entre as fontes secundárias e os sensores de erro, tornando assim, possível controlar independentemente cada sensor de erro. Desta forma consegue-se melhor a convergência, eliminar sensores de erro insignificantes e reduzir esforços excessivos dos atuadores de controle.

2.3 Alterando a função de custo

O método de controle ativo de ruído baseado no algoritmo filtered-X LMS é projetado para minimizar o erro quadrático instantâneo fornecido pelo sensor de erro. Se o sensor de erro é um sensor de pressão o método está controlando a densidade de energia potencial; se o sensor de erro é um sensor de velocidade de partícula o método está controlando a densidade de energia cinética. Desta forma, a simples troca do sensor de erro proporciona ao método de controle ativo atingir objetivos diferentes.

Neste sentido, Sommerfeldt e Nahif (1994) utilizam como função de custo a densidade de energia total, que é a somatória da densidade de energia potencial e cinética. Eles também introduziram a possibilidade de um método de controle de intensidade, sendo que, neste caso, a função de custo é o produto da pressão pela velocidade de partícula. Os resultados experimentais

foram obtidos em dutos sujeitos a ondas planas e mostrou-se que o controle da energia acústica total é mais independente da posição dos sensores de erro do que simplesmente controlar a densidade de energia potencial ou cinética separadamente.

O primeiro controlador adaptativo que utiliza a intensidade ativa como função de custo foi implementado por Arruda et al. (1997) no controle de fluxo de potência em placas. O método é implementado no domínio da frequência. O controlador foi formulado para placas mas pode ser adaptado para controlar vigas, barras e guias de ondas unidimensionais, Pereira (1999).

O controle de intensidade ativa foi implementado no controle ativo de ruído gerado por transformadores elétricos por Qiu e Hansen (1997). Apesar do método estar baseado na estrutura do filtered-X LMS, o algoritmo de controle ajusta a amplitude e fase de cada tom a ser controlado no domínio da frequência e implementa o processo de síntese de onda no domínio do tempo.

Kang e Kim (1997) utilizaram a intensidade instantânea como função de custo (portanto, controlando tanto a intensidade ativa quanto a reativa) e o método foi implementado no domínio do tempo.

Outro método para controlar a intensidade ativa foi proposto por Swanson et al. (1999). É o método que mais se aproxima do método ASIC aqui utilizado. O ajuste dos pesos é feito no domínio da frequência, mas o processo de geração do sinal de controle é feito no domínio do tempo. Pode-se dizer que, enquanto o método de Swanson et al. é “implícito”, o método ASIC é “explícito”. No método de Swanson et al. é necessário identificar uma função de transferência em intensidade entre a fonte de controle (fonte secundária) e o sinal de erro (intensidade). Swanson et al. não souberam justificar teoricamente a necessidade desta função de transferência, o que fica claro na formulação do método ASIC.

As alterações na função de custo visam estabelecer novas abordagens para o método de controle ativo, proporcionando um sistema que apresente maior capacidade de atenuação e uma maior região de atenuação. Informações sobre qual a melhor escolha da função de custo devem vir do próprio sistema físico a ser controlado, como será visto a seguir.

2.4 Aplicação em guia de ondas unidimensionais

Guias de onda unidimensionais são todos os meios nos quais uma das coordenadas pode ser considerada muito maior que as demais e, principalmente, apenas para frequências abaixo da frequência de corte para a propagação de ondas planas, Kinsler et al. (1982).

A escolha de muitos autores para a investigação de sistemas de controle ativo de ruído em ambientes unidimensionais sujeitos a ondas planas está relacionada com a sua simplicidade; além disso, são bem conhecidos e relativamente fáceis de serem modelados. Na parte experimental, são fáceis de serem montados e podem ser relativamente bem controlados.

Como mencionado anteriormente, o controle ativo de ruído utilizando a teoria de filtragem adaptativa iniciou-se com o trabalho de Burges (1981) com a aplicação em dutos. Tratamentos analíticos envolvendo a física dos ambientes unidimensionais e as aplicações de controle ativo de ruído foram desenvolvidos por Curtis et al. (1987), onde foi estudado o caso de um duto com duas fontes sonoras, uma em cada terminação. Vários tipos de estratégias de controle foram testados teoricamente e os resultados mostraram que um padrão de ondas estacionárias se forma entre as fontes; além disso, melhorias substanciais na atenuação da energia acústica foram alcançadas com a utilização de mais fontes secundárias e mais sensores de erro. Foi mostrado também, que há uma distância ótima para a localização da fonte secundária em relação à fonte primária, isto é, a fonte secundária deve ser posicionada nos pontos de máxima pressão. Isto porque o sistema tratado consistia de um ambiente formado puramente por ondas estacionárias, significando que um ponto de nó de pressão é um ponto de pico de velocidade, e uma fonte sonora posicionada em um ponto de nó de pressão (que trabalha impondo uma velocidade) não consegue atuar, sendo a resposta do sistema proveniente apenas da fonte primária. Contudo, se a fonte secundária for posicionada em um ponto de pico de pressão, representando um ponto de nó de velocidade, ótimos níveis de atenuação são atingidos.

Snyder e Hansen (1989) demonstraram analiticamente que o sistema de controle ativo de ruído impede que a fonte primária injete potência no sistema acústico. Implementações

experimentais foram feitas apenas para comparar o modelo teórico com o experimental em termos das medidas de impedância. Além disso, medições de potência acústica radiada pelas fontes primária e secundária foram feitas enclausurando as fontes e medindo a alteração de pressão do sistema enclausurado para estimar a velocidade de volume das fontes primária e secundária.

Sommerfeldt e Nashif (1994), como mencionado anteriormente, utilizaram um controlador baseado na metodologia do LMS onde a função de custo é a energia acústica total. Os resultados experimentais são comparados com o método de controle de pressão sonora com o algoritmo filtered-X LMS. Assim, o objetivo foi comparar experimentalmente as diferenças entre minimizar a densidade de energia potencial e a densidade de energia total. Os resultados mostraram que a atenuação da pressão sonora utilizando um controlador que minimiza a densidade de energia total é mais independente das posições dos sensores de erro do que controladores que minimizam apenas a densidade de energia potencial. Esta diferença só é encontrada experimentalmente, já que em teoria os resultados atingidos são os mesmos. Na prática, porém, o sensor de erro pode captar mais ou menos sinal, dependendo de sua posição e de sua dinâmica. Contudo, é conhecido que a derivada espacial da pressão é proporcional à velocidade, Kinsler et al. (1982), assim, quando o sensor de pressão apresenta baixo nível de sinal o sensor de velocidade tende a apresentar um bom nível de sinal. Desta forma, utilizando o critério de minimizar ambas as densidades (potencial e cinética), sempre haverá sinal suficiente para atingir um bom nível de atenuação.

Kang e Kim (1997) implementaram um método de controle ativo de ruído baseado na estrutura do filtered-X LMS utilizando a intensidade instantânea como função de custo, controlando tanto a intensidade ativa quanto a reativa. A implementação experimental do método de controle ativo inclui a estimativa da velocidade através de uma sonda de intensidade utilizando o método de dois microfones, Fahy (1995). Foi demonstrado que, assim como a densidade de energia total, a intensidade instantânea torna a atenuação independente da posição dos sensores de erro.

Swanson et al. (1999) testaram e compararam o controlador filtered-X LMS e um controlador de intensidade ativa. Demonstraram teoricamente e experimentalmente que se o controlador atinge o ponto ótimo as fontes primária e secundária não injetam potência no sistema. Além disso, que se o sensor de erro (neste caso um sensor de intensidade) é posicionado após as fontes primária e secundária, a intensidade ativa após as fontes é atenuada e, se o sensor de erro é posicionado entre as fontes, é melhor que ele esteja em um ponto de nó de pressão, porque obtiveram a melhor relação sinal/ruído neste ponto. Caso contrário, a intensidade ativa após as fontes é aumentada devido à potência injetada pela fonte secundária.

Chen e Liu (2000) demonstraram analiticamente para um duto semi-infinito que se a solução ótima para a velocidade de volume da fonte secundária é implementada, o módulo da velocidade de volume da fonte secundária é maior ou no máximo igual ao módulo da velocidade de volume da fonte primária, demonstrando que é necessário mais velocidade de volume para controlar o distúrbio do sistema do que para introduzi-lo originalmente. Além disso, mostrou-se teoricamente que a fonte secundária não consegue controlar frequências onde a distância de separação entre as fontes primária e secundária são os múltiplos ímpares de $\frac{1}{4}$ de comprimento de onda.

Todas as análises anteriores foram aplicadas em sistemas unidimensionais com uma terminação anecóica ou rígida e não foram tratadas analiticamente terminações abertas para o ambiente. Além disso, os modelos teóricos desenvolvidos são aplicáveis apenas para o caso em questão, sendo necessário desenvolver um novo modelo para qualquer alteração no sistema.

2.5 Aplicações no controle de ruído radiado para o interior de cavidades

O controle ativo de ruído em cavidades cilíndricas utilizando atuadores estruturais iniciou-se com Fuller e Jones (1987), que propuseram um esquema denominado ASAC. O experimento consistiu de uma cavidade cilíndrica excitada por fontes pontuais acústicas posicionadas do lado externo da cavidade, o atuador de controle foi um excitador eletrodinâmico fixado na parede do cilindro e os sensores foram microfones posicionados no interior da cavidade cilíndrica. Foi demonstrado, experimentalmente, que, se a frequência de excitação fosse a mesma frequência de

ressonância da cavidade cilíndrica, grande atenuação do ruído interno era conseguida apesar da vibração da casca cilíndrica aumentar. Se a frequência de excitação fosse uma frequência de anti-ressonância da cavidade cilíndrica, amplificação do ruído interno era constatada.

Jones e Fuller (1989) estenderam os resultados de Fuller e Jones (1987) para o caso de múltiplas fontes secundárias e concluíram que menos fontes secundárias estruturais eram necessárias do que fontes acústicas para controlar o ruído radiado para a cavidade cilíndrica, assim, o esquema ASAC apresenta vantagens se comparado com o esquema ANC neste caso.

Borgiotti (1990) demonstrou que um número limitado de modos de radiação contribuem para o som radiado da estrutura vibrando, e este é o número que define a dimensão do sistema de controle (número de atuadores estruturais). Assim, torna-se indispensável a identificação dos modos estruturais mais acoplados com os modos acústicos por serem os modos que apresentam a maior eficiência de radiação.

Snyder e Hansen (1991) reportam que dois mecanismos são possíveis para resultar na atenuação do ruído interno da cavidade. O primeiro é o controle modal e o segundo é o rearranjo modal. Cada um deles é eficiente em um tipo de aplicação, isto é, para altas densidades modais estruturais acopladas com o modo acústico o rearranjo modal pode propiciar atenuação global, isto significa que a maior parte da energia está contida no modo acústico. Porém, se o modo acústico está acoplado com poucos modos estruturais, o controle modal é mais indicado, e isto significa que a maior parte da energia está contida na estrutura.

Sun et al. (1994) utilizou atuadores piezelétricos modais em uma casca cilíndrica a fim de controlar apenas os modos estruturais realmente acoplados com os modos acústicos. Esta utilização dos sensores piezelétricos atenuou o ruído interno sem aumentar a vibração da casca cilíndrica.

Investigações analíticas para melhorar o esquema ASAC foram feitas no sentido de correlacionar os modos estruturais que mais radiam som com a velocidade de volume imposta pela estrutura vibrando, Elliott e Johnson (1993) e Johnson e Elliott (1995). Assim, minimizando

a velocidade de volume imposta pela estrutura ocorre uma atenuação da radiação do som da estrutura para o ambiente.

Cazzolato e Hansen (1998,1999) apresentaram uma formulação para descrever os modos estruturais ortogonais de radiação com a energia potencial de uma cavidade acústica, sendo possível, através de medição de vibração na estrutura, estabelecer quais os modos estruturais que são mais correlacionados com a distribuição de pressão na cavidade acústica e, assim, aplicar um controle que minimiza somente estes modos.

Kim e Brennan (1999) demonstraram, analiticamente e experimentalmente, que um único atuador estrutural é efetivo para controlar os modos estruturais bem separados, enquanto que um único atuador acústico é efetivo para controlar os modos acústicos bem separados, propondo, assim, a combinação de fontes secundárias acústicas e estruturais, já que o fenômeno de radiação é composto tanto por modos estruturais quanto acústicos.

Os trabalhos desenvolvidos pelos autores citados são aplicados para o entendimento do fenômeno de controle. A utilização de outros sensores de erro, tais como o sensor de velocidade de partícula, não foi reportada na literatura. Além disso, nenhum trabalho envolvendo uma comparação efetiva entre os esquemas AVC, ANC e ASAC para a atenuação do ruído em uma cavidade ou na atenuação da vibração de uma estrutura foi encontrado.

2.6 Erros nas medidas de intensidade

Existem várias maneiras de realizar medidas de intensidade sonora. Podem ser utilizadas sondas de intensidade, das quais vários modelos podem ser encontrados em Fahy (1995). A direção do vetor de intensidade é fornecida pela direção do vetor de velocidade de partícula quando é utilizada uma sonda do tipo P-U (sonda formada por um microfone e um sensor de velocidade de partícula); se for utilizada uma sonda do tipo P-P (sonda constituída por apenas microfones) a direção da intensidade medida é dada pela direção de alinhamento dos microfones, Fahy (1995).

As medidas de intensidade utilizadas neste trabalho são baseadas na técnica P-P, onde a intensidade é proporcional ao espectro cruzado entre os sinais dos microfones. Porém, alguns cuidados devem ser tomados para garantir que as medidas de intensidade sejam corretas. A técnica de 2 microfones está sujeita principalmente a dois tipos de erros: o erro de fase e o erro de aproximação do gradiente de pressão por diferenças finitas.

O erro de aproximação por diferenças finitas é o mais fácil de ser contornado. Este tipo de erro ocorre devido à aproximação do gradiente espacial da pressão por diferenças finitas. Atua alterando em amplitude a medida de intensidade, e apresenta a característica de ser independente do tipo de campo acústico em que a medida é realizada, sendo dependente apenas da distância de separação entre os microfones, isto é, quanto mais próximos os microfones forem posicionados menor será o erro. A correção do erro de aproximação por diferenças finitas pode ser feita, por exemplo, pela técnica proposta por Thompson e Tree (1981), que consiste em multiplicar a intensidade por um fator de ajuste. Outra correção possível vem da configuração do tipo de campo acústico onde a medida de intensidade é realizada; por exemplo, se o campo acústico é basicamente de ondas planas pode-se aplicar com sucesso a técnica de componentes de onda, eliminando, assim, o erro de aproximação por diferenças finitas.

Os erros provenientes da diferença de fase entre os microfones corresponde ao erro mais significativo, já que em casos extremos uma intensidade nula ou negativa (sentido oposto ao esperado) pode ser medida. Além disso, é um tipo de erro que está diretamente relacionado ao tipo de campo sonoro onde é feita a medição, isto é, para campos mais reverberantes do que propagativos, o erro de diferença de fase entre os microfones deve ser menor para que a medida seja feita satisfatoriamente. Este é um tipo de erro que pode ser minimizado aumentando a separação entre os microfones. A correção do erro de fase pode ser feita através da compensação de fase entre os microfones, ou utilizando o método proposto por Chung (1978), consistindo em realizar duas medidas de intensidade onde a segunda medida é realizada com os microfones trocados.

2.7 Erros nos métodos de controle ativo

Os erros mais significativos encontrados nos métodos de controle são provenientes de erros ocasionados durante a estimativa das funções de transferência necessárias para a sua implementação, Kuo e Morgan (1996), e erros devido aos sensores de erro, Cazzolato e Hansen (2000). Em sua grande maioria, os erros diminuem a capacidade de atenuação do método de controle ou afetam radicalmente o tempo de convergência (tempo necessário para que o método iterativo atinja a solução ótima). Desta forma, o estudo da influência dos erros nos sistemas de controle é de vital importância para o desempenho do método de controle.

Nos métodos de controle ativo onde são necessárias medidas de velocidade de partícula, como é o caso do controle da intensidade ou da densidade de energia total, os autores preferem utilizar microfones ou sensores de velocidade com fase casada, isto é, microfones que apresentem diferença de fase próxima de zero, normalmente caros para aplicações industriais ou em larga escala. Outro tipo de erro de grande influência está relacionado com a sensibilidade (em amplitude ou a relação sinal/ruído) dos sensores, que afetam o nível de atenuação.

Assim, uma profunda investigação dos erros de medida deve ser feita a fim de evitar desempenho insatisfatório nos métodos de controle ativo.

Chapter 2 (English)

Bibliography Review

In order to design an active noise and/or vibration control system using adaptive filtering theory concepts, the complexity should be kept in mind, i.e., the number of variables being controlled as a function of the desired final objective. The majority of the feedforward active control systems using adaptive filtering theory are developed from the LMS (Least Mean Square.) methodology, Widrow and Steins (1985).

The most important active control method using adaptive filtering theory is filtered-X LMS in the time domain, which is relatively simple, if compared with other control methods (e.g., robust or optimal control). Moreover, it is easily implemented and it presents a satisfactory performance in simple applications, mainly where the noise source presents only one frequency (tonal control) or the fundamental frequency and its harmonics.

2.1 Active noise control adaptive algorithms

The active noise control applications for the ANC and for the ASAC schemes are based on the adaptive filtering theory, and can be implemented in the time or in the frequency domain using several types of the cost functions.

The first work using adaptive filtering theory applied to the active noise control was developed by Burges (1981). He used the LMS algorithm, which was first used for echo cancellation in telecommunications. The control system was configured with the error sensor

located past the primary and secondary sources and placed at a maximum amplitude point. He showed that if the duct system is assumed as a waveguide where only plane waves propagate, the problem of active noise control can be solved. However, if the error sensor is placed between the sources or if the control system is implemented in acoustic cavities with frequencies above the cut-off frequency for plane waves, the active control system proposed by Burges (1981) needs to be improved to achieve good levels of noise attenuation. The first response to this necessity came with Elliott et al. (1987), where it was tested and implemented the same algorithm used by Burges (1981) but using multiple error sensors. Elliott and Nelson (1992) used the multichannel filtered-X LMS where the active control method based upon the LMS algorithm can be used with multiple error sensors, multiple secondary sources and multiple references.

2.2 Improvements and trends

The active control method used by Elliott and Nelson (1992), when applied to a broadband disturbance, where large frequency band with the contribution of several natural modes of the system to be actively controlled, presents some convergence difficulties due to the fact that the method is not normalized, and works in the time domain. When the method is not normalized, the step size value must take into account convergence requirements based upon the eigenvalues of the filtered reference autocorrelation matrix, Kuo and Morgan (1996). More details can be seen in Appendix D.

The method of Elliott and Nelson (1992) is based upon the steepest descent algorithm, where the least mean square error is approximated by the instantaneous quadratic error. The instantaneous value of the autocorrelation matrix of the filtered reference and the minimization method based upon the steepest descent algorithm can be replaced by the self-orthogonalizing algorithm, as shown by Cowan (1987). This normalization allows the step-size to be normalized between 0 and 1. That normalization helps to find a more adequate step-size for all the frequency band where the control system is implemented. Other forms of normalization can be found in Kuo and Morgan (1996) and Haykin (1996).

The active control method can also be implemented in the frequency domain. The adaptive methods in the frequency domain can be found in Shynk (1992) and have been applied to active noise control by Shen and Spanias (1996). The advantages of working in the frequency domain are several, between them can be highlighted the accuracy, the adaptation ratio and, mainly, the possibility of adapting each frequency independently, Shen and Spanias (1996). However, fast Fourier transforms and inverse fast Fourier transforms (FFTs and IFFTs) need to be processed in real time and this operation reduces the frequency range where the control method can be used.

Cabell and Fuller (1999) introduced an alternative to the multichannel filtered-X LMS algorithm through singular value decomposition of the matrix of transfer functions between the secondary sources and the error sensors. That approach allows independently controlling each error sensor, thus improving convergence by eliminating insignificant error sensors and reducing extreme efforts of the control actuators.

2.3 Changing the cost function

The active noise control method based upon the filtered-X LMS algorithm is designed to minimize the instantaneous quadratic error supplied by the error sensor. If the error sensor is a pressure sensor, the method is controlling the potential energy density; if the error sensor is a particle velocity sensor, the method is controlling the kinetic energy density. Therefore, a simple change of the error sensor implies that active control method will achieve different objective.

In this way, Sommerfeldt and Nahif (1994) used as cost function the total energy density, which is the sum of the potential and kinetic energy densities. They have also introduced the possibility of controlling the intensity, in which case, the cost function is the product of the pressure and particle velocity. The experimental results have been obtained for ducts subjected to plane waves and revealed that the total acoustic energy control is more independent of the error sensor position than simply to control the potential or kinetic energy densities separately.

The first adaptive controller that uses the active intensity as cost function was implemented by Arruda et al. (1997) in the control of the structural power flow. The method was implemented

in the frequency domain and the controller was originally formulated for plates. However, by changing the weight adjustment equations the method can be easily adapted to control the active intensity in beams, bars or in one-dimensional acoustic waveguides, Pereira (1999).

Qiu and Hansen (1997) used the active sound intensity to control the noise generated by electric transformers. Despite the method being based upon the filtered-X LMS structure, the control algorithm adjusts the amplitude and phase of each frequency tone in the frequency domain and implements the process of wave synthesis in the time domain.

Kang and Kim (1997) used the instantaneous intensity as cost function, therefore controlling both the active and the reactive parts of the intensity, and the method was implemented in the time domain.

Swanson et al. (1999) proposed a control method based upon the active intensity. It is the method that most resembles the ASIC method used here. The weight adjustment is implemented in the frequency domain, but the process of generation of the control signal is made in the time domain. One can say that the method proposed by Swanson et al. is “implicit” while the ASIC method is “explicit”. In Swanson et al.’s method, it is necessary to identify a transfer function for the active intensity between the control source (secondary source) and the error signal (intensity). Swanson et al. could not explain why it is necessary to filter the reference signal with this transfer function, which is made clear in the explicit ASIC formulation.

The changes in the cost function are used to establish a new methodology for the active control methods, supplying to the system more attenuation capacity and a larger region of attenuation. Information about which cost function should be used can come from the physical system itself, as it will be seen later.

2.4 Application to one-dimensional acoustic waveguides

One-dimensional waveguides are acoustic fields where one dimension can be considered much larger than the others and, mainly, where only frequencies below of the cut-off frequency for plane waves propagate, Kinsler et al. (1982).

Many authors choose to investigate active noise control systems in one-dimensional waveguides because of its simplicity if compared with other fields, and they are well known and relatively easy to be modeled. In the experimental aspects, they are easy to be set up and they can be relatively well controlled.

As mentioned previously, the active control of noise using adaptive filtering theory began with Burges (1981), with the application in ducts. Analytical treatments involving the physics of one-dimensional waveguides and the active noise control applications have been developed by Curtis et al. (1987), where the case of a duct with two acoustic sources was studied, one source to each termination. Some types of control strategies have been tested theoretically and the results have shown that a standing wave pattern is formed between the sources; moreover, substantial improvements in the attenuation of the acoustic energy have been achieved with the use of more secondary sources and error sensors. They have shown, also, that there is an optimal distance for the secondary source localization in relation to the primary source location, i.e., the secondary source must be located in the maxima of the pressure field. This happened because the system investigated consisted purely of standing waves, meaning that a “knot” of pressure is a particle velocity peak, and an acoustic source located at a point of pressure knot (that works by introducing a volume velocity) can not act, and the system response is purely due to the primary source. However, if the secondary source is located at a point of pressure peak, representing a point of particle velocity knot, the attenuation level achieved is much stronger.

Snyder and Hansen (1989) demonstrated analytically that, when the active noise control system is acting, the primary source does not inject power into the acoustic system. Experimental implementations were made only to compare the theoretical model with the experimental one in

terms of the impedance measurements. Moreover, the radiated acoustic power for the primary and secondary sources was measured enclosing the back side of the sources and measuring the changes of the pressure in the enclosed volume to predicted the volume velocity of the primary and secondary sources.

Sommerfeldt and Nashif (1994), as mentioned previously, used a controller based upon the LMS methodology where the cost function was changed to the total acoustics energy. The experimental results were compared with the filtered-X LMS control of the acoustic pressure. Thus, the objective was to compare the differences between minimizing the potential energy density and the total energy density experimentally. The results showed that the attenuation of the pressure using a controller that minimizes the total acoustic energy density is more independent of the error sensor position than a controller that minimizes only the potential energy density. This difference is only found experimentally, since in the theory the results are the same. However, in practical applications, the error sensor can measure more or less signal, depending on its location and dynamic range. However, the spatial derivative of the pressure is proportional to the particle velocity, Kinsler et al. (1982); thus, when the pressure sensor measures a low signal level, the velocity sensor tends to measure a good signal level. Thus, using a criterion that minimizes both the potential and the kinetic energy densities will always have signal level enough high to achieve good attenuation levels.

Kang and Kim (1997) implemented an active noise control method based upon the filtered-X LMS structure using the instantaneous intensity as cost function, therefore controlling both the active and the reactive intensity. The experimental implementation of the active noise control method included an estimate of the particle velocity using an intensity probe, where the particle velocity was estimated using the two-microphone technique, Fahy (1995). It was demonstrated that, as well as the total acoustic energy density, the control of the instantaneous intensity yield good the attenuation independently of the error sensor position.

Swanson et al. (1999) tested and compared the filtered-X LMS controller and an active intensity controller. They demonstrated theoretically and experimentally that, if the controller achieves the optimal performance point, the primary and secondary source do not inject power

into the acoustic system. Moreover, if the error sensor (in this in case an intensity sensor) is located past the primary and secondary sources, the active intensity past the sources is attenuated. If the error sensor is located between the sources, it is better that the error sensor is placed at a point of pressure knot, as this configuration achieved the best signal/noise relation. However, if the error sensor is placed at other locations, the active intensity past the sources is increased due to power injected by the secondary source.

Chen and Liu (2000) demonstrated analytically, using a semi-infinite duct that if the optimal solution for the secondary source volume velocity is implemented, the magnitude of the secondary source volume velocity is larger or equal to the primary source volume velocity, demonstrating that more volume velocity is necessary to control the acoustic system than to introduce the noise originally. Moreover, they showed theoretically that the secondary source does not control odd multiples of $\frac{1}{4}$ of wavelength.

The previous analyses have been applied in one-dimensional systems with an anechoic termination or rigidly terminated and the methodology was not applied to study analytically an opened-ended termination. In addition, the theoretical models developed by the authors are applicable only for a specific case, and a new formulation is necessary for any changes in the one-dimensional waveguide.

2.5 Active noise control of the sound radiated to cavities

Fuller and Jones (1987) proposed the active noise control in a cylindrical cavity using structural actuators, where the ASAC scheme was implemented. The experiment consisted of a cylindrical shell excited by acoustic point sources located in the external side of the cylindrical cavity, the control actuator was an electrodynamic shaker attached to the cylindrical shell, and the sensors were microphones placed in the cylindrical shell interior. It was demonstrated experimentally that if the frequency of the disturbance is the same resonance frequency of the cylindrical shell, great attenuation of the internal noise is obtained despite the fact that the vibration of the cylindrical shell increases. If the disturbance frequency is a frequency of anti-resonance of the cylindrical shell, amplification of the internal noise is measured.

Jones and Fuller (1989) extended the results of Fuller and Jones (1987) to the case of multiple secondary sources and concluded that less structural secondary sources than acoustic secondary sources are necessary to control the noise radiated by the cylindrical shell. Thus, the ASAC presents advantages if comparative with ANC in this case.

Borgiotti (1990) demonstrated that a limited numbers of radiation modes contribute to the sound radiated of a structure vibrating, and this is the number that defines the dimension of the control system (number of structural actuators). Thus, the identification of the structural modes connected to the acoustic modes is essential because those modes have the biggest radiation efficiency.

Snyder and Hansen (1991) report that two mechanisms are possible to result in the attenuation of the interior noise of a cavity. The first one is the modal control and the second is the modal rearrangement. Each one is efficient in a type of application, i.e., for high structural modal densities connected with the acoustic mode the modal rearrangement can propitiate global attenuation, which means that the biggest energy is contained in the acoustic mode. However, if the acoustic mode is connected to a few structural modes, the modal control is more indicated, which means that most of the energy is contained in the structure.

Sun et al. (1994) used modal piezoelectric actuators in a cylindrical shell to control only the structural modes really connected to the acoustic modes. The use of the piezoelectric sensors attenuated the internal noise without increasing the vibration of the cylindrical shell.

Analytical investigations have been made to improve the ASAC scheme to correlate the structural modes that radiate more sound with the volume velocity imposed by the structure vibrating, Elliott and Johnson (1993) and Johnson and Elliott (1995). Thus, minimizing the volume velocity imposed by the structure an attenuation of the sound radiation was verified.

Cazzolato and Hansen (1998,1999) presented a formulation to describe the realtion between the orthogonal structural radiation modes and the potential energy of the acoustic cavity. This

methodology establishes, using measurements of the vibration in the structure, what structural modes are more correlated with the pressure distribution in the acoustic cavity. In order to apply a control that minimizes only these modes.

Kim and Brennan (1999) demonstrated, both analytically and experimentally, that only one structural actuator is effective to control well-separated structural modes, while only one acoustic actuator is effective to control well separate acoustic modes. Thus, they proposed a combination of secondary structural and acoustical sources, since the radiation phenomenon is composed by both structural and acoustic modes.

The works developed by the cited authors are applied for the understanding of the control phenomenon. The use of other error sensors, such as the particle velocity sensor was not reported in literature. Moreover, works involving an effective comparison between AVC, ANC and ASAC schemes in the noise attenuation in cavities or in the vibration attenuation in structures was not found in the literature.

2.6 Errors in the intensity measurement

There are several ways to measure the sound intensity. The measurements can be performed using intensity probes, of which some models can be found in Fahy (1995). The direction of the particle velocity gives the direction of the intensity vector when the intensity is measured with a P-U probe (probe made using a microphone and a particle velocity sensor). If the probe is a P-P type (probe using only microphones), the axis passing through the microphones supplies the direction of the intensity vector, Fahy (1995).

The sound intensity measurements used in this work are based on the P-P technique, where the intensity is proportional to the crosspower between the signals of the microphones. However, some care must be taken to guarantee that the measures of sound intensity are correct. The two-microphone technique is mainly subjected to two types of error: the phase mismatch and the finite difference approximation to estimate the pressure gradient.

The finite-difference error is easier to overcome. This error type appears due the estimate of the space gradient of the pressure for finite differences. The finite difference approximation error modifies the amplitude of the sound intensity, and is independent of the acoustic field where the measure is performed, although it is dependent of the separation distance between the microphones, which means that the as closer the microphones are located the smaller is the error. The correction of the error due to the finite difference approximation can be made, for example, by applying the technique proposed by Thompson and Tree (1981) which consists of multiplying the intensity by a correction factor. Another possible correction comes from the type of acoustic field where the measure is performed; for example, if the acoustic field consists basically of plane waves, the wave component technique can be applied successfully, eliminating, thus, the error due to the finite difference approximation.

The error due to the phase mismatch between the microphones correspond to the most significant error, since in extreme cases a null or negative sound intensity (opposed direction to the true one) can be measured. Moreover, it is an error type related directly to the acoustic field where the measurement is made, i.e., for more reverberant than propagating sound fields, the phase mismatch between the microphones must be much smaller to guarantee the accuracy of sound intensity measurement. This is a type of error that can be minimized by increasing the separation distance between the microphones. The phase mismatch correction can be made using phase compensation between the microphones, or using the method proposed by Chung (1978), which consists of performing two intensity measurements where the second measurement is performed with the microphones switched.

2.7 Errors in the active control methods

The most significant errors in the performance of the control methods proceed from errors caused during the transfer function estimation necessary for the implementation, Kuo and Morgan (1996), and errors due to the error sensors, Cazzolato and Hansen (2000). The majority of the errors either decreases the capacity of attenuation of the control method or affects the convergence time radically (time necessary for the method to achieve the optimal solution).

Therefore, it is important for the performance of the control method to study the error influence in the control system.

In the active control methods where it is necessary to measure the particle velocity, as it is the case of the sound intensity or the total acoustic energy density, the authors prefer to use microphones or particle velocity sensors with matched phases, i.e., microphones with phase mismatch close to zero, normally expensive for industrial applications or in commercial scale. Another error type with great influence is related to sensitivity (in amplitude or the signal/noise relation) of the sensors that affect the attenuation level.

Thus, a deep investigation of the measurement errors must be made in order to prevent unsatisfactory performance in the active control methods.

Chapter 3

Basic concepts in acoustics

This chapter is a review of basic concepts in acoustics, and it is the starting point to the following chapters. Because of this, the concepts are introduced briefly. Most of the content of this chapter can be found in fundamentals acoustic literature, Kinsler et al. (1982) and Fahy (1995, 2001).

The term *particle* means a small quantity of fluid, but large enough to ensure that it is a continuous medium and that the basic acoustic variables, pressure and particle velocity, may be considered nearly constant. Besides, the concepts are applicable to linear acoustics limited to small disturbances, below 135 dB of Sound Pressure Level (SPL), so that changes in density of the medium will be small compared with its equilibrium value. In addition, it is not considered any net flux, which means that after the passage of the acoustic wave the fluid returns to its original position and the gravitational forces are neglected.

3.1 Pressure and velocity equations

The wave equation relates the spatial gradient with the second temporal derivative of the pressure P as, Kinsler et al. (1982),

$$\nabla^2 P(t) - \frac{1}{c^2} \frac{\partial^2 P(t)}{\partial t^2} = 0 \quad (3.1)$$

where $c = \sqrt{\beta/\rho_0}$ is the sound speed in the medium, β is the Bulk modulus and ρ_0 is the nominal air density.

The Euler's equation or particle velocity equation relates the first temporal derivative of the particle velocity u with the spatial gradient of the pressure P as, Kinsler et al. (1982),

$$\nabla P(t) + \rho_0 \frac{\partial u(t)}{\partial t} = 0 \quad (3.2)$$

It is interesting to note that the pressure is a scalar, which does not have direction while the particle velocity is related to the Gradient operator (∇) and a vector quantity.

The wave equation and Euler's equation can be easily transformed to the frequency domain using Fourier series, as defined in Table 3.1. The wave equation in the frequency domain is denominated as Helmholtz equation and it is defined as,

$$\nabla^2 P(\omega) + K^2 P(\omega) = 0 \quad (3.3)$$

where $K = \frac{\omega}{c}$ is the wavenumber and $P(\omega)$ is the pressure in the frequency domain.

The Euler's equation in the frequency domain is defined as,

$$u(\omega) = \frac{i}{\rho_0 \omega} \nabla P(\omega) \quad (3.4)$$

where $u(\omega)$ is the particle velocity in the frequency domain.

Working in the frequency domain allows the study of both stationary and transient phenomena, and most of the equations developed ahead are in the frequency domain.

Table 3.1: Fourier series and Fourier transform properties

Time		Frequency
$F(t)$	\rightarrow	$F(\omega)$
$\nabla^2 F(t)$	\rightarrow	$\nabla^2 F(\omega)$
$\frac{\partial F(t)}{\partial t}$	\rightarrow	$i\omega F(\omega)$
$\frac{\partial^2 F(t)}{\partial t^2}$	\rightarrow	$-\omega^2 F(\omega)$

3.2 Energy in acoustic fields

The energies in acoustic fields are the potential and the kinetic energy. However, these energies are difficult to be assessed in practical applications because they represent an overall measurement of the acoustic field. The measurements of the acoustic energies are performed using sensors spread over the acoustic field and each sensor is capable of measuring the energy density in its neighborhood. Thus, the energy can be evaluated by summing all energy densities over the sensors multiplied by the corresponding volume.

The acoustic kinetic energy density, E_K , is related to the particle velocity in the acoustic field, Kinsler et al. (1982), and is given by,

$$E_K = \frac{1}{2} \rho_0 |u(\omega)|^2 \quad (3.5)$$

The acoustic potential energy density, E_P , is related to changes in volume when the acoustic wave propagates, Kinsler et al (1982), and is given by,

$$E_P = \frac{1}{2} \frac{|P(\omega)|^2}{\rho_0 c^2} \quad (3.6)$$

The acoustic total energy density, E_T , is defined as the sum of the acoustic potential and kinetic energy densities, so,

$$E_T = E_K + E_P = \frac{1}{2} \left(\rho_0 |u(\omega)|^2 + \frac{|P(\omega)|^2}{\rho_0 c} \right) \quad (3.7)$$

The expression of the total acoustic energy density can be applied to any sound field in which the small disturbance criterion and the zero mean flow condition are satisfied.

3.2 Acoustic intensity

The acoustic intensity, I , is related to the energy flow in the acoustic field. In the time domain, it is defined as the product of the instantaneous pressure and particle velocity as, Fahy (1995),

$$I(t) = P(t)u(t) \quad (3.8)$$

If complex amplitude representation is employed³, then, Fahy (1995),

$$I(\omega) = \frac{1}{2} P(\omega)u^*(\omega) \quad (3.9)$$

where $*$ denotes the complex conjugate.

The acoustic intensity points in the direction of the particle velocity, and defines the direction of the energy flow. Thus, using the acoustic intensity it is possible to identify sources and sinks of energy in the acoustic field.

As pressure and particle velocity are complex quantities, the acoustic intensity is a complex quantity, the real part is related to the energy flow while the imaginary part is related to the stored energy. The real part of the acoustic intensity is defined as active intensity, I_a , and is given by,

$$I_a(\omega) = \frac{1}{2} \Re \{ P(\omega)u^*(\omega) \} \quad (3.10)$$

where \Re represents the real part of a complex quantity.

³ If Fourier transform technique is employed, the $\frac{1}{2}$ is replaced by 2.

The imaginary part of the acoustic intensity is defined as reactive intensity, I_r , and is given by,

$$I_r(\omega) = \frac{1}{2} \Im \{ P(\omega) u^*(\omega) \} \quad (3.11)$$

where \Im represents the imaginary part of a complex quantity.

In fields formed by purely standing waves the active part of the acoustic intensity is zero while in fields formed by purely progressive waves the reactive acoustic intensity is zero. These kinds of fields are difficult to be found in practice and in the majority of the fields the intensity is composed by active and reactive intensity.

The comparison between the instantaneous intensity, the active intensity, the reactive intensity, and the total intensity is shown in Figure 3.1.

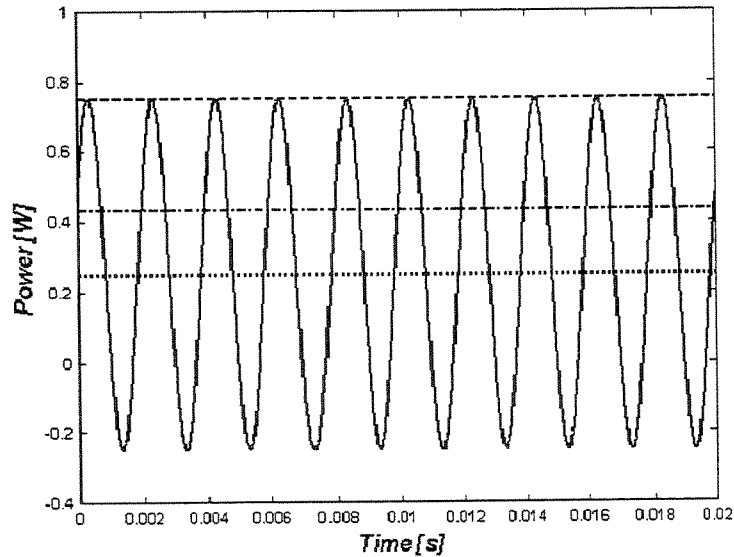


Figure 3.1: Comparison between the “-” instantaneous intensity, $I(t)$, “...” active intensity, I_a , “-.-” reactive intensity, I_r , and the “---” total intensity, $I_t = I_a + \sqrt{I_a^2 + I_r^2}$.

3.3 Particle velocity using P-P approach

The particle velocity can be measured using a particle velocity sensor, Bree et al. (1994,1996) and Eerden et al. (1998), or using two or more microphones aligned, Fahy (1995) and Kestell et al. (2000). Here, it is discussed the formulation for assessing the particle velocity using two microphones, named as the P-P approach.

The P-P approach consist of evaluating the particle velocity using two microphones spaced by δ in the acoustic field, and the velocity direction will be the same as that of the microphones, Fahy (1995). This technique will be used throughout the text. Using P_1 and P_2 to represent the measured pressures at the positions 1 and 2, respectively, the pressure at any location between the microphones is evaluated assuming a 1st order approximation as,

$$P(x) = ax + b \quad (3.12)$$

The conditions at position 1 are $x = 0$ and $P(0) = P_1$, and the conditions at position 2 are $x = \delta$ and $P(\delta) = P_2$, so,

$$\left. \begin{array}{l} P(0) = P_1 = a(0) + b \\ P(\delta) = P_2 = a\delta + b \end{array} \right\} \Rightarrow \begin{cases} b = P_1 \\ a = \frac{P_2 - P_1}{\delta} \end{cases} \quad (3.13)$$

Thus, the first order approximation of the pressure at any location between the two microphones is given by,

$$P(x) = \frac{P_2 - P_1}{\delta} x + P_1 \quad (3.14)$$

The pressure evaluated between the microphones, at position $\delta/2$ and represented by P_{12} , can be evaluated substituting x by $\delta/2$ in Equation (3.14), resulting in,

$$P_{12} = P\left(\frac{\delta}{2}\right) = \frac{P_1 + P_2}{2} \quad (3.15)$$

The particle velocity is given approximating the spatial pressure gradient by finite differences of 1st order, which is given by differentiating Equation (3.14) with respect to x ,

$$\nabla P(x) = \frac{P_2 - P_1}{\delta} \quad (3.16)$$

So, the particle velocity evaluated in the position between the microphones, u_{12} , is given by substituting the gradient approximation using two-microphone technique in Euler's equation in the frequency domain, Equation (3.4), as,

$$u_{12} = \frac{i}{\rho_0 \omega} \frac{P_2 - P_1}{\delta} \quad (3.17)$$

Equation (3.17) is the simplest approximation to the particle velocity. This method will be used because it is simple and can be implemented in the frequency domain; besides, the errors in this estimate are well known, Fahy (1995), Jacobsen (1994), and Chung (1978).

3.4 Acoustic intensity using P-P approach

The expression for evaluating the acoustic intensity using the P-P approach, I_{12} , is obtained by substituting Equations (3.17) and (3.15) in (3.9),

$$I = \frac{1}{2} P_{12} u_{12}^* = \frac{1}{2} \left(\frac{P_2 + P_1}{2} \right) \left(\frac{-i}{\rho_0 \omega} \frac{P_2^* - P_1^*}{\delta} \right) = \frac{i}{4\rho_0 \omega \delta} (P_1 + P_2)(P_1 - P_2)^* \quad (3.18)$$

The active intensity using the P-P approach, I_{a12} , is given by,

$$I_{a12} = \frac{1}{4\rho_0 \omega \delta} \Re \{ i (P_1 + P_2)(P_1 - P_2)^* \} \quad (3.19)$$

As $\Re \{ i (P_1 + P_2)(P_1 - P_2)^* \} = 2\Im \{ P_1 P_2^* \}$, so, the active intensity using the P-P approach is given by,

$$I_{a12} = \frac{1}{2} \Re \{ P_{12} u_{12}^* \} = \frac{1}{2\omega \rho_0 \delta} \Im \{ P_1 P_2^* \} \quad (3.20)$$

The reactive intensity using the P-P approach, I_{r12} , is given by,

$$I_{r12} = \frac{1}{4\rho_0 \omega \delta} \Im \{ i (P_1 + P_2)(P_1 - P_2)^* \} \quad (3.21)$$

As $\Im\{(P_1 + P_2)(P_1 - P_2)^*\} = |P_1|^2 - |P_2|^2$, so, the reactive intensity using the P-P approach is given by,

$$I_{r12} = \frac{1}{2} \Im\{P_{12} u_{12}^*\} = \frac{1}{4\omega\rho\delta} (|P_1|^2 - |P_2|^2) \quad (3.22)$$

The acoustic intensity using the P-P approach is subject of many errors, Fahy (1995), Thompson and Tree (1981), and Chung (1978). The influence of the errors in the acoustic intensity measurement and in the particle velocity measurement will be discussed later when the acoustic field will be modeled.

3.5 Acoustic impedance

The impedance is a complex quantity that relates pressure and particle/volume velocity. It is termed in several ways, depending on the medium where the definition is applied, Kinsler et al. (1982). The ratio of pressure and particle velocity is the specific acoustic impedance, z . It is useful to describe the transmission of the acoustic waves from one medium to another. It is defined as,

$$z = \frac{P}{u} \quad (3.23)$$

The acoustic impedance, Z , is defined as the ratio of the pressure and volume velocity, it is useful to describe acoustic radiation from vibrating bodies, and the transmission through lumped acoustic elements or through ducts and horns. It is given by,

$$Z = \frac{P}{uS} = \frac{P}{U} = \frac{z}{S} \quad (3.24)$$

where S is the area where the impedance is evaluated, and U is the volume velocity.

The radiation impedance, Z_R , is defined as the ratio of the force and velocity; it is useful to calculate the coupling between acoustic waves and driving sources or driven loads. It is part of the mechanical impedance, Z_m , of a vibrating system associated with the radiation of the sound, and it is given by,

$$Z_R = \frac{F}{u} = \frac{PS}{u} = zS = ZS^2 \quad (3.25)$$

3.6 Sources in acoustic fields

When one acoustic source is introduced in an acoustic field, the pressure at any location of the field can be expressed using the acoustic impedance relations. Assuming that the acoustic source is vibrating and imposing in the acoustic field a volume velocity Q , the pressure P at a given location in the acoustic field is given by,

$$P = ZQ \quad (3.26)$$

where Z is the “transfer” impedance because Q is the particle velocity immediately in front of the acoustic source multiplied by the area of the source, S .

In the same way, it is possible to define a “transfer” particle velocity response function, Y , that relates the volume velocity of a source in the acoustic field with the particle velocity measured at any location in the field as,

$$u = YQ \quad (3.27)$$

The volume velocity of an acoustic source can be measured enclosing the back of the acoustic source with a microphone inside, and a simple relation of lumped acoustic systems gives the volume velocity from the source as used by Chen and Lin (2000). Another way to measure the volume velocity of an acoustic source is to measure the velocity of the vibrating surface generating the sound, such as loudspeaker. The velocity may be measured using an accelerometer attached to the surface or a non-contact transducer as a laser Doppler vibrometer.

3.7 Acoustic power introduced by vibrating sources

The acoustic power introduced by an acoustic source is related to the energy in the acoustic system. The acoustic power of a single source is defined as Hansen and Snyder (1997),

$$W = \int_S I \cdot n ds \quad (3.28)$$

where \mathbf{n} is the outward normal vector from the surface S enclosing the source. It can be expressed as,

$$W = \frac{1}{2} P Q^* \quad (3.29)$$

where P is the acoustic pressure acting in front of the acoustic source and Q is its volume velocity.

The acoustic power radiated by an acoustic source is defined as,

$$W_r = \frac{1}{2} \Re\{P Q^*\} \quad (3.30)$$

and the acoustic power stored by an acoustic source is defined as,

$$W_s = \frac{1}{2} \Im\{P Q^*\} \quad (3.31)$$

It is interesting to note that the acoustic power from vibrating acoustic sources is directly related to the intensity measured in front of the source, which can be observed comparing Equations (3.29) and (3.9).

The active and reactive acoustic power from acoustic sources can be interpreted using the analogy to electrical circuits, where, if the current and voltage phasors are orthogonal (90° out-of-phase), the source power is purely reactive. However, if the current and voltage phasors are not orthogonal, the source has both the active and reactive power components, which means that there is a resistor dissipating energy in the electrical circuit. Turning back to the acoustic system, the electric resistor is equivalent to an energy dissipation mechanism such as an opening to the free field in a duct.

3.8 Experimental measurements of the acoustical properties

The acoustic power radiated from acoustic sources, Equation (3.29), can be evaluated experimentally taking the crosspower between the total pressure immediately in front of the

source and the volume velocity of the source. The pressure in front of the source can be measured with a microphone array located as close as possible to the source. The volume velocity of the source can be measured using a laser Doppler vibrometer measuring the surface velocity of the source. Thus, the acoustic power radiated from the source is given by,

$$W_T = \frac{1}{2} \Re \{P_T Q^*\} = \Re \{G_{QP_T}\} \quad (3.32)$$

where G_{QP_T} is the crosspower between the volume velocity Q and total pressure P_T .

The active acoustic intensity can be evaluated using the P-P approach, Fahy (1995),

$$I_{a_{12}} = \frac{1}{2\omega\rho\delta} \Im \{P_1 P_2^*\} = \frac{1}{\omega\rho\delta} \Im \{G_{P_2 P_1}\} \quad (3.33)$$

where $G_{P_2 P_1}$ is the crosspower between the two microphones placed close to each other, and δ is the separation distance between them.

However, the method of measuring the active intensity using the P-P approach, Equation (3.33), is subject to many errors, Fahy (1995). Among them, it can be highlighted the systematic error due to phase mismatch between the two microphones, which can become critical when performing the intensity measurement in a reverberant field or when the two microphones are placed very close to each other in order to minimize the error due to the finite difference approximation.

The phase mismatch can be minimized by using a “geometric mean” in the crosspower between the sensors as proposed by Chung (1978),

$$\tilde{G}_{P_2 P_1} = \sqrt{{}_s G_{P_2 P_1} G_{P_2 P_1}} \quad (3.34)$$

where $G_{P_2 P_1}$ is the crosspower with the sensors in the original order and ${}_s G_{P_2 P_1}$ is the crosspower with the sensors in the switched order.

The finite difference approximation error correction can be overcome as proposed by Jacobsen (1994), by multiplying the crosspower by a correction factor given by,

$$\frac{K\delta}{\sin K\delta} = \frac{1}{\text{sinc}(K\delta)} \quad (3.35)$$

Thus, the acoustic active intensity using the P-P principle with the error correction of Equations (3.34) and (3.35) can be expressed as,

$$I_{a_{12}} = \frac{1}{\omega \rho \delta} \frac{K\delta}{\sin K\delta} \Im \left\{ \tilde{G}_{P_2 P_1} \right\} \quad (3.36)$$

The acoustic potential energy density can be evaluated as,

$$E_p = \frac{1}{2\rho c^2} |P|^2 = \frac{1}{\rho c^2} G_{PP} \quad (3.37)$$

where G_{PP} is the auto-spectrum of the pressure signal.

Chapter 4

Active control methods

This chapter describes the active control methods, which are developed using the equations in terms of primary and secondary sources and error sensors, basically pressure and velocity equations.

The control methods are based upon minimizing cost functions such as the acoustic potential energy density, the acoustic kinetic energy density, the total acoustic energy density, and the acoustic active and reactive intensity. These cost functions give information about the energetic behavior of the acoustic system.

In the first part of the chapter, the optimal solution for the secondary volume velocity for each control method is developed. In the second part, the adaptive control methods, which are the practical implementations of the optimal solutions, are developed.

The optimal solution analyses are important because they represent the best performance the cost function can achieve. The adaptive control method is the method that can be implemented in real time to minimize the cost function.

4.1 Optimal solutions

The optimal solutions are obtained by taking the gradient of cost the function in relation to the secondary volume velocity. Thus, it is necessary to write the pressure and particle velocity equations of the acoustic system in terms of the primary and secondary volume velocities.

Assuming that there are N_p primary sources, N_s secondary sources, the pressure measured at N_e locations in the acoustic field are given by,

$$\begin{Bmatrix} P_1 \\ \vdots \\ P_{N_e} \end{Bmatrix} = \begin{bmatrix} Z_{p_{1,1}} & \cdots & Z_{p_{1,N_p}} \\ \vdots & \ddots & \vdots \\ Z_{p_{N_e,1}} & \cdots & Z_{p_{N_e,N_p}} \end{bmatrix} \begin{Bmatrix} Q_{p_1} \\ \vdots \\ Q_{p_{N_p}} \end{Bmatrix} + \begin{bmatrix} Z_{s_{1,1}} & \cdots & Z_{s_{1,N_s}} \\ \vdots & \ddots & \vdots \\ Z_{s_{N_e,1}} & \cdots & Z_{s_{N_e,N_s}} \end{bmatrix} \begin{Bmatrix} Q_{s_1} \\ \vdots \\ Q_{s_{N_s}} \end{Bmatrix} \quad (4.1)$$

where Q_p and Q_s are the volume velocity of the primary and secondary sources, respectively, Z_p and Z_s are the “transfer” impedances measured between the pressure and the primary and secondary sources, respectively.

The above equation can be rewritten in shorthand notation as,

$$P_{(N_e,1)} = Z_{p_{(N_e,N_p)}} Q_{p_{(N_p,1)}} + Z_{s_{(N_e,N_p)}} Q_{s_{(N_p,1)}} \quad (4.2)$$

As for the pressure field, the particle velocity measured at N_e locations in the acoustic field are given by,

$$\begin{Bmatrix} u_1 \\ \vdots \\ u_{N_e} \end{Bmatrix} = \begin{bmatrix} Y_{p_{1,1}} & \cdots & Y_{p_{1,N_p}} \\ \vdots & \ddots & \vdots \\ Y_{p_{N_e,1}} & \cdots & Y_{p_{N_e,N_p}} \end{bmatrix} \begin{Bmatrix} Q_{p_1} \\ \vdots \\ Q_{p_{N_p}} \end{Bmatrix} + \begin{bmatrix} Y_{s_{1,1}} & \cdots & Y_{s_{1,N_s}} \\ \vdots & \ddots & \vdots \\ Y_{s_{N_e,1}} & \cdots & Y_{s_{N_e,N_s}} \end{bmatrix} \begin{Bmatrix} Q_{s_1} \\ \vdots \\ Q_{s_{N_s}} \end{Bmatrix} \quad (4.3)$$

where Y_p and Y_s are the “transfer” particle velocity response functions measured between the particle velocity and the primary and secondary sources, respectively.

The above equation can be rewritten in shorthand notation as,

$$u_{(N_e,1)} = Y_{p_{(N_e,N_p)}} Q_{p_{(N_p,1)}} + Y_{s_{(N_e,N_p)}} Q_{s_{(N_p,1)}} \quad (4.4)$$

It is important to remember that the pressure is a scalar quantity while the particle velocity is a vectorial quantity. Therefore, in 2-D or 3-D acoustic fields the direction of the particle velocity must be observed to perform correctly the sum in Equation (4.4).

4.1.1 Optimal solution for the secondary source base upon controlling the acoustic potential energy density

The acoustic potential energy is a real scalar quadratic function in terms of Q_s ; therefore, there is only one global minimal point. Besides, it can be measured using microphones spread over the acoustic field. So, it is easy to be applied in ANC and ASAC schemes. Using the sum of the acoustic potential energy densities over the sensors as cost function,

$$J = E_p = \frac{1}{2\rho_0 c^2} |P|^2 \quad (4.5)$$

The optimal solution that minimizes the potential energy density is found substituting the pressure, Equation (4.2), in the cost function defined in Equation (4.5), resulting in,

$$J = \frac{1}{2\rho_0 c^2} |P|^2 = \frac{1}{2\rho_0 c^2} P^H P = \frac{1}{2\rho_0 c^2} (Z_p Q_p + Z_s Q_s)^H (Z_p Q_p + Z_s Q_s) \quad (4.6)$$

Expanding the terms,

$$J = \frac{1}{2\rho_0 c^2} \left[(Z_p Q_p)^H Z_p Q_p + (Z_p Q_p)^H Z_s Q_s + (Z_s Q_s)^H Z_p Q_p + (Z_s Q_s)^H Z_s Q_s \right] \quad (4.7)$$

Each term of Equation (4.7) is a real scalar function. The gradient of each term in relation to the secondary sources Q_s is performed using the relations presented in Appendix A, so,

$$\nabla (Z_p Q_p)^H Z_p Q_p = 0 \quad (4.8)$$

$$\nabla (Z_p Q_p)^H Z_s Q_s = Z_s^H Z_p Q_p \quad (4.9)$$

$$\nabla (Z_s Q_s)^H Z_p Q_p = Z_s^H Z_p Q_p \quad (4.10)$$

$$\nabla (Z_s Q_s)^H Z_s Q_s = 2Z_s^H Z_s Q_s \quad (4.11)$$

Therefore, the gradient of the cost function in relation to Q_s is given by,

$$\nabla E_p = \frac{1}{2\rho_0 c^2} (2Z_s^H Z_p Q_p + 2Z_s^H Z_s Q_s) \quad (4.12)$$

The optimal solution to the secondary source volume velocities that minimizes the acoustic potential energy density is obtained by equating Equation (4.12) to zero and solving for Q_s , resulting in,

$$Q_s = -(Z_s^H Z_s)^{-1} Z_s^H Z_p Q_p \quad (4.13)$$

which is the same final result obtained by Qiu and Hansen (1998).

It is interesting to note that $(Z_s^H Z_s)$ cannot vanish, which means that the secondary sources must be able to act upon the pressure at the error sensors (controllability condition).

4.1.2 Optimal solution for the secondary source based upon controlling the acoustic kinetic energy density

As the acoustic potential energy density, the acoustic kinetic energy density is a real scalar quadratic function in terms of Q_s . Using the sum of the acoustic kinetic energy density over the sensors as cost function,

$$J = E_k = \frac{\rho_0}{2} |u|^2 \quad (4.14)$$

Substituting the particle velocity, Equation (4.4), in Equation (4.14),

$$J = \frac{\rho_0}{2} |u|^2 = \frac{\rho_0}{2} u^H u = \frac{\rho_0}{2} (Y_p Q_p + Y_s Q_s)^H (Y_p Q_p + Y_s Q_s) \quad (4.15)$$

Expanding the terms,

$$J = \frac{\rho_0}{2} [(Y_p Q_p)^H Y_p Q_p + (Y_p Q_p)^H Y_s Q_s + (Y_s Q_s)^H Y_p Q_p + (Y_s Q_s)^H Y_s Q_s] \quad (4.16)$$

The terms present in the cost function that minimize the acoustic kinetic energy are the same that minimizes the acoustic potential energy density, with Z replacing Y , compare Equation (4.16) with (4.7). Therefore, the gradient of Equation (4.16) in relation to the Q_s is given by,

$$\nabla E_K = \frac{\rho_0}{2} (2Y_s^H Y_p Q_p + 2Y_s^H Y_s Q_s) \quad (4.17)$$

The optimal solution to the secondary source volume velocities that minimize the acoustic kinetic energy density is given by equaling Equation (4.17) to zero and solving for Q_s , resulting in,

$$Q_s = -(Y_s^H Y_s)^{-1} Y_s^H Y_p Q_p \quad (4.18)$$

which is the same final result obtained by Qiu and Hansen (1998).

As it happened with the optimal solution for the secondary source based upon controlling the acoustic potential energy density, it is necessary that the term $(Y_s^H Y_s)$ in Equation (4.18) does not vanish, which means that the secondary source should have the ability of acting upon the particle velocity at the error sensors (controllability condition).

4.1.3 Optimal solution for the secondary source based upon controlling the acoustic total energy density

The acoustic energy density is defined as the sum of the acoustic potential and kinetic energy densities. Using the sum of the acoustic energy density over the sensors as cost function,

$$J = E_T = E_P + E_K = \frac{1}{2\rho_0 c^2} |P|^2 + \frac{\rho_0}{2} |u|^2 \quad (4.19)$$

Substituting the pressure and particle velocity, Equations (4.2) and (4.4), in Equation (4.19),

$$J = \frac{1}{2\rho_0 c^2} (Z_p Q_p + Z_s Q_s)^H (Z_p Q_p + Z_s Q_s) + \frac{\rho_0}{2} (Y_p Q_p + Y_s Q_s)^H (Y_p Q_p + Y_s Q_s) \quad (4.20)$$

The gradient of Equation (4.20) was already computed in Equations (4.12) and (4.17). Therefore, the gradient of the acoustic total energy density in relation to Q_s is the sum of Equations (4.12) and (4.17),

$$\nabla E_T = \nabla E_P + \nabla E_K = \frac{1}{2\rho_0 c^2} (2Z_s^H Z_p Q_p + 2Z_s^H Z_s Q_s) + \frac{\rho_0}{2} (2Y_s^H Y_p Q_p + 2Y_s^H Y_s Q_s) \quad (4.21)$$

Equating the result in Equation (4.21) to zero and solving for Q_s , the optimal solution for the secondary source volume velocities that minimize the acoustic total energy density is given by,

$$Q_s = -(Z_s^H Z_s + \rho_0^2 c^2 Y_s^H Y_s)^{-1} (Z_s^H Z_p + \rho_0^2 c^2 Y_s^H Y_p) Q_p \quad (4.22)$$

which is the same final result obtained by Qiu and Hansen (1998).

It is obvious that it is necessary that the denominator of the above equation should not vanish, which means that the secondary sources should be able to influence the pressure and particle velocity at the error sensors (controllability condition).

4.1.4 Optimal solution for the secondary source based upon controlling the acoustic active intensity

The acoustic active intensity is a real function in terms of Q_s , but it should be used as cost function very carefully because the acoustic active intensity is a vector quantity. Using the sum of the acoustic active intensity over the sensors as cost function,

$$J = I_a = \frac{1}{2} \Re\{u^H p\} = \frac{1}{2} \Re\{p^H u\} \quad (4.23)$$

Substituting the pressure and the particle velocity, Equations (4.2) and (4.4), in Equation (4.23),

$$\begin{aligned} J = I_a &= \frac{1}{2} \Re\{(Y_p Q_p + Y_s Q_s)^H (Z_p Q_p + Z_s Q_s)\} \\ &= \frac{1}{2} \Re\{(Y_p Q_p)^H Z_p Q_p + (Y_p Q_p)^H Z_s Q_s + (Y_s Q_s)^H Z_p Q_p + (Y_s Q_s)^H Z_s Q_s\} \end{aligned} \quad (4.24)$$

Expanding Equation (4.24), taking the gradient of each term in relation to the Q_s , and using the relations present in Appendix A,

$$\nabla \Re \{ (Y_p Q_p)^H Z_p Q_p \} = 0 \quad (4.25)$$

$$\nabla \Re \{ (Y_p Q_p)^H Z_s Q_s \} = Z_s^H Y_p Q_p \quad (4.26)$$

$$\nabla \Re \{ (Y_s Q_s)^H Z_p Q_p \} = Y_s^H Z_p Q_p \quad (4.27)$$

$$\nabla \Re \{ (Y_s Q_s)^H Z_s Q_s \} = (Z_s^H Y_s + Y_s^H Z_s) Q_s \quad (4.28)$$

Therefore, the gradient of Equation (4.24) in relation to Q_s is given by,

$$\nabla I_a = \frac{1}{2} \left((Y_s^H Z_p + Z_s^H Y_p) Q_p + (Z_s^H Y_s + Y_s^H Z_s) Q_s \right) \quad (4.29)$$

The optimal solution to the volume velocity of the secondary sources that minimizes the acoustic active intensity is given by equating Equation (4.29) to zero and solving to Q_s , resulting in,

$$Q_s = - (Z_s^H Y_s + Y_s^H Z_s)^{-1} (Y_s^H Z_p + Z_s^H Y_p) Q_p \quad (4.30)$$

which is the same final result obtained by Qiu and Hansen (1998), but they consider only the active acoustic intensity in the radial direction.

It is observed that is necessary that $(Z_s^H Y_s + Y_s^H Z_s)$ should not vanish, which means that the error sensors, acoustic active intensity error sensors, should “see” some acoustic intensity from the secondary sources (controllability condition).

4.1.5 Optimal solution for the secondary source based upon controlling the acoustic reactive intensity

As the acoustic active intensity, the acoustic reactive intensity is a real function in terms of Q_s , but it should be used as cost function very carefully because the acoustic reactive intensity is

also a vector quantity. Using the sum of the acoustic reactive intensity over the sensors as cost function,

$$J = I_r = \frac{1}{2} \Im \{ \mathbf{u}^H \mathbf{P} \} \quad (4.31)$$

Substituting the pressure and particle velocity, Equations (4.2) and (4.4), in Equation (4.31),

$$J = I_r = \frac{1}{2} \Im \{ (\mathbf{Y}_p \mathbf{Q}_p + \mathbf{Y}_s \mathbf{Q}_s)^H (\mathbf{Z}_p \mathbf{Q}_p + \mathbf{Z}_s \mathbf{Q}_s) \} \quad (4.32)$$

Expanding the terms of Equation (4.32), and taking the gradient of each term in relation to \mathbf{Q}_s , and using the relations in Appendix A,

$$\nabla \Im \{ (\mathbf{Y}_p \mathbf{Q}_p)^H \mathbf{Z}_p \mathbf{Q}_p \} = 0 \quad (4.33)$$

$$\nabla \Im \{ (\mathbf{Y}_p \mathbf{Q}_p)^H \mathbf{Z}_s \mathbf{Q}_s \} = \frac{1}{2} j \mathbf{Z}_s^H \mathbf{Y}_p \mathbf{Q}_p \quad (4.34)$$

$$\nabla \Im \{ (\mathbf{Y}_s \mathbf{Q}_s)^H \mathbf{Z}_p \mathbf{Q}_p \} = -\frac{1}{2} j \mathbf{Y}_s^H \mathbf{Z}_p \mathbf{Q}_p \quad (4.35)$$

$$\nabla \Im \{ (\mathbf{Y}_s \mathbf{Q}_s)^H \mathbf{Z}_s \mathbf{Q}_s \} = \frac{1}{2} j (\mathbf{Z}_s^H \mathbf{Y}_s - \mathbf{Y}_s^H \mathbf{Z}_s) \mathbf{Q}_s \quad (4.36)$$

Therefore, the gradient of the acoustic reactive intensity is given by,

$$\nabla I_r = \frac{1}{2} j ((\mathbf{Z}_s^H \mathbf{Y}_p - \mathbf{Y}_s^H \mathbf{Z}_p) \mathbf{Q}_p + (\mathbf{Z}_s^H \mathbf{Y}_s - \mathbf{Y}_s^H \mathbf{Z}_s) \mathbf{Q}_s) \quad (4.37)$$

The optimal solution to the volume velocity of the secondary sources that minimizes the acoustic reactive intensity is given by equating Equation (4.37) to zero and solving to \mathbf{Q}_s , resulting in,

$$\mathbf{Q}_s = -(\mathbf{Z}_s^H \mathbf{Y}_s - \mathbf{Y}_s^H \mathbf{Z}_s)^{-1} (\mathbf{Z}_s^H \mathbf{Y}_p - \mathbf{Y}_s^H \mathbf{Z}_p) \mathbf{Q}_p \quad (4.38)$$

Analyzing the above equation it is noted that is necessary for the error sensors, acoustic reactive intensity sensors, to “see” some reactive intensity from the secondary sources.

4.1.6 Optimal solution for the secondary source based upon controlling the acoustic power radiated by two sources

The acoustic power radiated by two acoustic sources is defined as Hansen and Snyder (1997) by,

$$W_R = \frac{1}{2} \Re \{ (P_p(x_p) + P_s(x_p)) Q_p^* + (P_p(x_s) + P_s(x_s)) Q_s^* \} \quad (4.39)$$

where x_p and x_s are the position of the primary and secondary source, respectively.

The first term at the right side of Equation (4.39) is the contribution of the primary source and the second term is the contribution of the secondary source to the total radiated acoustic power. It is interesting to note that in the radiated acoustic power the sensors are located in front of the sources.

It is observed that the acoustic power radiated by the sources is a real function. Therefore, expanding the radiated acoustic power using the pressure, Equations (4.2),

$$J = W_R = \frac{1}{2} \Re \{ (Z_p(x_p) Q_p + Z_s(x_p) Q_s) Q_p^* + (Z_p(x_s) Q_p + Z_s(x_s) Q_s) Q_s^* \} \quad (4.40)$$

where $Z_p(x_p)$ is the “transfer” impedance from the primary source at the primary source, $Z_s(x_p)$ is the “transfer” impedance from the secondary source at the primary source, $Z_p(x_s)$ is the “transfer” impedance from the primary source at the secondary source, and $Z_s(x_s)$ is the “transfer” impedance from the secondary source at the secondary source.

Expanding the terms of Equation (4.40) and taking the gradient of each term in relation to Q_s , and using the relation in the Appendix A,

$$\nabla \Re \{ (Z_p(x_p) Q_p) Q_p^* \} = 0 \quad (4.41)$$

$$\nabla \Re \{ (Z_s(x_p) Q_s) Q_p^* \} = Z_s^*(x_p) Q_p \quad (4.42)$$

$$\nabla \Re\{(Z_p(x_s)Q_p)Q_s^*\} = Z_p(x_s)Q_p \quad (4.43)$$

$$\nabla \Re\{(Z_s(x_s)Q_s)Q_s^*\} = (Z_s(x_s) + Z_s^*(x_s))Q_s \quad (4.44)$$

Thus, the gradient of the radiated acoustic power from the sources in relation to Q_s is given by,

$$\nabla W_R = (Z_s^*(x_p) + Z_p(x_s))Q_p + (Z_s(x_s) + Z_s^*(x_s))Q_s \quad (4.45)$$

The optimal solution to the volume velocity of the secondary sources that minimizes the radiated acoustic power is given by equaling Equation (4.45) to zero and solving to Q_s , resulting in, as suggested by Snyder and Hansen (1997),

$$Q_s = -\frac{Z_p(x_s) + Z_s^*(x_s)}{2\Re\{Z_s(x_s)\}}Q_p = -Q_p \frac{\Re\{Z_s(x_p)\}}{\Re\{Z_s(x_s)\}} \quad (4.46)$$

where, by the reciprocity theorem, Kinsler et al. (1982), $Z_s(x_p) = Z_p(x_s)$.

4.1.7 Summary and observations about the optimal solutions

It is important to note that the acoustic potential, kinetic, and total energy are real quadratic functions. Therefore, cost functions formed by these functions are suitable for control applications because they have a global minimum.

However, the acoustic active and reactive intensities are real functions but are not quadratic functions, since the highest term of Q_s can be either positive or negative. Thus, one way to guarantee the convergence is to assure that the term of highest Q_s in the acoustic active/reactive intensity should obey the following relations,

$$\Re\{Q_s^H Y_s^H Z_s Q_s\} \geq 0 \quad (4.47)$$

for the acoustic active intensity, and

$$\Im\{Q_s^H Y_s^H Z_s Q_s\} \geq 0 \quad (4.48)$$

for the acoustic reactive intensity.

It is interesting to note that $Z_s Q_s$ and $Y_s Q_s$ are the pressure and particle velocity imposed by the secondary source at the error sensors, which means that the secondary source should act with a positive intensity at the error sensors.

On the other hand, it is possible to use the squared active intensity and the squared reactive intensity as cost functions, which, in this case, form quadratic cost functions in terms of Q_s , but the final optimal result is the same result, as shown below.

Taking for example the cost function based upon the squared active intensity as,

$$J = I_a^2 \quad (4.49)$$

The gradient of above equation is given by,

$$\nabla J = \nabla I_a^2 = 2I_a \nabla I_a \quad (4.50)$$

Equation (4.50) is equal to zero either I_a is equal to zero or ∇I_a is equal to zero. The ∇I_a is equal to zero if the optimal solution to the secondary volume velocity is given by Equation (4.30).

A summary of the optimal solutions is shown in Table 4.1.

Table 4.1: Optimal solutions for the volume velocity of the secondary sources

Cost Function	Optimal solution for the secondary source volume velocity Q_s
E_P	$-(Z_s^H Z_s)^{-1} Z_s^H Z_p Q_p$
E_K	$-(Y_s^H Y_s)^{-1} Y_s^H Y_p Q_p$
E_T	$-(Z_s^H Z_s + \rho_0^2 c^2 Y_s^H Y_s)^{-1} (Z_s^H Z_p + \rho_0^2 c^2 Y_s^H Y_p) Q_p$
I_a	$-(Z_s^H Y_s + Y_s^H Z_s)^{-1} (Y_s^H Z_p + Z_s^H Y_p) Q_p$
I_r	$-(Z_s^H Y_s - Y_s^H Z_s)^{-1} (Y_s^H Z_p - Z_s^H Y_p) Q_p$

In some applications the optimal solution is implemented for one error sensor, one primary source and one secondary source; in this case, the optimal solutions are shown in Table 4.2, where can be seen that the hermitian (^H) was substituted by the conjugate (*).

Table 4.2: Optimal solutions for the volume velocity of the secondary source for one error sensor, one primary source and one secondary.

Cost Function	Optimal solution for the secondary source volume velocity Q_s
E_p	$-\frac{Z_p}{Z_s} Q_p$
E_k	$-\frac{Y_p}{Y_s} Q_p$
E_T	$-\frac{Z_s^* Z_p + \rho^2 c^2 Y_s^* Y_p}{ Z_s ^2 + \rho^2 c^2 Y_s ^2} Q_p$
I_a	$-\frac{Y_s^* Z_p + Z_s^* Y_p}{2\Re\{Z_s^* Y_s\}} Q_p$
I_r	$-\frac{Y_s^* Z_p - Z_s^* Y_p}{2j\Im\{Y_s^* Z_s\}} Q_p$
W_r	$-\frac{\Re\{Z_s(x_p)\}}{\Re\{Z_s(x_s)\}} Q_p$

4.1.8 Optimal solution using two microphones to estimate the particle velocity

Some optimal solutions need the “transfer” particle velocity, Y_s or Y_p , to be successfully implemented. However, the particle velocity can be estimated using the P-P approach, Fahy (1995), and, then, the optimal solution can be calculated. On the other hand, the estimated particle velocity using the P-P approach can be inserted into the optimal solution to reduce the computational complexity. In order to exemplify the introduction of the particle velocity estimated using the P-P approach, the optimal solutions are developed for one primary source, one secondary source, and one error sensor.

The particle velocity estimated using the P-P approach is given by, from chapter 3,

$$u_{12} = \frac{i}{\rho_0 \omega} \frac{P_2 - P_1}{\delta} \quad (4.51)$$

Using the definitions of impedance and particle velocity and knowing that $P_{1,2} = Z_{1,2}Q$ and $u_{12} = Y_{12}Q$, the particle velocity, Equation (3.17), can be written in a more suitable form as,

$$u_{12} = Y_{12}Q = \frac{i}{\rho_0 \omega} \frac{Z_2 - Z_1}{\delta} Q \quad (4.52)$$

Thus, it is obvious that the transfer particle velocity can be estimated using the transfer impedances in the following form,

$$Y_{12} = \frac{i}{\rho_0 \omega} \frac{Z_2 - Z_1}{\delta} \quad (4.53)$$

The same way as particle velocity, the transfer impedance between the microphones is given by,

$$Z_{12} = \frac{Z_1 + Z_2}{2} \quad (4.54)$$

Now, considering the case where two sources are acting in the acoustic field, one primary source and one secondary source, the pressure and particle velocity between the two microphones can be written using the Equations (4.53) and (4.54) as,

$$P_{12} = \frac{Z_{p1} + Z_{p2}}{2} Q_p + \frac{Z_{s1} + Z_{s2}}{2} Q_s \quad (4.55)$$

$$u_{12} = \frac{i}{\rho_0 \omega} \frac{Z_{p2} - Z_{p1}}{\delta} Q_p + \frac{i}{\rho_0 \omega} \frac{Z_{s2} - Z_{s1}}{\delta} Q_s \quad (4.56)$$

Applying Equations (4.53) and (4.54) to the optimal solution of the volume velocity controlling the acoustic kinetic energy density, Equation (4.18), is found,

$$Q_s = -\frac{Y_p}{Y_s} Q_p = \frac{\frac{i}{\rho_0 \omega} \frac{Z_{p_2} - Z_{p_1}}{\delta}}{\frac{i}{\rho_0 \omega} \frac{Z_{s_2} - Z_{s_1}}{\delta}} Q_p = -\frac{Z_{p_2} - Z_{p_1}}{Z_{s_2} - Z_{s_1}} Q_p \quad (4.57)$$

In the optimal solution for the secondary volume velocity that minimizes the acoustic energy density, Equation (4.22), it is necessary that pressure and particle velocity should be evaluated at the same point; therefore, it is necessary to substitute the impedance transfer function to form the correct optimal solution. Applying Equations (4.55) and (4.56) to the optimal solution of the volume velocity controlling the acoustic energy, Equation (4.22), yields,

$$Q_s = -\frac{\rho \omega^2 \delta^2 (Z_{s_2} + Z_{s_1})^* (Z_{p_2} + Z_{p_1}) + 4\rho c^2 (Z_{s_2} - Z_{s_1})^* (Z_{p_2} - Z_{p_1})}{\rho \omega^2 \delta^2 |Z_{s_2} + Z_{s_1}|^2 + 4\rho c^2 |Z_{s_2} - Z_{s_1}|^2} Q_p \quad (4.58)$$

The optimal solution for the secondary source that minimizes the acoustic active intensity, Equation (4.30), must have the pressure and particle velocity measured at the same point. So, the optimal solution to the secondary source that minimizes the acoustic active intensity using the P-P approach is found substituting Equations (4.55) and (4.56) in (4.30) given,

$$Q_s = -\frac{\left(\frac{i}{\rho_0 \omega} \frac{Z_{s_2} - Z_{s_1}}{\delta}\right)^* \left(\frac{Z_{p_1} + Z_{p_2}}{2}\right) + \left(\frac{Z_{s_1} + Z_{s_2}}{2}\right)^* \left(\frac{i}{\rho_0 \omega} \frac{Z_{p_2} - Z_{p_1}}{\delta}\right)}{2\Re\left\{\left(\frac{Z_{s_1} + Z_{s_2}}{2}\right)^* \left(\frac{i}{\rho_0 \omega} \frac{Z_{s_2} - Z_{s_1}}{\delta}\right)\right\}} Q_p \quad (4.59)$$

Simplifying the above equation is found,

$$Q_s = -\frac{\frac{i}{2\rho_0 \omega \delta} (Z_{s_1} + Z_{s_2})^* (Z_{p_2} - Z_{p_1}) - \frac{i}{2\rho_0 \omega \delta} (Z_{s_2} - Z_{s_1})^* (Z_{p_1} + Z_{p_2})}{\frac{1}{\rho_0 \omega \delta} \Re\left\{i(Z_{s_1} + Z_{s_2})^* (Z_{s_2} - Z_{s_1})\right\}} Q_p \quad (4.60)$$

Thus, the optimal solution to control the acoustic active intensity using the P-P approach to estimate the particle velocity is given by,

$$Q_s = -\frac{Z_{s_2}^* Z_{p_1} - Z_{s_1}^* Z_{p_2}}{2i\Im\{Z_{s_1} Z_{s_2}^*\}} Q_p \quad (4.61)$$

The optimal solution for the secondary source that minimizes the acoustic reactive intensity, Equation (4.38), must have the pressure and particle velocity measured at the same point. So, the optimal solution for the secondary source that minimizes the acoustic reactive intensity using the P-P approach is found substituting Equations (4.55) and (4.56) in (4.38) giving,

$$Q_s = - \frac{\left(\frac{Z_{s_1} + Z_{s_2}}{2}\right)^* \left(\frac{i}{\rho_0 \omega} \frac{Z_{p_2} - Z_{p_1}}{\delta}\right) - \left(\frac{i}{\rho_0 \omega} \frac{Z_{s_2} - Z_{s_1}}{\delta}\right)^* \left(\frac{Z_{p_1} + Z_{p_2}}{2}\right)}{2i \Im \left\{ \left(\frac{Z_{s_1} + Z_{s_2}}{2}\right)^* \left(\frac{i}{\rho_0 \omega} \frac{Z_{s_2} - Z_{s_1}}{\delta}\right) \right\}} Q_p \quad (4.62)$$

Simplifying the above equation,

$$Q_s = - \frac{\frac{i}{2\rho_0 \omega \delta} (Z_{s_1} + Z_{s_2})^* (Z_{p_2} - Z_{p_1}) + (Z_{s_2} - Z_{s_1})^* (Z_{p_1} + Z_{p_2})}{\frac{i}{\rho_0 \omega \delta} \Im \{ (Z_{s_1} + Z_{s_2})^* (Z_{s_2} - Z_{s_1}) \}} Q_p \quad (4.63)$$

Thus, the optimal solution to control the acoustic reactive intensity using the P-P approach to estimate the particle velocity is given by,

$$Q_s = - \frac{1}{2} \frac{Z_{s_2}^* Z_{p_2} - Z_{s_1}^* Z_{p_1}}{|Z_{s_2}|^2 - |Z_{s_1}|^2} Q_p \quad (4.64)$$

A summary of the control methods using the P-P approach to estimate the particle velocity can be seen in Table 4.3. Analyzing the optimal solutions it can be observed that if the separation distance δ of the microphone pair is much less than the wavelength λ , Z_{s_1} and Z_{s_2} are similar, as well as Z_{p_1} and Z_{p_2} . It means that the denominator of the optimal solution that minimizes the acoustic kinetic energy density and the acoustic reactive intensity and the numerator of the optimal solution that minimizes the acoustic active intensity are close to zero. Therefore, a previous analysis is indicated before applying the optimal solutions.

Table 4.3: Optimal solution for the volume velocity of the secondary sources using the P-P approach to estimate the particle velocity.

Cost Function	Optimal solution for the secondary source volume velocity Q_s
E_k	$-\frac{Z_{p_2} - Z_{p_1}}{Z_{s_2} - Z_{s_1}} Q_p$
E_t	$-\frac{\rho\omega^2\delta^2(Z_{s_2} + Z_{s_1})^*(Z_{p_2} + Z_{p_1}) + 4\rho c^2(Z_{s_2} - Z_{s_1})^*(Z_{p_2} - Z_{p_1})}{\rho\omega^2\delta^2 Z_{s_2} + Z_{s_1} ^2 + 4\rho c^2 Z_{s_2} - Z_{s_1} ^2} Q_p$
I_a	$-\frac{Z_{s_2}^*Z_{p_1} - Z_{s_1}^*Z_{p_2}}{2i\Im\{Z_{s_1}Z_{s_2}^*\}} Q_p$
I_r	$-\frac{1}{2} \frac{Z_{s_2}^*Z_{p_2} - Z_{s_1}^*Z_{p_1}}{ Z_{s_2} ^2 - Z_{s_1} ^2} Q_p$

4.2 Adaptive Control Methods

The control methods presented here are based upon the feedforward adaptive filter theory, Haykin (1996), which consists of filtering the reference by a Finite Impulse Response (FIR) filter and using the resulting signal as the control signal. The reference signal is correlated with the error sensor signal and contains information about frequency and phase from the noise generated by the primary source. Without loss of generality, the reference is represented by the volume velocity for the primary source “ Q_p ”. The control law is represented by the volume velocity for the secondary source “ Q_s ”. So, the volume velocity of the secondary source is evaluated as,

$$Q_{s_{(N_s,1)}} = W_{(N_s,N_p)} Q_{p_{(N_p,1)}} \quad (4.65)$$

where W is a weight function which will be found recursively by an adaptive law.

The control law, Equation (4.65), shows that the number of the weight functions is proportional to the number of primary and secondary sources only, and not to the number of the error sensors. In order to reduce the complexity of the equations, the adaptive control methods are developed for the case of one primary source, one secondary source and one error sensor, i.e., $N_p = 1$, $N_s = 1$, and $N_e = 1$. Nevertheless, the adaptive control methods can be expanded to more than

one primary and one secondary source. The pressure and particle velocity equations are reduced to,

$$P = Z_p Q_p + Z_s W Q_p \quad (4.66)$$

$$u = Y_p Q_p + Y_s W Q_p \quad (4.67)$$

where the variables are scalar quantities.

The adaptive law will be developed using a self-orthogonalizing adaptive filtering algorithm as proposed by Haykin (1996) and Cowan (1987),

$$W(n+1) = W(n) - \mu R^{-1} \nabla J(n) \quad (4.68)$$

where n is the iteration time, μ is the step-size defined between 0 and 1, R^{-1} is the inverse of a correlation matrix R , and $\nabla J(n)$ is the gradient of the cost function at iteration n . R and ∇J will be outlined for each control method depending on each cost function.

Equation (4.68) is a modified formulation of the steepest-descent method, which is more suitable in control applications because the step-size μ is normalized between 0 and 1, Kuo and Morgan (1996). In addition, it guarantees a constant rate of convergence for all frequency lines, Haykin (1996) and Cowan (1987). Furthermore, as the equations are in the frequency domain, it is possible to control each frequency line independently from each other, because there is one weight W to each frequency.

4.2.1 Adaptive control method based upon controlling the potential energy density

Using the acoustic potential energy density as cost function, Equation (4.5), and substituting Equation (4.66),

$$J = E_p = \frac{1}{2\rho_0 c^2} (Z_p Q_p + Z_s W Q_p)^* (Z_p Q_p + Z_s W Q_p) \quad (4.69)$$

Expanding the above equation and taking the gradient in relation to W to each term using the relation in Appendix A, is easy to find,

$$\nabla(Z_p Q_p)^* Z_p Q_p = 0 \quad (4.70)$$

$$\nabla(Z_p Q_p)^* Z_s W_{Qp} = (Z_s Q_p)^* Z_p Q_p \quad (4.71)$$

$$\nabla(Z_s W_{Qp})^* Z_p Q_p = (Z_s Q_p)^* Z_p Q_p \quad (4.72)$$

$$\nabla(Z_s W_{Qp})^* Z_s W_{Qp} = 2(Z_s Q_p)^* Z_s W_{Qp} \quad (4.73)$$

Therefore, the gradient of Equation (4.69) in relation to W is given by,

$$\nabla J = \frac{1}{\rho_0 c^2} (Z_s Q_p)^* (Z_p Q_p + Q_s W_{Qp}) = \frac{1}{\rho_0 c^2} (Z_s Q_p)^* P \quad (4.74)$$

The correlation matrix R is formed by the terms that multiply the weight function W in the cost function gradient, Equation (4.74), so,

$$R = \frac{1}{2\rho_0 c^2} 2(Z_s Q_p)^* Z_s Q_p = \frac{1}{\rho_0 c^2} |Z_s Q_p|^2 \quad (4.75)$$

Finally, taking the results in Equations (4.75) and (4.74) and substituting in the adaptive law, Equation (4.68), the adaptive control method that minimizes the potential energy density is found as,

$$W(n+1) = W(n) - \mu \frac{(Z_s Q_p)^*}{|Z_s Q_p|^2} P \quad (4.76)$$

The above equation is known as the frequency-domain filtered-X LMS, Haykin (1996), in its normalized version. It must be assured that the denominator will not vanish, which won't happen if the error sensor, in this case a microphone, "sees" some response from the secondary source. The method will adapt until the numerator is equal to zero, which happens if the pressure P is equal to zero. This method will be named in a shorthand notation as LMS-P.

4.2.2 Adaptive control method based upon controlling the kinetic energy density

Using the acoustic kinetic energy density as cost function, Equation (4.14), and substituting Equation (4.67),

$$J = E_K = \frac{\rho_0}{2} (Y_p Q_p + Y_s W Q_s)^* (Y_p Q_p + Y_s W Q_s) \quad (4.77)$$

Thus, it is noted that the equation to control E_K is analogous to the equation to control E_P , but with Z replaced by Y . Therefore, the gradient of Equation (4.77) is given by,

$$\nabla J = \frac{\rho_0}{2} (Y_s Q_p)^* u \quad (4.78)$$

The correlation matrix R is given by,

$$R = \frac{\rho_0}{2} |Y_s Q_p|^2 \quad (4.79)$$

Thus, the adaptive control method which minimizes the kinetic energy density is evaluated using Equation (4.76) by replacing Z by Y and P by u ,

$$W(n+1) = W(n) - \mu \frac{(Y_s Q_p)^*}{|Y_s Q_p|^2} u \quad (4.80)$$

Thus, the method presented in Equation (4.80) is the same frequency-domain filtered-X LMS presented in (4.76), but now based upon controlling the kinetic energy density. The same observations about the convergence did for Equation (4.76) valid for Equation (4.80), where it is necessary for the velocity sensor to “see” some response from the secondary source. This method will be named in shorthand notation as LMS-U.

The LMS-U can be successfully implemented where the pressure sensor (a microphone) can't give good signal levels to be used as error signal, which happens if the microphone is placed near a pressure node.

4.2.3 Adaptive control method based upon controlling the acoustic energy density

Using the acoustic total energy density as cost function, Equation (4.19), and substituting Equation (4.66) and (4.67),

$$J = E_T = \frac{1}{2\rho_0 c^2} (Z_p Q_p + Z_s W Q_p)^* (Z_p Q_p + Z_s W Q_p) + \frac{\rho_0}{2} (Y_p Q_p + Y_s W Q_s)^* (Y_p Q_p + Y_s W Q_s) \quad (4.81)$$

The gradient of the acoustic total energy density is the sum of the gradients of the acoustic potential and kinetic energy densities, Equations (4.74) and (4.78), so,

$$\nabla J = \frac{1}{\rho_0 c^2} (Z_s Q_p)^* P + \rho_0 (Y_s Q_p)^* u \quad (4.82)$$

The correlation matrix R is formed by the terms that multiplies the weight function, W , in the gradient of the cost function, so,

$$R = \frac{1}{\rho_0 c^2} (Z_s Q_p)^* Z_s Q_p + \rho_0 (Y_s Q_p)^* Y_s Q_p = \frac{1}{\rho_0 c^2} |Z_s Q_p|^2 + \rho_0 |Y_s Q_p|^2 \quad (4.83)$$

Finally, taking the results in Equations (4.82) and (4.83) and substituting in the adaptive law, Equation (4.68), the adaptive control method that minimizes the total acoustic energy density is given by,

$$W(n+1) = W(n) - \mu \frac{(Z_s Q_p)^* P + \rho_0^2 c^2 (Y_s Q_p)^* u}{|Z_s Q_p|^2 + \rho_0^2 c^2 |Y_s Q_p|^2} \quad (4.84)$$

The above Equation corresponds to the same control algorithm suggested by Sommerfeldt and Nahif (1994), but here it is expressed in the frequency domain.

4.2.4 Adaptive control method based upon controlling the acoustic active intensity using the P-U approach

Using the acoustic intensity as cost function, Equation (4.23), and substituting Equations (4.66) and (4.67),

$$J = I_a = \frac{1}{2} \Re \{ (Z_p Q_p + Z_s W Q_p) (Y_p Q_p + Y_s W Q_p)^* \} \quad (4.85)$$

Expanding Equation (4.85) and taking the gradient in relation to W of each term using the relations in Appendix A is easy to find,

$$\nabla \Re \{ (Y_p Q_p)^* Z_p Q_p \} = 0 \quad (4.86)$$

$$\nabla \Re \{ (Y_p Q_p)^* Z_s W_{Qp} \} = (Z_s Q_p)^* Y_p Q_p \quad (4.87)$$

$$\nabla \Re \{ (Y_s W_{Qp})^* Z_p Q_p \} = (Y_s Q_p)^* Z_p Q_p \quad (4.88)$$

$$\nabla \Re \{ (Y_s W_{Qp})^* Z_s W_{Qp} \} = (Y_s Q_p)^* Z_s W_{Qp} + (Z_s Q_p)^* Y_s W_{Qp} \quad (4.89)$$

Therefore, the gradient of the acoustic active intensity is given by,

$$\begin{aligned} \nabla J &= (Y_s Q_p)^* (Z_p Q_p + Z_s W_{Qp}) + (Z_s Q_p)^* (Y_p Q_p + Y_s W_{Qp}) \\ &= (Y_s Q_p)^* P + (Z_s Q_p)^* u \end{aligned} \quad (4.90)$$

The correlation matrix R is formed by the terms that multiplies the weight function, W , in Equation (4.90), so,

$$R = \frac{1}{2} (Y_s Q_p)^* Z_s Q_p + \frac{1}{2} (Z_s Q_p)^* Y_s Q_p = \Re \{ Z_s Q_p (Y_s Q_p)^* \} \quad (4.91)$$

Finally, the adaptive method that effectively minimizes the active intensity using the P-U approach is found substituting Equations (4.90) and (4.91) into Equation (4.68), resulting in,

$$W(n+1) = W(n) - \frac{\mu}{2} \frac{(Y_s Q_p)^* P + (Z_s Q_p)^* u}{\Re \{ Z_s Q_p (Y_s Q_p)^* \}} \quad (4.92)$$

It's noted that the control method proposed in Equation (4.92) will have convergence problems if the denominator is near zero, or, in other words, it's necessary for the error sensor to "see" some active intensity from the secondary source, which means $\Re \{ Z_s Q_p (Y_s Q_p)^* \}$ should not vanish. This method will be named in a shorthand notation as ASIC-PU.

4.2.5 Adaptive control method based upon controlling the active intensity using the P-P approach

Two ways are possible to develop the adaptive control method; the first is substituting Equations (4.53) and (4.54) in Equation (4.92), the other way is to start with the active intensity

using P-P approach to estimate the particle velocity. As in the optimal solution the first way was adopted, now, the second way will be used.

The active intensity using the P-P approach is given by Fahy (1995),

$$I_a = \frac{1}{2} \Re \{ \mathbf{P}_{12} \mathbf{u}_{12}^* \} = \frac{1}{2\omega\rho\delta} \Im \{ \mathbf{P}_1 \mathbf{P}_2^* \} \quad (4.93)$$

Now, using the acoustic active intensity with the P-P approach as cost function and substituting Equation (4.66),

$$J = I_A = \frac{1}{2\omega\rho\delta} \Im \{ (Z_{p1} Q_p + Z_{s1} W_{Qp})(Z_{p2} Q_p + Z_{s2} W_{Qp})^* \} \quad (4.94)$$

where the pressure at positions 1 and 2 are given by,

$$\begin{aligned} P_1 &= Z_{p1} Q_p + Z_{s1} W_{Qp} \\ P_2 &= Z_{p2} Q_p + Z_{s2} W_{Qp} \end{aligned} \quad (4.95)$$

Expanding Equation (4.94) and taking the gradient in relation to W of each terms using the relations in Appendix A, is easy to find,

$$\nabla \Im \{ (Z_{p2} Q_p)^* Z_{p1} Q_p \} = 0 \quad (4.96)$$

$$\nabla \Im \{ (Z_{p2} Q_p)^* Z_{s1} W_{Qp} \} = i(Z_{s1} Q_p)^* Z_{p2} Q_p \quad (4.97)$$

$$\nabla \Im \{ (Z_{s2} W_{Qp})^* Z_{p1} Q_p \} = -i(Z_{s2} Q_p)^* Z_{p1} Q_p \quad (4.98)$$

$$\nabla \Im \{ (Z_{s2} W_{Qp})^* Z_{s1} W_{Qp} \} = i(Z_{s1} Q_p)^* Z_{s2} W_{Qp} - i(Z_{s2} Q_p)^* Z_{s1} W_{Qp} \quad (4.99)$$

Therefore, the gradient of the acoustic active intensity, Equation (4.94), is given by,

$$\begin{aligned} \nabla J &= \frac{i}{2\omega\rho\delta} \left((Z_{s1} Q_p)^* (Z_{p2} Q_p + Z_{s2} W_{Qp}) - (Z_{s2} Q_p)^* (Z_{p1} Q_p + Z_{s1} W_{Qp}) \right) \\ &= \frac{i}{2\omega\rho\delta} \left[(Z_{s1} Q_p)^* P_2 - (Z_{s2} Q_p)^* P_1 \right] \end{aligned} \quad (4.100)$$

The correlation matrix R is formed by the terms that multiply the weight function, W , in the gradient, Equation (4.100), so,

$$R = \frac{i}{2\omega\rho\delta} [(Z_{s_1}Q_p)^* Z_{s_1}Q_p - (Z_{s_2}Q_p)^* Z_{s_2}Q_p] = \frac{1}{2\omega\rho\delta} \Im\{Z_{s_1}Q_p(Z_{s_2}Q_p)^*\} \quad (4.101)$$

Finally, the method that minimizes the active intensity using the P-P approach is obtained by substituting Equations (4.100) and (4.101) in Equation (4.68),

$$W(n+1) = W(n) - \frac{i\mu}{2} \frac{(Z_{s_1}Q_p)^* P_2 - (Z_{s_2}Q_p)^* P_1}{\Im\{Z_{s_1}Q_p(Z_{s_2}Q_p)^*\}} \quad (4.102)$$

Equation (4.102) will be named in a shorthand notation as ASIC-PP. It is noted that the control method expressed in Equation (4.102) may have convergence problems if the denominator is close to zero. Or, in other words, it's necessary for the error sensor to “see” some active intensity from the secondary source.

4.2.6 Summary of the adaptive control methods

The summary of the adaptive control methods can be seen in Table 4.4.

Table 4.4: Summary of the adaptive control methods

Cost Function	Adaptive control law
E_P	$W(n+1) = W(n) - \mu \frac{(Z_s Q_p)^*}{ Z_s Q_p ^2} P$
E_K	$W(n+1) = W(n) - \mu \frac{(Y_s Q_p)^*}{ Y_s Q_p ^2} u$
E_T	$W(n+1) = W(n) - \mu \frac{(Z_s Q_p)^* P + \rho_0^2 c^2 (Y_s Q_p)^* u}{ Z_s Q_p ^2 + \rho_0^2 c^2 Y_s Q_p ^2}$
Ia – P-U approach	$W(n+1) = W(n) - \frac{\mu}{2} \frac{(Y_s Q_p)^* P + (Z_s Q_p)^* u}{\Re\{Z_s Q_p (Y_s Q_p)^*\}}$
Ia – P-P approach	$W(n+1) = W(n) - \frac{i\mu}{2} \frac{(Z_{s_1} Q_p)^* P_2 - (Z_{s_2} Q_p)^* P_1}{\Im\{Z_{s_1} Q_p (Z_{s_2} Q_p)^*\}}$

4.2.7 Optimal solution

The optimal solutions to the adaptive control laws can be found assuming that at the convergence $W(n+1)$ is equal to $W(n)$, which means that the second term in the right side of equations present in Table 4.4 are equal to zero. In that way, the equations of pressure and particle velocity are substituting in the adaptive control law replacing W by W_{opt} .

For the adaptive control method based upon controlling the acoustic potential energy density, Equation (4.76),

$$\mu \frac{(Z_s Q_p)^*}{|Z_s Q_p|^2} (Z_p Q_p + Z_s W_{\text{opt}} Q_p) = 0 \quad (4.103)$$

As the denominator can not be close to zero and the quantities involved are scalar, the optimal solution for the weights W to the adaptive control method based upon controlling the acoustic potential energy density is given by,

$$W_{\text{opt}} = -\frac{Z_p}{Z_s} \quad (4.104)$$

Doing the same thing with the adaptive control method based upon controlling the acoustic kinetic energy density, Equation (4.80), it is found the optimal solution for the weights W to the adaptive control method based upon controlling the acoustic kinetic energy density,

$$W_{\text{opt}} = -\frac{Y_p}{Y_s} \quad (4.105)$$

Now, for the adaptive control method based upon controlling the acoustic energy density, Equation (4.84),

$$(Z_s Q_p)^* (Z_p Q_p + Z_s W_{\text{opt}} Q_p) + \rho_0^2 c^2 (Y_s Q_p)^* (Y_p Q_p + Y_s W_{\text{opt}} Q_p) = 0 \quad (4.106)$$

Rearranging the terms, the optimal solution for the weights W to the adaptive control method based upon controlling the acoustic energy density is given by,

$$W_{\text{opt}} = -\frac{(Z_s)^* Z_p + \rho_0^2 c^2 (Y_s)^* Y_p}{|Z_s|^2 + \rho_0^2 c^2 |Y_s|^2} \quad (4.107)$$

Now, for the adaptive control method based upon controlling the acoustic active intensity using the P-U approach, Equation (4.92),

$$(Y_s Q_p)^* (Z_p Q_p + Z_s W_{\text{opt}} Q_p) + (Z_s Q_p)^* (Y_p Q_p + Y_s W_{\text{opt}} Q_p) = 0 \quad (4.108)$$

Rearranging the terms, the optimal solution for the weights W to the adaptive control method based upon controlling the acoustic intensity using the P-U approach is given by,

$$W_{\text{opt}} = -\frac{Y_s^* Z_p + Z_s^* Y_p}{Y_s^* Z_s + Z_s^* Y_s} = -\frac{Y_s^* Z_p + Z_s^* Y_p}{2\Re\{Y_s^* Z_s\}} \quad (4.109)$$

Now, for the adaptive control method based upon controlling the acoustic active intensity using the P-P approach, Equation (4.102),

$$(Z_{s_1} Q_p)^* (Z_{p_2} Q_p + Z_{s_2} W_{\text{opt}} Q_p) - (Z_{s_2} Q_p)^* (Z_{p_1} Q_p + Z_{s_1} W_{\text{opt}} Q_p) = 0 \quad (4.110)$$

Rearranging the terms, the optimal solution for the weights W to the adaptive control method based upon controlling the acoustic intensity using the P-P approach is given by,

$$W_{\text{opt}} = -\frac{Z_{s_1}^* Z_{p_2} - Z_{s_2}^* Z_{p_1}}{Z_{s_1}^* Z_{s_2} - Z_{s_2}^* Z_{s_1}} = -\frac{Z_{s_2}^* Z_{p_1} - Z_{s_1}^* Z_{p_2}}{2i\Im\{Z_{s_1} Z_{s_2}^*\}} \quad (4.111)$$

Chapter 5

Active noise control in enclosed space

This chapter describes an application of the active noise control system in vehicles. The control method implemented is the filtered-X LMS in the time domain controlling the pressure at a point using a model of one primary source, one secondary source and one error sensor implemented in a dSPACE 1102 control board.

The development of the algorithm and the implementation in real time were first performed in quiet room, with cut-off frequency around 450 Hz, where two point sources (loudspeakers) and a microphone array were located in order to test the performance of the controller.

Once the controller has been tested, the active noise control system was implemented in the cabin of a pickup model S10, year 2000, from General Motors. The objective was to attenuate the sound from the engine in the cabin interior. This experiment was part of an investigation on the viability of implementing active noise control in vehicles.

5.1 Active noise control in acoustic rooms

The objective of this implementation was to test the performance of the filtered-X LMS in acoustic rooms subject to harmonic sound fields. The investigations allow analyzing the performance of the controller at multiple frequencies, the region of attenuation and the performance of the error sensor.

5.1.1 Experimental set up

The experimental set up shown in Figure 5.1 consists of two acoustic sources (loudspeakers) located 57 cm far from each other located in the acoustic room and one microphone (the error sensor) located between the sources but 175 cm far from the sources. A microphone array composed of 8 microphones separated by 15 cm located parallel to the source axis. Details of the acoustic sources and the microphone array can be seen in Figure 5.2. The devices used in the experiment are shown in Figure 5.3.

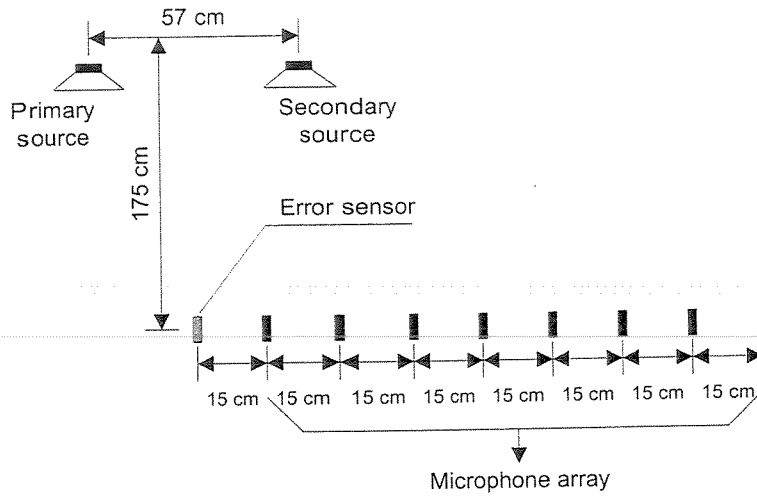


Figure 5.1: Microphone array in the acoustic chamber

The electrical signal send to the primary source (the reference x in the filtered-X LMS) was a sawtooth with fundamental frequency of 270 Hz. Thus, in the room there are the fundamental frequency and the harmonics. The sawtooth was chosen as primary noise because of the amplitude of the harmonics are different.

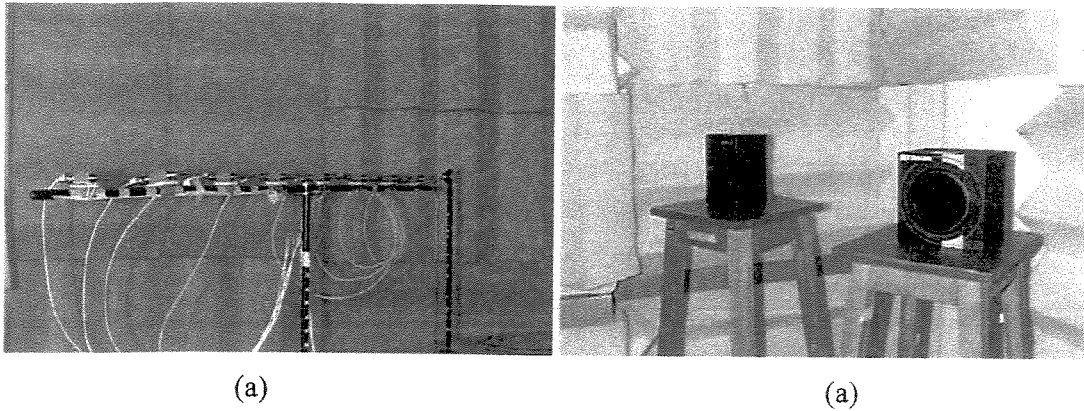


Figure 5.2: Detail of (a) the microphone array and (b) the primary and secondary sources



Figure 5.3: Devices used in the experimental set up – 3 power amplifiers, 2 analog filters, 1 function generator, 1 oscilloscope, 1 signal conditioning unit, 1 DSP control board and 1 spectral analyzer.

5.1.2 Identification of the secondary source

In Figure 5.4 the experimental set up used to identify the secondary path is shown. This set up was chosen in order to filter the high frequencies, above 540 Hz. Thus, inside the acoustic room there are all the harmonic components of 270 Hz with different amplitudes, but only the frequencies under 600 Hz, i.e., 270 and 540 Hz, will be controlled.

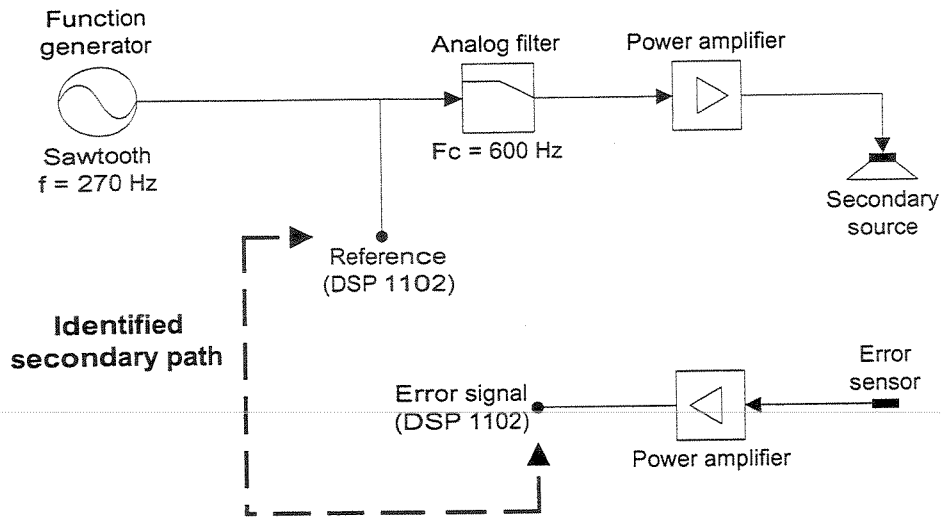


Figure 5.4: Block diagram of the identification of the secondary path

The identification of the secondary path was performed using the filtered-X LMS as an estimator, Appendix C, using 0,4ms as sampling time. The approximation to the secondary source was a FIR with 24 weights. The identified secondary path FIR weights are shown in Figure 5.5.

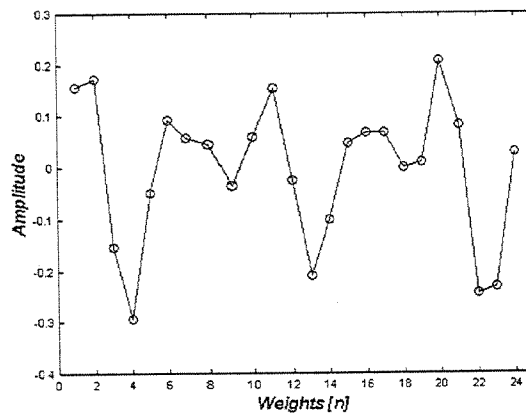


Figure 5.5: Secondary path FIR weights identified in the low reverberant room

It is important to remember that the configuration used in the system identification must be used in the control implementation, which means that the cut-off frequency of the analog filter and the power amplifier gain should not be changed. Most attention should be paid to the cut-off

frequency from the analog filter because it can easily shift the phase of the estimated secondary path if it is changed.

5.1.3 Implementation of the controller in real time

The schematic block diagram used in the control implementation is shown in Figure 5.6. The filtered-X LMS in the time domain was implemented using 0,4ms as sampling time and with 24 weights to model the filter $W(z)$, the step-size was adjusted “on-line” to improve the convergence rate. When the control method converged, the adaptation was stopped and the acquisition of the sound pressure level in the microphone array was performed.

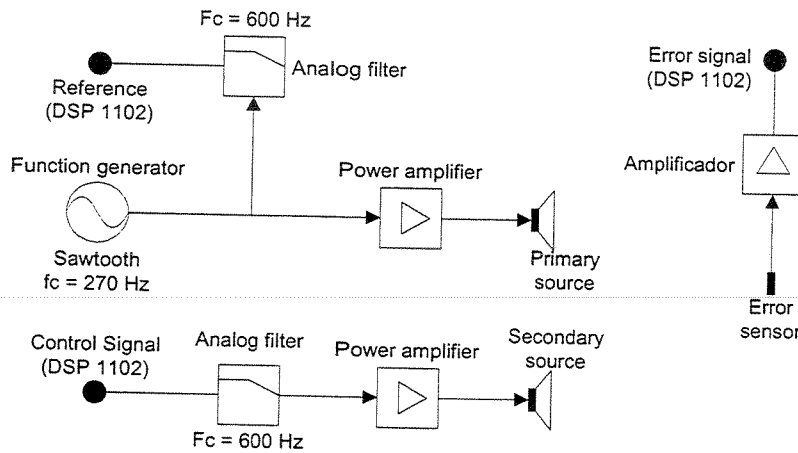
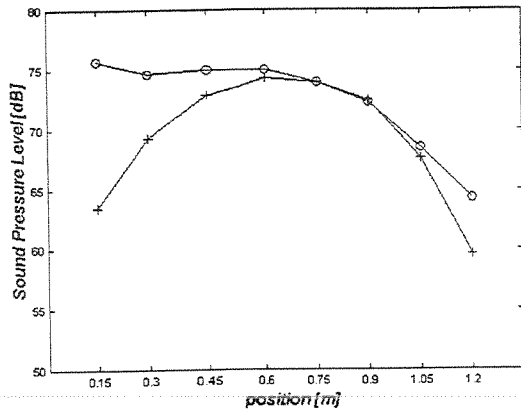
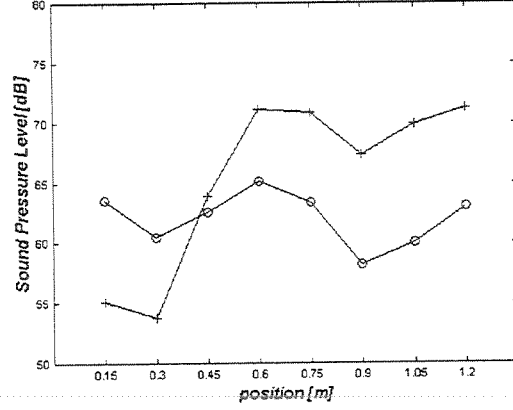


Figure 5.6: Block diagram of the control implementation

In Figure 5.7 the sound pressure level (SPL) measured with the microphone array is shown. It can be observed regions of attenuation and regions of amplification of the pressure. In addition, the attenuation was the highest close to the error sensor. This means that more error sensors should be used to increase the attenuation region. Moreover, the attenuation region is dependent of the frequency, since different attenuation regions were achieved at different frequencies.

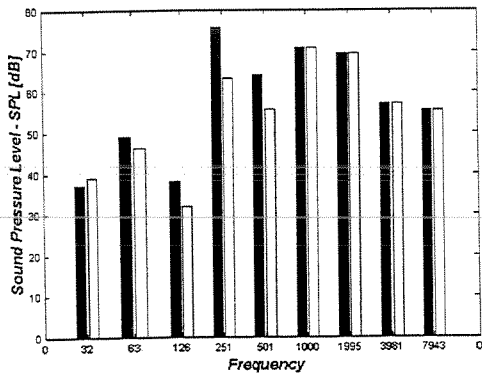


(a)

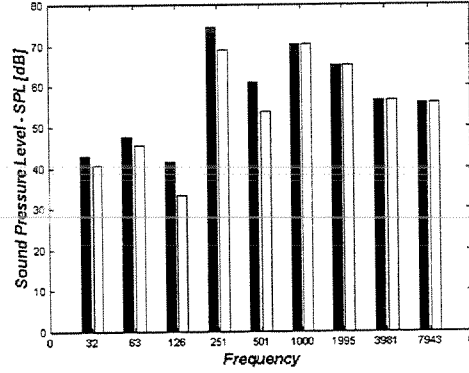


(b)

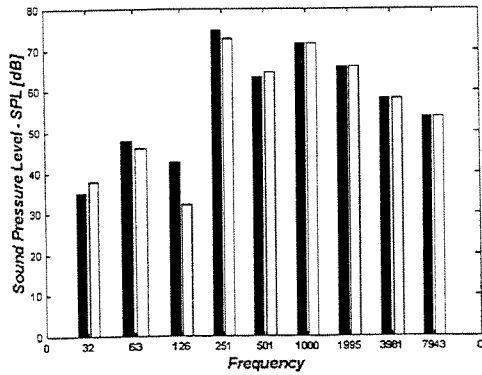
Figure 5.7: Sound pressure level measured with the microphone array at (a) 270 Hz and (b) 540 Hz. -o- no control, +- controlled



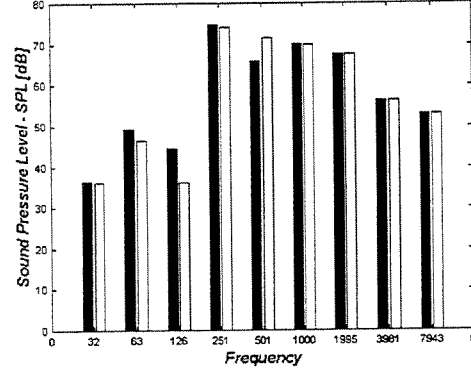
(a)



(b)



(c)



(d)

Figure 5.8: Sound pressure level in the room measured in octaves by the microphone at position (a) 15 cm, (b) 30 cm, (c) 45 cm, and (d) 60 cm from the error sensor. -■- no control, -□- controlled.

In Figure 5.8 the sound pressure level measured in octaves by the microphone array is shown. It is observed that the control method attenuated only the frequency bands that are in the reference signal, frequencies below 600 Hz, without changing the sound pressure level of the frequencies above 600 Hz.

In Figure 5.9 and Figure 5.10 the signals acquired by the error sensor and their spectra are shown. It is observed a strong attenuation in the sound pressure level for the 250 Hz band while less attenuation was achieved for the 500 Hz band. This fact occurred because the controller, which works in the time domain, has the characteristic of attenuating more the frequency with higher amplitude. Moreover, the controller attenuated the 250 Hz component until it was buried in the background noise; thus, the more sensitive a sensor is, the better is the attenuation of the sound pressure level achieved by the controller.

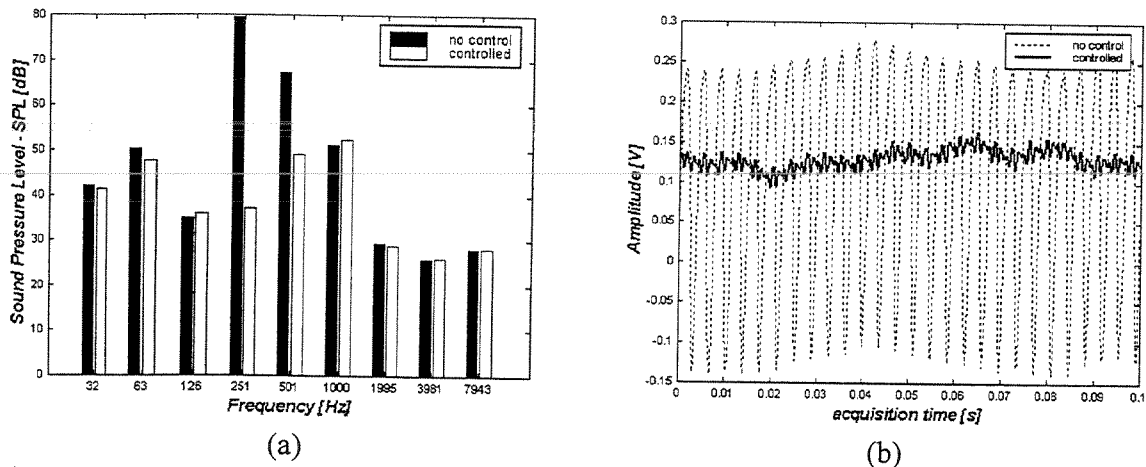


Figure 5.9: Results acquired with the error sensor. (a) SPL in octaves, measured by a spectral analyzer; (b) signal acquired with the dSPACE 1102 control board.

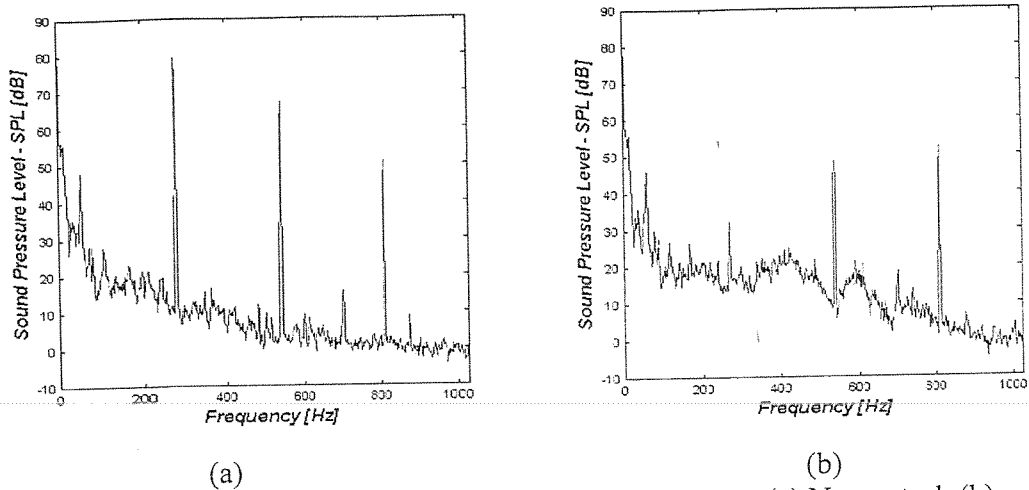


Figure 5.10: Comparison of the auto-spectrum of the error sensor. (a) No control, (b) controlled

5.1.4 Conclusion

The filtered-X LMS in the time domain showed good performance, but the environment where the test was performed is more easily controllable, because the transfer functions involved in the control process are easier predictable and stable, besides, there is no influence from other noise sources. Therefore, a more realistic implementation (inside the cabin of the pickup) should be verified.

It was observed that better attenuation is achieved close to the error sensor. The region of attenuation is dependent of the frequency, and more than one error sensor is necessary to increase the attenuation region.

5.2 Active noise control of the engine in the cabin of a vehicle

The vehicle chosen to implement the active noise control system was a pickup model S10 from General Motors. The objective was to attenuate the noise generated by the engine in the cabin interior. A microphone, the error sensor, was located close to the head of the driver; a secondary source was located in the right low side of the front panel, Figure 5.11. The reference was an accelerometer fixed in the engine block.

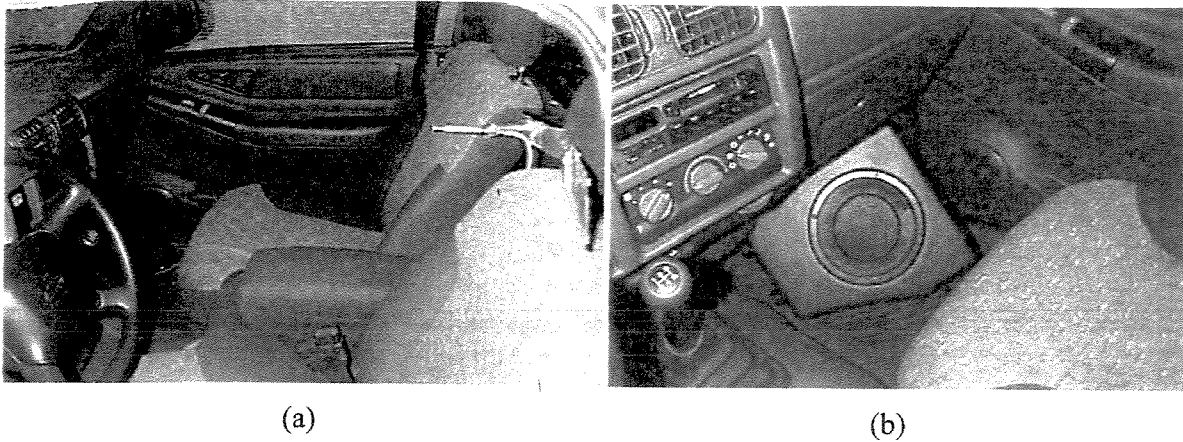


Figure 5.11: Localization of (a) the microphone, (b) the secondary source in the vehicle cabin.

The vehicle was positioned inside an anechoic chamber, and it was accelerated to 3600 rpm in 5th gear, the speed was around 127 Km/h. The fundamental frequency was 60 Hz and, because of the engine characteristics the most important harmonic is the 2nd, which is around 120 Hz.

It was necessary to filter the reference signal, i.e., the signal of the accelerometer fixed in the engine block, because the signal was too noisy. This filtering process was implemented directly in the signal conditioner of the accelerometer. The reconstruction low-pass analog filter used for the secondary source was set to 250 Hz. The secondary source was identified using a FIR approximation with 24 weights, the sampling time was 0,4ms, and the system identification was performed using the filtered-X LMS estimator.

The application of the active noise control using the filtered-X LMS in the time domain as a controller is shown in Figure 5.12, where the signal were acquired using an artificial head and torso from B&K located at the driver s position. This means that the spectra observed in Figure 5.12 represent exactly what a person siting at the driver s position would hear.

In Figure 5.12(a) spectral maps of the sound pressure level generated by the engine are shown. It can be observed that the frequency of 120 Hz produced the highest level at the driver s position. In Figure 5.12(b) the sound pressure level with the system controlled is shown. It can be observed that the frequency of 120 Hz was highly attenuated, and 6 dB of global attenuation was achieved. In Figure 5.12(c) the signal of the controlled system was edited digitally and the

frequency of 180 Hz was artificially removed. With this simple improvement, 12 dB of global attenuation was achieved.

Apparently, the sound at 180 Hz didn't change between the uncontrolled and controlled cases, which means that the 180 Hz was not present in the reference signal. Therefore, it should be investigated where it is better to attach the accelerometer in order to the reference signal contains this frequency or what other signal should be used, e.g. a tacho signal. Another possibility is that the amplitude from 120 Hz is much greater than the 180 Hz in the reference signal, which affects directly the controller.

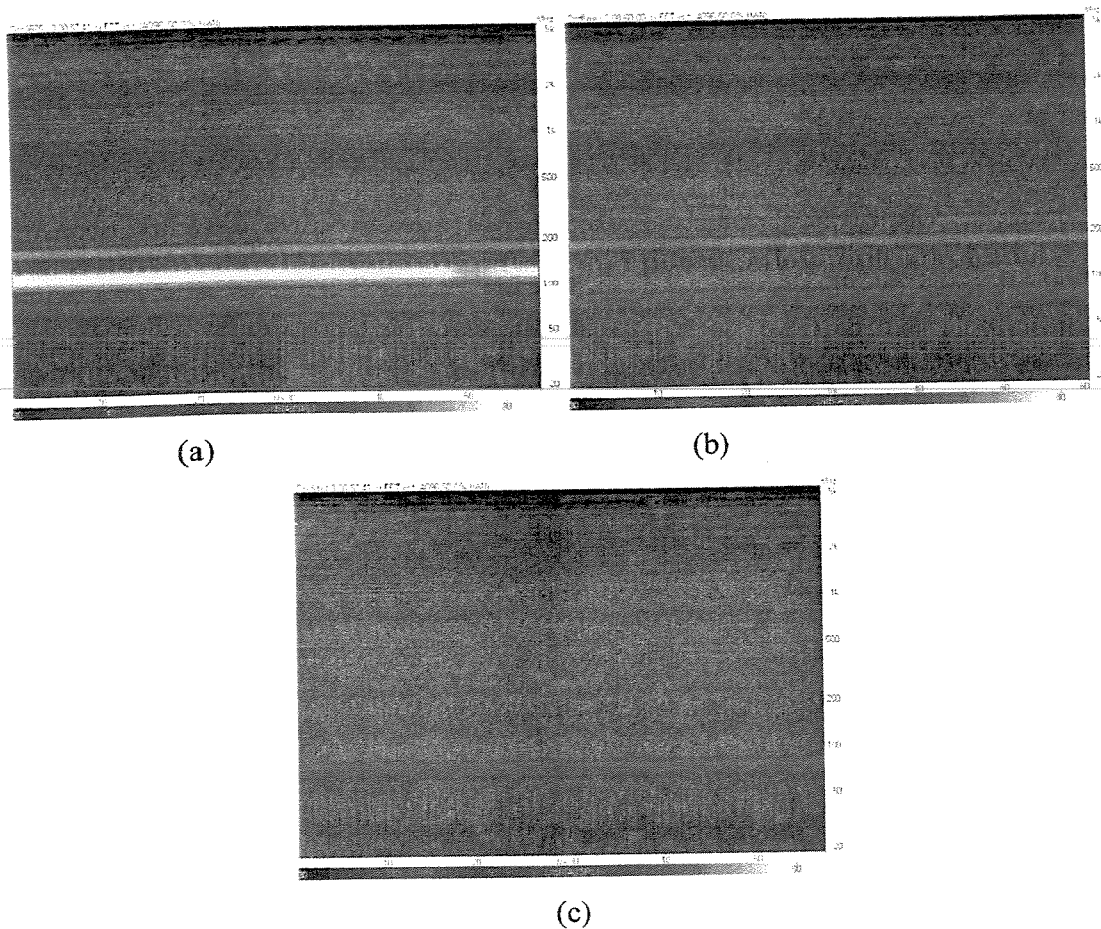


Figure 5.12: Time-frequency spectra of the signals acquired from the driver position obtained with the sliding short time Fourier Transform technique (a) no control, (b) controlled, and (c) controlled and edited.

5.2.1 Conclusion

As a conclusion, the vehicle example showed that ANC can be a useful tool to attenuate the noise from the engine in the cabin. Besides, the active noise control system can be improved to achieve more global attenuation than the original 6 dB. This could be achieved by using more error sensors and introducing the 180 Hz frequency in the reference signal.

The controller showed to be stable in attenuating the sound in the cabin even when the doors were opened or when the driver was changed.

On the other hand, when someone was sitting at the driver's position, he/she noticed that the noise apparently changed but not actually attenuated. This means that investigations using psychoacoustic tools should be made to verify why the attenuation wasn't clearly perceived by the driver.

5.3 General conclusion

The active noise control applications presented in this chapter, the ANC in the acoustic room and in the vehicle cabin, showed that the feedforward controller can be easily implemented, but care should be taken in order to improve the region and the level of attenuation. This can be achieved using more than one error sensor and more sensible error sensors.

Chapter 6

Active Noise Control applied to one-dimensional waveguide

This chapter describes the comprehension of the active noise control phenomena in waveguides where only plane waves propagate. In the first part, the Spectral Element Method (SEM) is developed to model a simple waveguide subject to only plane waves, which is validated by two experimental examples. In the second part, the SEM is applied to model a duct with two sources. In the third part, the duct model with two sources is used to investigate the energy phenomena when the secondary source is driven to its optimal solution. In the last part, the energy behavior described in the second part is verified experimentally using a simple duct where the adaptive control method was employed to drive the secondary source to the optimal solution.

6.1 Spectral Element Method for one-dimensional acoustic waveguides

The spectral element method (SEM) was used by Doyle (1997) to study wave propagation in bars and beams. However, it is widely known that the acoustic equation for plane waves is the same as that of the bar. Therefore, the spectral element method can be applied in acoustic waveguides when the assumption of plane waves is made.

The Spectral Element Method cannot be considered as a new way of modeling one-dimensional waveguides, as it yields the same equations as the conventional wave propagation approach, but it is a new systematic modeling technique that can be easily implemented in digital computers.

In order to develop an element matrix for the spectral element method, two equations are necessary. The first is the Helmholtz equation, Kinsler et al. (1982),

$$\frac{\partial^2 P}{\partial x^2} + K^2 P = 0 \quad (6.1)$$

where P is the complex pressure in the frequency domain, K is the wavenumber, and x is the one-dimensional coordinate of the waveguide where the waves propagate.

The second is the linear Euler equation in the frequency domain, Kinsler et al. (1982),

$$u = -\frac{1}{i\omega\rho_0} \frac{\partial P}{\partial x} \quad (6.2)$$

where u is the particle velocity in the frequency domain, ω is the angular frequency, ρ_0 is the air density, and i is the complex number $\sqrt{-1}$.

6.1.1 Element Matrix

The solution of the Helmholtz equation, Equation (3.3), by wave propagation may be written in the form,

$$P(x) = Ae^{-iKx} + Be^{iKx} \quad (6.3)$$

where the terms Ae^{-iKx} and Be^{iKx} represent the wave propagating in the positive and negative axes direction, respectively.

The pressure at positions $x = 0$ and $x = L$ of an element with length L is given by,

$$\begin{aligned} P_1 &\equiv P(0) = A + B \\ P_2 &\equiv P(L) = Ae^{-iKL} + Be^{iKL} \end{aligned} \quad (6.4)$$

Using Equation (6.4), Equation (6.3) can be rewritten in the following form,

$$P(x) = g_1(x)P_1 + g_2(x)P_2 \quad (6.5)$$

where

$$\begin{aligned} g_1(x) &= \left[e^{iKx} - e^{iK(2L-x)} \right] / \Delta \\ g_2(x) &= \left[e^{iK(L-x)} - e^{iK(L+x)} \right] / \Delta \\ \Delta &= \left[1 - e^{i2KL} \right] \end{aligned} \quad (6.6)$$

In Equation (6.6), the functions $g_1(x)$ and $g_2(x)$ are the interpolation functions of the spectral element. Thus, the pressure in any arbitrary point along the element is given by,

$$P(x) = \frac{1}{1 - e^{i2KL}} \left[\left(e^{iKx} - e^{iK(2L-x)} \right) P_1 + \left(e^{iK(L+x)} - e^{iK(L-x)} \right) P_2 \right] \quad (6.7)$$

Now, using Equation (6.5) in Euler's equation, Equation (6.2),

$$u(x) = -\frac{1}{i\omega\rho_0} \frac{\partial P(x)}{\partial x} = -\frac{1}{i\omega\rho_0} \left[\frac{\partial g_1(x)}{\partial x} P_1 + \frac{\partial g_2(x)}{\partial x} P_2 \right] \quad (6.8)$$

Performing the derivative of Equation (6.6) and using the result in Equation (6.8), the particle velocity at any arbitrary point along the element can be written as,

$$u(x) = -\frac{K}{\omega\rho_0(1 - e^{i2KL})} \left[\left(-e^{iKx} - e^{iK(2L-x)} \right) P_1 + \left(e^{iK(L+x)} + e^{iK(L-x)} \right) P_2 \right] \quad (6.9)$$

Now, making the following relations of the particle velocity,

$$\begin{aligned} u_1 \equiv u(0) &= -\frac{K}{\omega\rho_0(1 - e^{i2KL})} \left[\left(1 + e^{2iKL} \right) P_1 + \left(-2e^{iKL} \right) P_2 \right] \\ u_2 \equiv -u(L) &= -\frac{K}{\omega\rho_0(1 - e^{i2KL})} \left[\left(-2e^{iKL} \right) P_1 + \left(1 + e^{2iKL} \right) P_2 \right] \end{aligned} \quad (6.10)$$

Putting Equation (6.10) in matrix form,

$$\begin{Bmatrix} u_1 \\ u_2 \end{Bmatrix} = -\frac{1}{\rho_0 c(1 - e^{i2KL})} \begin{bmatrix} 1 + e^{2iKL} & -2e^{iKL} \\ -2e^{iKL} & 1 + e^{2iKL} \end{bmatrix} \begin{Bmatrix} P_1 \\ P_2 \end{Bmatrix} \quad (6.11)$$

The element matrix in Equation (6.11) is obtained using the particle velocity and can easily be converted to volume velocity as,

$$\begin{Bmatrix} U_1 \\ U_2 \end{Bmatrix} = -\frac{S}{\rho_0 c(1 - e^{i2KL})} \begin{bmatrix} 1 + e^{2iKL} & -2e^{iKL} \\ -2e^{iKL} & 1 + e^{2iKL} \end{bmatrix} \begin{Bmatrix} P_1 \\ P_2 \end{Bmatrix} \quad (6.12)$$

where S is the cross section area.

6.1.2 Throw-off element

When ducts with infinite or anechoic termination are modeled, the best choice is the throw-off element. This can be performed taking the solution of the Helmholtz equation, Equation (6.3), but now applied for waves propagating only in one direction, without reverberation,

$$P(x) = Ae^{-iKx} \quad (6.13)$$

As was done before,

$$P_1 \equiv P(0) = A \quad (6.14)$$

Using the definition in Equation (6.13) in order to rewrite Equation (6.14) in the following form,

$$P(x) = g_1(x)P_1 \quad (6.15)$$

where

$$g_1(x) = e^{-iKx} \quad (6.16)$$

Now, doing the same thing with Euler's equation,

$$u(x) = -\frac{1}{i\omega\rho_0} \frac{\partial g_1(x)}{\partial x} = \frac{1}{\rho_0 c} e^{-iKx} \quad (6.17)$$

Defining the throw-off element in terms of particle velocity,

$$u_1 = u(0) = \frac{1}{\rho_0 c} P_1 \quad (6.18)$$

or, rewriting Equation (6.18) in terms of volume velocity,

$$U_1 = \frac{S}{\rho_0 c} P_1 \quad (6.19)$$

It is interesting to note that in Equations (6.18) and (6.19) the constant $(1/\rho_0 c)$ is the specific acoustic impedance of the duct for plane waves without reverberation, Kinsler et al. (1982).

6.1.3 Imposing boundary conditions

The greatest advantage of using the spectral element method is that it is straightforward to treat pipe networks by assembling spectral elements and to add specific impedances only by identifying its position in the global matrix, obtained by a direct stiffness approach, Craig (1981).

In the case of a rigid termination boundary condition, the element matrix in Equation (6.11) is applied directly. For an opened-ended termination, the impedance at the end of the duct can be approximated by the radiation acoustic impedance of a circular piston, which must be added to the corresponding diagonal term in the global matrix. For an unflanged open-ended case the mechanical impedance at the end of the circular duct Z_{mL} may be expressed as Kinsler et al. (1982),

$$\frac{Z_{mL}}{\rho_0 c S} = \frac{1}{4} (Ka)^2 + i0.6Ka \quad (6.20)$$

where a is radius of the duct.

6.1.4 Wave component

The Spectral Element Method is a useful tool to estimate the particle velocity in one-dimensional waveguides, since that there is no need for a finite difference approximation to estimate the gradient of the pressure in the two-microphone technique, Fahy (1995). With Equation (6.9) is possible to evaluate the velocity particle between two points of pressure measurements, where L , now, is the distance between the measurement points.

Thus, the particle velocity between the two microphones separated by a distance δ is given substituting in Equation (6.9) the length of the element, L , by the distance δ . The particle velocity is evaluated in the mid-span of the element, at position $x = \delta/2$, resulting in,

$$u_{SEM} = u\left(\frac{\delta}{2}\right) = \frac{1}{\rho_0 c} (P_1 - P_2) \frac{e^{iK\delta/2}}{1 - e^{iK\delta}} = \frac{i}{2\rho_0 c} \frac{(P_2 - P_1)}{\sin(K\delta/2)} \quad (6.21)$$

Equation (6.21) represents the exact solution to the particle velocity when the assumption of plane waves is made in contrast to the particle velocity estimated using the finite differences approach, which is given by,

$$u_{PP} = \frac{i}{K\rho_0 c} \frac{P_2 - P_1}{\delta} \quad (6.22)$$

Thus, the error arising in the particle velocity, when the finite difference approach is used to estimate the particle velocity, is given by,

$$\frac{u_{PP}}{u_{SEM}} = \frac{\frac{i}{K\rho_0 c} \frac{P_2 - P_1}{\delta}}{\frac{i}{2\rho_0 c} \frac{(P_2 - P_1)}{\sin(K\delta/2)}} = \frac{2\sin(K\delta/2)}{K\delta} = \text{sinc}\left(\frac{K\delta}{2}\right) \quad (6.23)$$

As the particle velocity, the pressure in the middle point between the two microphones can be evaluated using the Equation (3.14) and substituting L by δ and x by $\delta/2$,

$$P_{SEM} = P\left(\frac{\delta}{2}\right) = (P_1 + P_2) \frac{e^{iK\delta/2}}{1e^{iK\delta}} = \frac{(P_1 + P_2)}{2\cos(K\delta/2)} \quad (6.24)$$

Now, the active intensity in the middle point between the microphones is evaluate as,

$$I_{ASEM} = \frac{1}{2} \Re\{P_{SEM} u_{SEM}^*\} = \frac{1}{2} \Re\left\{ \frac{(P_1 + P_2)}{2\cos(K\delta/2)} \left(\frac{i}{2\rho_0 c} \frac{(P_2 - P_1)}{\sin(K\delta/2)} \right)^* \right\} \quad (6.25)$$

Resulting in,

$$I_{ASEM} = \frac{\Re\{i(P_1 + P_2)(P_1 - P_2)^*\}}{8\rho_0 c \cos(K\delta)\sin(K\delta)} = \frac{2\Im\{P_1 P_2^*\}}{8\rho_0 c \cos(K\delta)\sin(K\delta)} \quad (6.26)$$

Equation (6.26) is the exact solution to the intensity when the assumption of plane waves is done in contrast to the active intensity using finite difference approach to estimate the particle velocity, which is given by,

$$I_{APP} = \frac{1}{4K\rho_0 c \delta} \Re\{i(P_1 + P_2)(P_1 - P_2)^*\} \quad (6.27)$$

Thus, the error in the active intensity, when the finite difference approximation is used to estimate the particle velocity, and assuming plane wave propagation in one-dimensional waveguide, is given by,

$$\frac{I_{APP}}{I_{ASEM}} = 2 \cos\left(K \frac{\delta}{2}\right) \frac{\sin\left(K \frac{\delta}{2}\right)}{K \delta} = \frac{\sin(K \delta)}{K \delta} = \text{sinc}(K \delta) \quad (6.28)$$

which is the same result shown by Thompson and Tree (1981).

The correction factors in Equations (6.23) and (6.28) are shown in Figure 6.1, where it is observed that the closer the microphones are placed the smaller is the error due to the finite difference approximation.

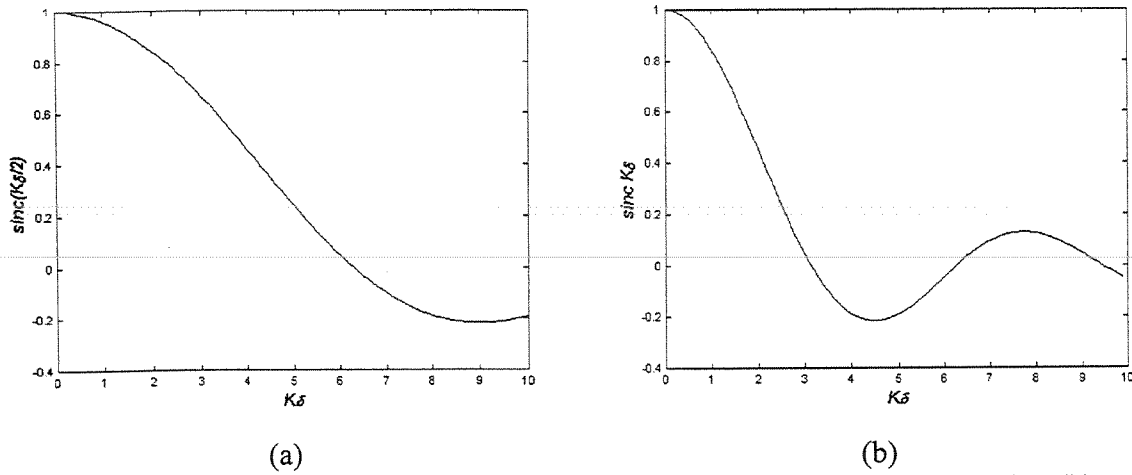


Figure 6.1: Errors due to the finite difference approximation in: (a) particle velocity, (b) active intensity.

6.1.5 T-Duct Example one

The experimental setup to verify the spectral element method applied to acoustic one-dimensional waveguide consists of a T-shaped 6" PVC duct with 3 mm of wall thickness, shown in Figure 6.2, with a loudspeaker in one end and with the other two ends open. The cut-off frequency for this case is around 1.3 kHz, Kinsler et al. (1982). Seven omnidirectional 1/4" microphones were placed along the T-duct, at position 2, 3, 4, 5, 6, 8, and 9. The volume velocity of the primary source was measured using a laser Doppler vibrometer, which measured the velocity of the loudspeaker cone.

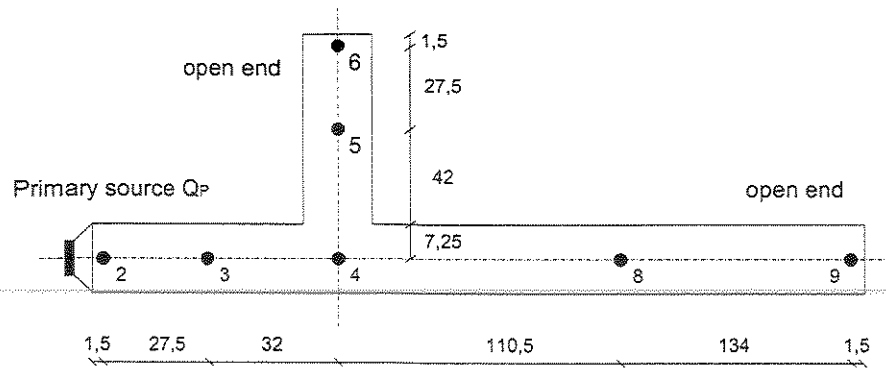


Figure 6.2: Experimental setup for the T-duct. Units in centimeters.

The theoretical model via SEM for the T-Duct is shown in Figure 6.3, and the global matrix in Equation (6.30). It was used in the SEM model the wavenumber K as,

$$\tilde{K} = \alpha K - i\beta \quad (6.29)$$

where \tilde{K} is the complex wavenumber used in the SEM model, and $\alpha = 0.96$ and $\beta = 0.04$. The coefficient α is used to adjust the sound speed c to improve the correlation between prediction and measurement, and the coefficient β is the damp factor. It should be noted that only three spectral elements are necessary in this case and the pressure and particle velocity at the other locations can be predicted using the interpolation function of the spectral element. However, more than three elements were used for simplicity. When using SEM, increasing the number of elements does not improve the accuracy of the results because the solution using SEM is exact (within the framework of the basic theory used).

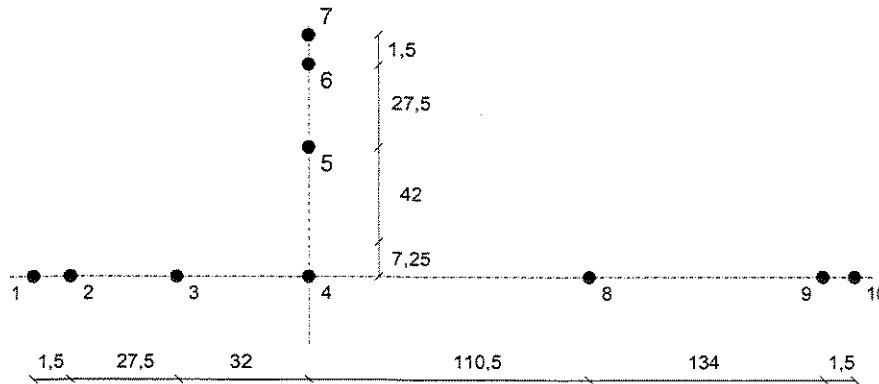


Figure 6.3: SEM model of the T-duct. Units in centimeters.

Applying the SEM methodology described in Figure 6.3, the global matrix is found as,

$$\begin{Bmatrix} u_1 \\ u_2 \\ u_3 \\ u_4 \\ u_5 \\ u_6 \\ u_7 \\ u_8 \\ u_9 \\ u_{10} \end{Bmatrix} = \begin{bmatrix} x & x & & & & & & & & \\ & x & x & x & & & & & & \\ & & x & x & x & & & & & \\ & & & x & x & x & & x & & \\ & & & & x & x & x & & & \\ & & & & & x & x & x & & \\ & & & & & & x & \otimes & & \\ & & & x & & & & & x & x \\ & & & & & & & x & x & x \\ & & & & & & & & x & \otimes \end{bmatrix} \begin{Bmatrix} P_1 \\ P_2 \\ P_3 \\ P_4 \\ P_5 \\ P_6 \\ P_7 \\ P_8 \\ P_9 \\ P_{10} \end{Bmatrix} \quad (6.30)$$

where x are the non-zero elements and \otimes indicate the positions of the radiation impedances. Equation (6.30) can be written in a shorthand notation as,

$$\{u\} = [M]\{P\} \quad (6.31)$$

where $[M]$ is the mobility matrix.

The system in Equation (6.30) is solved for u_1 equal to 1 and the other particle velocity terms equal to zero. The comparison between the measured impedances and the theoretical impedances predicted by the acoustic spectral element method is shown in Figure 6.4.

It can be observed in Figure 6.4 that the loss factor β varies with frequency because at low frequencies more damping must be added in the SEM model to match the experimental impedances. At higher frequencies, the theoretical model does not exactly match the experimental results. This fact can be associated with several factors, such as: the radiation impedance, Equation (6.20), which is not exact, the flexibility and damping of the duct walls, and the non-ideal sound source (loudspeaker shape, flexibility and misadjustment).

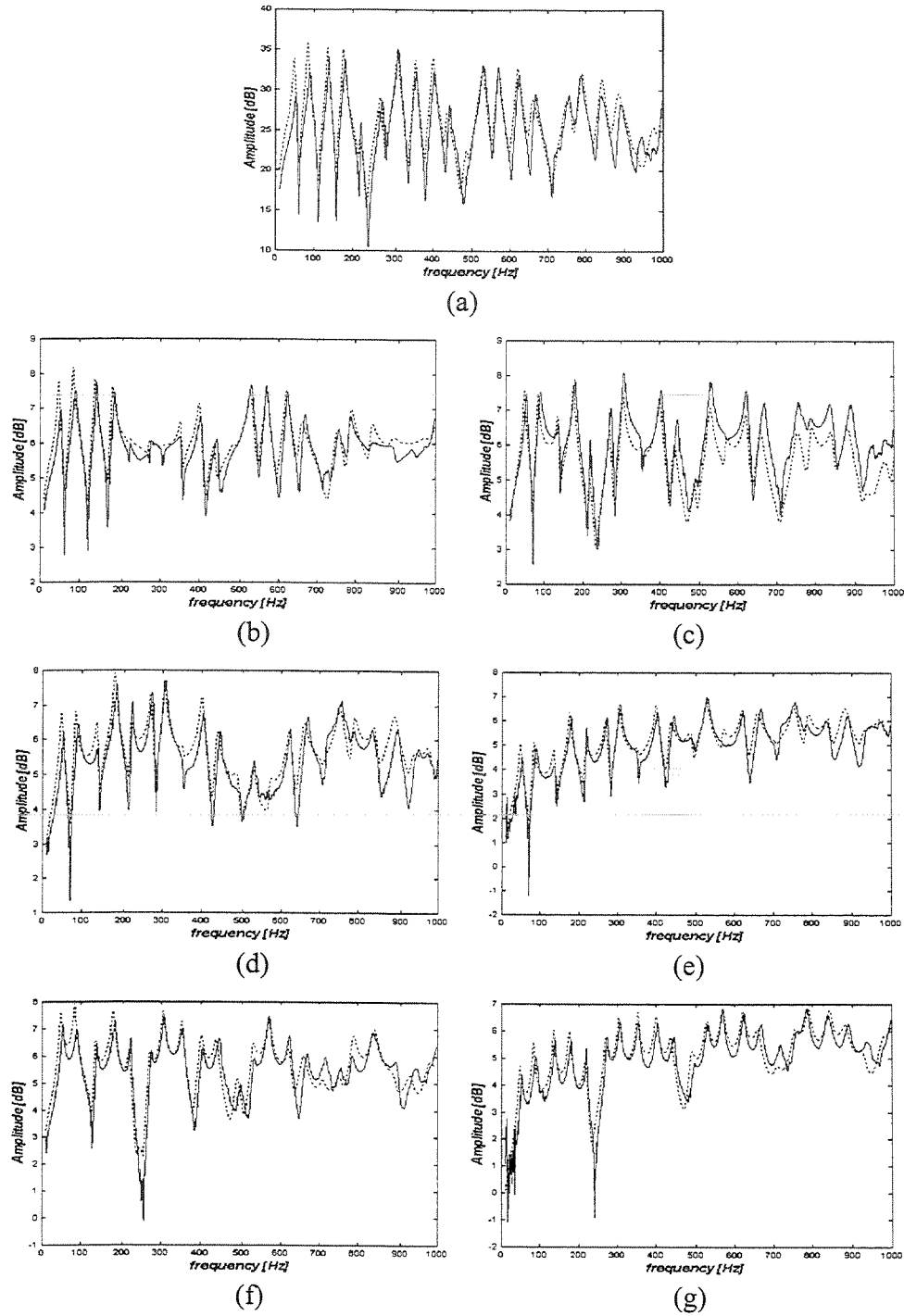


Figure 6.4: Comparison between the theoretical and experimental impedances in the T duct at: (a) position 2, (b) position 3, (c) position 4, (d) position 5, (e) position 6, (f) position 8, (g) position 9. “-” Experimental, “....” theoretical. Units in Pa/V.

6.1.6 Testing a particle velocity sensor

Particle velocity sensors probe can be used to measure the particle velocity field of the sound field instantly in one single measurement. The sensitivity for particle velocity is in the orthogonal direction of the probe main axe. It can also be used for a direct measurement of the sound intensity field, when combined with a pressure microphone.

The measurement principle of the particle velocity sensor is based on the temperature difference between two resistive sensors. A travelling acoustic wave causes movements of the air. The heat is transferred from the first sensor to the second sensor through convection. This causes a difference in temperature of the two sensors that will cause a differential electrical resistance variation that can be measured, Bree et al. (1996) and Eerden et al. (1998).

The particle velocity sensor was tested in a impedance tube, Figure 6.5, which consists of a straight 6" PVC duct with 7 mm of wall thickness and a loudspeaker in one end and the other end open. The particle velocity sensor was placed at 90° from the microphone's line and at the same position along the duct as the microphone #2. The volume velocity of the loudspeaker was measured with a laser Doppler vibrometer This experimental set up enables to compare the experimental transfer impedances (pressure relative to the source volume velocity) with the transfer impedances given by the SEM, to compare the particle velocity at different locations relative to the source volume velocity estimated using the P-P approach with the particle velocity given by the particle velocity sensor and with the theoretical particle velocity given by the SEM.

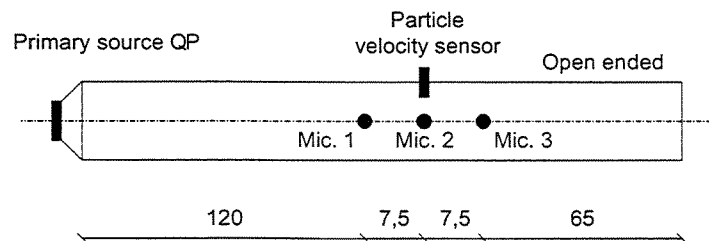


Figure 6.5: Experimental setup to the straight duct. Units in centimeters.

In order to match the SEM model with the experimental model was necessary to introduce a loss factor in the wavenumber as defined in Equation (6.29) with $\alpha = 1$ and $\beta = 0.05$.

In Figure 6.6 the comparison between the impedances measured experimentally and the impedances evaluated using the spectral element method are shown. It can be observed a good agreement between theoretical and experimental impedances. However, at low frequencies (below 100 Hz) the amplitudes at peaks do not match exactly because the loss factor is different for each frequency range and, at high frequencies (above 800 Hz), the divergences are related to the approximate model for the radiation impedance and to the flexibility of the duct wall.

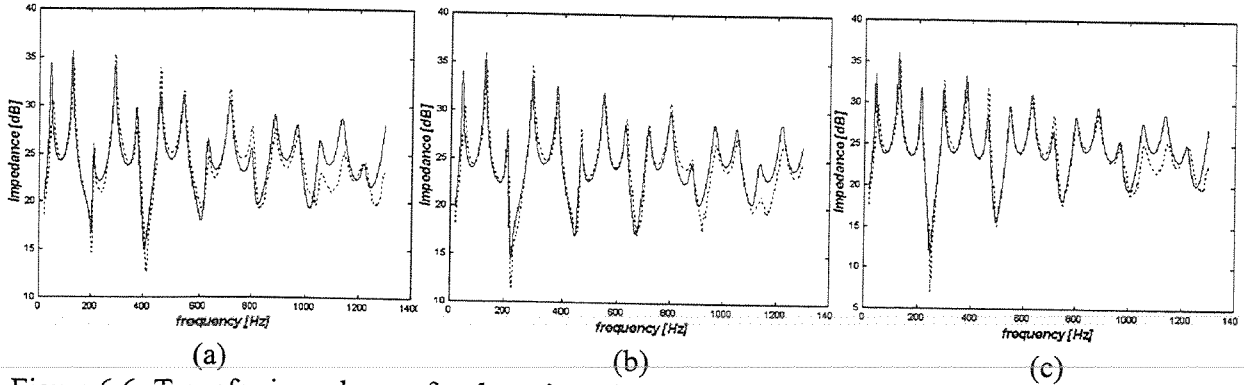


Figure 6.6: Transfer impedances for the microphones located at (a) position 1, (b) position 2, and (c) position 3. “-” Experimental, “....” theoretical. Units in dB ref. 1 Pa/(m/s).

In Figure 6.7 the particle velocity and the active intensity for a unity source volume velocity are shown. The sensitivity of the particle velocity sensor was given by comparing the measured particle velocity with the particle velocity estimated by the P-P approach and by the SEM model. Therefore, the sensitivity of the particle velocity sensor was estimated as,

$$\begin{cases} 100 \frac{\text{V}}{\text{m/s}} & f < 800 \text{ Hz} \\ \frac{1}{3 \times 10^{-6} i \omega} \frac{\text{V}}{\text{m/s}} & 800 \leq f \text{ Hz} \end{cases} \quad (6.32)$$

In Figure 6.7(a) the particle velocity shows that the results obtained with the particle velocity sensor and the P-P approach agree, while the SEM shows some divergence at higher frequencies, which happens due to the theoretical radiation impedance used in the SEM and the duct flexibility. In Figure 6.7(b) the transfer active intensity is shown. It can be noticed a large divergence between the methods used to estimate the active intensity. This happened because of

the phase mismatch between the sensors used in the experiment showing that it is important to correct the phase mismatch.

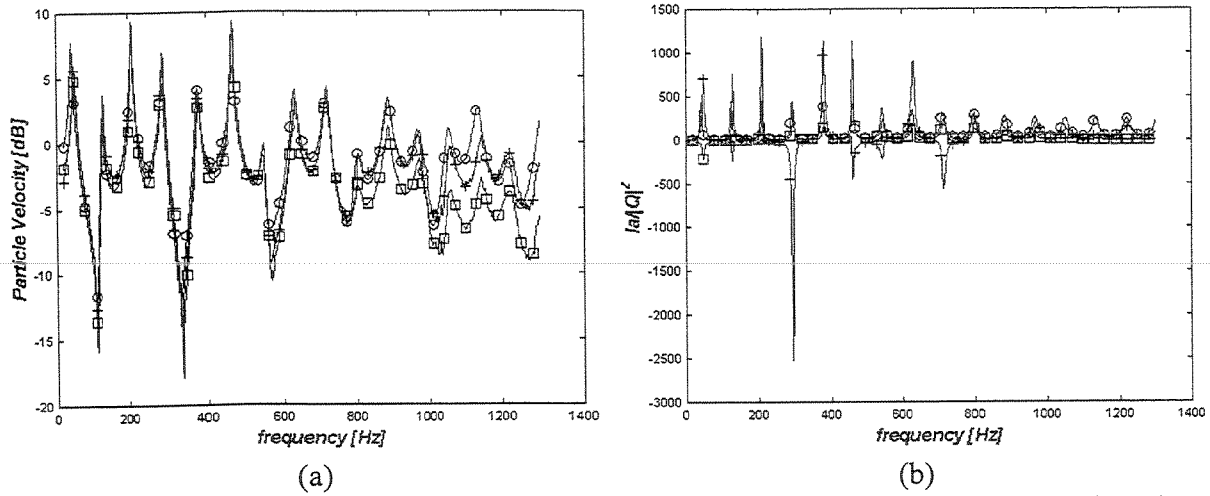


Figure 6.7: Comparison between the SEM, the particle velocity sensor, and the two microphones technique to measure the (a) transfer particle velocity, (b) active intensity. -o- SEM approach, +- particle velocity sensor, \square - P-P approach.

The errors arising in the finite difference approach for this experiment can be seen in Figure 6.8, where it can be observed that the particle velocity estimation is less affected than the active intensity estimation. The particle velocity corrected by the factor in Figure 6.8(a) is shown in Figure 6.9, where it can be noticed that the particle velocity sensor does not agree well with the P-P approach.

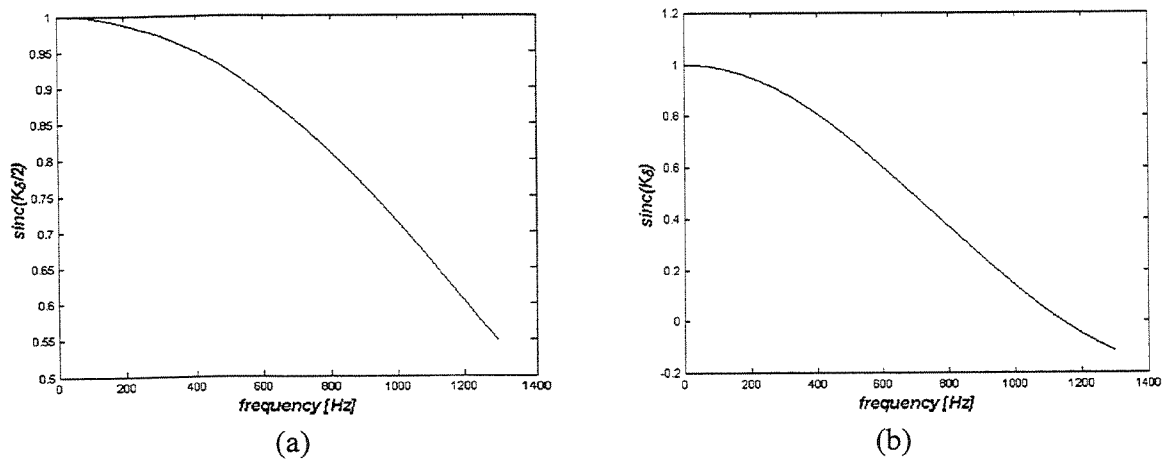


Figure 6.8: Errors arising from the finite difference approximation in the straight duct in (a) particle velocity, (b) active intensity.

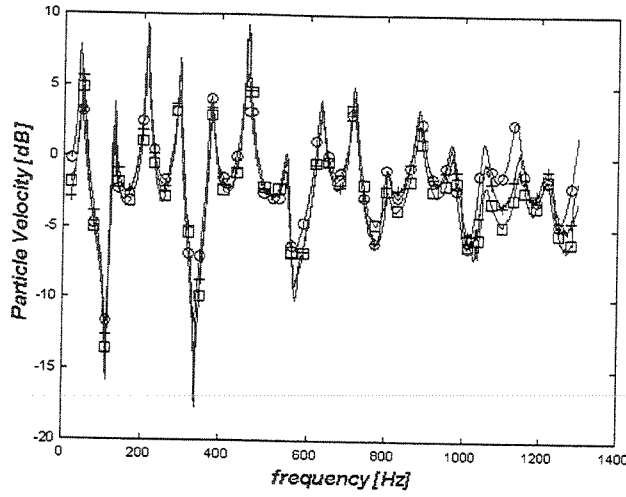


Figure 6.9: Comparison between the particle velocity predicted by the SEM model, and by particle velocity sensor and by the two-microphone technique corrected with the SEM interpolation function. -o- SEM approach, +- particle velocity sensor, -√ - P-P approach corrected.

6.2 Theoretical model of a duct with two acoustic sources

In this sub-section the case where two sources are acting in the acoustic field will be investigated. The primary source, the source that originally emits the noise, is represented by the subscript p , and the secondary source, the source added to the acoustic field to attenuate the noise generated by the primary source, is represented by the subscript s . The total pressure, P_T , can be written as, Hansen and Snyder (1997),

$$P_T(x, x_p, x_s) = Z_p(x, x_p)Q_p + Z_s(x, x_s)Q_s \quad (6.33)$$

where x_p is the primary source position, and x_s is the secondary source position. The pressure field generated by the primary source is $P_p(x, x_p) = Z_p(x, x_p)Q_p$, and the pressure field generated by the secondary source is $P_s(x, x_s) = Z_s(x, x_s)Q_s$.

In the same way as the pressure field, the total particle velocity field u_T generated by the two sources in the field can be written as,

$$u_T(x, x_p, x_s) = Y_P(x, x_p)Q_P + Y_S(x, x_s)Q_S \quad (6.34)$$

where the velocity field generated by the primary source is $u_p(x, x_p) = Y_P(x, x_p)Q_P$, and the velocity field generated by the secondary source is $u_s(x, x_s) = Y_S(x, x_s)Q_S$.

In order to simplify the notation, the positions x , x_s and x_p will be omitted unless where necessary for the understanding of the equations. Besides, it is important to remember that the total particle velocity, Equation (6.34), has a direction. So, it is a vectorial quantity and the direction must be observed mainly when the intensity is being evaluated, which will be done later.

The ideal duct is shown in Figure 6.10, The primary source was located at position $x_p = 0$, the secondary source at position x_s , and the error sensor at position x_E . The duct has a diameter d and its length is L ; it is assumed that $0 < x_s < x_E < L$.

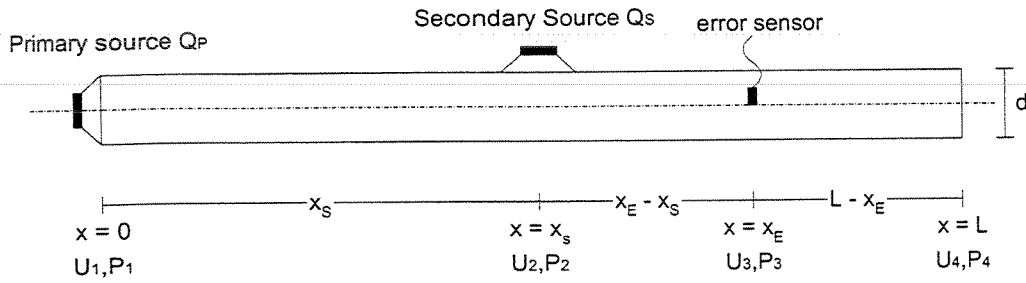


Figure 6.10. Diagram of the ideal duct

Applying the spectral element method, the global matrix can be found as,

$$[G] = \frac{-S}{\rho c} \begin{pmatrix} \frac{1+e^{2iKx_s}}{1-e^{2iKx_s}} & \frac{-2e^{iKx_s}}{1-e^{2iKx_s}} & 0 & 0 \\ -2e^{iKx_s} & \frac{1+e^{2iKx_s}}{1-e^{2iKx_s}} + \frac{1+e^{2iK(x_E-x_s)}}{1-e^{2iK(x_E-x_s)}} & \frac{-2e^{2iK(x_E-x_s)}}{1-e^{2iK(x_E-x_s)}} & 0 \\ 0 & \frac{-2e^{2iK(x_E-x_s)}}{1-e^{2iK(x_E-x_s)}} & \frac{1+e^{2iK(x_E-x_s)}}{1-e^{2iK(x_E-x_s)}} + \frac{1+e^{2iK(L-x_E)}}{1-e^{2iK(L-x_E)}} & \frac{-2e^{2iK(L-x_E)}}{1-e^{2iK(L-x_E)}} \\ 0 & 0 & \frac{-2e^{2iK(L-x_E)}}{1-e^{2iK(L-x_E)}} & \frac{-\rho c}{SZ_R} + \frac{1+e^{2iK(L-x_E)}}{1-e^{2iK(L-x_E)}} \end{pmatrix} \quad (6.35)$$

and rewriting in a shorthand notation the above matrix,

$$\begin{Bmatrix} U_1 \\ U_2 \\ U_3 \\ U_4 \end{Bmatrix} = [\mathbf{G}] \begin{Bmatrix} P_1 \\ P_2 \\ P_3 \\ P_4 \end{Bmatrix} \Rightarrow \{U\} = [G]\{P\} \quad (6.36)$$

It is important to note that the ideal duct is modeled using volume velocity and not particle velocity as was done in the previous sections.

6.2.1 Primary source transfer functions

Now, the primary source pressure transfer functions can be found by making U_1 equal to 1 and the other volume velocity terms equal to 0,

$$\begin{Bmatrix} Z_p(x_p) \\ Z_p(x_s) \\ Z_p(x_e) \\ Z_p(L) \end{Bmatrix} = [\mathbf{G}]^{-1} \begin{Bmatrix} 1 \\ 0 \\ 0 \\ 0 \end{Bmatrix} \quad (6.37)$$

Solving Equation (6.37), it is easy to find,

$$Z_p(x_p) = \frac{\rho_0 c}{S} \frac{(1 + e^{2iKL})Z_{mL} + \rho_0 cS(-1 + e^{i2KL})}{(-1 + e^{i2KL})Z_{mL} + \rho_0 cS(1 + e^{i2KL})} \quad (6.38)$$

$$Z_p(x_s) = \frac{\rho_0 c}{S} e^{iKx_s} \frac{(1 + e^{2iK(L-x_s)})Z_{mL} + \rho_0 cS(-1 + e^{2iK(L-x_s)})}{(-1 + e^{i2KL})Z_{mL} + \rho_0 cS(1 + e^{i2KL})} \quad (6.39)$$

$$Z_p(x_e) = \frac{\rho_0 c}{S} e^{iKx_e} \frac{(1 + e^{2iK(L-x_e)})Z_{mL} + \rho_0 cS(-1 + e^{2iK(L-x_e)})}{(-1 + e^{i2KL})Z_{mL} + \rho_0 cS(1 + e^{i2KL})} \quad (6.40)$$

$$Z_p(L) = \frac{\rho_0 c}{S} \frac{2e^{iKL}Z_{mL}}{(-1 + e^{i2KL})Z_{mL} + \rho_0 cS(1 + e^{i2KL})} \quad (6.41)$$

The primary source velocity transfer functions can be found using the element matrix defined in Equation (6.11), the following results can be easily found,

$$Y_p(x_p) = 1 \quad (6.42)$$

$$Y_p(x_s) = e^{iKx_s} \frac{(-1 + e^{2iK(L-x_s)})Z_{mL} + \rho_0 cS(1 + e^{2iK(L-x_s)})}{(-1 + e^{i2KL})Z_{mL} + \rho_0 cS(1 + e^{i2KL})} \quad (6.43)$$

$$Y_p(x_E) = e^{iKx_E} \frac{(-1 + e^{-2iK(L-x_E)})Z_{mL} + \rho_0 cS(1 + e^{2iK(L-x_E)})}{(-1 + e^{i2KL})Z_{mL} + \rho_0 cS(1 + e^{i2KL})} \quad (6.44)$$

$$Y_p(L) = \frac{2\rho_0 cS e^{iKL}}{(-1 + e^{i2KL})Z_{mL} + \rho_0 cS(1 + e^{i2KL})} \quad (6.45)$$

The pressure field from the primary source can be evaluated using,

$$\begin{aligned} P_p(x) &= g_1(x)Z_p(x_p)Q_p + g_2(x)Z_p(L)Q_p \\ &= \frac{\rho_0 c}{S} Q_p e^{-iKx} \frac{(e^{2iKL} + e^{2iKx})Z_{mL} + \rho_0 cS(e^{2iKL} - e^{2iKx})}{(-1 + e^{i2KL})Z_{mL} + \rho_0 cS(1 + e^{i2KL})} \end{aligned} \quad (6.46)$$

The particle velocity field from the primary source can be evaluated as,

$$u_p(x) = -\frac{1}{i\omega\rho_0} \frac{\partial}{\partial x} P_p(x) = Q_p \frac{e^{-iKx}}{S} \frac{(e^{2iKL} - e^{2iKx})Z_{mL} + \rho_0 cS(e^{2iKL} + e^{2iKx})}{(-1 + e^{i2KL})Z_{mL} + \rho_0 cS(1 + e^{i2KL})} \quad (6.47)$$

The acoustic impedance for the primary source can be evaluated as,

$$Z_p(x) = \frac{P_p(x)}{u_p(x)S} = \frac{\rho_0 c}{S} \frac{(e^{2iKL} + e^{2iKx})Z_{mL} + \rho_0 cS(e^{2iKL} - e^{2iKx})}{(e^{2iKL} - e^{2iKx})Z_{mL} + \rho_0 cS(e^{2iKL} + e^{2iKx})} \quad (6.48)$$

6.2.2 Secondary source transfer functions

Applying the same procedure for the secondary source, making U_2 equal to 1 and the other terms equal to 0,

$$\begin{Bmatrix} Z_s(x_p) \\ Z_s(x_s) \\ Z_s(x_E) \\ Z_s(L) \end{Bmatrix} = [G]^{-1} \begin{Bmatrix} 0 \\ 1 \\ 0 \\ 0 \end{Bmatrix} \quad (6.49)$$

Solving Equation (6.49), it is easy to find,

$$Z_S(x_p) = \frac{\rho_0 c}{S} e^{iKx_s} \frac{(1 + e^{2iK(L-x_s)})Z_{mL} + \rho_0 cS(-1 + e^{2iK(L-x_s)})}{(-1 + e^{i2KL})Z_{mL} + \rho_0 cS(1 + e^{i2KL})} \quad (6.50)$$

$$Z_S(x_s) = \frac{\rho_0 c}{2S} (1 + e^{2iKx_s}) \frac{(1 + e^{2iK(L-x_s)})Z_{mL} + \rho_0 cS(-1 + e^{2iK(L-x_s)})}{(-1 + e^{i2KL})Z_{mL} + \rho_0 cS(1 + e^{i2KL})} \quad (6.51)$$

$$Z_S(x_E) = \frac{\rho_0 c}{2S} e^{iK(x_E-x_s)} (1 + e^{2iKx_s}) \frac{(1 + e^{2iK(L-x_s)})Z_{mL} + \rho_0 cS(-1 + e^{2iK(L-x_s)})}{(-1 + e^{i2KL})Z_{mL} + \rho_0 cS(1 + e^{i2KL})} \quad (6.52)$$

$$Z_S(L) = \frac{\rho_0 c}{S} \frac{e^{iK(L-x_s)}(1 + e^{2iKx_s})Z_{mL}}{(-1 + e^{i2KL})Z_{mL} + \rho_0 cS(1 + e^{i2KL})} \quad (6.53)$$

The primary source velocity transfer functions can be found using the elementary matrix defined in Equation (6.11) but dividing both sides by Q_s , and the following results can be found easily,

$$Y_S(x_p) = 0 \quad (6.54)$$

$$Y_S(x_s) = \frac{1}{2} (1 + e^{2iKx_s}) \frac{(-1 + e^{2iK(L-x_s)})Z_{mL} + \rho_0 cS(1 + e^{2iK(L-x_s)})}{(-1 + e^{i2KL})Z_{mL} + \rho_0 cS(1 + e^{i2KL})} \quad (6.55)$$

$$Y_S(x_E) = \frac{1}{2} e^{iK(x_E-x_s)} (1 + e^{2iKx_s}) \frac{(-1 + e^{2iK(L-x_s)})Z_{mL} + \rho_0 cS(1 + e^{2iK(L-x_s)})}{(-1 + e^{i2KL})Z_{mL} + \rho_0 cS(1 + e^{i2KL})} \quad (6.56)$$

$$Y_S(L) = \frac{\rho_0 cS e^{iK(L-x_s)}(-1 + e^{2iKx_s})Z_{mL}}{(-1 + e^{i2KL})Z_{mL} + \rho_0 cS(1 + e^{i2KL})} \quad (6.57)$$

The pressure field from the secondary source must be divided in two parts, the first one upstream from secondary source, and the other downstream from secondary source. The pressure field upstream ($0 \leq x \leq x_s$) is given by,

$$\begin{aligned} P_u(x) &= g_1(x)Z_S(x_p)Q_s + g_2(x)Z_S(x_s)Q_s \\ &= \frac{\rho_0 c}{2S} Q_s e^{iK(x_s-x)} (1 + e^{2iKx}) \frac{(1 + e^{2iK(L-x_s)})Z_{mL} + \rho_0 cS(-1 + e^{2iK(L-x_s)})}{(-1 + e^{i2KL})Z_{mL} + \rho_0 cS(1 + e^{i2KL})} \end{aligned} \quad (6.58)$$

and the pressure field downstream ($x_s \leq x \leq L$) is given by,

$$\begin{aligned}
P_d(x) &= g_1(x)Z_s(x_s)Q_s + g_2(x)Z_s(L)Q_s \\
&= \frac{\rho_0 c}{2S} Q_s e^{-iK(x+2x_s)} (1 + e^{2iKx_s}) \frac{(e^{2iKL} + e^{2iK(x+x_s)})Z_{mL} + \rho_0 cS(e^{2iKL} - e^{2iK(x+x_s)})}{(-1 + e^{i2KL})Z_{mL} + \rho_0 cS(1 + e^{i2KL})} \quad (6.59)
\end{aligned}$$

The particle velocity from the secondary source, as well as the pressure, must be divided in two parts, one upstream and the other downstream from secondary source. Therefore, the particle velocity upstream ($0 \leq x \leq x_s$) is given by,

$$u_u(x) = \frac{Q_s}{2S} e^{iK(x_s-x)} (1 - e^{2iKx}) \frac{(1 + e^{2iK(L-x_s)})Z_{mL} + \rho_0 cS(-1 + e^{2iK(L-x_s)})}{(-1 + e^{i2KL})Z_{mL} + \rho_0 cS(1 + e^{i2KL})} \quad (6.60)$$

and the particle velocity field downstream ($x_s \leq x \leq L$) is given by,

$$u_d(x) = \frac{Q_s}{2S} e^{-iK(x+2x_s)} (1 + e^{2iKx_s}) \frac{(e^{2iKL} - e^{2iK(x+x_s)})Z_{mL} + \rho_0 cS(e^{2iKL} + e^{2iK(x+x_s)})}{(-1 + e^{i2KL})Z_{mL} + \rho_0 cS(1 + e^{i2KL})} \quad (6.61)$$

6.3 Analytical results using the optimal solution to the secondary source

In this section it is analyzed what happens with the energy when the secondary source is driven to its optimal value controlling the potential energy density, the active intensity, and the radiated acoustic power. The results include the changes in the impedances, the resulting total energy density (potential + kinetic), the active and reactive intensity, and the radiated and stored acoustic power.

It is assumed that the secondary source is placed at position $x_s = 1.5$ m, the error sensor at position $x_E = 2.25$ m, and length of the duct is $L = 3$ m.

The primary source was chosen to be $Q_p = 1 \times 10^{-5}(1+i)$ [m³/(m/s)] in the frequencies of 50 Hz to 550 Hz with frequency resolution of 5 Hz.

6.3.1 Optimal Control Volume Velocity Q_s

The optimal volume velocity controlling the potential energy density can be obtained by substituting Equations (6.40) and (6.52) in the optimal solution for the control of the acoustic potential energy density,

$$Q_s = -Q_p \frac{Z_p(x_E)}{Z_s(x_E)} = -Q_p \frac{2e^{iKx_s}}{1 + e^{2iKx_s}} = -Q_p \frac{1}{\cos(Kx_s)} \quad (6.62)$$

Doing the same procedure for the optimal volume velocity controlling the active intensity, yields,

$$Q_s = -Q_p \frac{Z_s^*(x_E)Y_p(x_E) + Y_s^*(x_E)Z_p(x_E)}{Z_s^*(x_E)Y_s(x_E) + Y_s^*(x_E)Z_s(x_E)} = -Q_p \frac{1}{\cos(Kx_s)} \quad (6.63)$$

Now, controlling the radiated acoustic power by the sources,

$$Q_s = -Q_p \frac{\Re\{Z_s(x_p)\}}{\Re\{Z_s(x_s)\}} = -Q_p \frac{1}{\cos(Kx_s)} \quad (6.64)$$

The optimal secondary volume velocity is the same for the three control methods. The identical result of Equations (6.62) to (6.64) is shown in Figure 6.11 where two features can be observed. Firstly, the optimal volume velocity is independent of the duct termination and the position of the error sensor. Secondly, the secondary source cannot control the frequencies where,

$$Kx_s = (2n - 1)\frac{\pi}{2} \quad ; \quad n = 1, 2, \dots \quad (6.65)$$

or simply,

$$x_s = (2n - 1)\frac{\lambda}{4} \quad ; \quad n = 1, 2, \dots \quad (6.66)$$

which are the positions where the primary and secondary sources are spaced of odd multiples of a quarter wavelength, which correspond to the peaks in Figure 6.11.

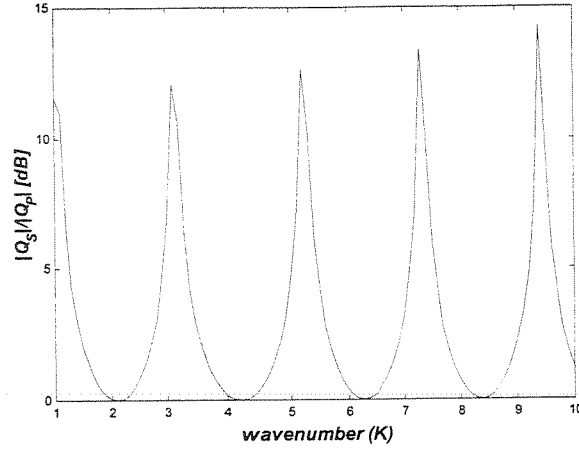


Figure 6.11. The optimal volume velocity “same result produced by the three control strategies”.

The physical meaning of the frequencies where $Kx_s = (2n-1)\pi/2$ is that at these frequencies the pressure is equal to zero and the particle velocity is maximum at the secondary source. Thus, the secondary source cannot increase the particle velocity where the velocity is already at a maximum.

Another interesting observation about Figure 6.11 and Equations (6.62) to (6.64) is that,

$$|Q_s| \geq |Q_p| \quad (6.67)$$

as pointed out by Chen and Liu (2000).

Therefore, it will always be necessary to use the same or more volume velocity of the secondary source in order to control the primary source.

6.3.2 Pressure and velocity fields with optimal secondary source

When the volume velocity from the secondary source is driven to its optimal value, Equation (6.62), the pressure field generated by the secondary source can be evaluated substituting Equation (6.62) in Equations (6.58) and (6.59). Thus, the pressure field upstream from secondary source is given by,

$$P_u(x) = -\frac{\rho_0 c}{S} Q_P e^{-iK(x-2x_s)} \frac{(1 + e^{2iKx})(1 + e^{2iK(L-2x_s)})Z_{mL} + \rho_0 cS(-1 + e^{2iK(L-2x_s)})}{(1 + e^{2iKx_s})(-1 + e^{i2KL})Z_{mL} + \rho_0 cS(1 + e^{i2KL})} \quad (6.68)$$

and the pressure field downstream from secondary source is given by,

$$P_d(x) = -\frac{\rho_0 c}{S} Q_P e^{-iK(x+x_s)} \frac{(e^{2iKL} + e^{2iK(x+x_s)})Z_{mL} + \rho_0 cS(e^{2iKL} - e^{2iK(x+x_s)})}{(-1 + e^{i2KL})Z_{mL} + \rho_0 cS(1 + e^{i2KL})} \quad (6.69)$$

The particle velocity field generated by the secondary source can be evaluated by substituting Equation (6.62) in Equations (6.60) and (6.61). Thus, the particle velocity field upstream from secondary source is given by,

$$u_u(x) = \frac{Q_P}{S} e^{iK(x-2x_s)} \frac{(e^{2iKx} - 1)(1 + e^{2iK(L-x_s)})Z_{mL} + \rho_0 cS(-1 + e^{2iK(L-x_s)})}{(1 + e^{2iKx_s})(-1 + e^{i2KL})Z_{mL} + \rho_0 cS(1 + e^{i2KL})} \quad (6.70)$$

and the particle velocity field downstream from secondary source is given by,

$$u_d(x) = -\frac{Q_P}{S} e^{-iK(x-x_s)} \frac{(e^{2iKL} - e^{2iK(x+x_s)})Z_{mL} + \rho_0 cS(e^{2iKL} + e^{2iK(x+x_s)})}{(-1 + e^{i2KL})Z_{mL} + \rho_0 cS(1 + e^{i2KL})} \quad (6.71)$$

It is necessary to remember that L in Equations (6.68), (6.69), (6.70), and (6.71) is the length of the duct; however, the coordinate position x in Equations (6.69) and (6.71) needs to be changed to $x' = x - x_s$ in order to match the coordinate position used in Equations (6.46) and (6.47).

Therefore, the total pressure field in the duct can be evaluated using the following expressions,

$$P_T(x) = \frac{\rho_0 c}{S} Q_P \frac{e^{-iK(x-2x_s)} - e^{iKx}}{1 + e^{2iKx_s}} \quad ; \quad 0 \leq x < x_s \quad (6.72)$$

$$P_T(x) = 0 \quad ; \quad x_s \leq x \leq L \quad (6.73)$$

The particle velocity at the same positions as above can be evaluated using,

$$u_T(x) = \frac{Q_P}{S} \frac{e^{-iK(x-2x_s)} + e^{iKx}}{1 + e^{2iKx_s}} \quad ; \quad 0 \leq x < x_s \quad (6.74)$$

$$u_T(x) = 0 \quad ; \quad x_s \leq x \leq L \quad (6.75)$$

Thus, the mechanism of the acoustic suppression consists of the superposition of the sound fields generated by the primary and secondary sources. Downstream from secondary source there is neither pressure nor particle velocity. This is because the pressure and the particle velocity generated by the primary source is in opposite phase with respect to the pressure and particle velocity generated by the secondary source, while upstream from secondary source there will be the presence of standing waves. The phenomena can be observed in details in Figure 6.12 and Figure 6.13, where the resultant pressure and particle velocity fields are shown.

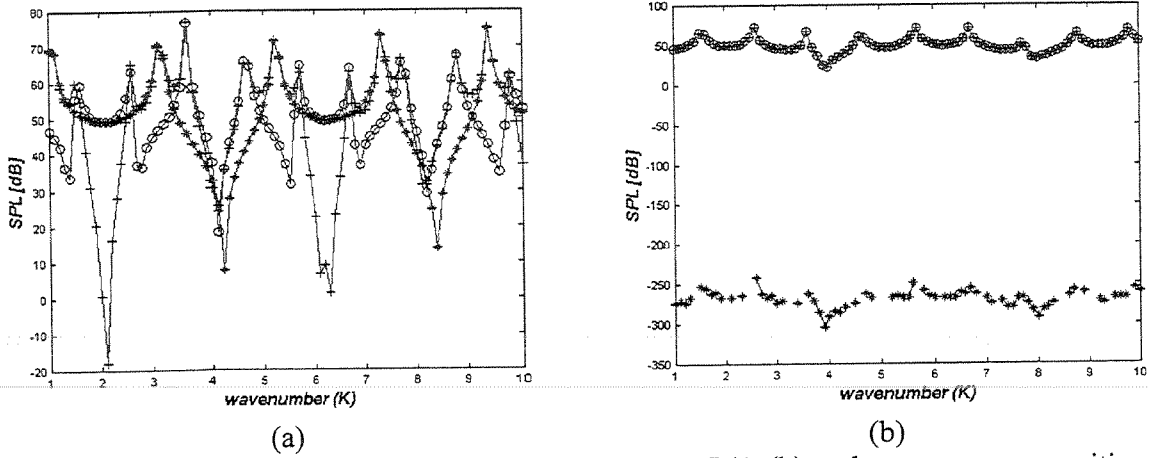


Figure 6.12. Pressure field in the duct: (a) at position $x = L/4$; (b) at the error sensor position. -o- P_P ; +- P_S , -* - P_T . $P_{ref} = 20 \mu\text{Pa}$.

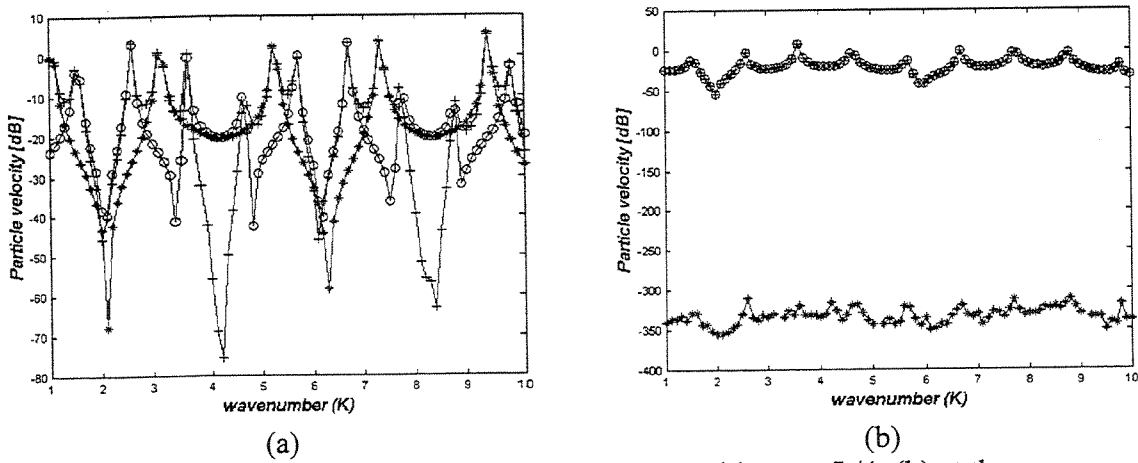


Figure 6.13. Particle velocity field in the duct: (a) at position $x = L/4$; (b) at the error sensor position. -o- u_P ; +- u_S , and -* - u_T . $u_{ref} = P_{ref} / \rho_0 c$.

6.3.3 Acoustical impedance with optimal secondary source

The acoustical impedance upstream from secondary source can be obtained taking the quotient between Equations (6.72) and (6.74),

$$Z_{\text{control}}(x) = \frac{P_T(x)}{U_T(x)} = \frac{\rho_0 c}{S} \frac{e^{2iKx_s} - e^{2iKx}}{e^{2iKx_s} + e^{2iKx}} ; \quad 0 \leq x \leq x_s \quad (6.76)$$

Now, going back to Equation (6.48), and making $Z_{mL} \rightarrow 0$ and $x_s = L$, i.e., considering a duct with length x_s ,

$$\lim_{Z_{mL} \rightarrow 0} Z_p(x) = \frac{\rho_0 c}{S} \frac{e^{2iKx_s} - e^{2iKx}}{e^{2iKx_s} + e^{2iKx}} \quad (6.77)$$

Therefore, when the control is acting, the duct behaves as if it were cut at the location of the control source. Furthermore, the radiation acoustic impedance is zero, instead of Z_R ,

$$\lim_{x \rightarrow x_s} \frac{P(x)}{u(x)S} = 0 \quad \text{and} \quad \lim_{x \rightarrow x_E} \frac{P(x)}{u(x)S} = 0 \quad (6.78)$$

It is interesting to note that the zero impedance corresponds to a duct with an ideal open-ended termination. Another interesting result is that the resultant impedance is independent of the termination; so, no matter if the duct is rigidly terminated, open-ended or infinite (anechoic), the resultant acoustic impedance will be the same since the control law was that of Equations (6.62) to (6.64). The changes in the impedance can be observed in Figure 6.14.

The acoustic impedance downstream from secondary source can't be evaluated, because there is neither pressure nor volume velocity downstream from secondary source when the control is acting in the duct.

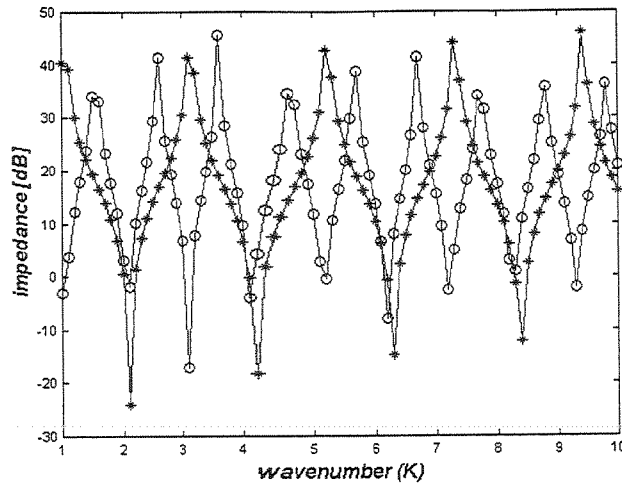


Figure 6.14. Theoretical impedance at the primary source position. -o- Z_P ; -* Z_T , +- impedance of a duct with $L/2$ and $Z_R \rightarrow 0$. $Z_{Ref} = 1 \text{ Pa/(m/s)}$.

6.3.4 Total energy in the duct with optimal secondary source

The total energy density at 0.05m upstream and 0.05m downstream from secondary source can be observed in Figure 6.15. As shown before, there is neither pressure nor velocity downstream from secondary source; therefore, there is no energy density either. However, upstream from secondary source there is a resultant pressure and velocity; so, there is a resultant energy density, as suggested by Snyder and Hansen (1989).

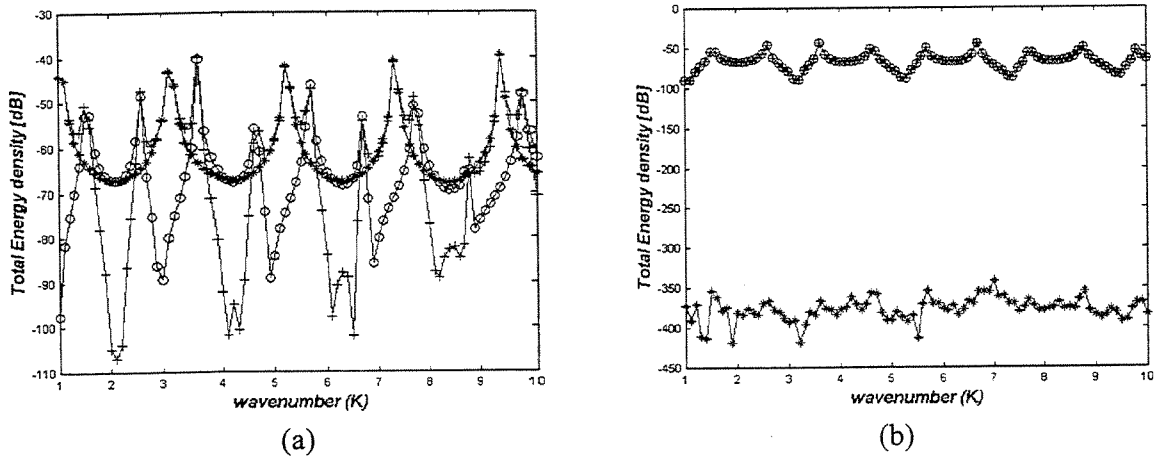


Figure 6.15. Total energy density before and after the control action: (a) upstream (b) downstream. -o- primary source acting alone; +- secondary source acting alone with optimal volume velocity Q_S , -* sources acting (control on). $E_{Ref} = 1 \text{ J}$.

6.3.5 The Intensity with optimal secondary source

The active intensity upstream and downstream from secondary source can be observed in Figure 6.16. It can be noticed that the primary source alone produces active intensity, but after the secondary source is driven to its optimal value, the primary source does not produce any active intensity. Thus, it is expected that neither the primary nor the secondary source will radiate acoustic power when the control is on. Moreover, the secondary source alone does not produce active intensity upstream, but only downstream, because in the upstream branch the secondary source sees the duct as closed-ended, and, in the downstream branch it sees the duct as opened-ended.

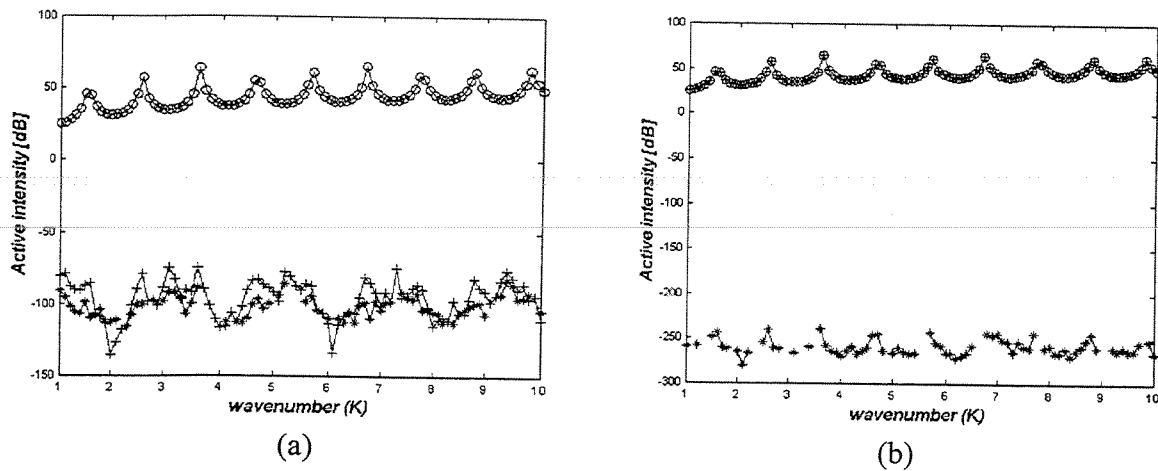


Figure 6.16. Active intensity before and after the control action. The measurement point was at 0,05 m before and 0,05 m past the secondary source: (a) upstream (b) downstream. -o- primary source acting alone; +- secondary source acting alone with optimal volume velocity Q_s , and *- is the sources acting (control on). $I_{ref} = 10^{-12} \text{ W/m}^2$.

The reactive intensity measured at 0.05 m upstream and downstream from secondary source is shown in Figure 6.17. The results show that downstream there is no reactive intensity, but upstream there is. This happens because upstream there is acoustic energy after the control is turned on, whereas downstream there is none, because the resultant pressure and the particle velocity are both equal to zero.

In short, when the control is off, part of the intensity is active and part is reactive, whereas when the control is on, the intensity changes to purely reactive.

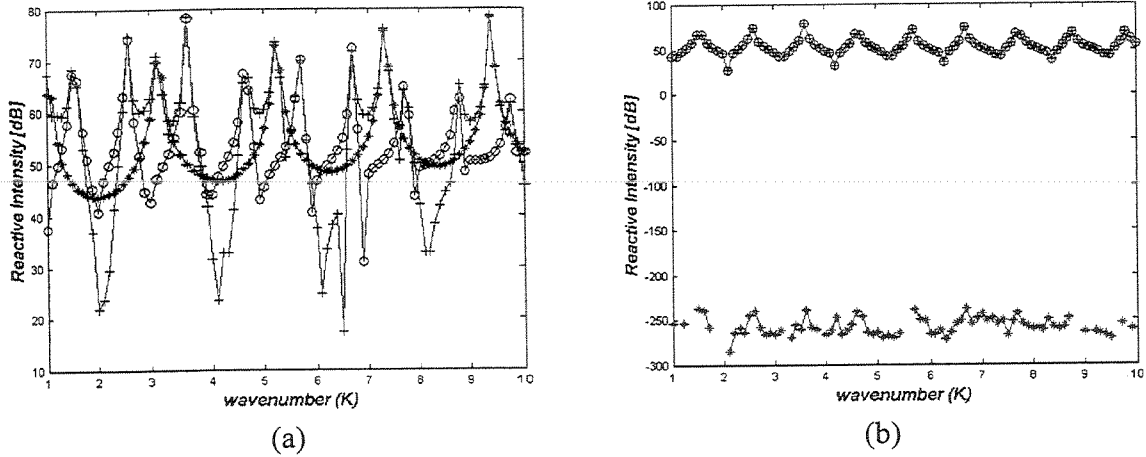
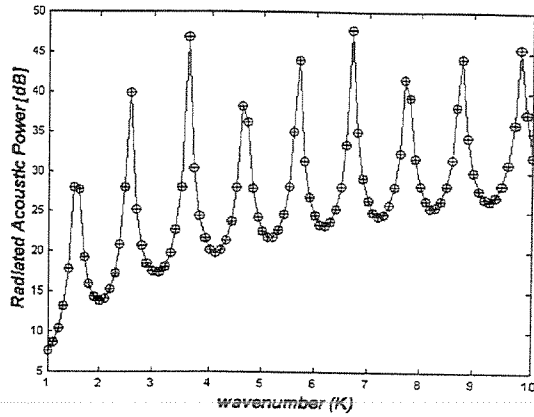


Figure 6.17. Reactive intensity before and after the control action: (a) upstream (b) downstream. - o- primary source acting alone; +- secondary source acting alone with optimal volume velocity Q_s , and -* sources acting (control on). $I_{ref} = 10^{-12} \text{ W/m}^2$.

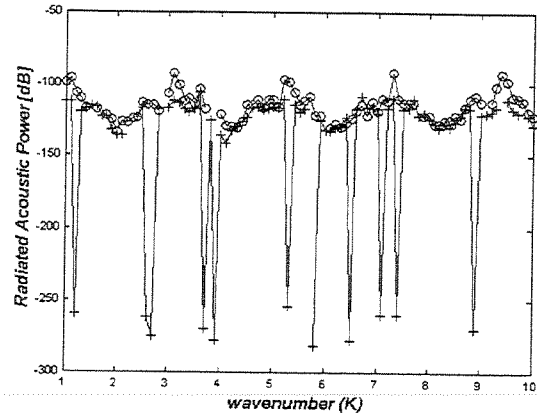
6.3.6 The radiated acoustic power from the sources with optimal secondary source

Figure 6.18 shows the acoustic power radiated by the sources. It can be observed that when the control is acting, neither the primary source nor the secondary source radiate acoustic power, as suggested by Snyder and Hansen (1989). This fact can be easily explained. It was shown that a controlled duct behaves as if it were a passive duct with only one source terminated in zero impedance at the secondary source position. So, there is no power flow in this case, that is, neither the primary nor the secondary source can inject acoustic power in the system.

It can be observed that the sources acting one at a time in the field produce the same radiated acoustic power (Figure 6.18) and this fact also can be easily explained. As the duct is an idealized case, by the principle of energy conservation, the sources can only inject the power that can be absorbed by the radiation impedance.



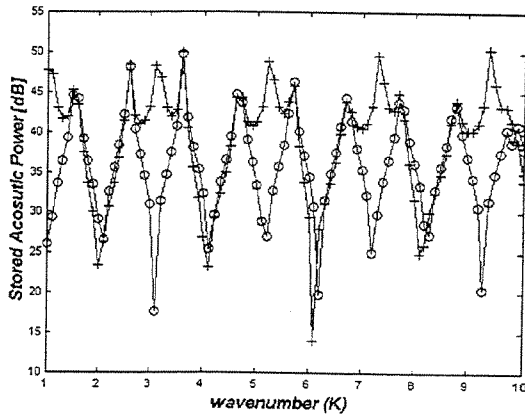
(a)



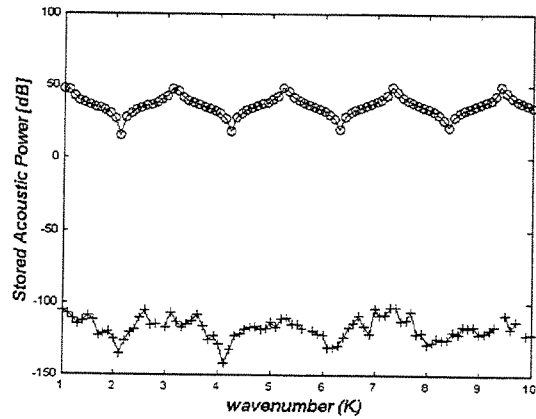
(b)

Figure 6.18. Acoustic power radiated by the primary and secondary sources: (a) sources acting one at a time, (b) sources acting simultaneously. -o- primary source; +- secondary source with optimal volume velocity Q_s . $W_{\text{ref}} = 10^{-12}$ W.

The acoustic power stored by the sources is shown in Figure 6.19. It can be noticed that there is stored acoustic power with the sources acting alone in the field, but when they are working together there is stored acoustic power only at the primary source. Furthermore, all energy changes from radiated and stored to stored only when the control is acting.



(a)



(b)

Figure 6.19. Acoustic power stored (reactive) by the primary and secondary sources: (a) sources acting one at a time, (b) sources acting simultaneously. -o- primary source; +- secondary source with optimal volume velocity Q_s . $W_{\text{ref}} = 10^{-12}$ W.

In short, the introduction of a secondary source impedes the primary source from radiating acoustic power to the field.

A better understanding about what happens with the acoustic field can be observed in Table 6.1 where three cases are reported. If the volume velocity of the primary source “ Q_p ” is an imaginary quantity, the total pressure “ P_T ” between the sources will be a real quantity, the total particle velocity “ U_T ” will be an imaginary quantity, and the volume velocity from the secondary source “ Q_s ” will be an imaginary quantity. The other two cases can be interpreted analogously.

It can be noticed that the phase between the pressure and volume velocity at the sources is always 90° , so that there is no radiated acoustic power.

Table 6.1: Phase relations (\Re real, \Im imaginary)

Q_p	Q_s	$P_T(x)$	$U_T(x)$
\Re	\Re	\Im	\Re
\Im	\Im	\Re	\Im
$\Re = \Im$	$\Re = \Im$	$\Re = -\Im$	$\Re = \Im$

6.3.7 Conclusions

The energetic analysis of actively controlled acoustic systems is an important tool for global optimization of the controller in a more global control design.

Three kinds of control methods were applied to a simple ideal duct system with a primary source at one end and a secondary source placed upstream. It was observed that the three methods investigated produced the same optimal control volume velocity. Therefore, in ideal one-dimensional waveguides, there is no difference between controlling the potential energy density, the active intensity or the total radiated acoustic power.

It was shown that the optimal control volume velocity is independent of the error sensor position, as well as the type of termination of the duct. However, it is dependent of the distance between the primary and secondary sources.

When the secondary source is driven to the optimal control volume velocity, both sources do not radiate acoustic power, and the resulting duct is equivalent to a shorter duct, ended at the section where the secondary source is located with the radiation impedance equal zero.

It was also shown that numerical and symbolic modeling an ideal duct with the Spectral Element Method is suitable for numerical and analytical (symbolic processing) investigations.

6.4 Applying the adaptive control methods in a T-duct experimentally

The experimental set up to validate the above results is shown in Figure 6.20. It consists of a 6" diameter circular section PVC duct with 3 mm of wall thickness and with 2 loudspeakers. At all locations represented by subscripts 1-9, omnidirectional 1/4" microphones were placed, except for position 6, where a velocity sensor and a microphone were placed.

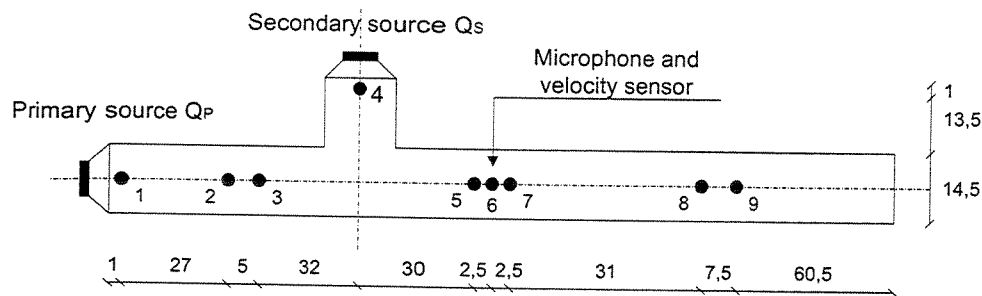


Figure 6.20: Position of sensors and actuators in the duct. Lengths are in centimeters

The duct configuration presented in Figure 6.20 enables the measurement of the radiated acoustic power from the sources using microphones located at positions 1 and 4, the measurement of the active intensity upstream and downstream from secondary source with the P-P approach using the microphones at positions 2 and 3 and at positions 8 and 9. The control of the potential energy density at position 5, the control of the kinetic energy density at position 6, the

control of the active intensity using the P-U approach at position 6 and the use of the P-P approach using the microphones at positions 5 and 7. A detail of the experimental setup is shown in Figure 6.21, where the velocity sensor (sensor at position 6) can be seen, placed between the microphones #5 and #7.

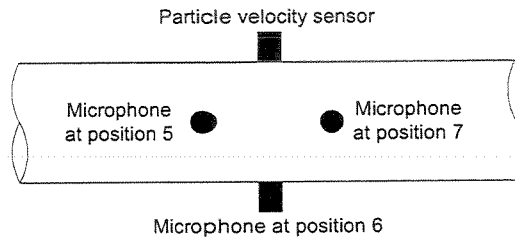


Figure 6.21: Experimental setup detail with the error sensors 5, 6 and 7.

The active noise control methods implemented in the duct is based upon controlling the acoustic potential energy density, the acoustic kinetic energy density, and the active sound intensity.

The adaptive control of the acoustic potential energy density has implemented using the LMS-P controller, the control of the acoustic kinetic energy density is implemented using the LMS-U controller, and the control of the acoustic active intensity is implemented using the ASIC-PP and ASIC-PU controllers. All adaptive methods were presented in the chapter 4.

The controllers were developed in Matlab/Simulink and implemented in real time using a dSPACE 1102 control board with 16 weights in frequency and with a sample rate of 1.5 ms. The step-size μ was changed on-line to promote a better adaptation rate. The block diagrams can be seen in Appendix B.

The electrical signal used to drive the primary source was a sawtooth with a fundamental frequency of 41.66 Hz. After being generated, the electrical signal was filtered by an analog filter with a roll-off of 48 dB per octave of attenuation and cut-off frequency of 110 Hz. Therefore, only the frequencies 41.66, 83.33 and 125 Hz were excited. A general block diagram can be found in Figure 6.22.

The low-pass filter in the reference signal was set up to 110 Hz because it was observed experimentally that the control methods could not control frequencies above 125 Hz due the low sampling frequency capacity of the control board. Therefore, if the filter cut-off frequency were set to more than 125 Hz (the last controllable frequency), some signal from 166.66 Hz would still be in the reference signal, although attenuated .

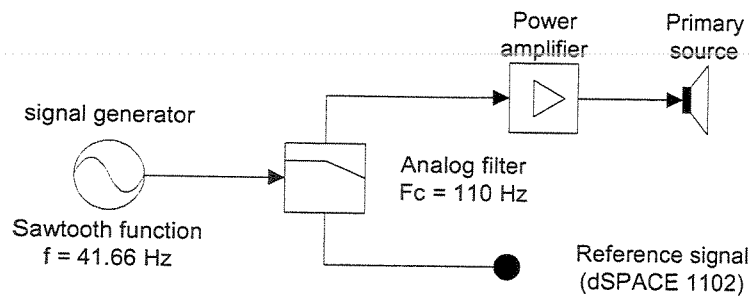


Figure 6.22: Block diagram of the excitation system

An analog low-pass filter with 180 Hz of cut-off frequency was used to reconstruct the digital control signal generated by the D/A converter of the dSPACE 1102 control board, and a block diagram can be seen in Figure 6.23.

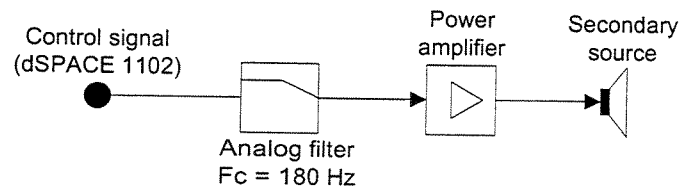


Figure 6.23: Block diagram of the control signal

6.4.1 Experimental measurements of the acoustical properties

The acoustic power radiated from the sources can be evaluated by measuring the total pressure immediately in front of the source and the volume velocity of the source as, Hansen and Snyder (1997),

$$W_R = \frac{1}{2} \Re\{PQ^*\} = \Re\{G_{QP}\} \quad (6.79)$$

where P is the pressure measured immediately in front of the source, Q is the volume velocity imposed by the source and G_{QP} is the one-side crosspower between the volume velocity and pressure.

In order to measure the radiated acoustic power properly, the microphones at positions 1 and 4 were placed as close as possible to the sources, and the volume velocities of the sources were measured using a laser Doppler vibrometer, which measured the velocity of the loudspeaker cone. The Doppler signal was improved by using a retro-reflective tape on the loudspeaker cone. Thus, the acoustic power radiated by the primary source is calculated as,

$$W_{RP} = \frac{1}{2} \Re\{P_1 u(x_P)^* S\} = \frac{1}{2} \Re\{P_1 Q_P^*\} = \Re\{G_{Q_P P_1}\} \quad (6.80)$$

where $u(x_P)$ is the particle velocity of the primary source measured by the laser vibrometer and S is the duct area. The acoustic power radiated by the secondary source is calculated as,

$$W_{RS} = \frac{1}{2} \Re\{P_4 u(x_S)^* S\} = \frac{1}{2} \Re\{P_4 Q_S^*\} = \Re\{G_{Q_S P_4}\} \quad (6.81)$$

where $u(x_S)$ is the particle velocity of the secondary source measured by the laser vibrometer.

The active intensity can be evaluated using the P-P approach as, Fahy (1995),

$$I_a = \frac{1}{2\omega\rho\delta} \Im\{P_1 P_2^*\} = \frac{1}{\omega\rho\delta} \Im\{G_{P_2 P_1}\} \quad (6.82)$$

where $G_{P_2 P_1}$ is the crosspower between the two microphones placed close to each other, and δ is the separation distance between them.

However, the method of measuring the active intensity using the P-P approach, Equation(3.33), is subject to many errors, Fahy (1995). Among them, the systematic error due to phase mismatch between the two microphones can be highlighted, which can become critical when performing the intensity measurement in a reverberant field or when the two microphones

are placed very close to each other in order to minimize the error due to the finite difference approximation.

The phase mismatch can be minimized by using a “geometric mean” in the crosspower between the sensors as proposed by Chung (1978),

$$\tilde{G}_{P_2P_1} = \sqrt{{}_s G_{P_2P_1} G_{P_2P_1}} \quad (6.83)$$

where $G_{P_2P_1}$ is the crosspower with the sensors in the original order and ${}_s G_{P_2P_1}$ is the crosspower with the sensors in switched order (the sensors must be physically switched). The necessity of phase correction can be observed in Figure 6.24, where the phase mismatch between the microphones used in the experiment measured in an impedance tube is shown.

The finite difference approximation error can be overcome as proposed in Jacobsen (1994), using the correction factor shown in Equation (6.28), i.e., multiplying the crosspower by a correction factor given by,

$$\frac{K\delta}{\sin K\delta} = \frac{1}{\text{sinc}(K\delta)} \quad (6.84)$$

Thus, the active intensity using the P-P principle with the correction of Equations (3.34) and (3.35) can be expressed as,

$$I_a = \frac{1}{\omega\rho\delta} \frac{K\delta}{\sin K\delta} \Im\{\tilde{G}_{P_2P_1}\} \quad (6.85)$$

Therefore, the active intensity between microphones placed at positions 2 and 3, I_{a23} , is given by,

$$I_{a23} = \frac{1}{2\omega\rho\delta} \Im\{P_2 P_3^*\} = \frac{1}{\omega\rho\delta} \frac{K\delta}{\sin K\delta} \Im\{\tilde{G}_{P_3P_2}\} \quad (6.86)$$

where P_2 and P_3 are the pressures measured at positions 2 and 3, respectively, δ is the separation distance between the microphones, and $\tilde{G}_{P_3P_2}$ is the crosspower corrected for phase mismatch. The active intensity flowing through the sensors 8 and 9, I_{a89} , is given by,

$$I_{a_{89}} = \frac{1}{2\omega\rho\delta} \Im\{P_8 P_9^*\} = \frac{1}{\omega\rho\delta} \frac{K\delta}{\sin K\delta} \Im\{\tilde{G}_{P_9 P_8}\} \quad (6.87)$$

where P_8 and P_9 are the pressures measured at position 8 and 9 respectively, and $\tilde{G}_{P_9 P_8}$ is the corrected crosspower without phase mismatch.

The potential energy density can be evaluated as,

$$E_p = \frac{1}{2\rho c^2} |P|^2 = \frac{1}{\rho c^2} G_{pp} \quad (6.88)$$

where G_{pp} is the auto-spectrum of the pressure signal.

The particle velocity used in the ASIC-PU and LMS-U methods can be measured using a particle velocity sensor, which has been developed by Microflown, Bree et al. (1996), Bree et al. (1999), and Eerden (1998).

The LMS-P controller used the microphone located at position 5 as an error sensor, the LMS-U used the particle velocity sensor located at position 6 as an error sensor, the ASIC-PP used the microphones located at positions 5 and 7 as error sensors, and the ASIC-PU used the microphone and the velocity sensor located at position 6 as error sensors.

6.4.2 Testing the error sensors

One of the first questions when implementing an ANC application deals with the error sensors that can be applied. The answer to this question frequently depends on the kind of controller that will be implemented. Normally, the filtered-X LMS has no particular problem with error sensors, however the ASIC can have a bad performance if the error sensors are not chosen very carefully.

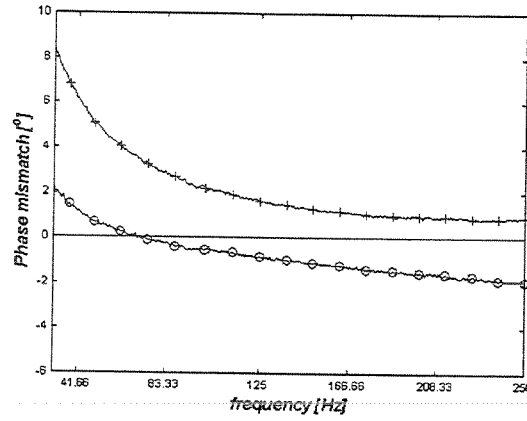
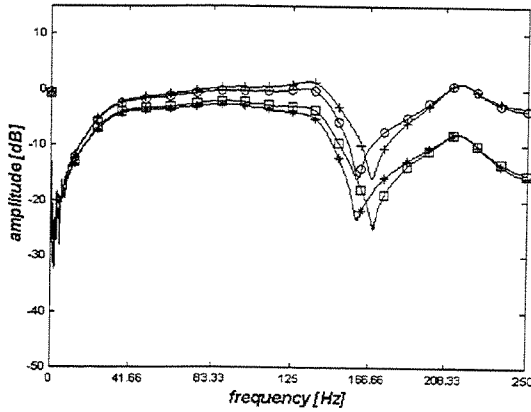
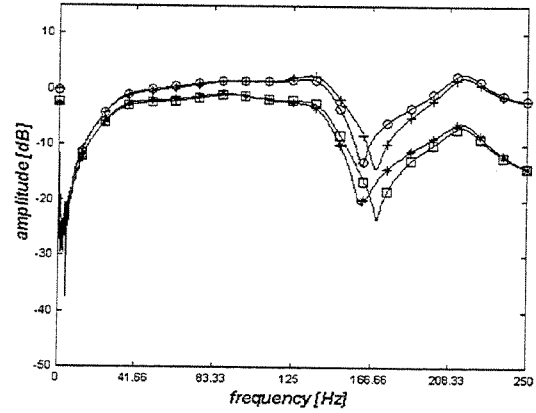


Figure 6.24: Phase mismatch between the two microphone pairs. -o- 1st sensor pair; +- 2nd sensor pair.

In order to investigate the performance of the ASIC-PP in the presence of the phase mismatch in the error sensors, two microphone pairs were chosen and analyzed - the phase mismatch between the microphones used in the experiment is shown in Figure 6.24. The control results were obtained theoretically and are shown in Figure 6.26, where the FRFs (Figure 6.25) were measured without the reconstruction filter, present in Figure 6.23.



(a)



(b)

Figure 6.25: Frequency response functions (FRFs) of the sensor pairs. (a) 1st microphone pair (b) 2nd microphone pair. -o- Zp₅; +- Zp₇; -* Zs₅; -□- Zs₇.

Comparing Figure 6.25 (a) and (b), the measured FRFs are nearly the same. Nevertheless, when applying the optimal control law to attenuate the active intensity using the P-P approach the results are very different, as shown in Figure 6.26(a). The “peaks” in Figure 6.26(a) occurred when the denominator of the ASIC-PP, which is proportional to the sound intensity from the secondary source, is close to zero, as it can be observed comparing Figure 6.26(a) and Figure 6.26(b). Therefore, the best microphone pair to be used as error sensors in the ASIC-PP controller is the 2nd microphone pair because its performance was more uniform than the 1st microphone pair in the whole frequency band of interest.

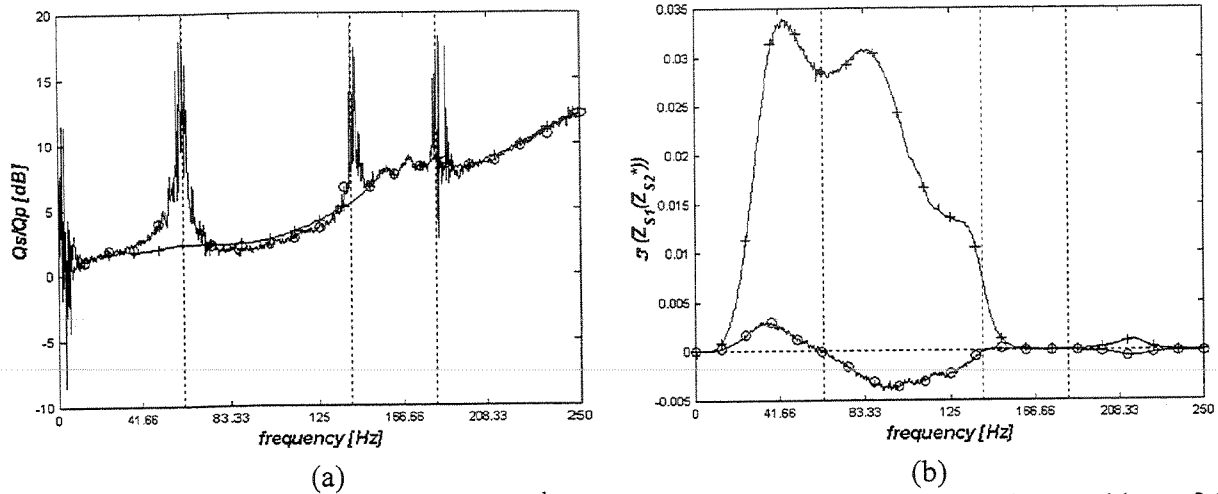


Figure 6.26: Comparison of the 1st and 2nd sensor pairs. (a) Theoretical optimal control law of the ASIC-PP; (b) denominator of the ASIC-PP. -o- 1st sensor pair; -+- 2nd sensor pair.

Figure 6.27 shows the phase of the complex intensity, which is given by the phase angle of the complex term $i(|Z_{s5}|^2 - Z_{s5}Z_{s7}^* + Z_{s7}Z_{s5}^* - |Z_{s7}|^2)$, for the 1st and 2nd microphone pairs located at position 5 and 7. It can be noticed that the 2nd microphone pair does not cross the $\pm 90^\circ$ line, which means zero active intensity, while the 1st sensor pair does. This explains why the 1st microphone pair in Figure 6.26(b) changes from positive to negative, that means, positive active intensity to negative active intensity due to the phase mismatch. The dotted vertical lines in Figure 6.26 and Figure 6.27 are the points where the denominator of the ASIC-PP, vanishes, which happens at frequencies of approximately 63 Hz, 141 Hz and 183 Hz.

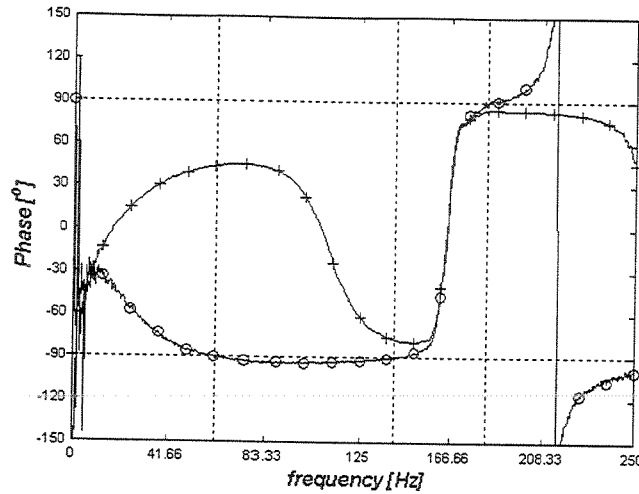


Figure 6.27: Sound intensity phase of the error sensors. -o- 1st sensor pair; +- 2nd sensor pair.

The above analysis was applied to the ASIC-PP, but can also be performed for the ASIC-PU, the same final results being expected. It is better to choose a sensor pair that measures a totally positive or totally negative active intensity from the secondary source. The analysis for the ASIC-PU is shown in the next section.

6.4.3 Off-line control analyses

After choosing a suitable pair of sensors (2nd microphone pair in this case), it is necessary to identify the FRFs once more, but now in the presence of the reconstruction filter. In the experiments performed, the presence of the reconstruction filters did not degrade the estimate of the active intensity because the phase mismatch which they introduced was negligible when compared with the phase mismatch error of the microphones. These FRFs are important both to verify the convergence of the control methods and to implement the methods in real time. In Figure 6.28, the FRFs between the sources and the error sensors are shown. It can be noticed that the FRFs for the secondary source are noisy above 160 Hz because of the presence of the reconstruction filter, set to 110 Hz cut-off frequency.

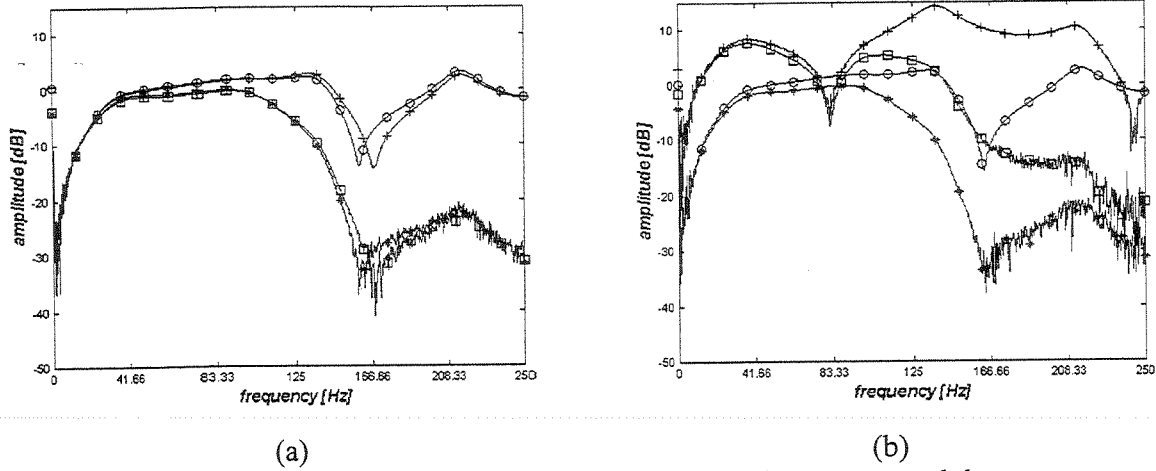


Figure 6.28: Frequency response functions (FRFs) between the sources and the error sensors in the presence of the reconstruction filter. (a) Error sensors at positions 5 and 7, -o- Z_{p5} ; +- Z_{p7} ; *- Z_{s5} ; -□- Z_{s7} ; (b) error sensors at position 6. -o- Z_{p6} ; +- Y_{p6} ; *- Z_{s6} ; -□- Y_{s6} .

The analysis of the convergence of the ASIC-PU controller can be observed in Figure 6.29, where the denominator of the ASIC-PU and the sound intensity phase for the P-U approach, i.e., the phase of the complex product $Z_{s6} Y_{z6}^*$ are shown. It can be noticed in Figure 6.29(b) that the phase of the sound intensity did not cross the $\pm 90^\circ$ line, which means zero intensity; thus, the denominator of the ASIC-PU did not vanish in the frequency range of interest, Figure 6.29(a). Therefore, the sensors of the ASIC-PU can be successfully used in this plane wave field.

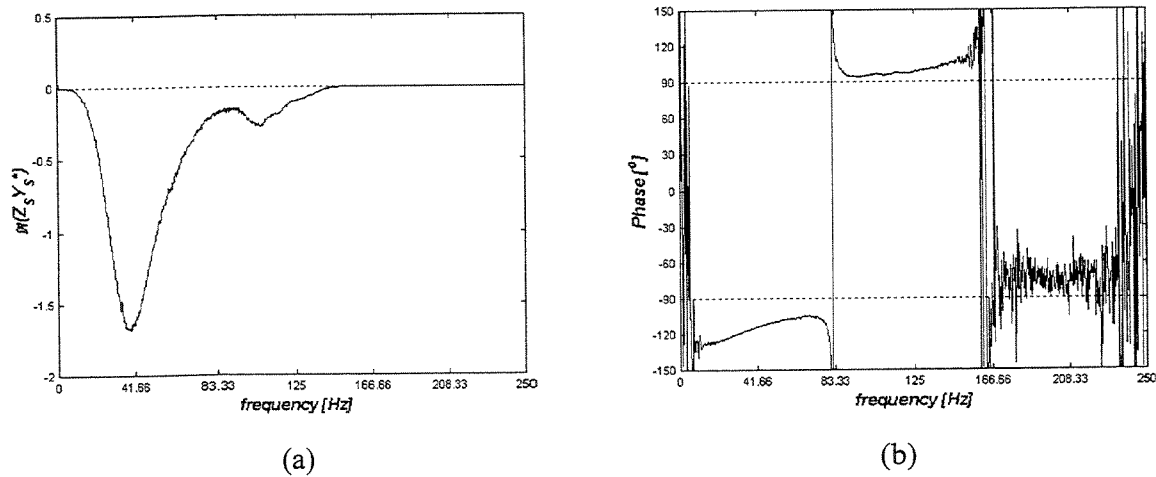


Figure 6.29: Analysis of the error sensor to the ASIC-PU controller. (a) Denominator of the ASIC-PU; (b) phase of the sound intensity.

The analysis of the convergence of the ASIC-PP controller can be observed in Figure 6.30, where the denominator of the ASIC-PU and the sound intensity phase for the P-P approach, i.e., the phase of the complex term $i(|Z_{s5}|^2 - Z_{s5}Z_{s7}^* + Z_{s7}Z_{s5}^* - |Z_{s7}|^2)$ are shown. It can be noticed in Figure 6.30(b) that the phase of the sound intensity, which is proportional to the denominator of the ASIC-PP (Figure 6.30(a)), didn't cross the $\pm 90^\circ$ line, which means zero intensity; thus, the denominator of the ASIC-PP did not vanish in the frequency range of interest. Therefore, the sensors of the ASIC-PP can be successfully used in this plane wave field.

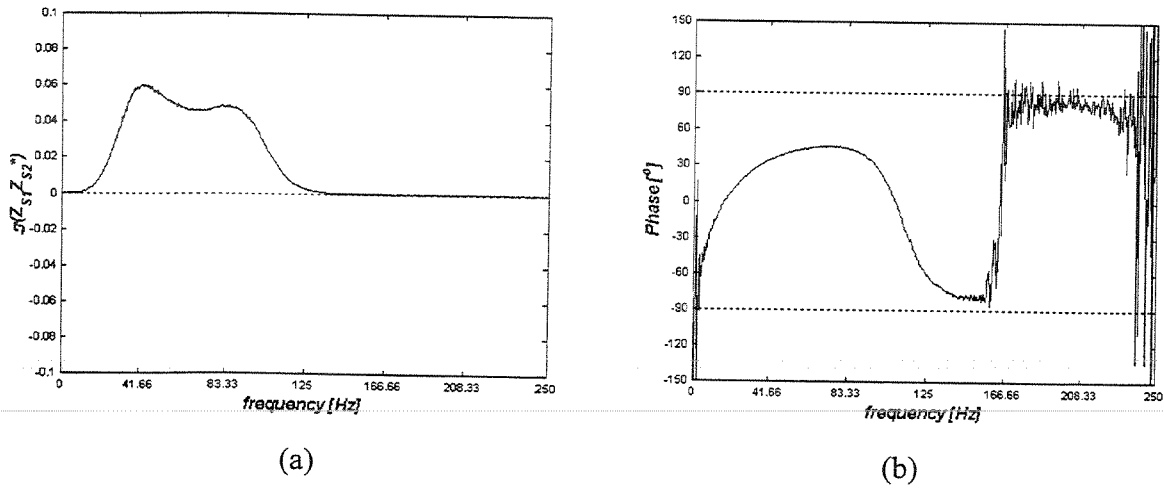


Figure 6.30: Analysis of the error sensor to the ASIC-PP controller. (a) Denominator of ASIC-PP; (b) phase of the sound intensity.

In Figure 6.31 the optimal volume velocity of the secondary source for different control methods is shown. These optimal volume velocities were evaluated substituting the measured FRFs shown in Figure 6.28 in the LMS-P, in the LMS-U, in the ASIC-PU, and the ASIC-PP. It can be observed that the different control methods yielded nearly the same final result, except for ASIC-PU, which presented more noisy results. That noise is related to the low signal levels of the FRFs for particle velocity at frequencies around 83.33 Hz, which can be observed in Figure 6.28(b).

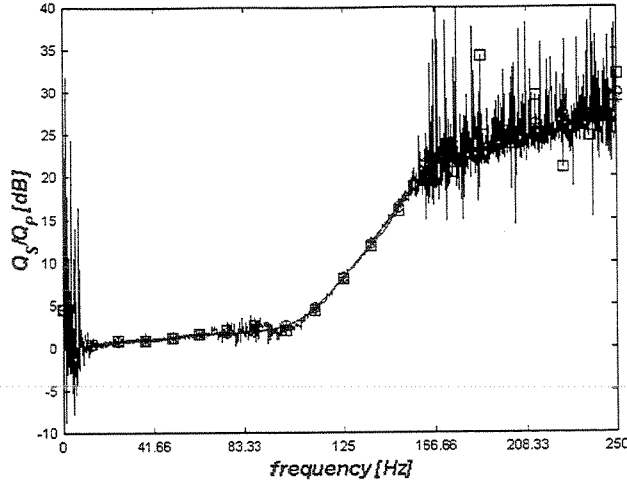


Figure 6.31: Optimal volume velocity of the secondary source. -o- LMS-P; +- LMS-U; -* ASIC-PP; -□- ASIC-PU.

The four control methods achieved nearly the same final result for the optimal volume velocity Q_s . However, it is known that the active intensity is subject to many errors, Fahy (1995); so, it is important to investigate the performance of the ASIC controller under the presence of phase mismatch in order to validate the results presented in Figure 6.31.

6.4.4 Performance of the ASIC under phase mismatch in the error sensors

In order to demonstrate the performance of the ASIC control method using the P-U and P-P approaches in the presence of phase mismatch, a $\pm 10^\circ$ of phase mismatch bias error was added to the experimental FRFs, Figure 6.28 as,

$$\begin{aligned}\hat{Z}_{s7} &= Z_{s7} e^{i\theta} \\ \hat{Y}_{s6} &= Y_{s6} e^{i\theta}\end{aligned}\tag{6.89}$$

where θ is the phase mismatch and \hat{Z}_{s7} and \hat{Y}_{s7} are the transfer functions with phase mismatch.

The optimal volume velocity of the secondary source was evaluated with phase mismatch. The results are presented in Figure 6.32, where it can be noticed that the control methods are not too sensitive to the phase mismatch, except when the denominator of the ASIC-PP and ASIC-PU

cross the zero line or are close to zero (see Figure 6.33). The dotted vertical lines in Figure 6.32 and Figure 6.33 correspond to the frequencies where the denominator of the ASIC-PP and ASIC-PU vanish with $\pm 10^\circ$.

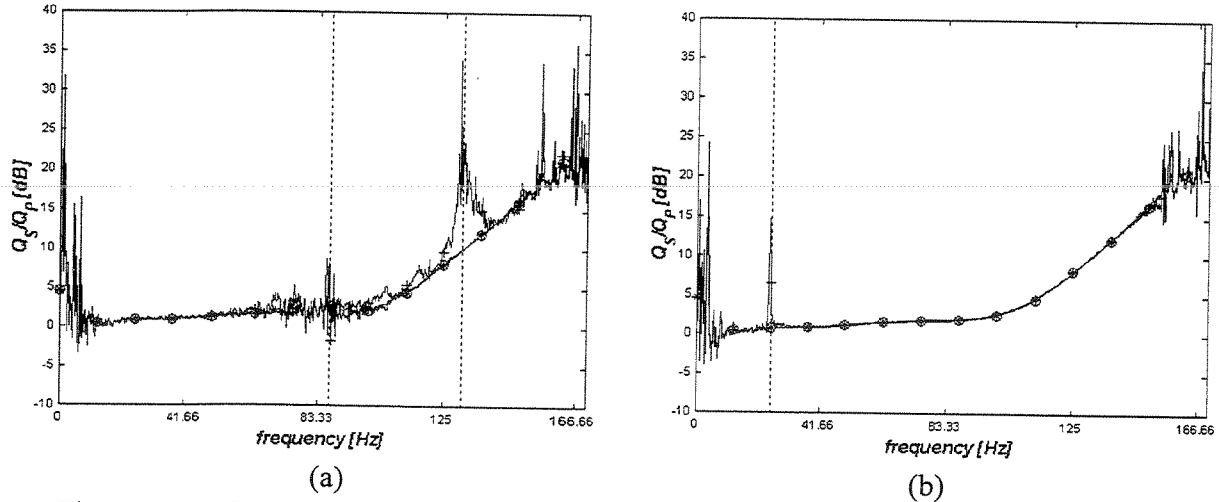


Figure 6.32: Optimal volume velocity of the secondary source with $\pm 10^\circ$ phase mismatch between the error sensors during the identification process. (a) ASIC-PU; (b) ASIC-PP. -o- without error phase; +- $+10^\circ$ phase; -* -10° phase.

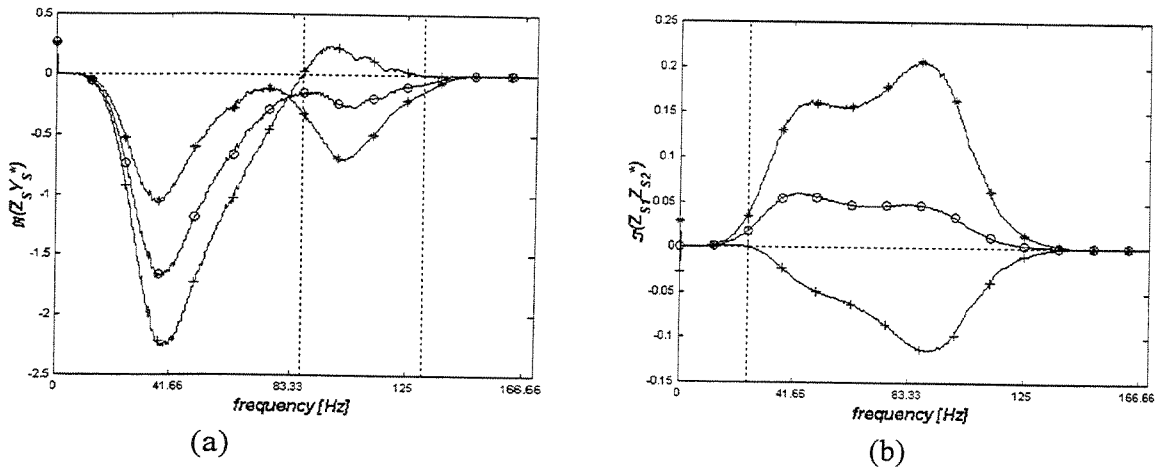


Figure 6.33: Denominator of the ASIC with $\pm 10^\circ$ phase mismatch between the error sensor pair. (a) denominator of the ASIC-PU; (b) denominator of the ASIC-PP. -o- without error phase; +- $+10^\circ$ phase; -* -10° phase.

However, if there is phase mismatch between the measured FRFs and the actual FRFs (which can happen, for instance, if one of the error sensors is replaced between the identification phase and the control operation), the control methods will have poor performance, as shown in Figure 6.34. In addition, in the case investigated, it is better to use a sensor pair with a negative rather than a positive phase mismatch.

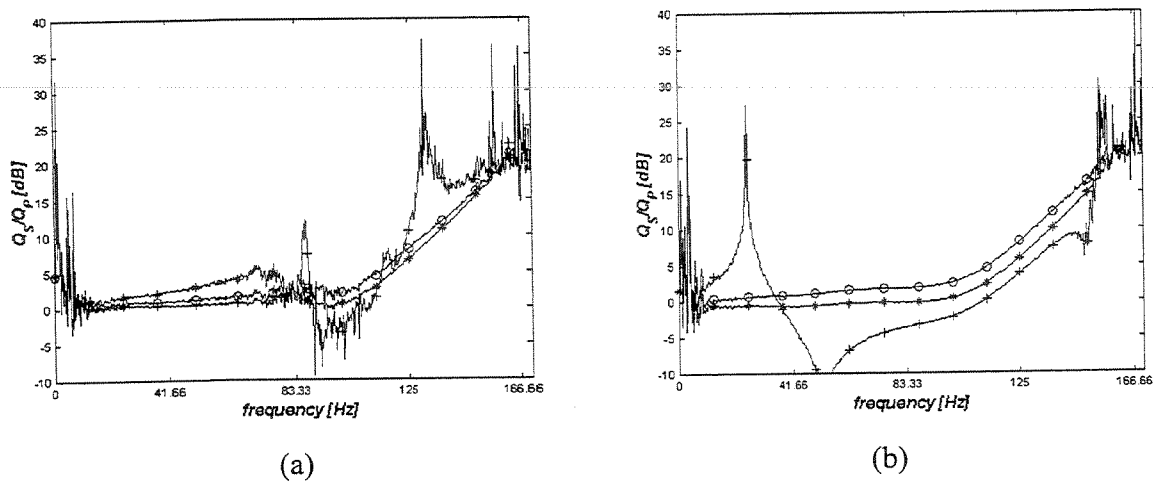


Figure 6.34: Optimal volume velocity of the secondary source with $\pm 10^\circ$ phase mismatch between the identification and control process. (a) ASIC-PU; (b) ASIC-PP. -o- without error phase; -+- $+10^\circ$ phase; -* -10° phase.

The analysis performed above becomes important for reverberant sound fields, where the angle between the real and imaginary parts of the complex intensity is close to 90° , which is the case in an open-ended duct, Kinsler et al. (1982). Because of this, the phase mismatch between the error sensors is relevant in this work.

The phase mismatch of $\pm 10^\circ$ was chosen because the phase between the imaginary and real parts of the complex intensity in the duct was identified between 85° and 95° .

6.4.5 Energetic analysis

Once the off-line investigations were finished, and the error sensors and the control method performances were defined, the real-time implementations, where the control methods were developed in Matlab/Simulink and implemented in a dSPACE 1102 control board could be started. The acoustic power radiated from the sources, the active intensity, and the potential energy density were measured with the control on and off.

It is important to note that results zero in Figure 6.35 to Figure 6.38 mean amplification. Besides, the controller was implemented only at 41.66, 83.33, and 125 Hz, and the 166.66, 208.33, and 250Hz are not controlled frequencies. Thus, in some cases, large gain variations in the not controlled frequencies are observed. This happened because very small magnitudes - before and after the controller is acting - are being divided. These small magnitudes are present in the system because of non-linear phenomena in the loudspeakers and non-ideal characteristics of the reconstruction filter (48 dB/octave).

In Figure 6.35, the changes in the volume velocity of the primary source caused by the presence of the secondary source can be observed. It can be noticed that the control methods change the volume velocity of the primary source slightly, the changes being basically the same for the four methods, except in the frequencies not controlled (166.66, 208.33 and 250 Hz), where the LMS-U decreased the volume velocity of the primary source. These changes are expected for real sources and not for ideal sources.

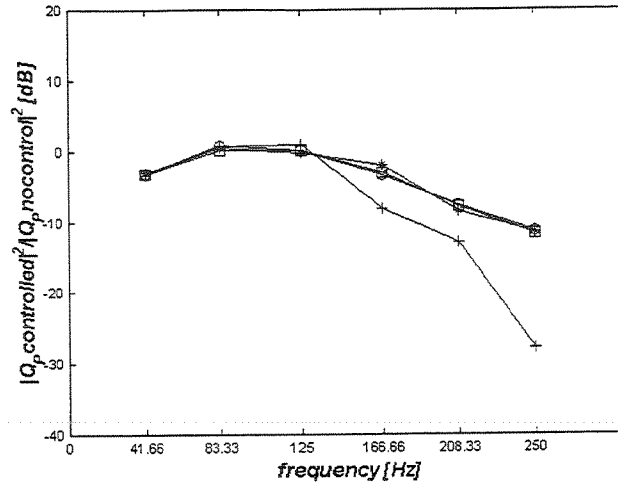


Figure 6.35: Change in the experimental volume velocity of the primary source caused by the controller. -o- LMS-P; -+- LMS-U; -*- ASIC-PP; -□- ASIC-PU.

The ratios between the acoustic power radiated from the sources with the controller on and off are shown in Figure 6.36. Figure 6.36(a) shows the attenuation in the power radiated by the primary source. It can be observed that, although the ASIC-PP achieved the best radiated power attenuation at 41.66 Hz, it achieved one of the worst results at 83.33 Hz. However, the active control methods effectively decreased the radiated acoustic power from the primary source in the controlled frequency range (41.66, 83.33 and 125 Hz). Furthermore, all the controllers, except for the LMS-P, decreased the radiated acoustic power also at the frequencies which were not controlled (166.66, 208.33 and 250 Hz). Figure 6.36(b) shows the ratio between the acoustic power radiated by the secondary source and the acoustic power radiated by the primary source working alone. The results show that the secondary source radiated less acoustic power than the primary source working alone in the controlled frequency range (41.66, 83.33 and 125 Hz), but radiated more acoustic power in the frequencies not controlled (166.66, 208.33 and 250 Hz).

It is import to notice that the control methods were implemented at different times. So, some variation in the radiated acoustic power is expected (this variation is caused by small changes in the gain of the power amplifier and environmental changes). Furthermore, the secondary source acts like a passive absorber when the controller is off.

The acoustic power radiated by the primary source was attenuated. Therefore, it is expected that the active intensity was attenuated too, but the secondary source is still radiating some acoustic power. So, the best way to observe what is happening with the energy in the duct is observing the active intensity.

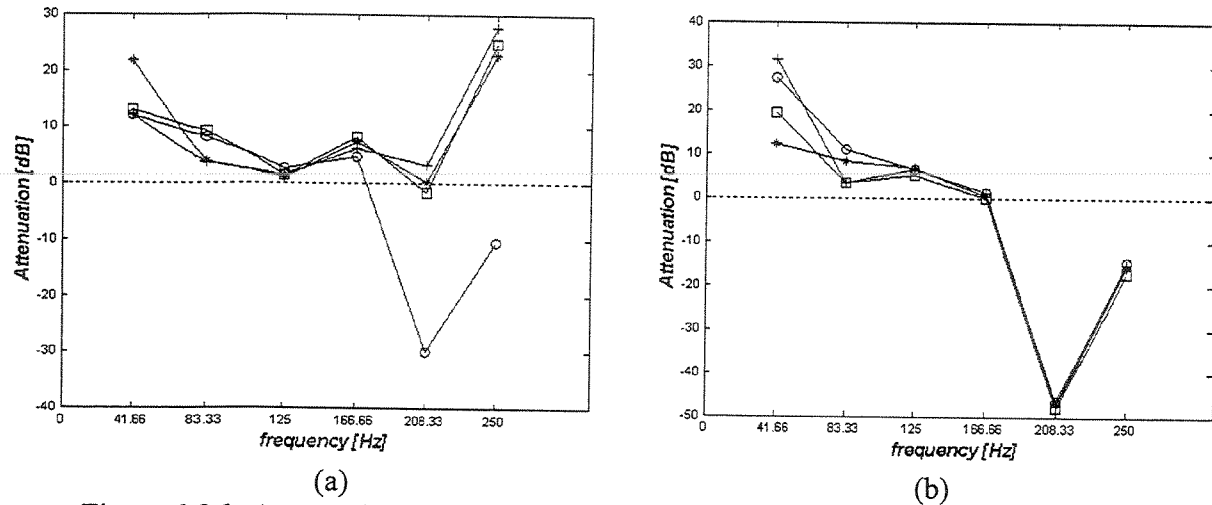


Figure 6.36: Attenuation in the radiated acoustic power W_R . (a) Primary source power attenuation; (b) power radiated by the secondary source relative to the power radiated by the primary source alone. -o- LMS-P; +- LMS-U; -* ASIC-PP; -□- ASIC-PU.

Figure 6.37 shows the attenuation in the active intensity. A great attenuation is obtained when the control methods are applied, mainly in the controlled frequencies (41.66, 83.33 and 125 Hz), and great amplification is observed in the not-controlled frequencies (166.66, 208.33 and 250 Hz).

This difference is related to the power radiated by the secondary source, that contains the frequencies that are not controlled (166.66, 208.33 and 250 Hz), which were introduced in the system by the control board. Although a reconstruction filter was used, some signal above the filter cut-off frequency could be found in the volume velocity of the secondary source, but none in the signal from the primary source working alone. Thus, there is no signal in the not-controlled case and some low amplitude signal in the controlled case, which explains the noticeable amplification.

Now, comparing Figure 6.37(a) and Figure 6.37(b) it can be observed that the active intensity was attenuated for both upstream and downstream from secondary source. Therefore, the power flow was effectively attenuated in the duct in the controlled frequency range (41.66, 83.33 and 125 Hz).

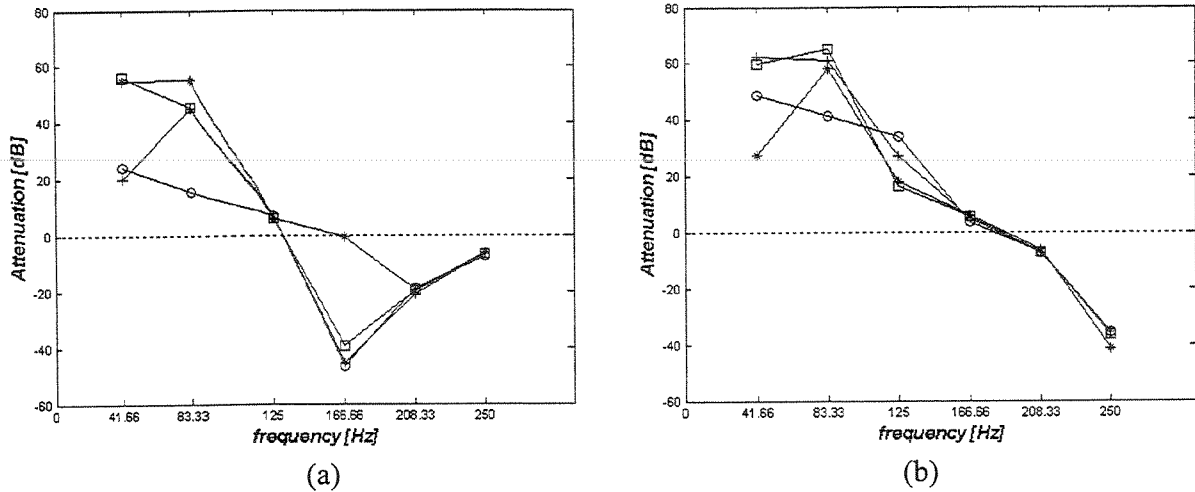


Figure 6.37: Attenuation in the active intensity I_A measured (a) between the error sensors at positions 2 and 3, (b) between the error sensors at positions 8 and 9. -o- LMS-P; -+- LMS-U; -*-* ASIC-PP; -□- ASIC-PU.

This investigation allowed the observation of what happens with the energy flow in the duct before and after the control methods are applied. Nevertheless, for a more complete understanding of the control phenomena, it is also important to observe the distribution of the potential energy density in the duct before and after the control is acting.

In Figure 6.38 the attenuation in the distribution of the potential energy density relative to the position of the secondary source is shown. It can be noticed that the potential energy is changed but not attenuated upstream from secondary source while it is heavily attenuated downstream.

It is interesting to observe in Figure 6.38(b) that the attenuation changes with the control method. Moreover, the best result was obtained at 83.33 Hz by the LMS-U and ASIC-PU, which

used the particle velocity sensor as error sensor although there was an anti-resonance at this frequency in the particle velocity, see Figure 6.28(b).

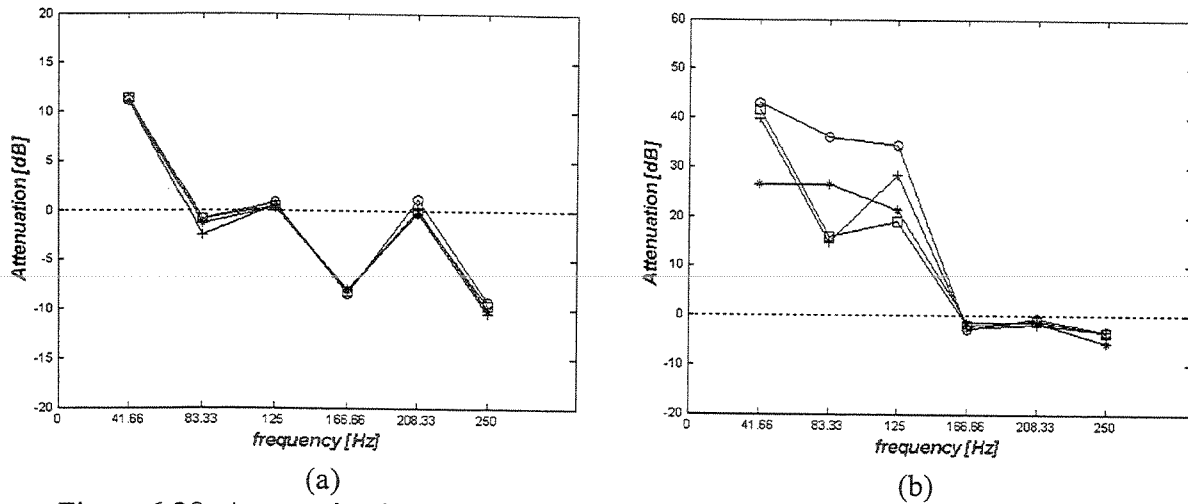


Figure 6.38: Attenuation in the potential energy density E_p measured at (a) position 2, (b) position 8. -o- LMS-P; +- LMS-U; -* ASIC-PP; -□ ASIC-PU.

6.4.6 Conclusions

Four active noise control methods were implemented in a one-dimensional acoustic waveguide. The four methods are the frequency-domain Filtered X LMS based upon controlling potential energy density and kinetic energy density and the Active Sound Intensity Control (ASIC) based upon controlling active intensity with the P-U and P-P approaches. The results showed that the methods achieved basically the same final result in all criteria observed, i.e., the minimization of the radiated acoustic power, the minimization of the active intensity and the minimization of the potential energy density. Furthermore, in the controlled case there is less energy flow than in the uncontrolled case, the sources radiated less acoustic power when working simultaneously than the primary source radiated when working alone (uncontrolled case).

It was observed that the ASIC is relatively insensitive to the phase mismatch between the error sensors, provided that the phase between the sensors do not cross the zero line, or, in other words, provided that the intensity “seen” by the error sensors from the secondary source is either totally positive or totally negative.

Moreover, it was shown that the particle velocity sensor can be successfully used as an error sensor in ANC application. It is an alternative to microphones and, when used, the cost function can either be the active intensity or the kinetic energy density.

6.5 General Conclusions

It was verified experimentally that the SEM could correctly predict the particle velocity field and the pressure field in one-dimensional waveguide with plane waves assumption. Therefore, it confirms that the SEM is suitable tool to model acoustic waveguides where plane wave assumption is made. Complex networks of pipes systems can be easily modeled with SEM. It is worth mentioning that it is possible to couple SEM with FEM.

The theoretical investigation under active noise control in one-dimensional waveguide showed that it is not necessary to use more than one error sensor and the controller achieved the same theoretical level of attenuation. Therefore, the least computationally complexity control method can be implemented successfully. Besides, it was demonstrated that it is necessary more volume velocity from the secondary source to control the primary source than was introduced by the primary source originally.

However, it is important to note that at frequencies where the primary and secondary sources are spatially apart odd multiples of a quarter wavelength, much effort from the secondary is necessary to attenuate the noise generated by the primary source. In practice, this means that other secondary sources must be introduced; if not, it is not possible to attenuate the sound perfectly.

The experimental investigations agreed heavily with the theoretical analysis, and the attenuation level achieved by the controllers was more heavily influenced by the sensor sensitivity than to the method used. Therefore, more attenuation can be achieved using more sensitivity error sensors.

The controllers implemented in the frequency domain showed good performance, but faster control boards must be used to improve the frequency range of control.

Chapter 7

Active control of the sound radiated into cylindrical acoustic cavities using structural actuators

This chapter addresses the problem of the active control of the sound radiated to an acoustic cavity formed by a cylindrical shell. The noise inside the cylindrical cavity is generated by both the structure radiating sound and by an acoustic source located outside the cylindrical cavity. This simple example allows understanding some of the basic issues of the active control inside an aircraft fuselage Palumbo et al. (2001), in coupled rooms, or in the control of the sound radiated from vibration structures such as plates Wang and Fuller (1992), or cylinders Maillard and Fuller (1999).

The control schemes tested in the cylindrical cavity are the ASAC and the AVC. While the ASAC technique consists of using structural actuators and acoustic sensors to control the sound radiated from the structure, the AVC technique consists of using structural actuators and sensors to control the vibration in the structure. Therefore, when the AVC and the ASAC are compared, what is actually being compared is the error sensor strategy. In this case, three kinds of error-sensing strategies can be applied successfully: accelerometers, as a structural error sensor, microphones and particle velocity sensors, as acoustic error sensors.

The control method, which is implemented in real time using a dSPACE 1102 control board, is the normalized filtered-X LMS in the time domain (see Appendix D). The use of three different error-sensing strategies with the normalized filtered-X LMS in the time domain

correspond to the use of three different cost functions, namely the attenuation of the structural kinetic energy density, the acoustic potential energy density, and the acoustical kinetic energy density, respectively.

When performing the active control it is important to choose correctly the positions of the actuators and sensors because they influence the performance of the controller. The shapes of the radiation modes suggest the position of the acoustic error sensors, Elliott and Jhonson (1993), and it is not necessary to control all the vibration modes, but only those related to the interior noise, Cazzolato and Hansen (1998). Thus, applying the structural and acoustic modal analyses is important to find the modes that actually are relevant to the noise radiated from the structure to the interior of the cavity.

Once the structural natural frequencies and mode shapes that are related to the interior noise are identified, the control method (normalized filtered-X LMS in the time domain) can be implemented. Thus, it is possible to compare the control schemes, AVC and ASAC, using the attenuation in the structural kinetic energy and the acoustic potential energy as error criteria for structural and acoustic disturbances. Two primary sources are used in the experience, a shaker to simulate a structural disturbance and a driver to simulate an acoustic disturbance. The secondary sources are a set of piezoelectric patches (PZT) fixed on the structure surface. The error sensors are accelerometers, microphones and particle velocity sensors to measure the vibration in the structure, the pressure and the particle velocity in the acoustic field, respectively.

Unfortunately, neither the ASIC controller nor the normalized filtered-X LMS in the frequency domain could be applied successfully due to the configuration of the control actuators (secondary source). As will be shown later in this chapter, the control actuators do not act properly below 150 Hz while the control board is not fast enough to work at frequencies above 125 Hz. Thus, only the normalized filtered-X LMS controller in the time domain could be employed.

It is important to comment that the cylindrical cavity was originally constructed for a previous research work. Thus, some construction features could not be changed. The cylindrical

cavity was designed to couple the second structural mode with the first acoustic mode, and these modes were originally intended to be controlled. Therefore, these initial thoughts influenced the experimental set up of the cylindrical shell shown below.

7.1 Experimental set up to the cylindrical cavity

The tested structure consists of an aluminum cylinder of 96 cm of radius and length of 2 meters. Two steel cables lifted the cylinder. Two covers are used to close the acoustic cavity formed by the cylinder. Orifices at the center of the covers allow the positioning of the microphones inside the cavity, but have the disadvantage of creating an airborne path for external noise. The experimental set up can be observed in Figure 7.1.

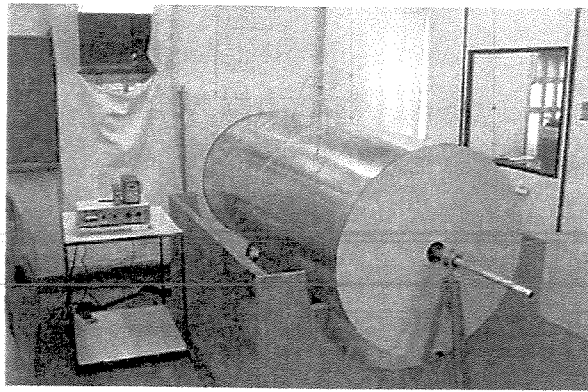


Figure 7.1: Experimental set up of the cylinder

The connections between the covers and the cylinder were made of a rubber ring and inside the covers wedges of an absorbent material was used, Figure 7.2. The rubber was used to increase the structural damping and the foam wedges to abate reflection at lower frequencies and to simulate an infinite cylindrical cavity at higher frequencies.

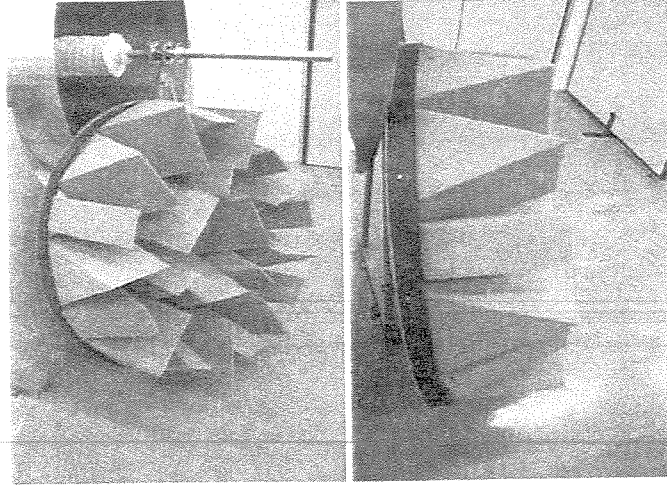


Figure 7.2: Cover details: foam wedges and rubber ring

The structural actuators were piezoelectric patches, Figure 7.3(a), and an electromagnetic shaker fixed to the structure through a stinger and a force transducer. The structural sensors were accelerometers, Figure 7.3(c), while the acoustic sensors were microphones, and a particle velocity sensor, Figure 7.3(b), the latter used only in the control application.

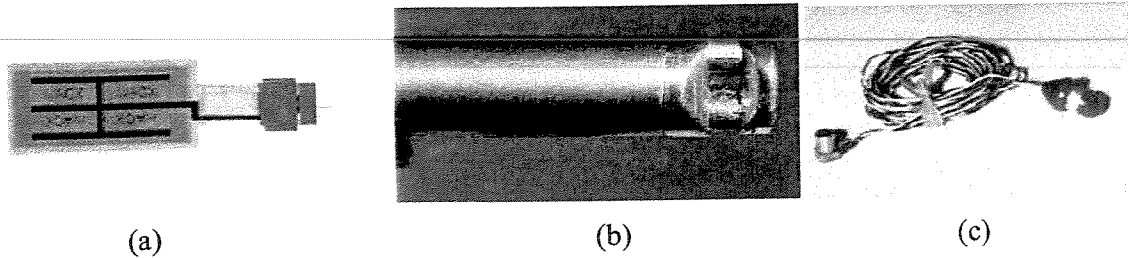


Figure 7.3: Actuators and sensors used in the experiment. (a) PZT; (b) velocity sensor; (c) accelerometers.

A shaker was fixed to the low part of the cylinder to simulate the structural disturbance. The control actuators were two pairs of PZT patches (piezoelectric patches) positioned at 90° intervals. The first PZT pair, located at 0° and 180° , was wired with the same phase while the second PZT, pair located at 90° and 270° , was wired with the same phase but in opposite phase to the first PZT pair. This arrangement was chosen to improve the actuation in the modal shapes that correspond to some of the circumferential flexural modes, particularly the 2^{nd} , 6^{th} , and 10^{th}

mode. The position of the actuators and sensors can be seen in Figure 7.4 and in Figure 7.5. As shown in Figure 7.4, the plane that contains the shaker and the array of accelerometers and microphones is not exactly the same as the one than that contains the PZT patches.

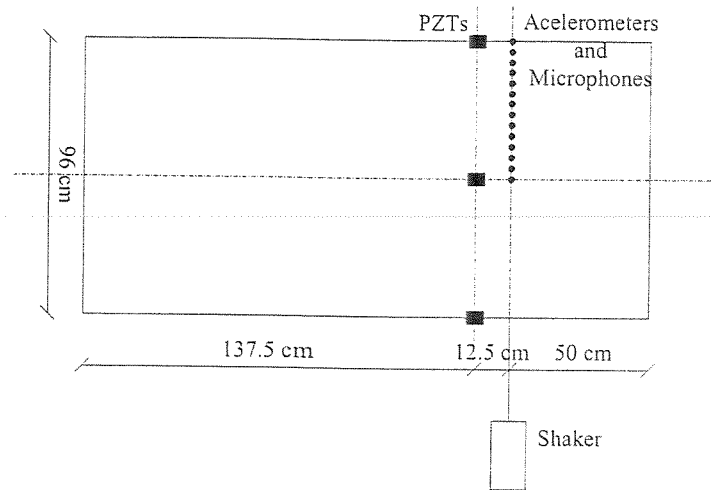


Figure 7.4: Schematic diagram to the position of the actuators and sensors along the cylinder.

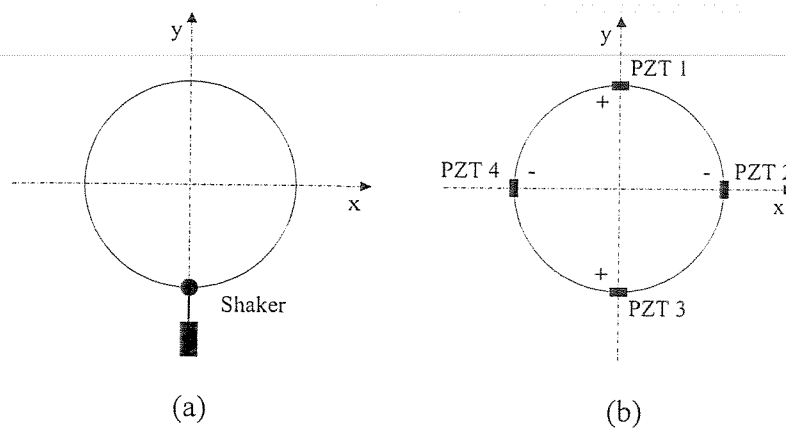


Figure 7.5: Actuator positions in the cylindrical plane. (a) Shaker position; (b) PZT positions.

The accelerometer array, which consists of 29 accelerometers separated of 6.43° from each other, was located at the same longitudinal position as the shaker, but located in the upper side of the cylinder. The microphone array was introduced inside the cylinder and located at the same longitudinal position as the accelerometer array, it was composed of seven microphones located

in the radial direction, and was rotated from 0° to 180° with a 10.6° interval. The grid formed by the accelerometers and microphones can be seen in Figure 7.6.

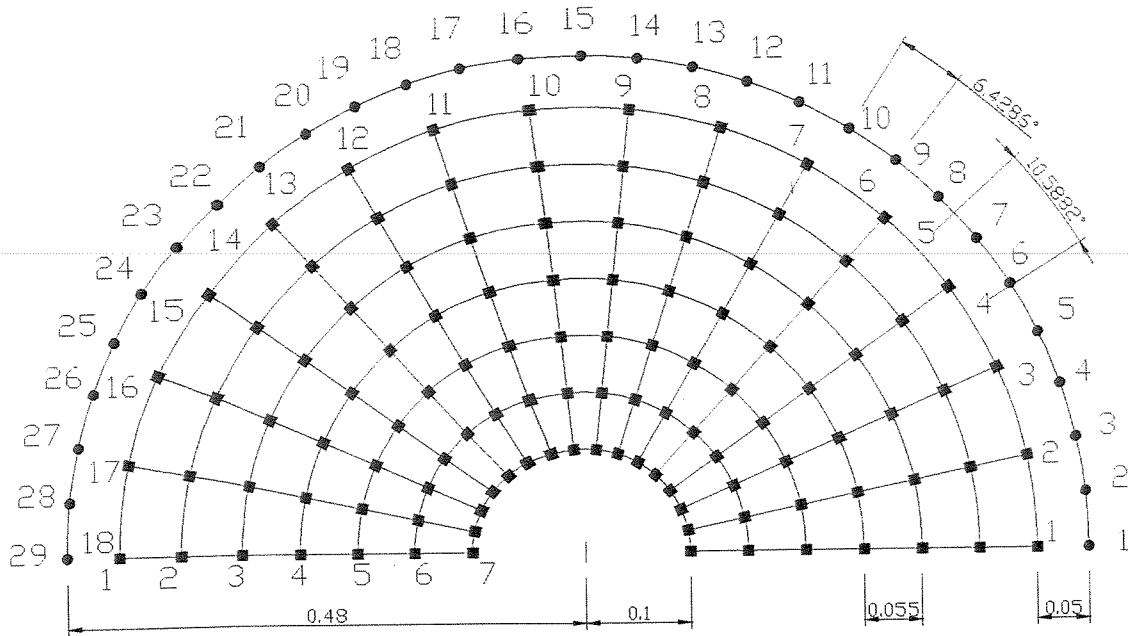


Figure 7.6: Sensor arrangement in the semi-circle in the cylinder – dimensions in centimeters; where • indicate the accelerometer positions and ■ indicate the microphone positions

In Figure 7.7, the position of the accelerometer array, the microphone array, and the velocity sensor position.

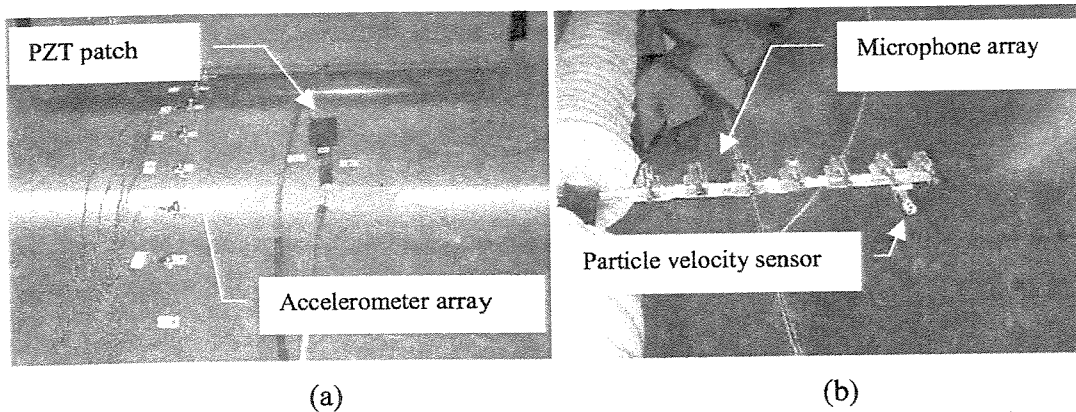


Figure 7.7: Sensors used in experimental set up. (a) Accelerometer array, (b) microphone array and velocity sensor.

7.2 Modal Analysis using structural disturbance

A modal analysis was performed using the structural disturbance to verify the capacity of the actuators (shaker and PZT) in exciting both the cylinder structure and the acoustic cavity. As well as to identify the resonance frequencies of the structure and those of the acoustic field formed by the cylindrical cavity, and the coupling between structural mode shapes and acoustical mode shapes.

Identifying the structural mode shapes that are coupled with the acoustic mode shapes is important due to the fact that the radiation efficiency of the coupled modes is greater than the radiation efficiency of the modes that are not coupled. Therefore, when the objective is to control the sound radiation from vibrating structures it is not necessary to control all the structural modes, but only the structural modes that are coupled to the acoustic modes.

In order to extract the modal parameters (natural frequencies and mode shapes) from the experimental frequency response functions, the Orthogonal Chebycheff Polynomials method was applied, Appendix C. This identification method works in the frequency domain and does not require equally spaced frequency lines. Therefore, it is possible to choose the identification range of interest, reducing the computational effort.

7.2.1 Structural Modal Analysis

Three types of frequency response functions were evaluated. The first type was the frequency response of the accelerometers using as reference the signal from the force transducer. The second type were the frequency response functions of the accelerometers using as reference the electric signal sent to the shaker. The third type were the frequency response functions of the accelerometers using as reference the electric signal sent to the PZT patches. The electrical signal sent to the actuators (shaker and PZT patches) was a white noise in the range of 0 to 1024 Hz with sampling frequency of 2048 Hz.

In Figure 7.8 the frequency response functions measured for the accelerometer array is shown. It is observed that in the frequency responses obtained using the shaker there are more resonance peaks than in the frequency responses for the PZT patches. This difference is related to

the configuration of the PZT patches that increases the actuation for the modes related to the adopted configuration. This situation occurred near 216 Hz. Besides, the magnitude of the response is very different when using the shaker and the PZT patches, and the PZT patches do not actuate properly below 150 Hz.

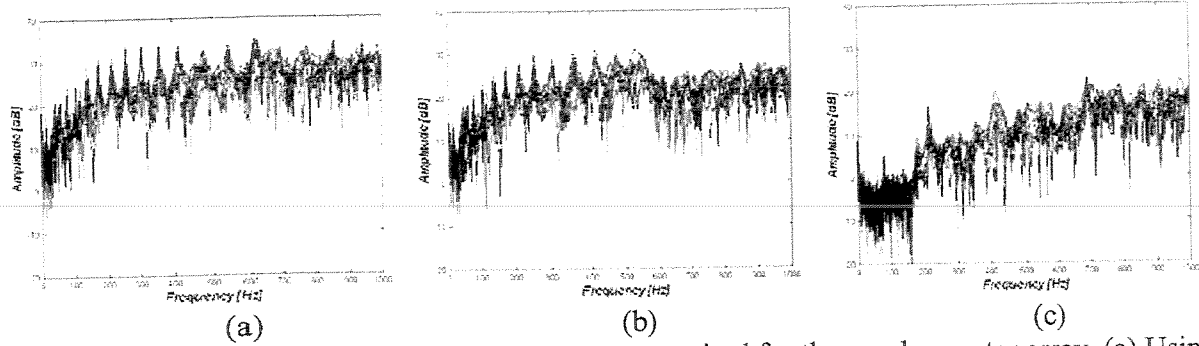


Figure 7.8: Typical structural frequency responses acquired for the accelerometer array. (a) Using as reference the signal from the force transducer; (b) using as reference the electric signal sent to the shaker; (c) using as reference the electric signal sent to the PZT. Units: dB relative to (a) $1 \text{ m/s}^2/\text{N}$; (b) and (c) $10 \text{ m/s}^2/\text{V}$.

In Figure 7.9 the narrow-band structural response to a white noise (a zoom from Figure 7.8) is shown. It can be noticed that around the frequency of 216 Hz the amplitude is the greatest and a stationary wave was well defined. The notches correspond to the nodes and the peaks to the maximum amplitude (positive or negative) of the stationary wave.

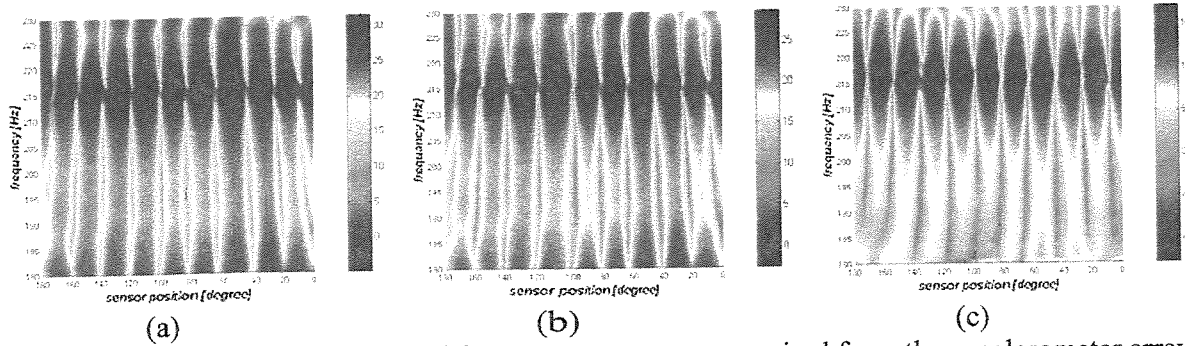


Figure 7.9: Narrow-band structural frequency responses acquired from the accelerometer array. (a) Using as reference the signal from the force transducer; (b) using as reference the electric signal sent to the shaker; (c) using as reference the electric signal sent to the PZT set. Colormap units are in dB relative to (a) $1 \text{ m/s}^2/\text{N}$, (b) and (c) $10 \text{ m/s}^2/\text{V}$.

The results obtained using the Orthogonal Chebycheff Polynomials method, Appendix C, to extract the natural frequencies and mode shapes from the frequency responses in Figure 7.8 are shown in Table 7.1. The identification was performed only in the range of 150 to 250 Hz. It can be noted from the tables that the 216 Hz mode is present in all measured frequency responses. The exact natural frequency identified was 215.75 Hz using the force transducer as reference, 216.16 Hz using the Electrical signal sent to the shaker as reference, and 215.98 Hz using the electrical signal sent to the PZT patches as reference.

Table 7.1: Results of the structural modal analysis.

Reference Signal					
Force transducer		Electrical signal sent to the shaker		Electrical signal sent to the PZT patches	
Nat. Freq. [Hz]	Damping coeff.	Nat. Freq. [Hz]	Damping coeff.	Nat. Freq. [Hz]	Damping coeff.
166.67	0.0155	148.35	0.0158	152.47	0.0002
175.60	0.0040	154.98	0.0085	160.79	0.0043
175.63	0.0139	166.66	0.0111	174.97	0.0045
183.10	0.0139	174.78	0.0077	180.29	0.0119
204.90	0.0106	182.04	0.0140	194.57	0.0146
215.75	0.0073	213.77	0.0072	215.98	0.0086
220.46	0.0097	216.16	0.0113	218.76	0.0088
232.27	0.0133	231.00	0.0118	235.14	0.0124
240.67	0.0123	240.16	0.0115	242.21	0.0087
245.74	0.0165	245.67	0.0166	246.59	0.0122

The identified mode shapes and natural frequencies were compared with the analytical solution for a cylindrical shell of infinite length, Blevins (1995), which are given by,

$$f_i = \frac{\lambda_i}{2\pi R} \left[\frac{E}{\mu(1-\nu^2)} \right]^{\frac{1}{2}} \quad (7.1)$$

where

$$\lambda_i = \frac{1}{12^{\frac{1}{2}}} \frac{h}{R} \frac{i(i^2-1)}{(1+i^2)^{\frac{1}{2}}} \quad i = 2,3,4,\dots \quad (7.2)$$

and the mode shape as,

$$\Psi = \sin i\theta \quad (7.3)$$

The analytical natural frequencies for the radial-circumferential flexural modes are given in Table 7.2, where the natural frequency of 216 Hz can be found to correspond to the 10th mode shape. However, it is important to note that a minimal variation in the thickness changes considerably the natural frequency, but not the mode shape. For example, if h were 0.002 instead of 0.0021, the same 10th mode shape would have a natural frequency of 205.92 Hz.

Table 7.2: Natural frequency of a cylindrical shell of infinite length, with $E = 70\text{GPa}$, $\nu = 0.3$, $R = 0.48\text{ m}$, $h = 0.0021\text{ m}$ and $\rho = 2800\text{ kg/m}^3$.

Mode	Nat. Freq. [Hz]
1	0
2	5.88
3	16.65
4	31.94
5	51.65
6	75.77
7	104.29
8	137.21
9	174.51
10	216.21
11	262.30
12	312.78
13	367.65
14	426.91
15	490.56

The comparison between the 10th analytical mode shape and the ODS (Operational Deflection Shape) obtained from the experimental structural frequency responses is presented in Figure 7.10(a), where it can be observed that there is a good agreement. Therefore, the ODS at a frequency of 216 Hz can be considered as dominated by a natural mode shape. The comparison of the 10th analytical mode shape and the mode shape identified from the frequency responses is shown in Figure 7.10(b), where the shape of the identified mode agrees very well with the analytical mode shape.

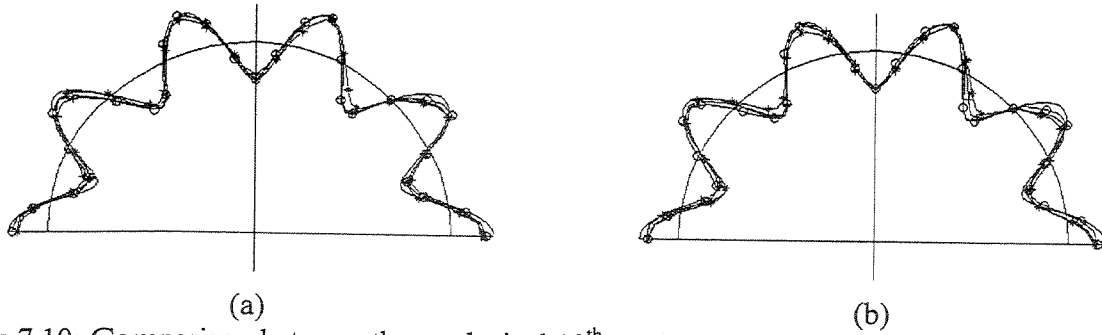


Figure 7.10: Comparison between the analytical 10th mode shape of the cylindrical shell with: (a) the ODS measured at 216 Hz, (b) the identified mode shape (Table 7.1). ---Theoretical mode shape; -o- experimental using the force transducer as reference; -+- experimental using the electrical signal sent to the shaker as reference; -* experimental using the electrical signal sent to the PZT patches as reference.

7.2.2 Vibro-acoustic Modal Analysis

The vibro-acoustic modal analysis was performed using a microphone array composed by seven microphones located along the radial direction of the cylinder. This array was rotated in 10.6° intervals to perform the measurements; so, 18 measurements were performed to complete the upper semi-circle.

The theoretical natural frequencies of the cylindrical acoustical cavity, Blevins (1995), are shown in Table 7.3, where it can be noticed that 4th natural frequency is related to the (0,0,1) mode shape, that is the first circumferential mode shape. The theoretical mode shape (0,0,1) is shown in Figure 7.11. However, a variation of 5 mm in the radius of the cylinder produces a natural frequency of 216.15 Hz rather than 218.5 Hz. Furthermore, if an infinite cylindrical waveguide is considered, the first sloshing mode is at 209.25 Hz, Kinsler et al. (1982).

Therefore, the theoretical analysis of a closed cylindrical acoustic cavity shows that there is an acoustical natural frequency around the 216 Hz, which nearly coincides with the structural natural frequency. On the other hand, the foam edges glued to the covers did not simulate an infinite cylindrical waveguide but only helped damping the longitudinal acoustic modes.

Table 7.3: Theoretical natural frequency of a closed cylindrical acoustic cavity.

Mode	Z-axis	Radius	θ angle	Nat. Freq. [Hz]
1	0	0	0	0.00
2	1	0	0	85.75
3	2	0	0	171.50
4	0	0	1	218.50
5	1	0	1	234.73
6	3	0	0	257.25
7	2	0	1	277.77
8	3	0	1	337.52
9	4	0	0	343.00
10	0	0	2	362.45

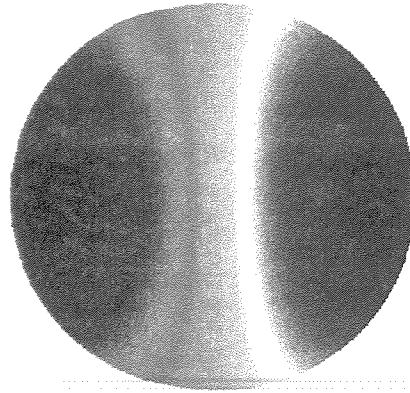


Figure 7.11: first circumferential analytical mode shape of a cylindrical cavity.

The acoustic frequency response functions measured by the microphone array are presented in Figure 7.12, where a large number of resonance peaks can be noticed. Besides, comparing Figure 7.12(a) and (b) with Figure 7.12(c) it can be observed that the PZT patches have smaller capacity of exciting the acoustic system than the shaker. Most of the peaks correspond to structural resonances rather than acoustic modes.

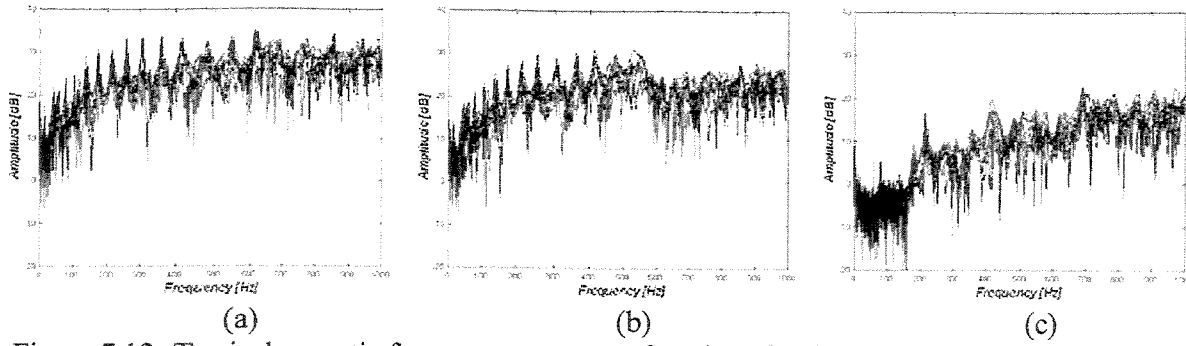


Figure 7.12: Typical acoustic frequency response functions for the microphone array. (a) Using as reference the signal from the force transducer; (b) using as reference the electric signal sent to the shaker; (c) using as reference the electric signal sent to the PZT patches. Units: dB relative to (a) 0.1 Pa/N; (b) and (c) 1 Pa/V.

In Figure 7.13 the frequency response functions for the microphones located in the line number 9 (position near the top of the cylinder) are shown. It can be noticed that the frequency of 216 Hz is present in the measurements but its value decreased for the sensors located near the center of the cylinder.

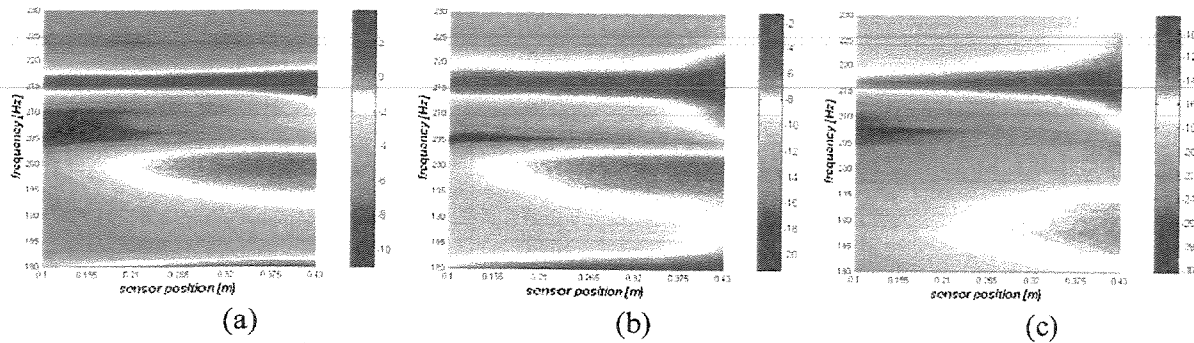


Figure 7.13: Narrow band frequency response functions for the microphone array in the line number 9. (a) Using as reference the signal from the force transducer; (b) using as reference the electric signal sent to the shaker; (c) using as reference the electric signal sent to the PZT patches. Colormap units in dB relative to (a) 0.1 Pa/N, (b) and (c) 1 Pa/V.

The amplitude of the frequency response functions at 216 Hz is presented in Figure 7.14. It can be noticed that the predominant mode shape is the acoustical mode shape; the structural mode shape influencing only near the cylinder wall and decreasing fast towards the center. This happened because below 216 Hz only some modes can propagate, and the 10th structural mode is not one of them.

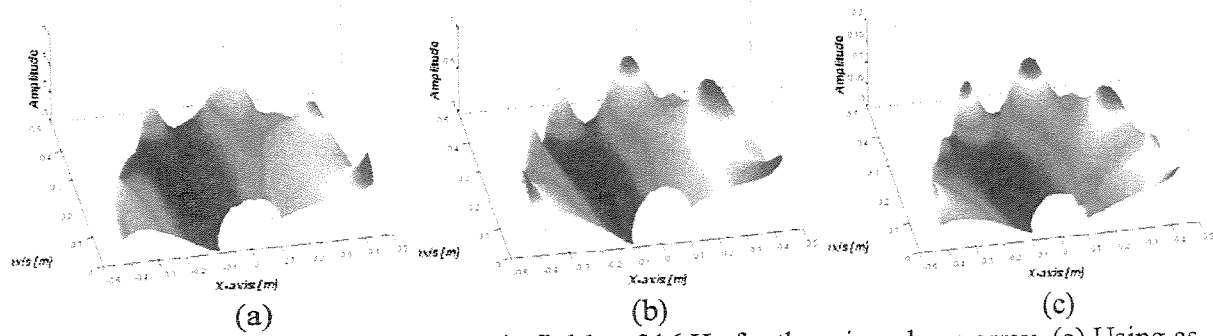


Figure 7.14: Amplitude of the acoustic field at 216 Hz for the microphone array. (a) Using as reference the signal from the force transducer; (b) using as reference the electric signal sent to the shaker; (c) using as reference the electric signal sent to the PZT patches. Units are in (a) Pa/Kgf, (b) and (c) Pa/V.

The results obtained using the Orthogonal Chebycheff Polynomials method, Appendix C, to extract the natural frequencies and mode shapes from the frequency responses in Figure 7.12 are shown in Table 7.4. The identification was performed only in the range of 150 to 250 Hz. It can be noticed from Table 7.4 that the 216 Hz mode is present in all measured frequency responses. The exact natural frequency identified was 215.63 Hz using the force transducer as reference, 215.78 Hz using the Electrical signal sent to the shaker as reference, and 217.63 Hz using the electrical signal sent to the PZT patches as reference.

Table 7.4: Results of the vibro-acoustic modal analysis.

Reference signal					
Force transducer		Electrical signal sent to the shaker		Electrical signal sent to the PZT patches	
Nat. Freq. [Hz]	Damping coeff.	Nat. Freq. [Hz]	Damping coeff.	Nat. Freq. [Hz]	Damping coeff.
152.21	0.0075	152.25	0.0112	152.07	0.0028
155.84	0.0144	158.11	0.0127	161.36	0.0010
174.99	0.0112	172.29	0.0101	174.60	0.0030
177.28	0.0042	176.46	0.0069	184.75	0.0230
192.08	0.0189	191.60	0.0034	193.72	0.0129
202.16	0.0089	202.57	0.0122	213.86	0.0154
215.63	0.0041	215.78	0.0064	217.63	0.0083
232.41	0.0116	235.53	0.0174	234.80	0.0116
240.27	0.0128	239.38	0.0160	241.92	0.0052
245.56	0.0114	247.51	0.0096	247.35	0.0132

Figure 7.15 shows two time instants of the animation of the ODS obtained from measurements made with microphones number 1 and number 4 when they are rotated (180°). It is observed that the ODS measured closer to the cylinder axis (microphone 4) is dominated by the acoustic mode shape, while, in the ODS measured close to the cylinder inner surface (microphone 1), the near-field effects are predominant.

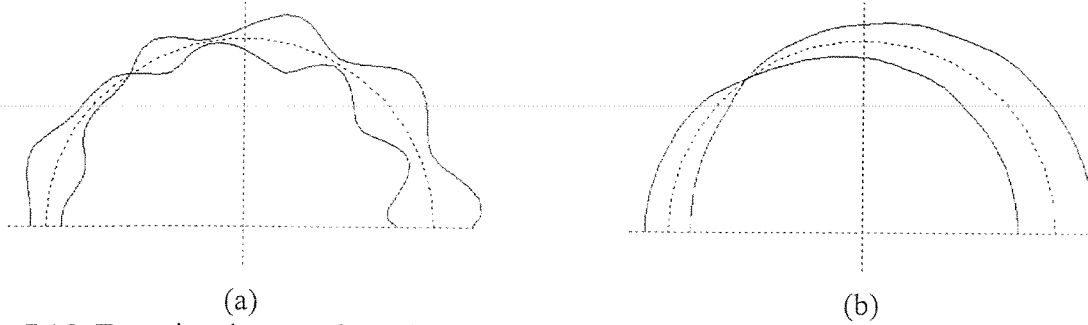


Figure 7.15: Two time instants from the animation of the ODS in the frequency of 216 Hz using as reference the signal from the force transducer. (a) Microphone array formed by the microphone at position 1 (near the wall), (b) microphone array formed by the microphone at position 4 (near the center).

7.2.3 Conclusion

In the structural modal analysis, it was observed the presence of a structural resonance frequency at 216 Hz, and its associated mode shape was well identified for the two kinds of actuators (shaker and PZT patches). Moreover, the configuration of the PZT patches increased the actuation performance related to this mode shape.

In the acoustic modal analysis, it was observed that a natural frequency of approximately 216 Hz is also present in the acoustical field. The measured acoustic field ODS at 216 Hz is a mix of the acoustical mode shape and the structural mode shape. The acoustical mode shape corresponds to the first circumferential mode of the acoustical cavity (slashing mode). Furthermore, the contribution of the radiated mode from the structure is larger near the interface between the structure and the acoustic field, decreasing fast towards the cylinder axis; or in other words, it only has influence in the acoustic near field (evanescent waves).

It was also noticed that the signals from the accelerometers have enough amplitude to be used as error sensors in AVC; however, the signal from the microphones should be amplified to apply the ASAC. Besides, the magnitude of the FRFs for the shaker are larger than the FRFs for the PZT patches; thus, in control applications the signals to be sent to the PZT patches need to be amplified.

Some problems with the repeatability of the measurements were found for the acoustic case, but not for the structural case. They were found related to the difficulty in placing the covers in the same position every time it was necessary to remove them.

The modal analysis using acoustic disturbances was tried, but the acoustic source, a driver, located at the same place of the shaker has shown to be inefficient in exciting both the structure and the acoustic field in a narrow band around 216 Hz.

The aspects highlighted above demonstrated that the control methods should be implemented in a narrow band around 216 Hz. However, it is interesting to note that there is a structural and acoustical natural frequency around 174 Hz, which can be observed in Table 7.2 and Table 7.3. This natural frequency corresponds to the 9th structural mode and to the 3rd acoustic mode. Although the acoustic cavity and the structure are coupled at this frequency, it could not be used in the control application. This fact can be explained, in part, by the structural configuration of the actuators and sensors and by the mode shapes. The PZT patches (control actuators) do not have effective actuation at this frequency because the structural mode corresponding to 174 Hz is the 9th mode, which is an odd circumferential mode. Besides, the acoustic mode is the 3rd mode, and corresponds to a longitudinal mode of the cavity, i.e., in the Z-axis. Because of these problems, the frequencies around 174 Hz could not be effectively controlled by the configuration specified in present experimental set up.

7.3 Experimental set up for control applications

A diagram of the experimental set up for the control application is shown in Figure 7.16, Figure 7.17, and Figure 7.18. In Figure 7.16, it is shown how the control signal, $y(n)$, is generated in the D/A converter of the dSPACE 1102, filtered in 350 Hz by a 8-poles, Butterworth, low-pass filter from Frequency Devices model 900, and sent to two amplifiers with a fixed gain of 20 times. The phase shift between the PZT patches was implemented by inverting, the wiring of the cable connected to the PZT.

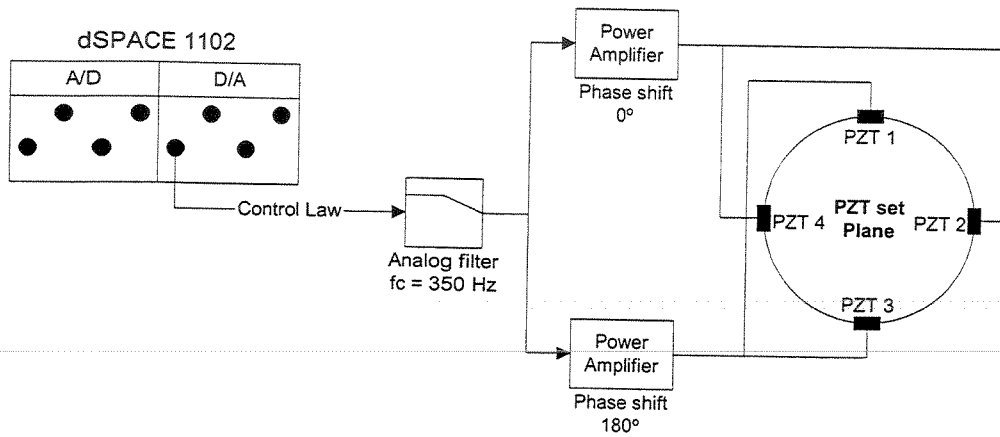


Figure 7.16: Control signal generation path from the dSPACE 1102 control board to the structure

In Figure 7.17 and Figure 7.18 the position of the error sensors, which are used in the control application, and the position of the primary disturbance are shown. It can be observed that the electrical signals from the error sensors were conditioned using a gain of 100 times and filtered with a low pass filter set to 1000 Hz. This was necessary due to the low signal level found in the error sensors.

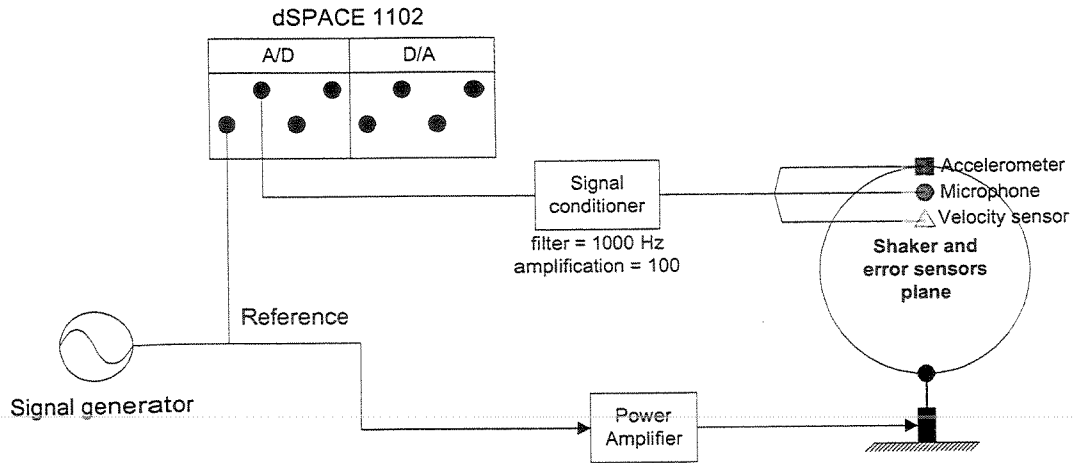


Figure 7.17: Diagram of the shaker and the error sensors to control the structural disturbance

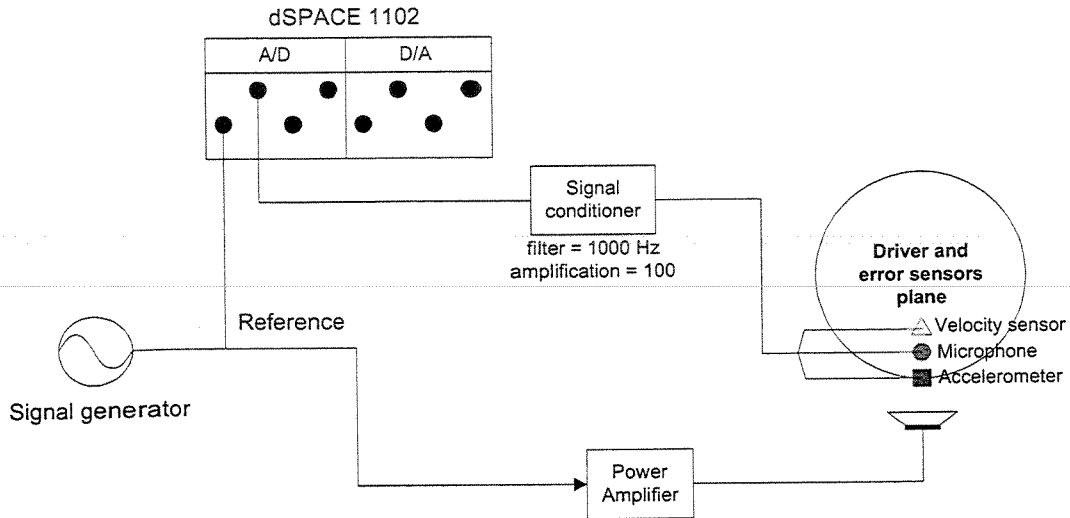


Figure 7.18: Diagram of the driver and the error sensors used to control the acoustic disturbance

7.4 Comparison between the ASAC and AVC methods for structural disturbances

The main objective here is to compare the performance of the ASAC and AVC techniques in the control of the structural vibration and of the sound radiated into the cylindrical cavity. For this purpose, seven accelerometers were located at the upper outer surface of the cylindrical shell, and seven microphones and one particle velocity sensor were positioned in the cylindrical cavity as indicated in Figure 7.19. The sensor positions are the same presented in Figure 7.6; but, only a few of the sensors used in the modal analysis were chosen to be used as error sensors in the active control application.

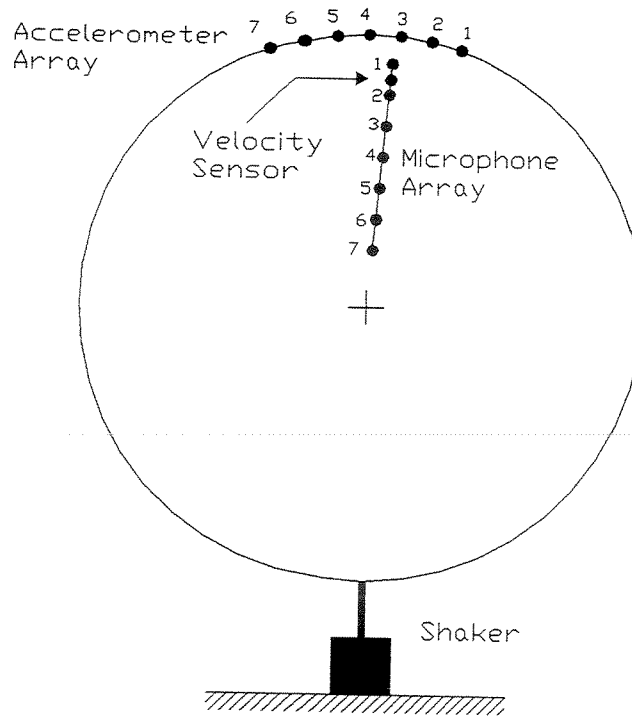
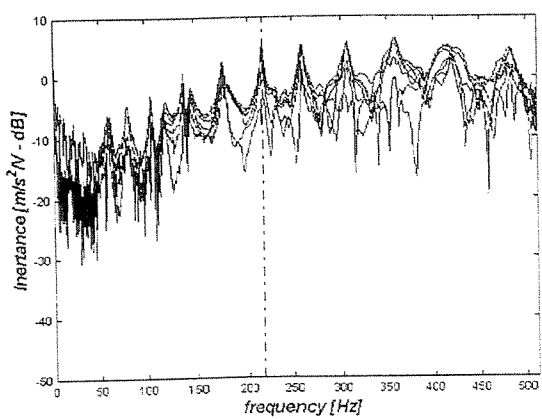


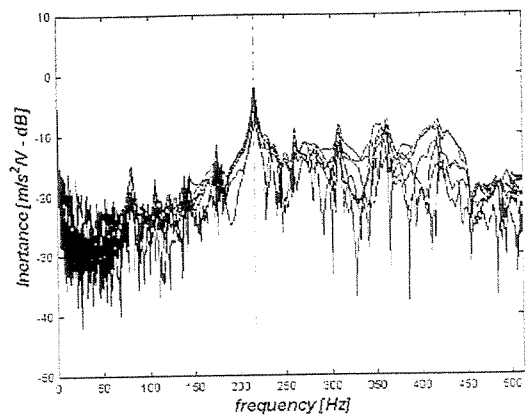
Figure 7.19: Error sensor placement on the cylindrical shell cavity for the structural disturbance experiment. Where \bullet represent the accelerometer positions, \bullet represent the microphone positions, and \bullet represent the velocity sensor position.

With the sensor scheme shown in Figure 7.19, it is possible to verify the performance of the three error sensing strategies and their responses in the structure and in the acoustic field. The use of three different error-sensing strategies represents three different cost functions. The use of the accelerometer, the microphone, or the particle velocity sensor imply the use of the structural kinetic energy density, the acoustic potential energy density, or the acoustical kinetic energy density as cost function, respectively.

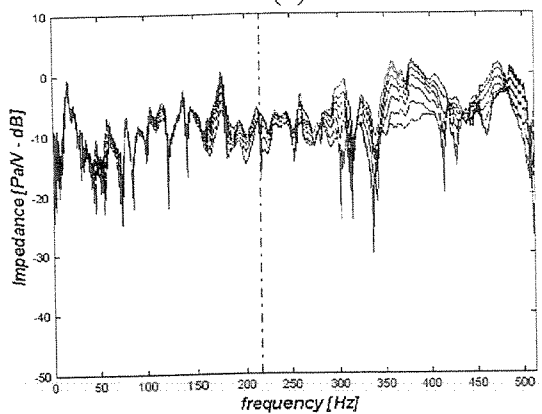
The configuration in Figure 7.19 allows investigating the error sensors, structural or acoustic, and their position. This investigation is performed for the two criteria, the minimization of the kinetic energy in the structure and the minimization of the potential energy in the acoustic field.



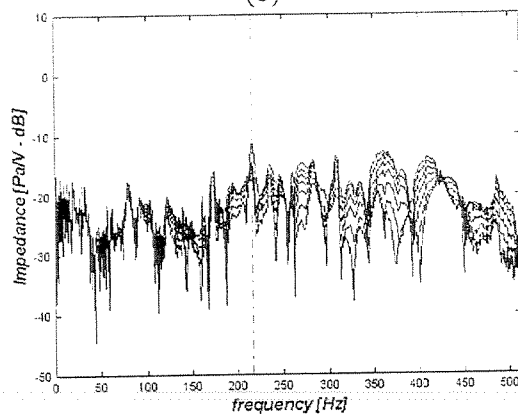
(a)



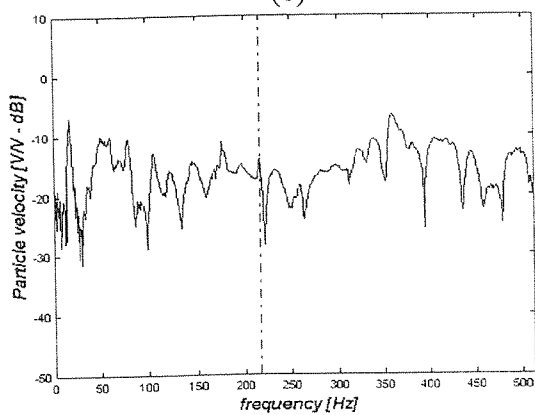
(b)



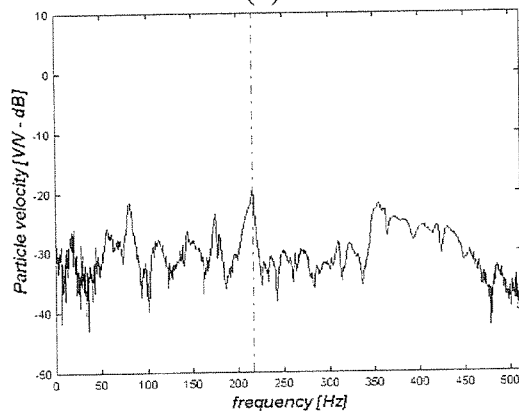
(c)



(d)



(e)



(f)

Figure 7.20: Frequency response functions measured at the sensors indicated in Figure 7.19. (a) Between the accelerometers and the shaker, (b) between the accelerometers and the PZT patches, (c) between the microphones and the shaker, (d) between the microphones and the PZT patches, (e) between the velocity sensor and the shaker, (f) between the velocity sensor and the PZT patches.

The frequency response functions (FRFs) measured in the cylinder for the sensors shown in Figure 7.19 are shown in Figure 7.20. It can be noticed that the shaker is capable of exciting all structural and acoustical modes while the PZT patches excites only the structural and acoustical modes related to their specific configuration. In other words, the shaker can excite all frequencies while the PZT patches could achieve their best performance only near 216 Hz. Moreover, the amplitudes obtained with the PZT patches are smaller than those obtained with the shaker; thus, the shaker is more efficient in inputting energy to the system than the PZT patches. This indicates that larger amplification in the control signal would be necessary.

Figure 7.21 shows the frequency response functions for the accelerometer array, where it is noticed that the main disturbance is around 216 Hz. Besides, the position of the sensor near 90° (sensor number 4) corresponding to the maximum amplitude.

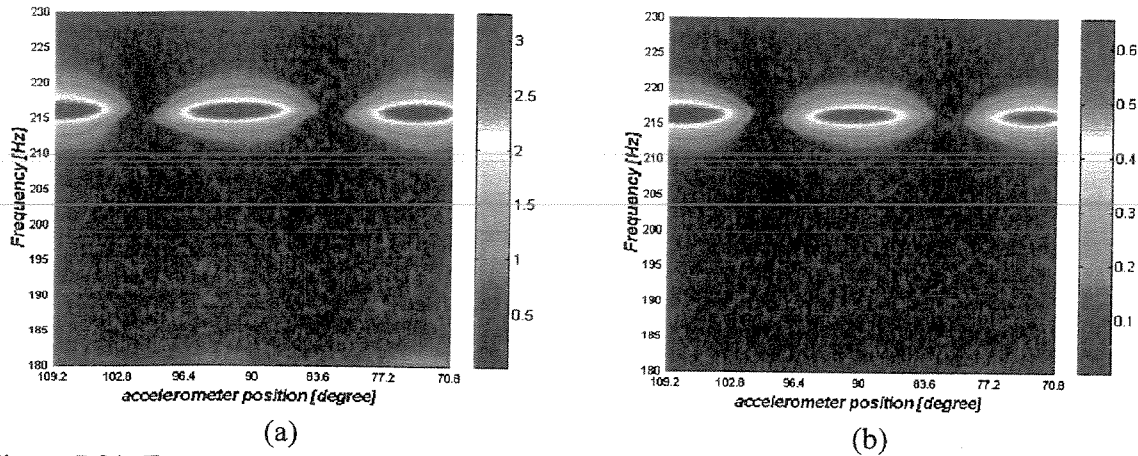


Figure 7.21: Frequency response functions of the accelerometer array using as reference the (a) shaker, and (b) PZT patches. Colormap units in $\text{m/s}^2/\text{V}$.

Figure 7.22 shows the frequency response functions for the microphone array. It can be observed that the acoustic field originated from the structural disturbance is more complicated than the structural field. In Figure 7.22(a) the main pressure is around 213 Hz at the location of microphone 3 while in Figure 7.22(b) the main pressure is around 216 Hz at microphone 1. Therefore, the shaker can excite all the acoustic modes while the PZT patches have only effect in the near field.

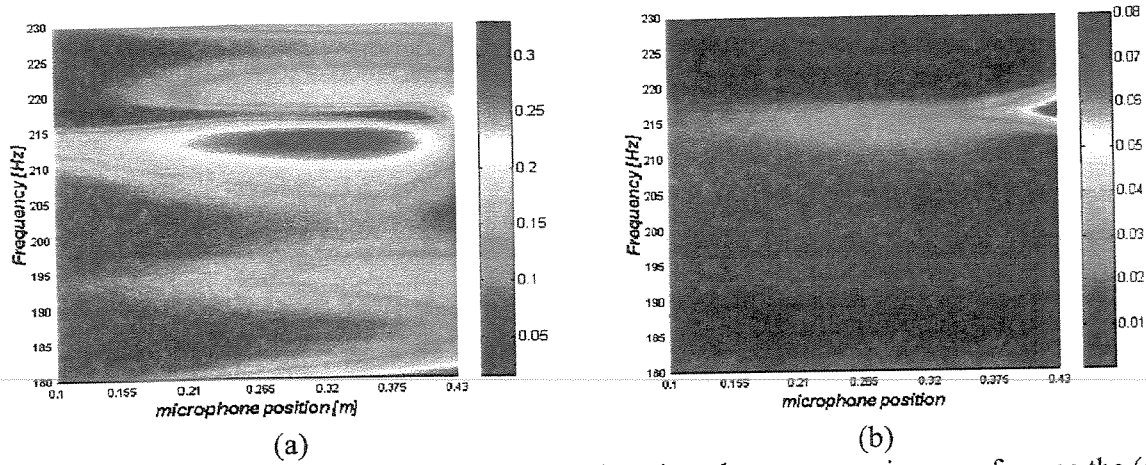


Figure 7.22: Frequency response functions for the microphone array using as reference the (a) shaker, and (b) PZT patches. Colormap units in Pa/V.

Comparing the structural field, Figure 7.21, with the acoustic field, Figure 7.22, it is observed that it is easier to control the vibration in the structure than the sound in the acoustic field because the structural field is more clearly defined than the acoustic field.

7.4.1 Identification of the secondary path

The estimated secondary path, $\hat{S}(z)$, was identified using the ERA (Eigensystem Realization Algorithm) method, Appendix C. The system identification was performed to generate the estimated secondary path $S(z)$ for one input (the reference $x(n)$) and three outputs, which were the responses of the accelerometer, the microphone, and the velocity sensor. The comparison between the measured FRFs and the identified ones are shown in Figure 7.23 and in Table 7.5. The secondary path was estimated using 1 ms as sample time and with 6 poles in the frequency band of 190 Hz to 230 Hz.

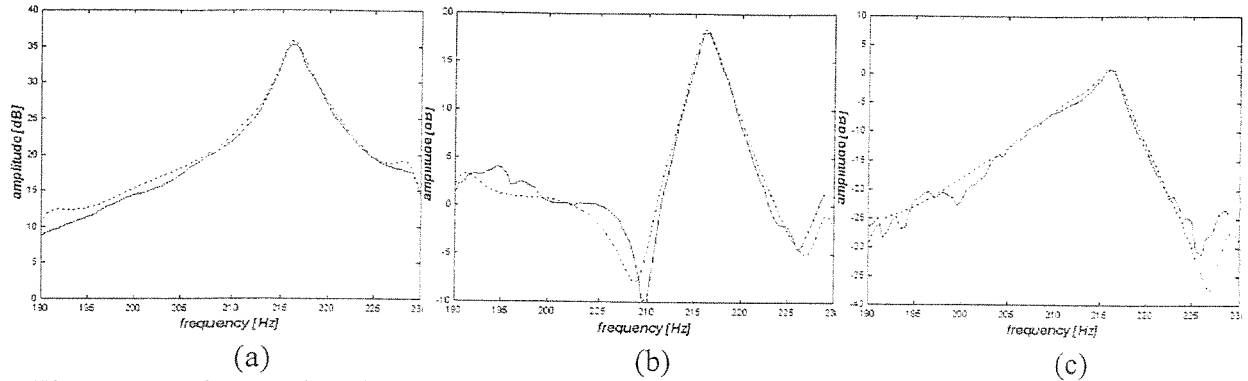


Figure 7.23: Comparison between the measured FRFs and the FRFs estimated using ERA. (a) Relative to the accelerometer at position 4; (b) to the microphone at position 1; (c) to the particle velocity sensor. “—” Measured FRFs, “---” FRFs reconstructed using the identified poles.

Table 7.5: Results of the system identification for the control of the structural disturbances

Freq. [Hz]	Damping	MCF
190.51	0.0100	0.9853
203.87	0.0451	0.9820
213.17	0.0145	0.9891
216.04	0.0057	0.9998
218.17	0.0190	0.9952
228.96	0.0053	0.9938

7.4.2 Theoretical comparison of multiple error-sensing strategies for a single frequency

In this section, the performance of the normalized filtered-X LMS in the time domain using the error sensors indicated in Figure 7.19 will be analyzed. The error-sensing strategy, the position and the number of the error sensors to control the structural disturbance at 216 Hz are analyzed. As the dSPACE 1102 control board has only 4 input channels, and one of them is reserved for the reference signal, a maximum of three inputs can be used in the normalized filtered-X LMS implementation. The formulation to the control algorithm can be seen in chapter 4 and the implementation in the Appendix C. The results using the optimal solution to the filtered-X LMS in the time domain are presented in Figure 7.24, Figure 7.25, and Figure 7.26.

The “error sensor set” represents a set of error sensors used in the control (Table 7.6). They were formed using the linear combination of all possible sensors in Table 7.6. The error sensor

set 10, for instance, for a set of 3 error sensors, consists of the error sensors at positions 1, 4 and 5.

The attenuation in the energy was defined as the ratio of the energy measured over the sensors with the system without control and the energy over the sensors with the system controlled. The energy over the sensors was simply the sum of the energy contribution of each sensor to the global energy.

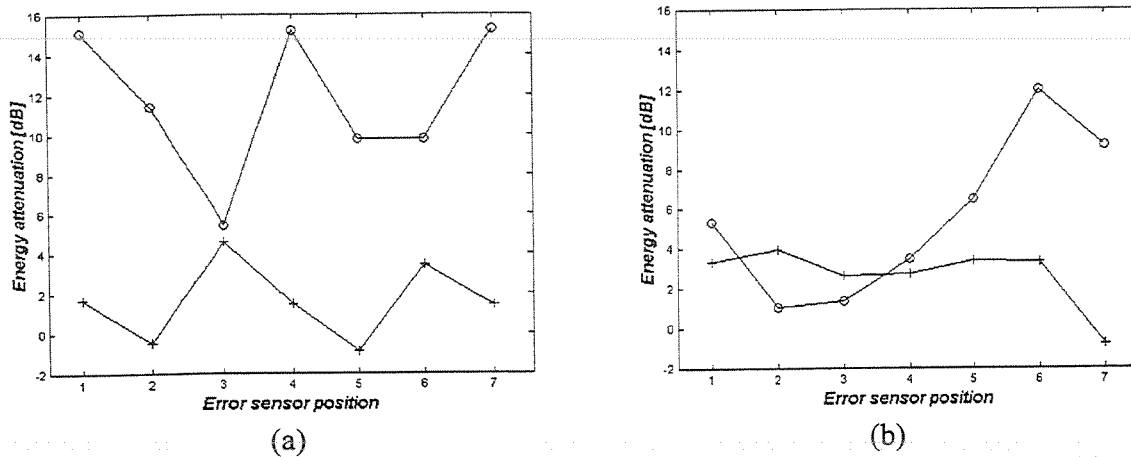


Figure 7.24: Attenuation in the energy when one error sensor is applied. Using (a) accelerometers, and (b) microphones as error sensors. Attenuation in the -o- structural kinetic energy, and +- acoustic potential energy.

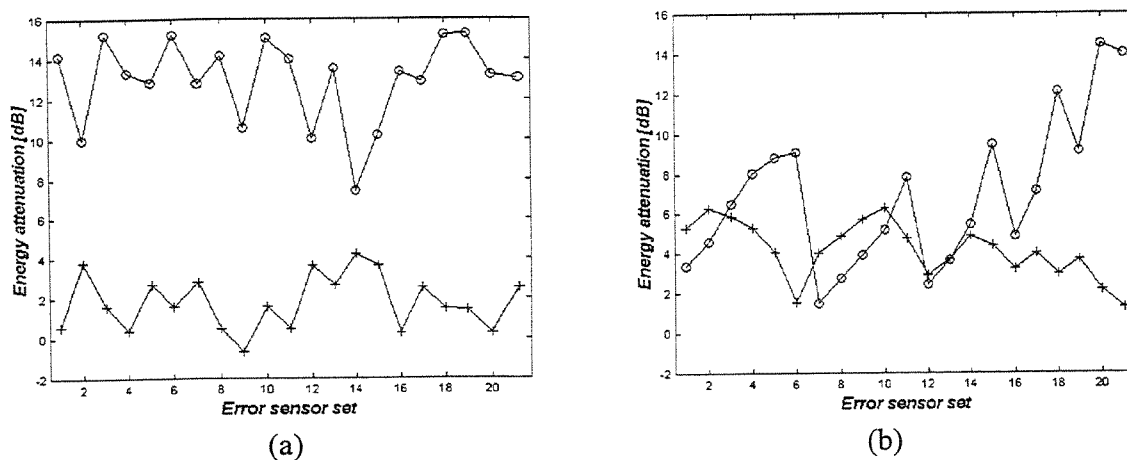


Figure 7.25: Attenuation in the energy when two error sensors are applied. Using (a) accelerometers, and (b) microphones as error sensors. Attenuation in the -o- structural kinetic energy, and +- acoustic potential energy.

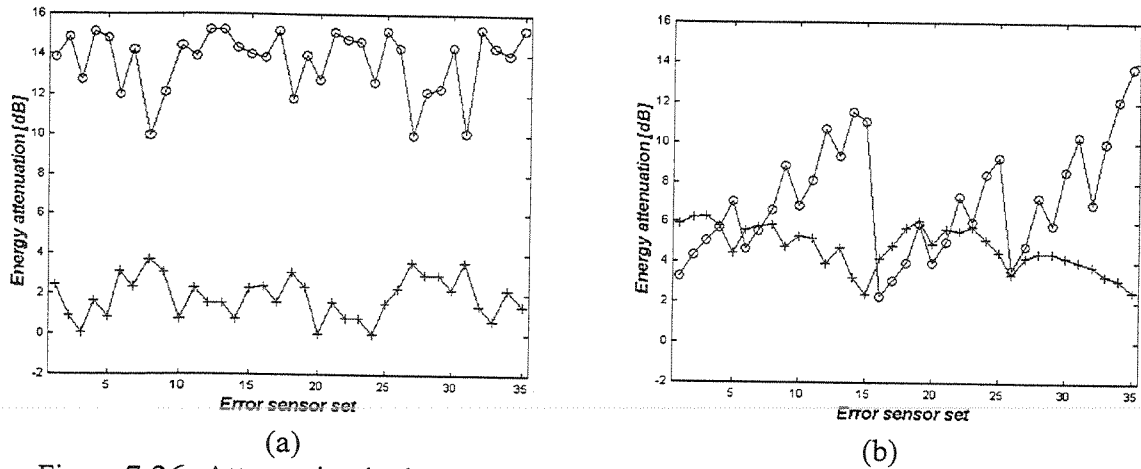


Figure 7.26: Attenuation in the energy when three error sensors are applied. Using (a) accelerometers, and (b) microphones as error sensors. Attenuation in the -o- structural kinetic energy, and -+- acoustic potential energy.

It is observed comparing Figure 7.24, Figure 7.25, and Figure 7.26 that it is better to use the structural error sensing to control the vibration in the structure, and to use the acoustic error sensing to control the sound radiated into the cylindrical cavity although some good kinetic energy attenuation was achieved using acoustic error sensing near the cylindrical wall, as the case in Figure 7.24(b) that represents the microphone located at position 6. Thus, it is better to use AVC to control the vibration in the structure and to use ASAC to control the sound in the acoustic field.

Moreover, increasing the number of error sensors the control method becomes independent of the sensor positions, although the best attenuation level achieved using one-error sensor is not different from the best attenuation level achieved using more error sensors. Therefore, if the system response is precisely described, the controller can be implemented successfully using only one error sensor.

There was only one velocity sensor and its position was fixed. It produced an attenuation of 9.8 dB in the structural kinetic energy and 3.4 dB in the acoustic potential energy. Therefore, the attenuation produced by the velocity sensor is somewhere in between the attenuation produced by the accelerometer and the attenuation produced by the microphone in both cases.

Table 7.6: Error sensor sets

Error Sensor Set	2 error sensors	3 error sensors	4 error sensors
1	1-2	1-2-3	1-2-3-4
2	1-3	1-2-4	1-2-3-5
3	1-4	1-2-5	1-2-3-6
4	1-5	1-2-6	1-2-3-7
5	1-6	1-2-7	1-2-4-5
6	1-7	1-3-4	1-2-4-6
7	2-3	1-3-5	1-2-4-7
8	2-4	1-3-6	1-2-5-6
9	2-5	1-3-7	1-2-5-7
10	2-6	1-4-5	1-2-6-7
11	2-7	1-4-6	1-3-4-5
12	3-4	1-4-7	1-3-4-6
13	3-5	1-5-6	1-3-4-7
14	3-6	1-5-7	1-3-5-6
15	3-7	1-6-7	1-3-5-7
16	4-5	2-3-4	1-3-6-7
17	4-6	2-3-5	1-4-5-6
18	4-7	2-3-6	1-4-5-7
19	5-6	2-3-7	1-4-6-7
20	5-7	2-4-5	1-5-6-7
21	6-7	2-4-6	2-3-4-5
22	-0-	2-4-7	2-3-4-6
23	-0-	2-5-6	2-3-4-7
24	-0-	2-5-7	2-3-5-6
25	-0-	2-6-7	2-3-5-7
26	-0-	3-4-5	2-3-6-7
27	-0-	3-4-6	2-4-5-6
28	-0-	3-4-7	2-4-5-7
29	-0-	3-5-6	2-4-6-7
30	-0-	3-5-7	2-5-6-7
31	-0-	3-6-7	3-4-5-6
32	-0-	4-5-6	3-4-5-7
33	-0-	4-5-7	3-4-6-7
34	-0-	4-6-7	3-5-6-7
35	-0-	5-6-7	4-5-6-7

7.4.3 Other possible control schemes

In Figure 7.27 and Figure 7.28 other possible control methods, which could not be implemented in real time due to limitations of the control board used, are shown. The first one is the filtered-X LMS using four error sensors. The second one is the ASIC-PP that cannot be implemented due to the fact that the control board is not fast enough (the ASIC is implemented in the frequency domain).

Figure 7.27 (a) and (b) show that the filtered-X LMS with 4 error sensors achieved a better result than the other three (Figure 7.24, Figure 7.25, and Figure 7.26). Using the ASIC, Figure 7.28, the structural error sensing was more independent from the error sensor position than the other control methods. The error sensor sets using 4 error sensors are in Table 7.6; the ASIC used the two-error-sensor sets.

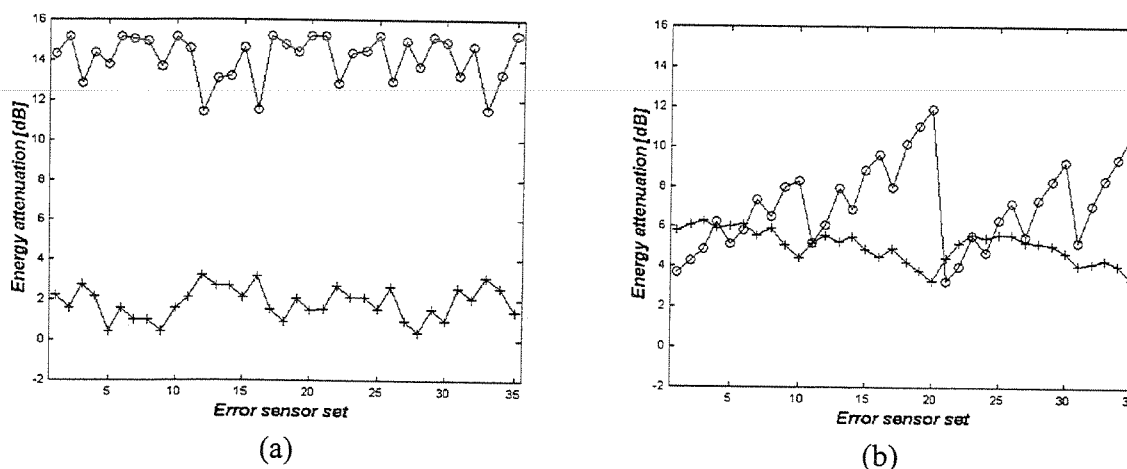


Figure 7.27: Attenuation in the energy when four error sensors are applied. Using (a) accelerometers, and (b) microphones as error sensors. Attenuation in the -o- structural kinetic energy, and +- acoustic potential energy.

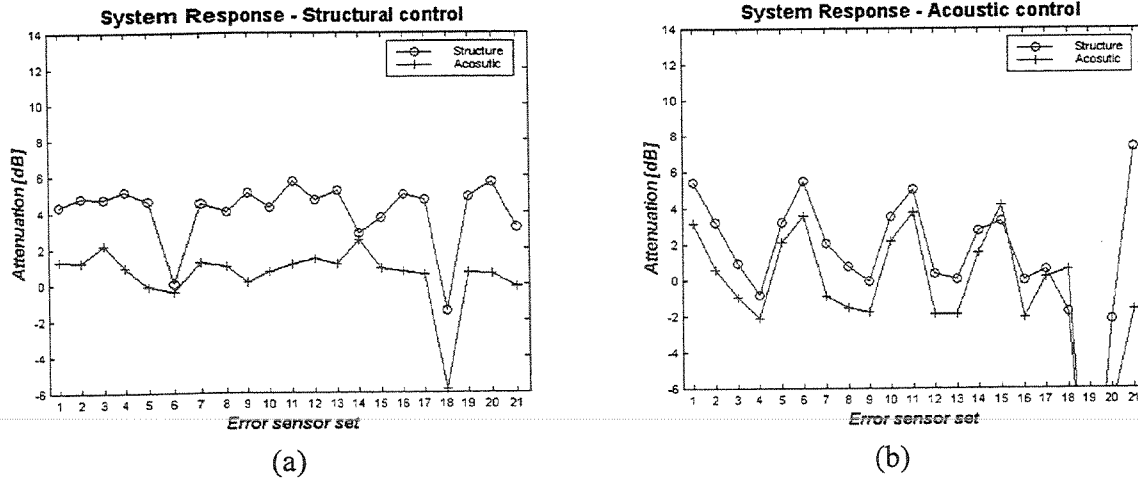


Figure 7.28: Attenuation in the energy when the ASIC is implemented. Using (a) accelerometers, and (b) microphones as error sensors. Attenuation in the -o- structural kinetic energy, and +- acoustic potential energy.

7.4.4 Theoretical comparison of single channel controlled for narrow band excitation

In this section, the performance of the normalized filtered-X LMS controller using three different error-sensing strategies, i.e., the accelerometer located at position 4, the microphone located at position 1, and the velocity sensor located between the microphones at positions 1 and 2 (Figure 7.19), is investigated.

Figure 7.29 shows the optimal control signals computed for the three error-sensing strategies. It can be observed that they differ substantially. Therefore, it is expected that the attenuation in the energy will be different too. Moreover, it can be noticed that the level of the secondary source for the optimal solution, $y(n)$, is greater than the level of the original structural disturbance, $x(n)$, which means that more energy is necessary from the secondary source to control the disturbance than it was necessary to introduce it originally. However, this observation cannot be generalized because the energy necessary for the secondary source to control the primary disturbance depends upon to the gains of the power amplifiers.

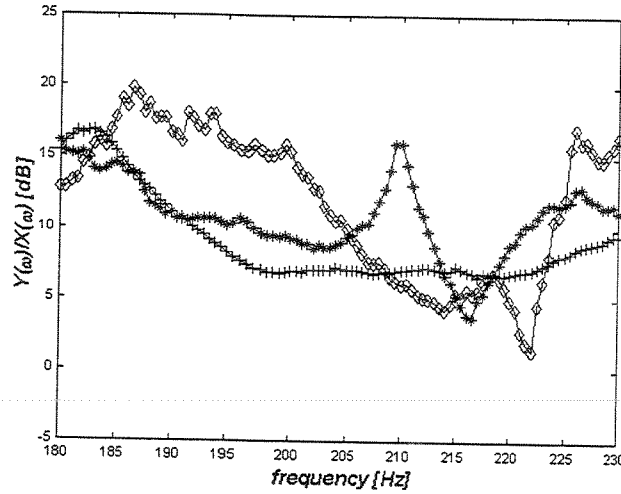
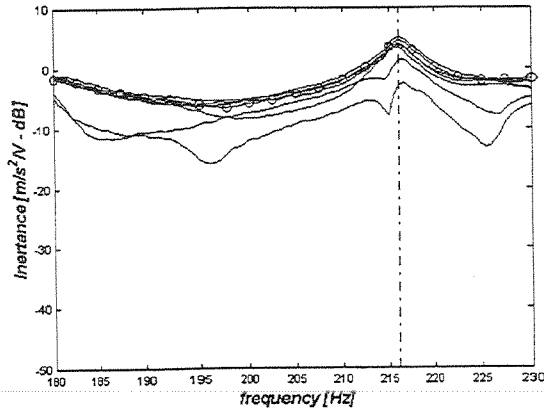


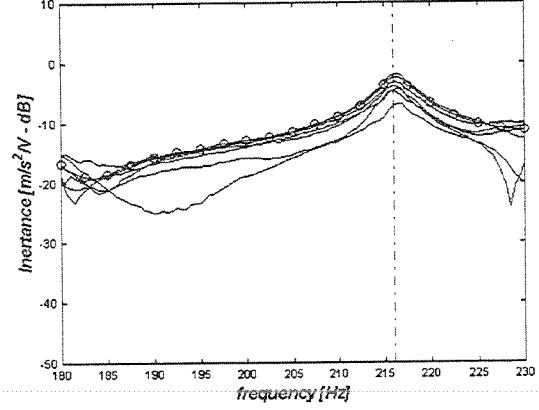
Figure 7.29: Optimal control signal generated using the three error-sensing strategies. Using as error sensor the $-+-$ accelerometer at position 4; $-*-$ microphone at position 1; $-□-$ velocity sensor.

Another important fact observed in Figure 7.29 is that using the accelerometer as error sensor a more uniform optimal control signal spectrum is produced in contrast to the other error-sensing strategies. This behavior is related to the frequency response functions between the error sensors and the actuators, which are more uniform for the accelerometer than for the other error sensors in this frequency range.

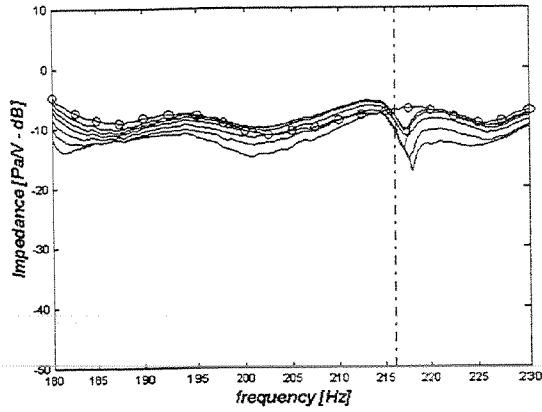
The peaks and notches observed in Figure 7.29 can be related to the frequency responses of the error sensor when the optimal control law is applied. In order to make this analysis clear, a zoom of Figure 7.20 is shown in Figure 7.30. When the FRF from the shaker (disturbance source) has a notch, for example in the case of the velocity sensor at the frequency of 223 Hz, the optimal control law will probably exhibit a notch also ($P(\omega)$ in the numerator of the optimal solution). However, if the notch is in the FRF from the PZT patches (control source), the optimal control law will probably have a peak, as it happens using the velocity sensor at frequency of 210 Hz ($S(\omega)$ in the denominator of the optimal solution).



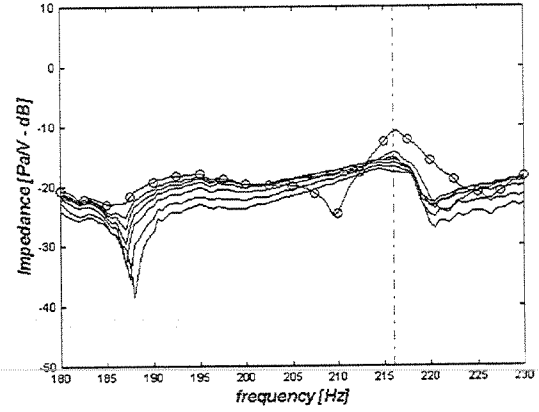
(a)



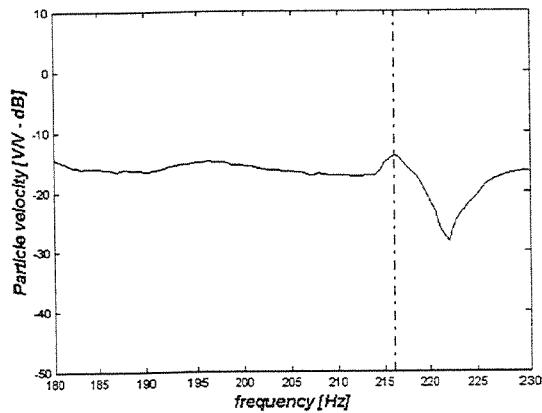
(b)



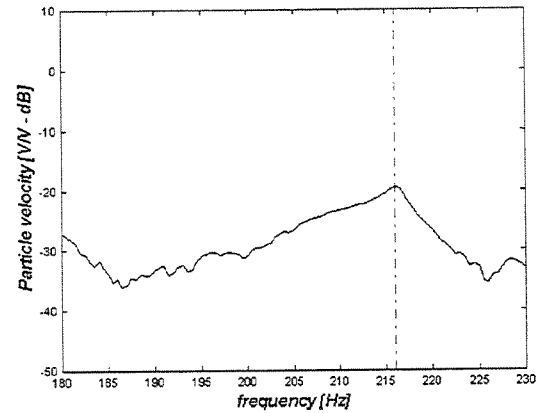
(c)



(d)



(e)



(f)

Figure 7.30: Frequency response functions measured at the sensors indicated in Figure 7.19 to narrow band. (a) Between the accelerometers and the shaker, (b) between the accelerometers and the PZT patches, (c) between the microphones and the shaker, (d) between the microphones and the PZT patches, (e) between the velocity sensor and the shaker, (f) between the velocity sensor and the PZT patches. —o— indicates the FRFs used to calculate the optimal solution to the secondary source

The analysis of the optimal control signal, Figure 7.29, is important. It can be observed that, for frequencies around 210 Hz, when the microphone is selected as error sensor, the attenuation in the energy level is small (deep in Figure 7.30) and, at this frequency, more energy must be introduced in the system to drive the error sensor to zero (peak in Figure 7.29). On the other hand, frequencies where the optimal control signal has a low energy level (Figure 7.29) represent the best frequencies to implement the controller, because a low energy level is sufficient to control the system at those frequencies and a higher attenuation is achieved (Figure 7.30).

Figure 7.31 shows the attenuation of the structural kinetic energy and of the acoustic potential energy. Both energies were estimated by summing the squared magnitudes of the seven signals measured with the sensor array shown in Figure 7.19. It can be observed that the error-sensing strategies achieved different results. The attenuation in the structural kinetic energy was greater at frequencies near 216 Hz, while the attenuation in the acoustic potential energy was not. This fact is directly related to the frequency responses shown in Figure 7.20 or Figure 7.30. As predicted before, where the control actuator has a good response level (a peak in the FRF) the energy level was attenuated, and where the actuator has a low response level (a deep in the FRF) low attenuation or even amplification was obtained.

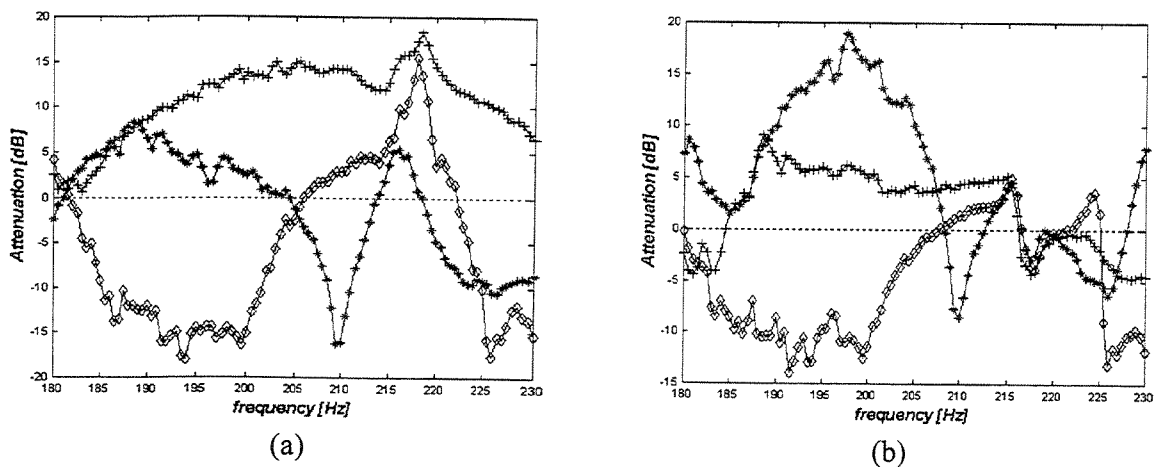


Figure 7.31: Attenuation in the (a) kinetic energy and (b) potential energy. Using as error sensor the +- accelerometer at position 4; -* microphone at position 1; -o- velocity sensor.

It is important to note that an attenuation below zero dB means, in fact, amplification. This happens when the energy level of the vibro-acoustic system when the control is acting was amplified, although the error sensor level was driven to zero. Amplification of the system energy level was observed at frequencies where great amplification in the optimal control signal spectrum was found. This fact can be observed clearly by comparing Figure 7.29 and Figure 7.31 at 210 Hz for the particle velocity error sensor.

Another important result is that the control method achieved a good performance in the frequency range near 216 Hz, where most of the energies were attenuated or remained at the same level.

Figure 7.32 shows the normalized response of the structure (acceleration for a normalized input signal) and of the acoustic field (pressure for a normalized perturbation input signal) when the optimal control law is applied at the frequency of 216 Hz. It can be noticed that the greatest attenuation in the inertance is achieved by structural error sensing (accelerometer), while for the acoustic impedance it is not clear what error sensing strategy is better. It should be noted that each error sensing strategy produced zero response at the error sensor (actually reduced it to the background noise level). Another important observation is that the results obtained with the particle velocity sensor are somewhere between the results achieved using the accelerometer and those obtained using the microphone.

The accelerometer located at position 4 yielded the best results because it was placed where the amplitude was at a maximum (at a wave peak). This situation is repeated for the accelerometers located at positions 1 and 7. As for the acoustic field, Figure 7.32(b), it doesn't present the spatially periodic feature of Figure 7.32(a), making it more difficult to find out the best location of the error sensor.

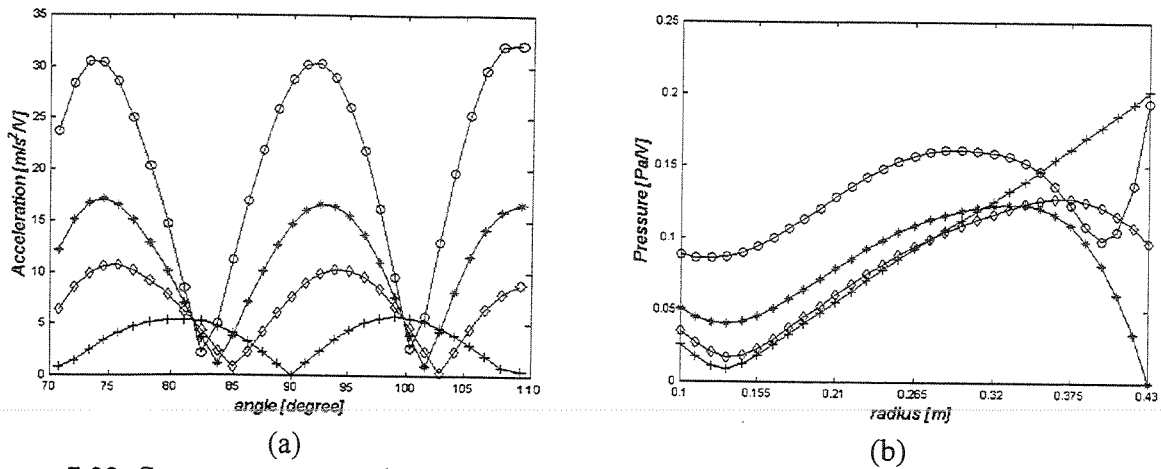


Figure 7.32: System response when the optimal control signal is applied at the frequency of 216 Hz measured with (a) accelerometers, and (b) microphones. -o- No control and controlled using as error sensor the +- accelerometer at position 4; -* microphone at position 1; -□ particle velocity sensor.

In contrast to the frequency of 216 Hz, results at the frequency of 210 Hz, shown in Figure 7.33, indicate that this is not a good frequency to control, because amplification happened when the error sensor was a microphone at position 1. This had been predicted in the preceding discussion.

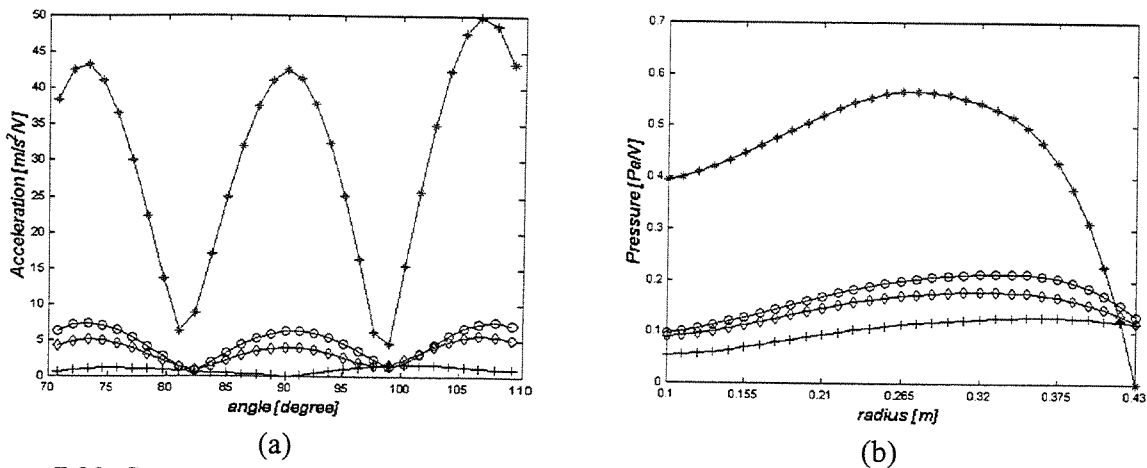


Figure 7.33: System response when the optimal control law is applied to the frequency of 210 Hz in the (a) accelerometers, and (b) microphones. -o- No control and controlled using as error sensor the +- accelerometer at position 4; -* microphone at position 1; -□ velocity sensor.

7.4.5 Experimental comparison of single channel control at a single frequency

The normalized filtered-X LMS controller in the time domain with one error sensor using structural error sensing (accelerometer at position 4) and acoustical error sensing (microphone at position 1 and velocity sensor located between the microphones at locations 1 and 2) was implemented for the tonal frequency of 216 Hz. The results are presented in Figure 7.34, where a good agreement with the theoretical results presented in Figure 7.32 is observed.

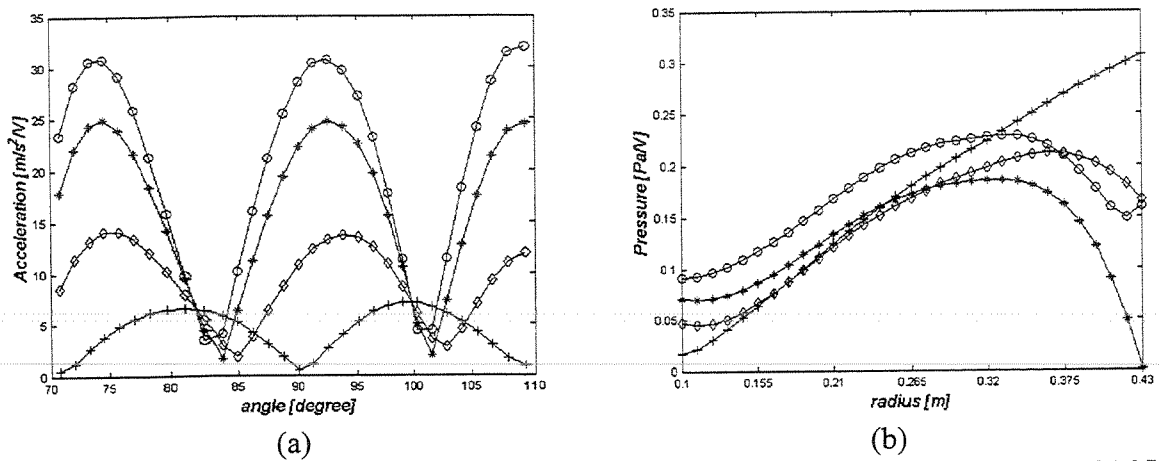


Figure 7.34: Experimental responses to the adaptive control using one error sensing at 216 Hz measured with (a) accelerometers and (b) microphones; -o- No control and controlled using as error sensor the +- accelerometer at position 4; -* microphone at position 1; -□- velocity sensor.

In Figure 7.35 and Figure 7.36, the signals acquired with the dSPACE 1102 control board during the control applications are shown. It can be noticed that great attenuation is achieved in the signal levels for the three error sensors. The signal levels are very different from each other in amplitude due to the fact that the error sensors have different sensibilities and the greatest one is that of the velocity sensor. Therefore, the velocity sensor is very suitable in this application. Besides, some noise in the acoustic sensing (microphone and velocity sensor) was observed with and without control, while the signal from the accelerometer was the cleanest one. This is related to the acoustic field being more influenced by environmental noise. The control law, Figure 7.36,

was larger for the structural error sensing and smaller for the microphone. So, a small energy level is necessary to control the pressure compared with the other error-sensing strategies.

It is interesting to note that in Figure 7.35, the signal from the control board were captured in distinct instant times, because of this the phase between the signals should be ignored.

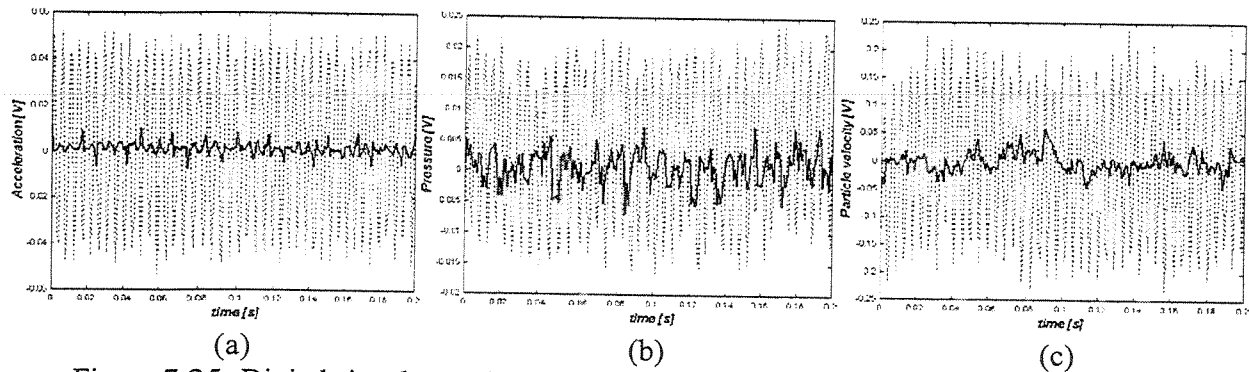


Figure 7.35: Digital signals acquired with the control board before and after the control application – (a) signal from accelerometer at position 4; (b) signal from the microphone at position 1; (c) signal from the velocity sensor; “.....” control off, “—” control on.

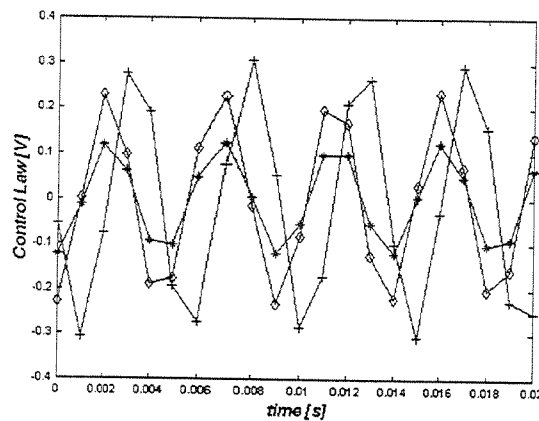


Figure 7.36: Control signal generated with the control board. Using as error sensor the +- accelerometer, -* microphone, and -v velocity sensor.

7.4.6 Experimental comparison of single channel control for narrow band random disturbance

A narrow band random noise in the frequency range 208-224 Hz was used as a structural disturbance signal. The error sensors were the accelerometer located at position 4, the microphone located at position 1, and the velocity sensor located between the microphones located at positions 1 and 2. The comparison of the results obtained with a normalized filtered-X LMS controller using structural and acoustic error sensing is shown in Figure 7.37. It can be observed that the attenuation in the kinetic energy is greater than the attenuation in the potential energy, as was predicted in the theoretical analysis of the previous section (Figure 7.31).

Another interesting fact is that all the error sensing strategies clearly achieved the best performance near the frequency of 216 Hz for the attenuation of the structural kinetic energy (Figure 7.37(a)) while it wasn't so for the acoustic potential energy (Figure 7.37(b)).

In addition, the best error sensor for the attenuation of the structural kinetic energy was the accelerometer and the worst was the microphone. However, it is not clear what error sensor achieved the best performance in the attenuation of the acoustic potential energy density.

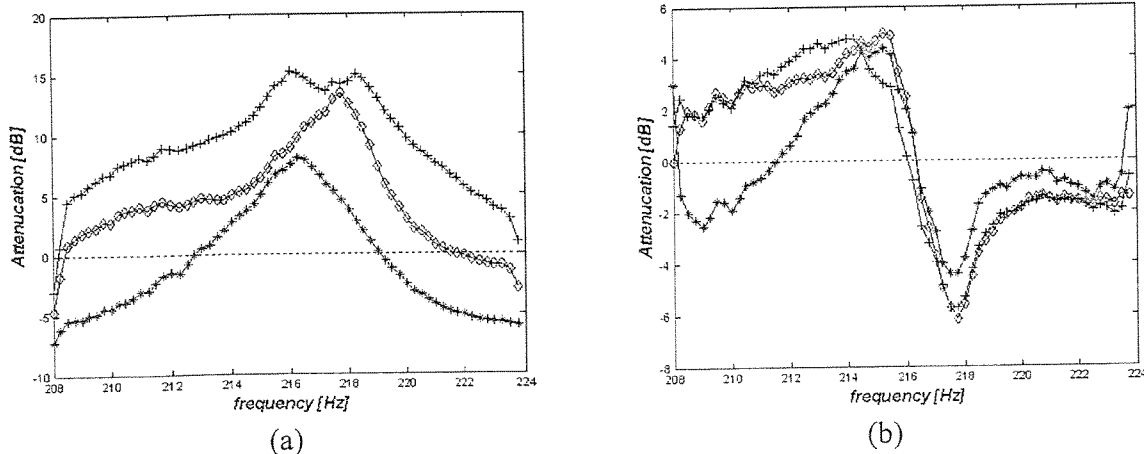


Figure 7.37: Attenuation in the (a) structural kinetic energy and (b) acoustic potential energy.

Using as error sensor the -+- accelerometer at position 4; -* microphone at position 1; -v- velocity sensor.

In Figure 7.38 the normalized structural response can be observed. Great amplification can be noticed at the frequencies around 216 Hz, Figure 7.38(a), for the uncontrolled system. When the accelerometer located at position 4 was selected as error sensor, great attenuation was achieved, Figure 7.38(b). However, when the other two error sensors were selected as error sensors, Figure 7.38(c and d), good levels of attenuation were achieved only around for frequencies close to 216 Hz.

Thus, it can be stated that the best choice was to use the accelerometer to control the vibration in the structure. If it was not possible to use accelerometers, the velocity sensor could be used as a suitable alternative. The microphone attenuated the vibration in the structure around 216 Hz although it increased the vibration at others frequencies, mainly at frequencies higher than 218 Hz. This happened due to the shape of the FRF, which has deeps before and after the resonance peak.

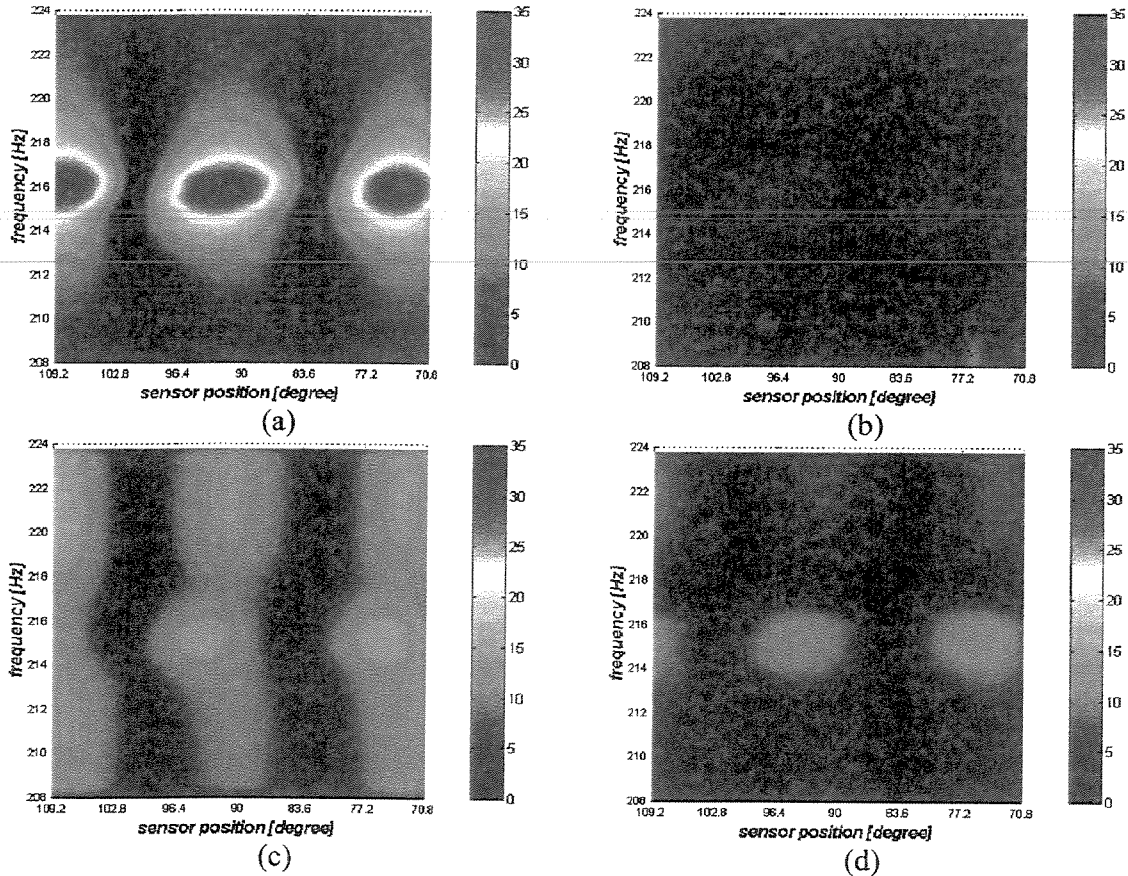


Figure 7.38: Normalized structural response. (a) No control and controlled using as the error sensor: (b) the accelerometer at position 4, (c) the microphone at position 1, and (d) the particle velocity. Colormap units in $\text{m/s}^2/\text{V}$.

In the normalized acoustic field response, Figure 7.39, it is observed that the greatest amplitude is around 213 Hz and not near the cylindrical shell, as was predicted in the acoustic modal analysis. This illustrates the low repeatability of the acoustic measurements commented before.

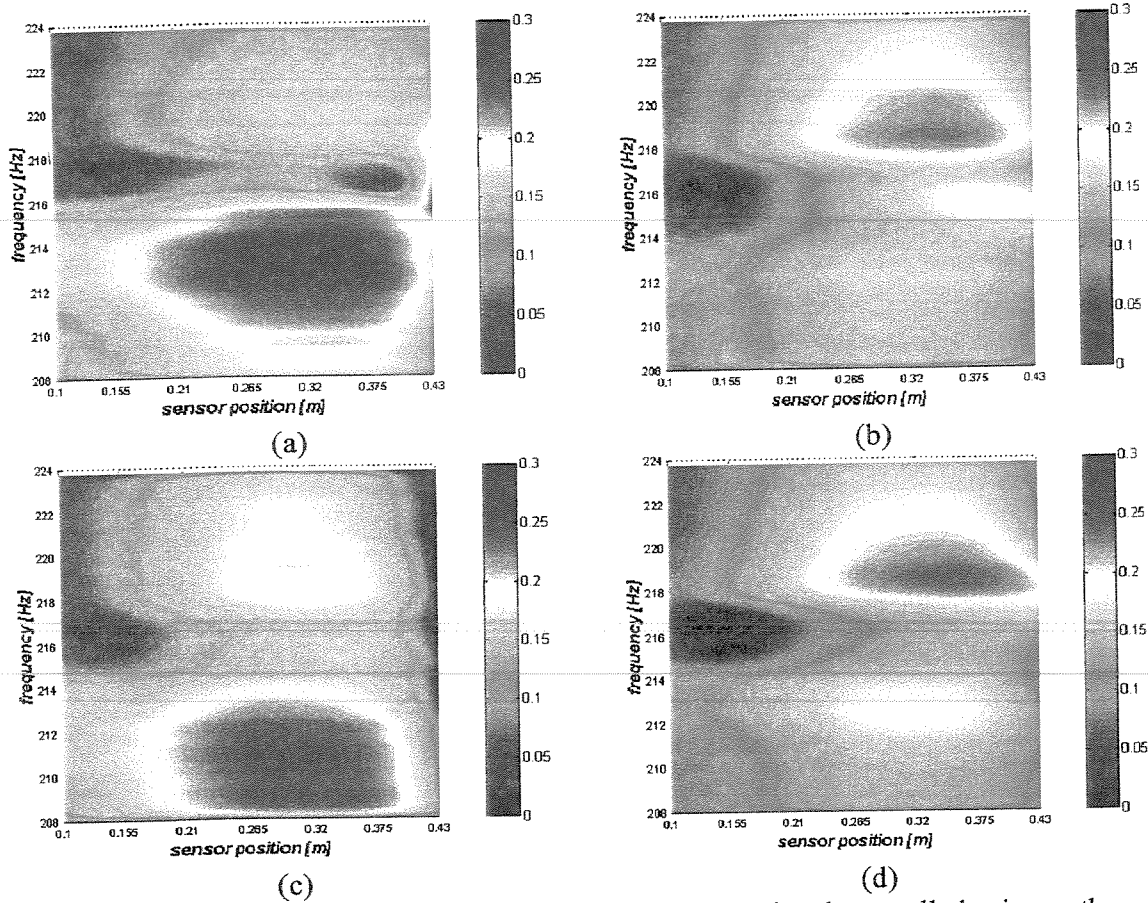


Figure 7.39: Normalized acoustic field response. (a) No control and controlled using as the error sensor, (b) the accelerometer at position 4, (c) the microphone at position 1, and (d) the particle velocity. Colormap units in Pa/V.

The best error sensing transducer to control the sound radiated to the acoustic cavity was the accelerometer. It reduced the pressure more uniformly while the microphone and the velocity sensor used as error sensors attenuated only the pressure close to the inner surface of the cylindrical shell.

Again, the performance of the velocity sensor was generally between the performance of the accelerometer and that of the microphone.

7.4.7 Conclusion

This investigation allowed observing theoretically and experimentally the application of a normalized filtered-X LMS in the time domain controller using structural and acoustical error sensing to attenuate the vibration in a structure and the noise in the acoustical cavity.

It was shown that it is easier to control the vibration in the structure than the noise radiated to the acoustic cavity. Besides, it was possible to achieve around 15 dB of attenuation in the structural kinetic energy in contrast to less than 4 dB of attenuation in the acoustic potential energy in the acoustic cavity. In addition, the best configuration to control the vibration is not the best configuration to control the noise; thus, different error sensing strategies should be used for each cost function. Moreover, there is no necessity of using more than one error sensor because single and multiple error sensor controllers achieved the same maximum attenuation in the energy; thus, the simplest case can be used successfully.

The AVC technique showed to be the best strategy to control the vibration in the structure (structural kinetic energy). The ASAC using microphones as error sensor and AVC seem to perform equally in the control of the pressure radiated to the cylindrical cavity. The performance of the particle velocity sensor (an acoustic kinetic error sensor) stayed between the performances of the accelerometer and the microphone.

7.5 Comparison between the ASAC and AVC methods for acoustic disturbances

The acoustic disturbance was implemented using a loudspeaker (horn drive) located at the same position as the shaker, which was removed first. During the implementation in real time, it was observed that great acoustic power from the loudspeaker was necessary for the error sensors to “see” some signal that could be used as error signal in the controller. Therefore, only tonal control could be implemented. Besides, the signal from the sensors in Figure 7.19 could not be used as error sensors because the signal levels were too small. Thus, it was necessary to move the error sensors to the lower part of the cavity, closer to the acoustic source, which was located

under the cylinder, Figure 7.40. The accelerometer was placed on the outside surface of the cylinder and immediately in front of the acoustic source, the microphone array and the particle velocity sensor inside the cavity were moved of 180° . The transducer used to control the acoustic disturbance were the same used to control the structural disturbance, but placed in the lower part of the cavity (Figure 7.40).

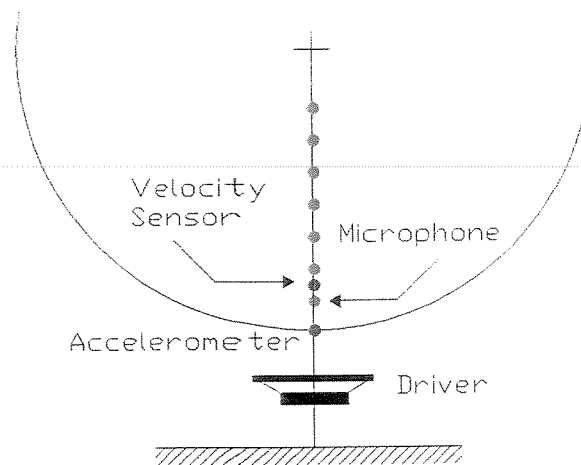


Figure 7.40: Position of the error sensors under acoustic disturbances

The frequency response functions between the error sensors and the PZT patches can be seen in Figure 7.41, where a large amplification can be noticed at the frequency of 216 Hz, as expected. In addition, many peaks are found, indicating that more difficulty is expected to control the acoustic disturbance when compared with the structural disturbance.

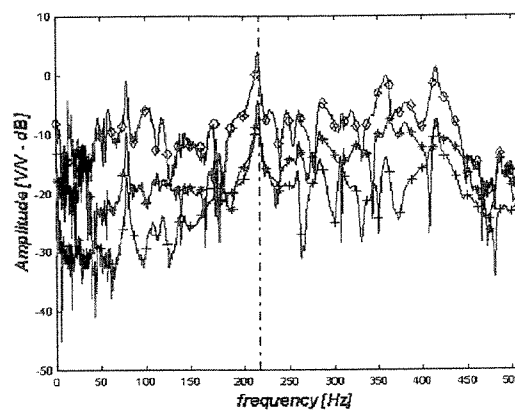


Figure 7.41: Frequency response functions measured in the error sensors using as reference the electrical signal sent to the PZT patches; -o- accelerometer; +- microphone; -* velocity sensor.

7.5.1 Identification of the secondary path

The estimated secondary path, $\hat{S}(z)$, was also identified using ERA, Appendix C. The system identification was performed to generate the estimated secondary path for one input (the reference $x(n)$) and three outputs that are the responses measured with the accelerometer, the microphone, and the velocity sensor. The comparison between the measured FRFs and the identified ones are shown in Figure 7.42 and the identified poles are given in Table 7.7. The secondary path was estimated using 1 ms as sample time.

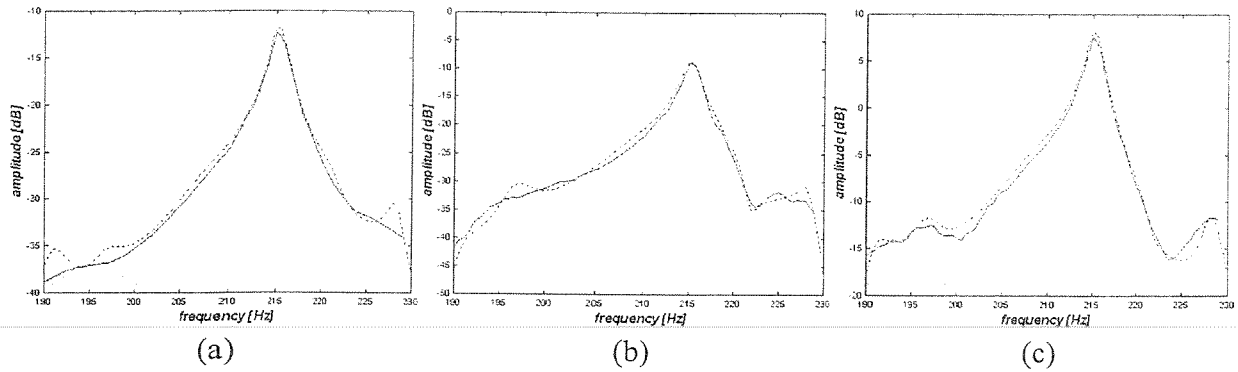


Figure 7.42: Comparison between the measured FRFs and the estimated by the ERA. (a) For the accelerometer; (b) For the microphone at position 1; (c) for the velocity sensor; — Measured FRFs, FRFs reconstructed using the identified poles.

Table 7.7: Results of the system identification for the control of the acoustic disturbances.

Freq [Hz]	Damping	MCF
181.18	0.0045	0.9691
196.13	0.0217	0.9913
211.57	0.0282	0.9965
215.57	0.0040	1.0000
220.38	0.0048	0.9804
227.57	0.0054	0.9810

7.5.2 Experimental comparison of single channel for tonal perturbation at 216 Hz

The results obtained with the normalized filtered-X LMS in the time domain controller are shown in Figure 7.43, where it can be noticed that the best control of the noise in the cylindrical cavity was achieved by using the microphone as error sensor. Besides, it is better to locate the error sensor near the region where the sound is introduced. Moreover, the structural sensing control achieved little attenuation. This fact shows that controlling purely the vibration at only one location on the structure surface does not imply that the structure stopped the sound transmission, because there are other transmission paths for the noise. In addition, the velocity sensor achieved good attenuation but the attenuation was smaller than the attenuation achieved by the microphone. This may have several reasons, but the most acceptable is the quality of the signal measured by the particle velocity sensor, which was noisier than that of the microphone in this case (Figure 7.44(b) and (c)).

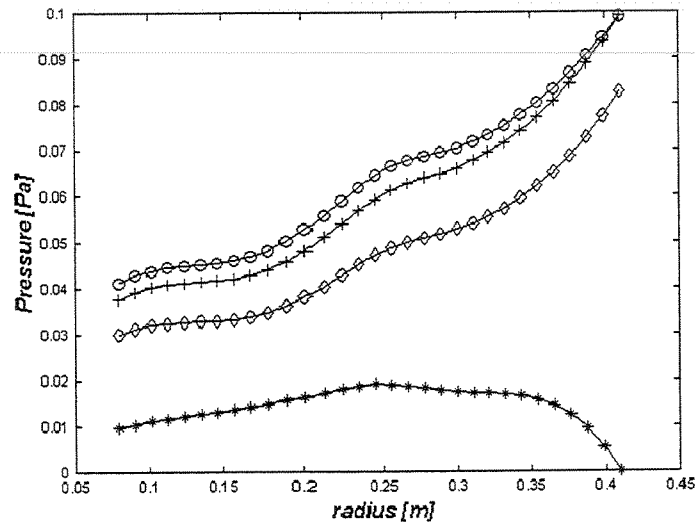


Figure 7.43: Impedance measured by the microphone array. -o- No control and controlled using the +- accelerometer; -* -microphone; -□- particle velocity sensor.

The great attenuation achieved using the microphone as error sensor is related to the path of the noise going from the loudspeaker to the interior of the acoustic cavity. The first path is

through airborne transmission as the cavity is not sufficiently closed and has small openings to the exterior. The second path is the structure-borne transmission that is related to the vibration of the cylindrical shell (fluid/structure interaction), but the signal level of the accelerometer was very low, so this transmission path wasn't important. The last one is the transmission that is related to the compression waves passing through the thickness of the cylindrical shell, which is negligible in this case. Therefore, the mechanism of the sound transmission acting when the acoustic disturbance was applied in this case is more related to the airborne path, since that the accelerometer signal level was very low in this case, which can be observed comparing Figure 7.44(a) with Figure 7.35(a).

The signals captured with the dSPACE 1102 control board, Figure 7.44, show that the signals from the accelerometer and the velocity sensor are contaminated with noise, and the best signal to be used as error sensor is that of the microphone.

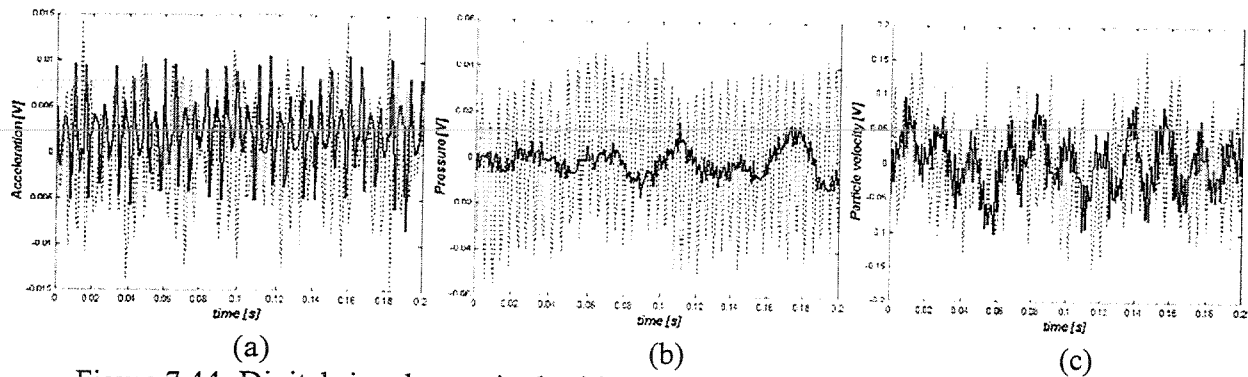


Figure 7.44: Digital signals acquired with the control board before and after the control application. (a) Signal from accelerometer at position 4; (b) signal from the microphone at position 1; (c) signal from the velocity sensor; ---- control off; — control on.

Moreover, Figure 7.45 shows that the amplitude of the control signal using the microphone as error sensor had higher amplitude than for the other error sensors. Another interesting fact is that the amplitude level of the control signal was equal for the accelerometer and for particle velocity sensor, but the particle velocity sensor achieved better levels of attenuation than the accelerometer. Thus, if were impossible to use the microphone the best choice would be the velocity sensor as error sensor. It is interesting to note that in Figure 7.45, the signals from the

control board were captured in distinct instants of time and, because of this, the phase between the signals should be ignored.

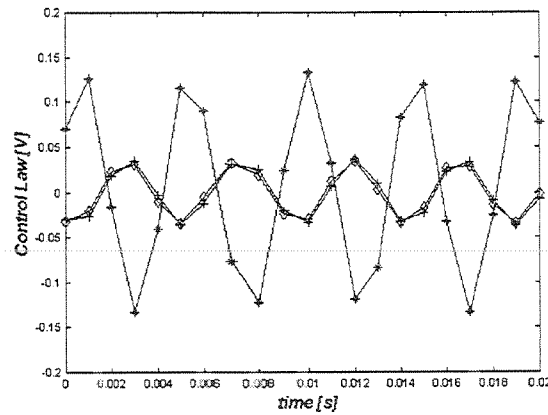


Figure 7.45: Control signal captured from the control board in distinct instant times during the control application. Where was implemented using as error sensor the +- accelerometer, -* microphone, and -□- velocity sensor.

7.5.3 Conclusion

It was observed that it is more difficult to excite the structure and the acoustic cavity using an acoustic source than using a vibration source. It was necessary to move the error sensors to the bottom part of the cylinder to capture some signal that could be used as error signal. Thus, it was not possible to measure the frequency response functions between the driver (acoustic source) and the sensors in the upper part, so that the theoretical analysis performed before couldn't be used with the acoustic source.

On the other hand, the best control configuration was achieved using the microphone as error sensor, and the accelerometer achieved the poorest result. Again, the velocity sensor stayed between the performance of the microphone and the performance of the accelerometer. Therefore, if the noise inside the cylindrical cavity is generated by an external acoustic source, it is better to apply the minimization of the potential energy density (microphone as error sensor), i.e., the ASAC technique.

7.6 General Conclusions

The most important observation in this investigations was that if disturbance in the cylindrical acoustic cavity is generated by structural vibrations, it is better to apply the AVC than the ASAC, or simply, to apply structural error sensing instead of acoustic error sensing. However, if the disturbance in the cylindrical acoustic cavity is generated by an external acoustic source, the best way is to apply acoustic error sensing instead of structural error sensing, i.e., to apply the ASAC instead of the AVC. Moreover, it is probable that if the disturbance is generated by vibration of the structure and by an external acoustic source, the best way to attenuate the noise in the acoustic field would be to chose the velocity sensor as error sensor, or to use a mix of structural error sensing and acoustic error sensing.

This simple experiment with a cylinder allowed setting a guideline for the decision regarding the use of AVC and ASAC controllers in aircraft. However, given that the experimental setup may be very far from the reality of an aircraft fuselage, this conclusion must be taken with due care.

In a real situation, it is necessary to identify what structural mode shapes are coupled to the acoustic modes and what are the energy paths. In order to improve the experimental setup, it is necessary to increase the natural frequency of 2nd structural mode to tune it to the 2nd acoustic mode shape of the cavity in order to amplify the coupling effects.

A faster control board should be used to implement the control method in order to make it possible implement other control methods, such as the frequency-domain filtered-X LMS and the ASIC, or a mix of error sensors.

Capítulo 8 (Português)

Conclusão

Neste capítulo são apresentados, de forma sucinta, os principais resultados obtidos no decorrer desta tese. De maneira geral, pode-se dizer que os sistemas de controle ativo nas configurações analisadas (AVC, ASAC e ANC) foram capazes de atingir níveis de atenuação acima de 6 dB mesmo nos casos mais complexos (exemplo da cavidade cilíndrica). Este resultado mostra que sistemas de controle ativo apresentam um grande potencial de aplicação industrial.

8.1 Controle ativo de ruído em guias de ondas unidimensionais

Observações gerais: Observou-se, analítica e experimentalmente, que o controle ativo de ruído em guia de ondas unidimensionais pode ser aplicado com sucesso e com baixo custo computacional atingindo excelentes níveis de atenuação do ruído original.

Posição dos atuadores e sensores: A distância da fonte secundária em relação à posição da fonte primária deve ser observada a fim de se evitem as posições em que a fonte secundária não consiga controlar a fonte primária. Além disso, o sensor de erro deve ser posicionado evitando regiões de nó para os tipos de medida necessária (distâncias múltiplas de um quarto de comprimento de onda).

Comparação dos métodos de controle: Admitindo a configuração de uma fonte primária, uma fonte secundária e um sensor de erro, posicionados nesta mesma ordem, demonstrou-se que, teoricamente, os métodos de controle não apresentam diferenças no desempenho. Porém,

experimentalmente, estes apresentaram pequenas diferenças, originadas por características dos sensores de erro, tais como diferenças de sensibilidade, de fase, de faixa dinâmica, e relação sinal/ruído.

Implementação no domínio da frequência: As implementações dos métodos de controle no domínio da frequência apresentaram desempenho satisfatório, convergência rápida, o que, juntamente com o fato de permitir controlar as frequências independentemente uma da outra, torna estes métodos de controle muito versáteis. Porém, placas de processamento digital mais rápidas devem ser utilizadas para permitir uma faixa de frequência adequada ao controle ativo de ruído, especialmente aumentar o número de frequências intermediárias.

Observações teóricas: Observou-se, primeiramente, que os métodos de controle fornecem a mesma velocidade de volume ótima para a fonte secundária, e esta é sempre maior, ou no mínimo igual, à velocidade de volume da fonte primária. Além disso, quando é implementada a solução ótima para a fonte secundária, ambas as fontes não radiam mais potência acústica, e a velocidade de partícula e a intensidade ativa são minimizadas nas regiões situadas após a fonte secundária.

Observações experimentais: Os mesmos fatos observados para a implementação teórica foram observados para a implementação experimental. Entretanto, os níveis de atenuação da pressão sonora, velocidade de partícula e intensidade ativa, são limitados pela faixa dinâmica do sensor de erro; sendo assim, a atenuação não atinge o zero e para no fundo de escala do sensor de erro.

Medidas experimentais: A vibrometria laser mostrou-se uma ótima técnica para estimar a velocidade de volume de uma fonte sonora. Além disso, a técnica de estimar a intensidade ativa através de dois microfones pode ser utilizada com sucesso, mas os níveis de ruído apresentados pela medida podem comprometer os resultados obtidos.

Elemento espectral acústico: A modelagem de guia de ondas unidimensionais pelo método dos elementos espectrais apresentou uma boa concordância com os resultados experimentais, mostrando-se capaz de modelar redes de guia de ondas onde a aproximação de ondas planas pode ser assumida.

8.2 Controle de vibração e ruído em cilindros

Análise modal: Observou-se, analiticamente e experimentalmente, que a frequência de 216 Hz estava presente tanto na estrutura quanto na cavidade acústica cilíndrica, porém a retirada das tampas e movimentações oriundas do posicionamento dos sensores acústicos acarretaram pequenas mudanças na frequência natural da cavidade acústica. Além disso, identificou-se a frequência natural de 216 Hz correspondendo ao 10º modo natural da estrutura e ao 1º modo circunferencial da cavidade acústica, este contaminado com o modo estrutural, sendo, assim, composto por uma combinação do modo acústico e do modo estrutural, que age somente em campo próximo e desaparece à medida que se aproxima do centro do cilindro.

Posicionamento dos atuadores e sensores: Observou-se que o posicionamento dos atuadores de controle (conjunto de PZTs) amplificou o a atuação nos modos 2, 6, 10, ..., porém os PZTs somente apresentaram desempenho satisfatório acima de 150 Hz, o que, juntamente com a limitação da placa de controle digital, limitou a aplicação do controle a uma faixa estreita de frequência em torno de 216 Hz.

Aplicação do controle ativo para o distúrbio estrutural: Observou-se que não é necessário utilizar mais de um sensor de erro desde que este esteja posicionado em ponto de máxima amplitude, porém pode-se tornar a atenuação atingida independente da posição aumentando o número de sensores de erro. Além disso, é mais fácil controlar a vibração na estrutura do que o ruído gerado por ela. Níveis de atenuação em torno de 15 dB foram atingidos para a energia cinética da estrutura utilizando o esquema AVC em contraste com apenas 4 dB para a energia potencial da cavidade acústica utilizando um esquema ASAC.

Aplicação do controle ativo para o distúrbio acústico: Observou-se que a excitação acústica não era captada pelo sensor estrutural (acelerômetro) e que o sensor de velocidade de partícula apresentava uma relação sinal/ruído muito alta. O microfone mostrou-se mais adequado para a aplicação do controle ativo de ruído tendo sido atingido mais de 10 dB de atenuação.

Apenas excitação tonal pôde ser empregada devido às características do atuador acústico e do arranjo experimental.

Comparação entre acelerômetro, microfone e sensor de velocidade de partícula:

Observou-se que o desempenho do controlador com o sensor de velocidade de partícula como sensor de erro está sempre entre o desempenho com o acelerômetro e com o microfone.

8.3 Sugestões de trabalhos futuros

No controle ativo de ruído em guia de ondas planas sugere-se que seja utilizada uma placa controladora mais rápida para permitir um aumento no número de frequências a serem controladas, e utilizar mais de uma fonte de controle afim de atenuar o ruído entre as fontes.

No controle ativo na cavidade cilíndrica, a utilização de uma placa controladora mais rápida é fundamental para a implementação de métodos de controle no domínio da frequência, permitindo assim, a utilização de métodos que controlam a intensidade ativa estrutural ou acústica. Além disso, o enrijecimento do cilindro aproximaria o experimento das condições encontradas em fuselagens de aeronaves, onde o segundo modo de vibrar da estrutura (o primeiro modo circunferencial) é geralmente o mais significativo para o ruído interno.

Além disso, a realização de um estudo detalhado dos fenômenos de interação entre a vibração da casca cilíndrica e o campo acústico da cavidade, tanto do lado teórico quanto do lado experimental precisa ser feito a fim de prever, identificar e medir os modos de radiação sonora da casca cilíndrica que são mais significativos para a formação do campo acústico da cavidade. Neste sentido, métodos como Elementos Finitos e Elementos de Contorno podem ser usados para prever os modos de radiação sonora, enquanto métodos experimentais como análise no plano $K \times \omega$ e análise da matriz de acoplamento podem ser usados para identificar e medir experimentalmente estes modos de radiação. Desta forma, as implementações de controle ativo de ruído poderiam ser direcionadas a obter melhores desempenhos.

8.4 Publicações geradas por esta tese

- Donadon, L.V., Arruda, J.R.F. Influence of the Filtered-X LMS controller in the impedances of a duct. In: *Congresso Brasileiro de Engenharia Mecânica, Cobem 99*, Águas de Lindóia-Brasil, CD-room, 1999.
- Nunes, R.F., Donadon, L.V., Arruda, J.R.F., Santos, J.M.C. Active noise control in ducts using adaptive algorithm. In: *Congresso Brasileiro de Engenharia Mecânica, Cobem 99*, Águas de Lindóia-Brasil, CD-room, 1999.
- Donadon, L.V., Arruda, J.R.F. Theoretical comparison of active noise control using potential energy error sensing and intensity error sensing. In: International Congress and Exposition on Noise Control Engineering, *Internoise 2000*, Nice-France, CD-room, 2000.
- Donadon, L.V., Arruda, J.R.F. Active Noise Control of Free-Field Radiation Using Near Field Error Sensing by Active Sound Intensity Control. In: International conference Noise & Vibration pre-design and characterization using Energy Methods, *NOVEM 2000*, Lion-France, CD-room, 2000.
- Donadon, L.V., Arruda, J.R.F. Energetic analysis of an actively controlled one-dimensional acoustic waveguide. *Applied Acoustics* (aceito para publicação).
- Donadon, L.V., Arruda, J.R.F. Experimental energetic analyses of an actively controlled one-dimensional acoustic waveguide. *Journal of Sound and Vibration* (condicionalmente aceito).
- Donadon, L.V., Arruda, J.R.F. Using particle velocity sensors in active noise and vibration control applications. In: International Congress and Exposition on Noise Control Engineering, *Internoise 2002*, Dearborn-USA, CD-room, 2002.

Chapter 8 (English)

Conclusion

In this chapter the main results obtained in this Ph.D. dissertation are presented. In general, the active control systems configurations analyzed (AVC, ASAC and ANC) were capable to achieve attenuation levels above 6 dB even in the most complex cases (example of the cylindrical cavity). This result shows that the active control system present a great potential for industrial applications.

8.1 Active noise control in one-dimensional acoustic waveguides

General comments: It was observed, both analytically and experimentally, that the active noise control in one-dimensional waveguides can be applied successfully and achieved excellent attenuation levels of the original noise with low computational cost.

Position of the actuators and sensors: The distance of the secondary source in relation to the position of the primary source should avoid the positions where the secondary source can not control the primary source. Moreover, the error sensor should be placed avoiding regions of modes for the wave type measured (multiple distances of $\frac{1}{4}$ of a wavelength).

Comparison of the control methods: Admitting the configuration of a primary source, a secondary source and a error sensor, located in this same order, it was demonstrated that, theoretically, the control methods do not present differences in the performance. However, experimentally, the control methods presented small differences because of the characteristics of

the error sensors used in the control experiment, such as differences of sensitivity, phase, dynamic range, and signal/noise ratio.

Implementation in the frequency domain: The control method implementations in the frequency domain presented satisfactory performance because of the fast convergence and the possibility of controlling frequencies lines independently. Thus, this methodology showed to be very versatile. However, faster digital signal processing boards should be used to allow a higher frequency band the active noise control, mainly to increase the number of frequency lines.

Theoretical comments: *It was observed that the control methods achieved the same final result for optimal volume velocity of the secondary source, which is larger or at least equal to the volume velocity of the primary source. In addition, when the optimal solution for the secondary source is implemented, both sources do not radiate acoustic power, and the particle velocity and the active intensity are minimized past the secondary source.*

Experimental comments: *The same facts observed for the theoretical implementation were observed for the experimental implementation. However, the attenuation levels of the pressure, particle velocity and active intensity are limited by the dynamic band of the error sensor; thus, the attenuation did not achieve the zero, but stopped at the background noise level of the error sensor.*

Experimental measurements: The laser vibrometer revealed to be an excellent technique to estimate the volume velocity of an acoustic source. The technique of estimating the active intensity using two microphones can be used successfully but the noise levels can effect the results.

The Spectral Element Method: *The modeling of one-dimensional acoustic waveguides using the spectral element method showed a good agreement with the experimental results, revealing the capacity to model pipe networks where the approach of plane waves can be assumed.*

8.2 Active noise and vibration control in cylinders

Modal analysis: It was observed, both analytically and experimentally, that the 216 Hz frequency was present in the structure and in the cylindrical cavity; however, movements in the covers and the positioning of the acoustic sensors caused small changes in the natural frequency of the acoustic cavity. In addition, the natural frequency of 216 Hz was identified to correspond to the 10th natural structural mode shape and the 1st circumferential mode shape of the acoustic cavity. The acoustic mode shape is contaminated with the structural mode, thus being a composition of the acoustic mode and the structural mode, which acts only in the nearfield and disappears towards the center of the cylinder.

Positioning of the actuators and sensors: It was observed that the positioning of the control actuators (PZT patches) amplified the performance in modes 2nd, 6th, 10th The PZT patches present satisfactory performance only above 150 Hz and the limitations of the digital signal processing board limited the application of the control to a narrow band of frequency around 216 Hz.

Application of the active control for the structural disturbances: It was observed that it is not necessary to use more than one error sensor provided it is located in point of maximum amplitude; however, increasing the number of error sensors, the attenuation becomes independent of the error sensor position. In addition, it is easier to control the vibration in the structure than the noise generated by it. Levels of attenuation around 15 dB were achieved for the structural kinetic energy using the AVC scheme in contrast to only 4 dB for the acoustic potential energy of the acoustic cavity using the ASAC scheme.

Application of the active control for the acoustic disturbances: It was observed that the structural sensors (accelerometers) did not measure the acoustic disturbance and the particle velocity sensor showed very high signal/noise ratio. The microphone revealed to be more adequate as error sensor for active noise control, having achieved more than 10 dB of attenuation, but only tonal disturbance could be employed due to the characteristics of the acoustic actuator and the experimental set up.

Comparison between accelerometer, microphone and particle velocity sensor: It was observed that the performance of the controller using the particle velocity sensor as error sensor is always between the performance with the accelerometer and with the microphone.

8.3 Suggestions to future researches

In the active noise control in one-dimensional waveguides it is suggested the use faster digital signal processing control boards to allow an increase in the number of frequencies lines to be controlled, and to use more than one secondary source to attenuate the noise between the sources.

In the active control of the cylindrical cavity, the use of a fast control board is essential for the implementation of controllers in the frequency domain; thus, allowing the use of methods that control the structural or the acoustic active intensity. Moreover, the cylinder should be stiffened to better represent the real situation of an aircraft fuselage, where the second structural mode is generally the most significant for the interior noise generation.

Moreover, a detailed investigation of the interaction between the vibrations of the cylindrical shell and the pressure field in the acoustical cavity, both theoretical and experimental, should allow predicting, identifying and measuring the modes of the cylindrical cavity that are more significant for the acoustic field generation. In this direction, Finite Element and Boundary Element Methods can be used to predict the radiation modes while methods as the analysis in the $K \times \omega$ plane and the analysis of the coupling matrix can be used to identify experimentally the noise radiation modes. In this sort, the active noise control implementations could be directed to obtain better performances.

8.4 Publication arising from this thesis

- Donadon, L.V., Arruda, J.R.F. Influence of the Filtered-X LMS controller in the impedances of a duct. In: *Congresso Brasileiro de Engenharia Mecânica, Cobem 99*, Águas de lindóia-Brasil, CD-room, 1999.
- Nunes, R.F., Donadon, L.V., Arruda, J.R.F., Santos, J.M.C. Active noise control in ducts using adaptive algorithm. In: *Congresso Brasileiro de Engenharia Mecânica, Cobem 99*, Águas de lindóia-Brasil, CD-room, 1999.
- Donadon, L.V., Arruda, J.R.F. Theoretical comparison of active noise control using potential energy error sensing and intensity error sensing. In: International Congress and Exposition on Noise Control Engineering, *Internoise 2000*, Nice-France, CD-room, 2000.
- Donadon, L.V., Arruda, J.R.F. Active Noise Control of Free-Field Radiation Using Near Field Error Sensing by Active Sound Intensity Control. In: International conference Noise & Vibration pre-design and characterization using Energy Methods, *NOVEM 2000*, Lion-France, CD-room, 2000.
- Donadon, L.V., Arruda, J.R.F. Energetic analysis of an actively controlled one-dimensional acoustic waveguide. *Applied Acoustics (accept for publication)*.
- Donadon, L.V., Arruda, J.R.F. Experimental energetic analyses of an actively controlled one-dimensional acoustic waveguide. *Journal of Sound and Vibration (conditionally accepted)*.
- Donadon, L.V., Arruda, J.R.F. Using particle velocity sensors in active noise and vibration control applications. In: International Congress and Exposition on Noise Control Engineering, *Internoise 2002*, Dearborn-USA, CD-room, 2002.

References

- Arruda, JRF, Rio, SAV, Santos, LASB. A space-frequency data compression method for spatially dense laser Doppler vibrometer measurements. *Acta Acustica*, v. 83, pp. 465-474, 1997.
- Arruda, JRF, Dehandschutter, W, Sas, P. Active vibration control in finite plates using a structural power flow approach. *Acta Acustica*, v. 83, pp. 465-474, 1997.
- Arruda, JRF. The structural Dynamics mid-frequency challenge: Bridging the gap between FEA and SEA. In: Congresso Brasileiro de Engenharia Mecânica, Cobem 2001, Uberlândia, CD-room.
- Bao, C, Sas, P, Brussel, HV. Adaptive active control of noise in 3-D reverberant enclosures. *Journal of sound and vibration*, v.191, n.3, pp. 501-514, 1993.
- Blevins, R.D., *Formulas for natural frequency and mode shape*, Krieger Publishing Company, 1995.
- Borgiotti, GV. The power radiated by a vibrating body in a acoustic fluid and its determination from boundary measurements. *Journal of the Acoustic Society of America*, v.88, n.4, pp.1884-1893, 1990.
- Bree, HE, Leussink, P, Korthorst, T, Jansen, H, Lammerink, T, Elwenspoek, M. The microflown: a novel device measuring acoustical flows. *Sensors and Actuators A*, v. 54, pp. 552-557, 1996.
- Bree, Druyvesteyn, WF, Elwenspoek, M. Realization and calibration of a novel half inch P-U sound intensity probe. In: 106th AES, Munchen, 1999.
- Burgess, JC. Active adaptive sound control in a duct: A computer simulation. *Journal of the Acoustic Society of America*, v. 70, n.3, pp. 715-726, 1981.
- Cabell, RH, Fuller, CR. A principal component algorithm for feedforward active noise and vibration control. *Journal of Sound and Vibration*, v.227, n.1, pp.159-181, 1999.
- Cazzolat, BS, Hansen, CH. Structural radiation mode sensing for active control of sound radiation into enclosed spaces. *Journal of the Acoustic Society of America*, v.104, n.5, pp.2878-2889, 1998.
- Cazzolat, BS, Hansen, CH. Structural radiation mode sensing for active control of sound radiation into enclosed spaces. *Journal of the Acoustic Society of America*, v.106, n. 6, pp.3732-3735, 1999.

- Cazzolat, BS, Hansen, CH. Errors in the measurement of acoustic energy density in one-dimensional sound fields. *Journal of Sound and Vibration*, v.236, n.5, pp.801-831, 2000.
- Chen, KT, Lin, JI. The determination of the acoustic properties of sound sources actively controlled in a square duct. *Applied Acoustics*, v.61, n.2, pp.399-411, 2000.
- Chen, KT, Liu, YH. A physical insight of the active control on sound source in a pipe. *Applied Acoustics*, v.61, n.1, pp.133-148, 2000.
- Chung, JY. Cross-spectral method of measuring acoustic intensity without error by instrument phase mismatch. *Journal of the Acoustic Society of America*, v.64, n.6, pp.1613-1616, 1978.
- Cowan, CFN. Performance comparisons of finite linear adaptive filters. *IEE Proceedings Part F*, v.134, n.3, pp.211-216, 1987.
- Craig, RR. *Structural Dynamics*. John Wiley, New York. 1981.
- Curtis, ARD, Nelson, SJ, Bullmore, AJ. Active suppression of acoustic resonance. *Journal of the Acoustic Society of America*, v.81, n.3, pp.624-631, 1987.
- Doyle, JF. *Wave propagation in structures : spectral analysis using fast discrete Fourier transforms*. Springer, 1997.
- Elliott, SJ, Stothers, IM, Nelson, PA. A multiple error LMS algorithm and its application to the active control of sound and vibration. *IEEE Transaction on acoustics, speech, and signal processing*, v.ASSP-35, n.10, pp.1423-1434, 1987.
- Elliott, S J, Nelson, P A. *Active control of sound*. London: Academic Press, 1992.
- Elliott, SJ, Johnson, ME. Radiation modes and the active control of sound power. *Journal of the Acoustic Society of America*, v.94, n.4, pp.2194-2204, 1993.
- Elliott, SJ. *Signal Processing for active control*. Academic Press, 2001.
- Eerden, FJM, Bree, HE, Tjeldeman, H. Experiments with a new acoustic particle velocity sensor in an impedance tube. *Sensors and Actuators A*, v.69, pp. 126-133, 1998.
- Fahy, FJ. *Foundations of engineering acoustics*. Academic Press, 2001.
- Fahy, FJ. *Sound Intensity*. 2a ed., E & FN Spon, 1995.
- Fuller, CR, Elliott, SJ, Nelson, PA. *Active control of Vibration*. Academic Press, 1996.
- Fuller, CR, Jones, JD. Experiments on reduction of propeller induced interior noise by active control of cylinder vibration. *Journal o Sound and Vibration*, v.112, pp. 389-395, 1987.
- Hansen, CH, Snyder, SD. *Active control of noise and vibration*. E&FN Spon, London, 1997.
- Haykin, S. *Adaptive filter theory*. 3^a Ed., Prentice Hall, New York, 1996.
- Jacobsen, F. A note on the accuracy of phase compensated intensity measurements. *Journal of Sound and Vibration*, v.174, n.1, pp.140-144, 1994.
- Johnson, ME, Elliott, SJ. Active control fo sound radiation using volume velocity cancellation. *Journal of the Acosutic Society of America*, v.98, n.4, pp.2174-2186, 1995.

- Jones, J, Fuller, CR. Active control of sound fields in elastic cylinders by multicontrol forces. *AIAA journal*, v.27, n.7, pp.845-852. 1989.
- Juang, JN, Pappa, R S, An Eigensystem Realization Algorithm for Modal Parameter Identification and Model Reduction. *Journal of Guidance, Control, and Dynamics*, v.8, n.5, pp. 620-627, 1985
- Juang, J.N. *Applied System Identification*. Prentice Hall. 1994.
- Kang, SW, Kim, YH. Active intensity control for the reduction of radiated duct noise. *Journal of sound and vibration*, v. 201, (5), pp. 596-611, 1997.
- Kelly, LG. *Handbook of Numerical methods and applications*, Addison-Wesley, Reading, MA, 1967.
-
- Kestell, C., Hansen, C.H., Cazzolato, B.S. Active noise control with virtual sensors in a long narrow duct. *International Journal of acoustics and vibration*, v.5, n.2, pp. 1-14, 2000.
- Kim, SM, Brennan, M. Active control of harmonic sound transmission into na acoustic enclosure using both structural and acoustic actuators. *Journal of the Acoustic Society of America*, v.107, n.5, Pt.1, pp.2523-2534, 2000.
- Kinsler, LE, Frey, AR, Coppens, AB, Sandres, JV. *Fundamentals of Acoustics*. Wiley, 1982.
- Kuo, SM, Morgan, DR. *Active noise control systems*. Wiley, 1996.
- Ljung, L. *System Identification - Theory for the user* Englewood Cliffs: Prentice Hall. 1987.
- Lima Jr, JJ. *Modelagem de sensores e atuadores piezelétricos com aplicações em controle ativo de estruturas*. Campinas: Faculdade de Engenharia Mecânica, Universidade Estadual de Campinas, 1999, 241 p. Tese (Doutorado).
-
- Maillard, JP, Fuller, CR, Active control of sound radiation from cylinders with piezoelectric actuators and structural acoustic sensing. *Journal of the Acoustic Society of America*, v.222, n.3, pp. 363-388, 1999.
- Palumbo, D, Cabell, R, Sullivan, B, Cline, J, Flight test of active acoustic noise control system. *Journal of Aircraft*, v.38, n.2, pp. 277-284, 2001.
- Park, YC, Sommerfeldt, SD. Global attenuation of broadband noise fields using energy density control. *Journal of the acousic society of america*, v.101, n.1, pp.350-359, 1997.
- Pereira, AK. Controle ativo de vibração em vigas e placas usando uma abordagem de intensidade estrutural. Campinas: Faculdade de Engenharia Mecânica, Universidade Estadual de Campinas, 1999. Tese (Doutorado).
- Qiu, X, Hansen, CH. An adaptive sound intensity control algorithm for active control of transformer noise. In Proceedings fo the 5th International Congress of Sound and Vibration, Adelaide, pp. 205-212, 1997.
- Qiu, X, Hansen, CH, Li, X. A comparison of near-field acoustic error sensing strategies for the active control of harmonic free field sound radiation. *Journal of Sound and Vibration*, v.215, n.1, pp. 81-103, 1998.
- Shen, Q, Spanias, A. Time- and frequency-domain X-block least-means-square algorithm for active noise control. *Noise Control Engeneering Journal*, v.44, n.6, pp.281-293, 1996.

- Shynk, JJ. Frequency-domain and multirate adaptive filtering. *IEEE SP Magazine*, pp.15-37, 1992.
- Snyder, SD, Hansen, CH. Active noise control in ducts: Some physical insights. *Journal of the Acoustic Society of America*, v.86, n.1, pp.184-194, 1989.
- Snyder, SD, Hansen, CH, Mechanisms of active noise control by vibration sources. *Journal of Sound and Vibration*, v.147, n.3 , pp. 519-525, 1991.
- Sommerfeldt, SD, Nahif, PJ. An adaptive filtered-X algorithm for energy-based active control. *Journal of the Acoustic Society of America*, v.96, n.1, pp.300-306, 1994.
- Sun, J, Rossetti, D, HighfillJ. Distributed piezoelectric actuators for shell interior noise control. *Journal of Vibration and Acoustics*. 1994.
-
- Swanson, DC, Hirsch, SM, Reichard, KM, Tichy, J. Development of a frequency-domain filtered-x intensity ANC algorithm. *Applied acoustics*, v.57, n.1, pp. 39-49, 1999.
- Thompson, JK, Tree, DR. Finite difference aproximation errors in acoustic intensity measurements. *Journal of Sound and Vibration*, v.75, n.2 , pp.229-238, 1981.
- Vold, H. Numerically robust frequency domain modal parameter estimation. *Sound and Vibration*, v.24, n.1, pp. 38-40, 1990.
- Wang, B, Fuller, CR. Near-field pressure, intensity, and wave-number distributions for active structural acoustic control of plate radiation: theoretical analysis. *Journal of the Acoustic Society of America*, v.92, n.3, pp. 1489-1498, 1992.
- Widrow, B., Stearns, S.D., 1985, *Adaptive Signal Processing*, New York, Prentice Hall.
-

Appendix A

A Derivation of complex variables

The purpose of this appendix is to address the more difficult issue of differentiating a real cost function with respect to a complex-valued parameter vector. These relations can be found in Haykin (1996), Nelson and Elliott (1991) and Qiu et al. (1998).

A.1 Basic definitions

The derivative of a complex function $G(x)$ with respect to a scalar complex variable x is performed as,

$$\frac{\partial G(x)}{\partial x} = \frac{1}{2} \left(\frac{\partial G(x)}{\partial x_R} - i \frac{\partial G(x)}{\partial x_I} \right) \quad (A.1)]$$

and

$$\frac{\partial G(x)}{\partial x^*} = \frac{1}{2} \left(\frac{\partial G(x)}{\partial x_R} + i \frac{\partial G(x)}{\partial x_I} \right) \quad (A.2)]$$

where x_R and x_I are the real and imaginary part of x , respectively, and i is the imaginary number.

The derivatives defined in Equations (A.1) and (A.2)] satisfy the two basic requirements,

$$\frac{\partial x}{\partial x} = 1 \quad (A.3)]$$

$$\frac{\partial x}{\partial x^*} = 0 \quad (\text{A.4})$$

Now, assuming \mathbf{X} as a complex vector in the following form,

$$\mathbf{X} = \begin{Bmatrix} x_1 \\ \vdots \\ x_n \end{Bmatrix}$$

The derivative of a real scalar function $G(x)$ with respect to \mathbf{X} is defined as,

$$\frac{\partial G(x)}{\partial \mathbf{X}} = \frac{1}{2} \begin{Bmatrix} \frac{\partial G(x)}{\partial x_{R1}} - i \frac{\partial G(x)}{\partial x_{I1}} \\ \vdots \\ \frac{\partial G(x)}{\partial x_{Rn}} - i \frac{\partial G(x)}{\partial x_{In}} \end{Bmatrix} \quad (\text{A.5})$$

and

$$\frac{\partial G(x)}{\partial \mathbf{X}^*} = \frac{1}{2} \begin{Bmatrix} \frac{\partial G(x)}{\partial x_{R1}} + i \frac{\partial G(x)}{\partial x_{I1}} \\ \vdots \\ \frac{\partial G(x)}{\partial x_{Rn}} + i \frac{\partial G(x)}{\partial x_{In}} \end{Bmatrix} \quad (\text{A.6})$$

However, if $G(x)$ is a real cost function, the gradient of $G(x)$ is defined as in Haykin (1996),

$$\nabla G(x) = \begin{Bmatrix} \frac{\partial G(x)}{\partial x_{R1}} + i \frac{\partial G(x)}{\partial x_{I1}} \\ \vdots \\ \frac{\partial G(x)}{\partial x_{Rn}} + i \frac{\partial G(x)}{\partial x_{In}} \end{Bmatrix} \quad (\text{A.7})$$

Thus, the gradient is related to the conjugate derivative as,

$$\nabla G(x) = 2 \frac{\partial G(x)}{\partial x^*} \quad (\text{A.8})$$

A.2 Case I

Assuming a real scalar function $G(x)$ in the form,

$$G(x) = \mathbf{F}^H \mathbf{X} \quad (\text{A.9})$$

where the vector \mathbf{F} is given by,

$$\mathbf{F} = \begin{Bmatrix} f_1 \\ \vdots \\ f_n \end{Bmatrix} = \begin{Bmatrix} f_{R1} + if_{I1} \\ \vdots \\ f_{Rn} + if_{In} \end{Bmatrix} \quad (\text{A.10})$$

Applying the gradient of the scalar function $G(x)$ with respect to the vector \mathbf{X} is found,

$$2 \frac{\partial G(x)}{\partial \mathbf{X}^*} = \frac{\partial}{\partial \mathbf{X}^*} \mathbf{F}^H \mathbf{X} = \begin{Bmatrix} \frac{\partial}{\partial x_1^*} \mathbf{F}^H \mathbf{X} \\ \vdots \\ \frac{\partial}{\partial x_n^*} \mathbf{F}^H \mathbf{X} \end{Bmatrix} = \begin{Bmatrix} \frac{\partial}{\partial x_1^*} (f_1^* x_1 + \dots + f_n^* x_n) \\ \vdots \\ \frac{\partial}{\partial x_n^*} (f_1^* x_1 + \dots + f_n^* x_n) \end{Bmatrix} = \begin{Bmatrix} \frac{\partial}{\partial x_1^*} f_1^* x_1 \\ \vdots \\ \frac{\partial}{\partial x_n^*} f_n^* x_n \end{Bmatrix} \quad (\text{A.11})$$

Expanding a generic term j of the above derivative as,

$$f_j^* x_j = (f_{Rj} - if_{Ij})(x_{Rj} + ix_{Ij}) = f_{Rj} x_{Rj} + if_{Rj} x_{Ij} - if_{Ij} x_{Rj} + f_{Ij} x_{Ij} \quad (\text{A.12})$$

It is important to remember that $f_j^* x_j$ must be a real number, so, $if_{Rj} x_{Ij} - if_{Ij} x_{Rj} = 0$. Thus, the above equation become,

$$f_j^* x_j = (f_{Rj} - if_{Ij})(x_{Rj} + ix_{Ij}) = f_{Rj} x_{Rj} + f_{Ij} x_{Ij} \quad (\text{A.13})$$

So, the gradient of the generic term j is given by,

$$2 \frac{\partial}{\partial x_j^*} f_j^* x_j = f_{Rj} + i(f_{Ij}) = f_j \quad (\text{A.14})$$

Thus, the gradient of the scalar function $G(x)$ with respect to the vector \mathbf{X} is,

$$\nabla \mathbf{F}^H \mathbf{X} = \begin{Bmatrix} f_1 \\ \vdots \\ f_n \end{Bmatrix} = \mathbf{F} \quad (\text{A.15})$$

Now, applying the gradient to the case of $G^H(x)$ as,

$$2 \frac{\partial G^H(\mathbf{x})}{\partial \mathbf{X}^*} = 2 \frac{\partial}{\partial \mathbf{X}^*} \mathbf{X}^H \mathbf{F} = 2 \begin{Bmatrix} \frac{\partial}{\partial \mathbf{x}_1^*} (f_1 x_1^* + \dots + f_n x_n^*) \\ \vdots \\ \frac{\partial}{\partial \mathbf{x}_n^*} (f_1 x_1^* + \dots + f_n x_n^*) \end{Bmatrix} = 2 \begin{Bmatrix} \frac{\partial}{\partial \mathbf{x}_1^*} f_1 x_1^* \\ \vdots \\ \frac{\partial}{\partial \mathbf{x}_n^*} f_n x_n^* \end{Bmatrix} \quad (\text{A.16})$$

Expanding one generic term j of the above derivative as,

$$f_j x_j^* = (f_{R_j} + i f_{I_j}) (x_{R_j} - j x_{I_j}) = f_{R_j} x_{R_j} - i f_{R_j} x_{I_j} + i f_{I_j} x_{R_j} + f_{I_j} x_{I_j} \quad (\text{A.17})$$

Remember again that the above relation must be a real number, so,

$$f_j x_j^* = (f_{R_j} + i f_{I_j}) (x_{R_j} - j x_{I_j}) = f_{R_j} x_{R_j} + f_{I_j} x_{I_j} \quad (\text{A.18})$$

Thus, the gradient of the generic term j is given by,

$$2 \frac{\partial}{\partial \mathbf{x}_j^*} f_j x_j^* = f_{R_j} + i (f_{I_j}) = f_j \quad (\text{A.19})$$

Thus, the gradient of the scalar function $G^H(\mathbf{x})$ with respect to the vector \mathbf{X} is,

$$\nabla(\mathbf{X}^H \mathbf{F}) = \begin{Bmatrix} f_1 \\ \vdots \\ f_n \end{Bmatrix} = \mathbf{F} \quad (\text{A.20})$$

Applying the gradient of the scalar function $\Re\{G(\mathbf{x})\}$ with respect to the vector \mathbf{X} is found,

$$2 \frac{\partial \Re\{G(\mathbf{x})\}}{\partial \mathbf{X}^*} = 2 \frac{\partial}{\partial \mathbf{X}^*} \Re\{\mathbf{F}^H \mathbf{X}\} = 2 \begin{Bmatrix} \frac{\partial}{\partial \mathbf{x}_1^*} (\Re\{f_1^* x_1\} + \dots + \Re\{f_n^* x_n\}) \\ \vdots \\ \frac{\partial}{\partial \mathbf{x}_n^*} (\Re\{f_1^* x_1\} + \dots + \Re\{f_n^* x_n\}) \end{Bmatrix} = 2 \begin{Bmatrix} \frac{\partial}{\partial \mathbf{x}_1^*} \Re\{f_1^* x_1\} \\ \vdots \\ \frac{\partial}{\partial \mathbf{x}_n^*} \Re\{f_n^* x_n\} \end{Bmatrix} \quad (\text{A.21})$$

Expanding one generic term j of the above derivative as,

$$\Re\{f_j^* x_j\} = \Re\{(f_{R_j} - i f_{I_j}) (x_{R_j} + i x_{I_j})\} = f_{R_j} x_{R_j} + f_{I_j} x_{I_j} \quad (\text{A.22})$$

So, the gradient of the generic term j is given by,

$$2 \frac{\partial}{\partial \mathbf{x}_j^*} \Re\{f_j^* x_j\} = f_{R_j} + i f_{I_j} = f_j \quad (\text{A.23})$$

Thus, the derivative of the scalar function $\Re\{G(\mathbf{x})\}$ with respect to the vector \mathbf{X} is,

$$\nabla(\Re\{\mathbf{F}^H \mathbf{X}\}) = \begin{Bmatrix} f_1 \\ \vdots \\ f_n \end{Bmatrix} = \mathbf{F} \quad (\text{A.24})$$

Now, applying the gradient to the case of $\Re\{G^H(\mathbf{x})\}$ as,

$$2 \frac{\partial \Re\{G^H(\mathbf{x})\}}{\partial \mathbf{X}^*} = 2 \frac{\partial}{\partial \mathbf{X}^*} \Re\{\mathbf{X}^H \mathbf{F}\} = 2 \begin{Bmatrix} \frac{\partial}{\partial x_1^*} (\Re\{f_1 x_1^*\} + \dots + \Re\{f_n x_n^*\}) \\ \vdots \\ \frac{\partial}{\partial x_n^*} (\Re\{f_1 x_1^*\} + \dots + \Re\{f_n x_n^*\}) \end{Bmatrix} = 2 \begin{Bmatrix} \frac{\partial}{\partial x_1^*} \Re\{f_1 x_1^*\} \\ \vdots \\ \frac{\partial}{\partial x_n^*} \Re\{f_n x_n^*\} \end{Bmatrix} \quad (\text{A.25})$$

Expanding one generic term j of the above derivative as,

$$\Re\{f_j x_j^*\} = \Re\{(f_{Rj} + if_{Ij})(x_{Rj} - ix_{Ij})\} = f_{Rj} x_{Rj} + f_{Ij} x_{Ij} \quad (\text{A.26})$$

So, the gradient of the generic term j is given by,

$$2 \frac{\partial}{\partial x_j^*} \Re\{f_j x_j^*\} = f_{Rj} + if_{Ij} = f_j \quad (\text{A.27})$$

Thus, the gradient of the scalar function $\Re\{G(\mathbf{x})\}$ with respect to the vector \mathbf{X} is,

$$\nabla(\Re\{\mathbf{X}^H \mathbf{F}\}) = \begin{Bmatrix} f_1 \\ \vdots \\ f_n \end{Bmatrix} = \mathbf{F} \quad (\text{A.28})$$

Now, applying the gradient to the case of $\Im\{G(\mathbf{x})\}$ as,

$$2 \frac{\partial \Im\{G(\mathbf{x})\}}{\partial \mathbf{X}^*} = 2 \frac{\partial}{\partial \mathbf{X}^*} \Im\{\mathbf{F}^H \mathbf{X}\} = 2 \begin{Bmatrix} \frac{\partial}{\partial x_1^*} (\Im\{f_1^* x_1\} + \dots + \Im\{f_n^* x_n\}) \\ \vdots \\ \frac{\partial}{\partial x_n^*} (\Im\{f_1^* x_1\} + \dots + \Im\{f_n^* x_n\}) \end{Bmatrix} = 2 \begin{Bmatrix} \frac{\partial}{\partial x_1^*} \Im\{f_1^* x_1\} \\ \vdots \\ \frac{\partial}{\partial x_n^*} \Im\{f_n^* x_n\} \end{Bmatrix} \quad (\text{A.29})$$

Expanding one generic term j of the above derivative as,

$$\Im\{f_j^* x_j\} = \Im\{(f_{Rj} - if_{Ij})(x_{Rj} + ix_{Ij})\} = f_{Rj} x_{Ij} - f_{Ij} x_{Rj} \quad (\text{A.30})$$

So, the gradient of the generic term j is given by,

$$2 \frac{\partial}{\partial \mathbf{x}_j^*} \Im\{\mathbf{f}_j^* \mathbf{x}_j\} = -\mathbf{f}_{lj} + i(\mathbf{f}_{Rj}) = i\mathbf{f}_j \quad (\text{A.31})$$

Thus, the gradient of the scalar function $\Im\{G(\mathbf{x})\}$ with respect to the vector \mathbf{X} is,

$$\nabla(\Im\{\mathbf{F}^H \mathbf{X}\}) = \begin{Bmatrix} i\mathbf{f}_1 \\ \vdots \\ i\mathbf{f}_n \end{Bmatrix} = i\mathbf{F} \quad (\text{A.32})$$

Now, applying the gradient to the case of $\Im\{G^H(\mathbf{x})\}$ as,

$$2 \frac{\partial \Im\{G^H(\mathbf{x})\}}{\partial \mathbf{X}^*} = \frac{2\partial}{\partial \mathbf{X}^*} \Im\{\mathbf{X}^H \mathbf{F}\} = 2 \begin{Bmatrix} \frac{\partial}{\partial \mathbf{x}_1^*} (\Im\{\mathbf{f}_1 \mathbf{x}_1^*\} + \dots + \Im\{\mathbf{f}_n \mathbf{x}_n^*\}) \\ \vdots \\ \frac{\partial}{\partial \mathbf{x}_n^*} (\Im\{\mathbf{f}_1 \mathbf{x}_1^*\} + \dots + \Im\{\mathbf{f}_n \mathbf{x}_n^*\}) \end{Bmatrix} = 2 \begin{Bmatrix} \frac{\partial}{\partial \mathbf{x}_1^*} \Im\{\mathbf{f}_1 \mathbf{x}_1^*\} \\ \vdots \\ \frac{\partial}{\partial \mathbf{x}_n^*} \Im\{\mathbf{f}_n \mathbf{x}_n^*\} \end{Bmatrix}$$

Expanding one generic term j of the above derivative as,

$$\Im\{\mathbf{f}_j \mathbf{x}_j^*\} = \Im\{(\mathbf{f}_{Rj} + i\mathbf{f}_{lj})(\mathbf{x}_{Rj} - i\mathbf{x}_{lj})\} = -\mathbf{f}_{Rj}\mathbf{x}_{lj} + \mathbf{f}_{lj}\mathbf{x}_{Rj} \quad (\text{A.33})$$

So, the gradient of the generic term j is given by,

$$2 \frac{\partial}{\partial \mathbf{x}_j^*} \Im\{\mathbf{f}_j \mathbf{x}_j^*\} = \mathbf{f}_{lj} + i(-\mathbf{f}_{Rj}) = -i\mathbf{f}_j \quad (\text{A.34})$$

Thus, the gradient of the scalar function $\Im\{G^H(\mathbf{x})\}$ with respect to the vector \mathbf{X} is,

$$\nabla(\Im\{\mathbf{X}^H \mathbf{F}\}) = \begin{Bmatrix} -i\mathbf{f}_1 \\ \vdots \\ -i\mathbf{f}_n \end{Bmatrix} = -i\mathbf{F} \quad (\text{A.35})$$

A.3 Case II

Assuming a real scalar function $G(\mathbf{x})$ in the form,

$$G(\mathbf{x}) = (\mathbf{A}\mathbf{X})^H \mathbf{B} \quad (\text{A.36})$$

where \mathbf{A} and \mathbf{B} are given by,

$$\mathbf{A} = \begin{Bmatrix} a_{11} & \cdots & a_{1n} \\ \vdots & \ddots & \vdots \\ a_{l1} & \cdots & a_{ln} \end{Bmatrix} \quad \text{e} \quad \mathbf{B} = \begin{Bmatrix} b_1 \\ \vdots \\ b_n \end{Bmatrix} \quad (\text{A.37})$$

Expanding $G(\mathbf{x})$ as,

$$(\mathbf{AX})^H \mathbf{B} = (a_{11}x_1 + \cdots + a_{1n}x_n)^* b_1 + \cdots + (a_{l1}x_1 + \cdots + a_{ln}x_n)^* b_n \quad (\text{A.38})$$

Applying the gradient of the scalar function $G(\mathbf{x})$ with respect to the vector \mathbf{X} is found,

$$2 \frac{\partial G(\mathbf{x})}{\partial \mathbf{X}^*} = 2 \frac{\partial}{\partial \mathbf{X}^*} (\mathbf{AX})^H \mathbf{B} = 2 \begin{Bmatrix} \frac{\partial}{\partial x_1^*} (a_{11}^* b_1 + \cdots + a_{l1}^* b_l) x_1^* \\ \vdots \\ \frac{\partial}{\partial x_n^*} (a_{1n}^* b_1 + \cdots + a_{ln}^* b_l) x_n^* \end{Bmatrix} = 2 \begin{Bmatrix} \frac{\partial}{\partial x_1^*} h_1 x_1^* \\ \vdots \\ \frac{\partial}{\partial x_n^*} h_n x_n^* \end{Bmatrix} \quad (\text{A.39})$$

where

$$h_j = a_{1j}^* b_1 + \cdots + a_{lj}^* b_l \quad (\text{A.40})$$

Using the result in Equation (A.19), replacing f with h , the gradient of the real scalar function $G(\mathbf{x})$ with respect to the vector \mathbf{X} is,

$$\nabla G(\mathbf{x}) = 2 \frac{\partial}{\partial \mathbf{X}^*} (\mathbf{AX})^H \mathbf{B} = \begin{Bmatrix} h_1 \\ \vdots \\ h_n \end{Bmatrix} = \mathbf{A}^H \mathbf{B} \quad (\text{A.41})$$

Now, performing the gradient of $G^H(\mathbf{x})$ with respect to the vector \mathbf{X} , doing $\mathbf{B}^H \mathbf{A} = \mathbf{F}^H$, and using the result in Equation (A.15), so, the gradient of the scalar function $G^H(\mathbf{x})$ with respect to the vector \mathbf{X} is,

$$\nabla G^H(\mathbf{x}) = \nabla ((\mathbf{AX})^H \mathbf{B})^H = \nabla \mathbf{B}^H \mathbf{AX} = \nabla \mathbf{F}^H \mathbf{X} = \mathbf{F} = \mathbf{A}^H \mathbf{B} \quad (\text{A.42})$$

Now, applying the gradient to the case of $\Re\{G(\mathbf{x})\}$ with respect to the vector \mathbf{X} as,

$$2 \frac{\partial \Re\{G(\mathbf{x})\}}{\partial \mathbf{X}^*} = 2 \frac{\partial}{\partial \mathbf{X}^*} \Re\{(\mathbf{AX})^H \mathbf{B}\} = 2 \begin{Bmatrix} \frac{\partial}{\partial x_1^*} \Re\{(a_{11}^* b_1 + \cdots + a_{l1}^* b_l) x_1^*\} \\ \vdots \\ \frac{\partial}{\partial x_n^*} \Re\{(a_{1n}^* b_1 + \cdots + a_{ln}^* b_l) x_n^*\} \end{Bmatrix} = 2 \begin{Bmatrix} \frac{\partial}{\partial x_1^*} \Re\{h_1 x_1^*\} \\ \vdots \\ \frac{\partial}{\partial x_n^*} \Re\{h_n x_n^*\} \end{Bmatrix} \quad (\text{A.43})$$

Using the result in Equation (A.27), replacing f with h , so, the gradient of the scalar function $\Re\{G(x)\}$ with respect to the vector \mathbf{X} is,

$$\nabla\left(\Re\left\{(\mathbf{A}\mathbf{X})^H\mathbf{B}\right\}\right)=\begin{Bmatrix} h_1 \\ \vdots \\ h_n \end{Bmatrix}=\mathbf{A}^H\mathbf{B} \quad (\text{A.44})$$

Now, performing the gradient of $\Re\{G^H(x)\}$ with respect to the vector \mathbf{X} , doing $\mathbf{B}^H\mathbf{A}=\mathbf{F}^H$, and using the result in Equation (A.24), so, the gradient of the scalar function $\Re\{G^H(x)\}$ with respect to the vector \mathbf{X} is,

$$\nabla\left(\Re\{G^H(x)\}\right)=\nabla\Re\left\{((\mathbf{A}\mathbf{X})^H\mathbf{B})^H\right\}=\nabla\Re\{\mathbf{B}^H\mathbf{A}\mathbf{X}\}=\nabla\Re\{\mathbf{F}^H\mathbf{X}\}=\mathbf{F}=\mathbf{A}^H\mathbf{B} \quad (\text{A.45})$$

Now, applying the gradient to the case of $\Im\{G(x)\}$ with respect to the vector \mathbf{X} as,

$$2\frac{\partial\Im\{G(x)\}}{\partial\mathbf{X}^*}=2\frac{\partial}{\partial\mathbf{X}^*}\Im\left\{(\mathbf{A}\mathbf{X})^H\mathbf{B}\right\}=2\begin{Bmatrix} \frac{\partial}{\partial x_1^*}\Im\{a_{11}^*b_1+\dots+a_{1n}^*b_n\}x_1^* \\ \vdots \\ \frac{\partial}{\partial x_n^*}\Im\{a_{n1}^*b_1+\dots+a_{nn}^*b_n\}x_n^* \end{Bmatrix}=2\begin{Bmatrix} \frac{\partial}{\partial x_1^*}\Im\{h_1x_1^*\} \\ \vdots \\ \frac{\partial}{\partial x_n^*}\Im\{h_nx_n^*\} \end{Bmatrix} \quad (\text{A.46})$$

Using the result in Equation (A.33), replacing f with h , so, the derivative of the scalar function $\Re\{G(x)\}$ with respect to the vector \mathbf{X} is,

$$\nabla\left(\Im\left\{(\mathbf{A}\mathbf{X})^H\mathbf{B}\right\}\right)=\begin{Bmatrix} -ih_1 \\ \vdots \\ -ih_n \end{Bmatrix}=-i\mathbf{A}^H\mathbf{B} \quad (\text{A.47})$$

Now, performing the gradient of $\Im\{G^H(x)\}$ with respect to the vector \mathbf{X} , doing $\mathbf{B}^H\mathbf{A}=\mathbf{F}^H$, and using the result in Equation (A.32),so, the gradient of the scalar function $\Im\{G^H(x)\}$ with respect to the vector \mathbf{X} is,

$$\nabla\left(\Im\{G^H(x)\}\right)=\nabla\Im\left\{((\mathbf{A}\mathbf{X})^H\mathbf{B})^H\right\}=\nabla\Im\{\mathbf{B}^H\mathbf{A}\mathbf{X}\}=\nabla\Im\{\mathbf{F}^H\mathbf{X}\}=i\mathbf{F}=i\mathbf{A}^H\mathbf{B} \quad (\text{A.48})$$

A.4 Case III

Assuming a scalar function $G(x)$ in the form,

$$G(\mathbf{x}) = (\mathbf{CX})^H \mathbf{DX} \quad (\text{A.49})$$

where the matrix \mathbf{C} and \mathbf{D} are given by,

$$\mathbf{C} = \begin{Bmatrix} c_{11} & \cdots & c_{1n} \\ \vdots & \ddots & \vdots \\ c_{l1} & \cdots & c_{ln} \end{Bmatrix} \quad \text{and} \quad \mathbf{D} = \begin{Bmatrix} d_{11} & \cdots & d_{1n} \\ \vdots & \ddots & \vdots \\ d_{l1} & \cdots & d_{ln} \end{Bmatrix} \quad (\text{A.50})$$

The gradient of the Equation (A.49) can be performed using the product rule of the derivative as,

$$\nabla G(\mathbf{x}) = \nabla(\mathbf{CX})^H \mathbf{DX} = \nabla(\mathbf{AX})^H \mathbf{B} + \nabla \mathbf{F}^H \mathbf{X} \quad (\text{A.51})$$

where \mathbf{A} and \mathbf{B} in the first term of the right hand is equal to \mathbf{C} and \mathbf{DX} , respectively, and \mathbf{F}^H in the second term of the right hand is equal to $(\mathbf{CX})^H \mathbf{D}$.

Thus, using the results in Equations (A.41) and (A.15), the gradient of $G(\mathbf{x})$ with respect to the vector \mathbf{X} is given by,

$$\nabla((\mathbf{CX})^H \mathbf{DX}) = 2\mathbf{A}^H \mathbf{B} + 0 = 2\mathbf{C}^H \mathbf{DX} \quad (\text{A.52})$$

Now, the gradient of the case for $G^H(\mathbf{x})$ is given by,

$$\nabla G^H(\mathbf{x}) = \nabla((\mathbf{CX})^H \mathbf{DX})^H = \nabla(\mathbf{DX})^H \mathbf{CX} = \nabla(\mathbf{AX})^H \mathbf{B} + \nabla \mathbf{F}^H \mathbf{X} \quad (\text{A.53})$$

where \mathbf{A} and \mathbf{B} in the first term of the right hand is equal to \mathbf{D} and \mathbf{CX} , respectively, and \mathbf{F}^H in the second term of the right hand is equal to $(\mathbf{DX})^H \mathbf{C}$.

Thus, the gradient of $G^H(\mathbf{x})$ with respect to \mathbf{X} is equal to the gradient of $G(\mathbf{x})$ but with \mathbf{C} and \mathbf{D} inverted. So,

$$\nabla G^H(\mathbf{x}) = 2 \frac{\partial}{\partial \mathbf{X}^*} ((\mathbf{CX})^H \mathbf{DX})^H = 2 \frac{\partial}{\partial \mathbf{X}^*} (\mathbf{DX})^H \mathbf{CX} = 2\mathbf{D}^H \mathbf{CX} \quad (\text{A.54})$$

Now, applying the gradient to the case of $\Re\{G(x)\}$, using the product rule to the derivative as,

$$\nabla(\Re\{G(x)\}) = \nabla\Re\{(\mathbf{C}\mathbf{X})^H \mathbf{D}\mathbf{X}\} = \nabla\Re\{(\mathbf{A}\mathbf{X})^H \mathbf{B}\} + \nabla\Re\{\mathbf{F}^H \mathbf{X}\} \quad (\text{A.55})$$

where \mathbf{A} and \mathbf{B} in the first term of the right hand is equal to \mathbf{C} and $\mathbf{D}\mathbf{X}$, respectively, and \mathbf{F}^H in the second term of the right hand is equal to $(\mathbf{C}\mathbf{X})^H \mathbf{D}$.

Thus, using the results in Equations (A.44) and (A.24), the gradient of $\Re\{G(x)\}$ with respect to the vector \mathbf{X} is given by,

$$\nabla(\Re\{G(x)\}) = \mathbf{C}^H \mathbf{D}\mathbf{X} + \mathbf{D}^H \mathbf{C}\mathbf{X} = (\mathbf{C}^H \mathbf{D} + \mathbf{D}^H \mathbf{C})\mathbf{X} \quad (\text{A.56})$$

Now, applying the gradient to the case of $\Re\{G^H(x)\}$, using the product rule to the derivative as,

$$\nabla(\Re\{G^H(x)\}) = \nabla\Re\{(\mathbf{D}\mathbf{X})^H \mathbf{C}\mathbf{X}\} = \nabla\Re\{(\mathbf{A}\mathbf{X})^H \mathbf{B}\} + \nabla\Re\{\mathbf{F}^H \mathbf{X}\} \quad (\text{A.57})$$

where \mathbf{A} and \mathbf{B} in the first term of the right hand is equal to \mathbf{D} and $\mathbf{C}\mathbf{X}$, respectively, and \mathbf{F}^H in the second term of the right hand is equal to $(\mathbf{D}\mathbf{X})^H \mathbf{C}$.

Thus, the gradient of $\Re\{G^H(x)\}$ with respect to \mathbf{X} is equal to the gradient of $\Re\{G(x)\}$ but with \mathbf{C} and \mathbf{D} inverted. So,

$$\nabla(\Re\{G^H(x)\}) = \mathbf{D}^H \mathbf{C}\mathbf{X} + \mathbf{C}^H \mathbf{D}\mathbf{X} = (\mathbf{D}^H \mathbf{C} + \mathbf{C}^H \mathbf{D})\mathbf{X} \quad (\text{A.58})$$

Now, applying the gradient to the case of $\Im\{G(x)\}$, using the product rule to the gradient as,

$$\nabla(\Im\{G(x)\}) = \nabla\Im\{(\mathbf{C}\mathbf{X})^H \mathbf{D}\mathbf{X}\} = \nabla\Im\{(\mathbf{A}\mathbf{X})^H \mathbf{B}\} + \nabla\Im\{\mathbf{F}^H \mathbf{X}\} \quad (\text{A.59})$$

where \mathbf{A} and \mathbf{B} in the first term of the right hand is equal to \mathbf{C} and $\mathbf{D}\mathbf{X}$, respectively, and \mathbf{F}^H in the second term of the right hand is equal to $(\mathbf{C}\mathbf{X})^H \mathbf{D}$.

Thus, using the results in Equations (A.47) and (A.32), the gradient of $\Im\{G(x)\}$ with respect to the vector \mathbf{X} is given by,

$$\nabla(\Im\{G(x)\}) = -i\mathbf{C}^H \mathbf{D}\mathbf{X} + i\mathbf{D}^H \mathbf{C}\mathbf{X} = i(\mathbf{D}^H \mathbf{C} - \mathbf{C}^H \mathbf{D})\mathbf{X} \quad (\text{A.60})$$

Now, applying the gradient to the case of $\Im\{G^H(x)\}$, using the product rule to the gradient as,

$$\nabla(\Im\{G^H(x)\}) = \nabla\Im\{(\mathbf{D}\mathbf{X})^H \mathbf{C}\mathbf{X}\} = \nabla\Im\{(\mathbf{A}\mathbf{X})^H \mathbf{B}\} + \nabla\Im\{\mathbf{F}^H \mathbf{X}\} \quad (\text{A.61})$$

where \mathbf{A} and \mathbf{B} in the first term of the right hand is equal to \mathbf{D} and $\mathbf{C}\mathbf{X}$, respectively, and \mathbf{F}^H in the second term of the right hand is equal to $(\mathbf{D}\mathbf{X})^H \mathbf{C}$.

Thus, the gradient of $\Im\{G^H(x)\}$ with respect to \mathbf{X} is equal to the gradient of $\Im\{G(x)\}$ but with \mathbf{C} and \mathbf{D} inverted. So,

$$\nabla(\Im\{G^H(x)\}) = -i\mathbf{D}^H \mathbf{C}\mathbf{X} + i\mathbf{C}^H \mathbf{D}\mathbf{X} = i(\mathbf{C}^H \mathbf{D} - \mathbf{D}^H \mathbf{C})\mathbf{X} \quad (\text{A.62})$$

A.5 Summary

The results of the gradient are in Table A.1.

Table A.1: Summary of the gradient relations

	Function	Derivative
$G(x) = \mathbf{F}^H \mathbf{X}$	$G(x)$	\mathbf{F}
	$G^H(x)$	\mathbf{F}
	$\Re\{G(x)\}$	\mathbf{F}
	$\Re\{G^H(x)\}$	\mathbf{F}
	$\Im\{G(x)\}$	$i\mathbf{F}$
	$\Im\{G^H(x)\}$	$-i\mathbf{F}$
$G(x) = (\mathbf{A}\mathbf{X})^H \mathbf{B}$	$G(x)$	$\mathbf{A}^H \mathbf{B}$
	$G^H(x)$	$\mathbf{A}^H \mathbf{B}$
	$\Re\{G(x)\}$	$\mathbf{A}^H \mathbf{B}$
	$\Re\{G^H(x)\}$	$\mathbf{A}^H \mathbf{B}$
	$\Im\{G(x)\}$	$-i\mathbf{A}^H \mathbf{B}$
	$\Im\{G^H(x)\}$	$i\mathbf{A}^H \mathbf{B}$
$G(x) = (\mathbf{C}\mathbf{X})^H \mathbf{D}\mathbf{X}$	$G(x)$	$2\mathbf{C}^H \mathbf{D}\mathbf{X}$
	$G^H(x)$	$2\mathbf{D}^H \mathbf{C}\mathbf{X}$
	$\Re\{G(x)\}$	$(\mathbf{C}^H \mathbf{D} + \mathbf{D}^H \mathbf{C})\mathbf{X}$
	$\Re\{G^H(x)\}$	$(\mathbf{D}^H \mathbf{C} + \mathbf{C}^H \mathbf{D})\mathbf{X}$
	$\Im\{G(x)\}$	$i(\mathbf{D}^H \mathbf{C} - \mathbf{C}^H \mathbf{D})\mathbf{X}$
	$\Im\{G^H(x)\}$	$i(\mathbf{C}^H \mathbf{D} - \mathbf{D}^H \mathbf{C})\mathbf{X}$

A.6 Other usual relations for complex numbers

Consider the two complex numbers,

$$A = a_R + ia_I \quad \text{and} \quad B = b_R + ib_I \quad (\text{A.63})$$

The relation,

$$\begin{aligned} AB^* + A^*B &= (a_R + ia_I)(b_R + ib_I)^* + (a_R + ia_I)^*(b_R + ib_I) \\ &= 2a_R b_R + 2a_I b_I = 2\Re\{AB^*\} \end{aligned} \quad (\text{A.64})$$

The relation,

$$\begin{aligned} AB^* - A^*B &= (a_R + ia_I)(b_R + ib_I)^* - (a_R + ia_I)^*(b_R + ib_I) \\ &= 2ia_R b_I + 2ia_I b_R = 2i\Im\{AB^*\} \end{aligned} \quad (\text{A.65})$$

A.7 Application to cost functions

In general, a cost function can be written proposed by Nelson and Elliott (1991) as,

$$F = Q^H a Q + b_1 Q + Q^H b_2 + c \quad (\text{A.66})$$

where c is independent of Q , Q is a vector quantity, a is a matrix quantity, b_1 and b_2 are vector quantities and c is a scalar quantity. Therefore, F is a scalar quantity.

The objective is to find Q that minimizes F . Taking the gradient of F with respect to Q using the relations above,

$$\nabla F = 2a + b_1^H + b_2 \quad (\text{A.67})$$

The minimum is found equaling to zeros, so,

$$Q = -\frac{1}{2}a(b_1^H + b_2) \quad (\text{A.68})$$

That is the same result as used by Qiu et al. (1998).

Appendix B

Matlab/Simulink programs

The real time implementation of the algorithms were performed in a dSPACE 1102 control board using Matlab 4.2 and Simulink 1.0 from the Mathworks, Inc.

B.1 Filtered-X LMS in the time domain

The implementation of the filtered-X LMS shown here was developed for the cylinder application. The block diagrams of the filtered-X LMS in the time domain are shown in Figure B.1, Figure B.2 and Figure B.3. In Figure B.1 the main block of the Filtered-X LMS in time domain is shown, where the gains “Gain A/D 1”, “Gain A/D 2”, and “Gain D/A 1” are observed. The gains were introduced to make the signals compatible with the input/output signals, since the dSPACE 1102 control board divides the input signals by 10 and amplifies the output signal by 10.

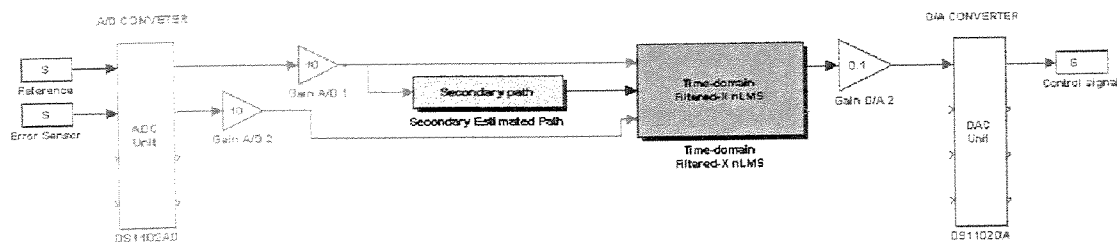


Figure B.1: Main block of the normalized Filtered-X LMS controller in the time domain.

In Figure B.2 the expansion of the block named “Time-Domain Filtered-X LMS” from Figure B.1 is shown, where it is noted the “Gain Control” and the “Gain Loop” blocks, which were introduced to make possible to turn the controller on and off during the real time implementations. In order to start the controller the gains “gct” and “glp” must be equal to 1.

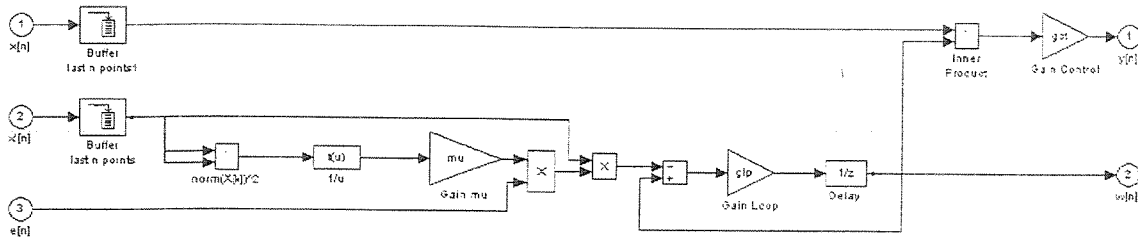


Figure B.2: Block of the normalized Filtered-X LMS algorithm.

In Figure B.3 the expansion of the block named “Secondary Estimated Path” is shown. The “Gain E”, “Gain M”, and “Gain V” blocks, where introduced in order to choose the sensor that is the error sensor. The blocks “Gain E”, “Gain M”, and “Gain V” represent the accelerometer, microphone and the velocity sensor used as error sensors, respectively. The values of the gains GA, GM and GV for each error sensor are given in Table B 1.

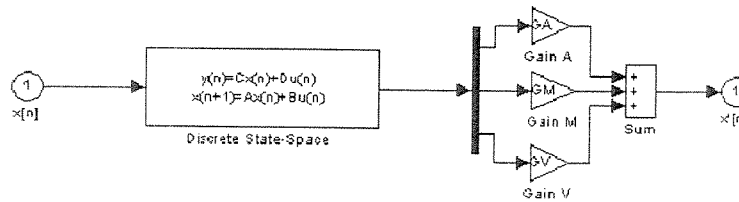


Figure B.3: Block diagram of the secondary path

Table B 1: Value of the gains to the secondary path block

Error sensor	GA	GM	GV
Accelerometer	1	0	0
Microphone	0	1	0
Velocity sensor	0	0	1

The on-line operation of the controller is possible due to the program Cockpit 1.0, where the options to turn the control on and off were implemented and are shown in Figure B.4. The step size μ ("Mu - Controller"), and the buttons to turn the control on and off ("Control"), to turn the loop on and off ("Loop"), and to chose the error sensor ("Accelerometer", "Microphone", "Velocity sensor") can be adjusted on-line.

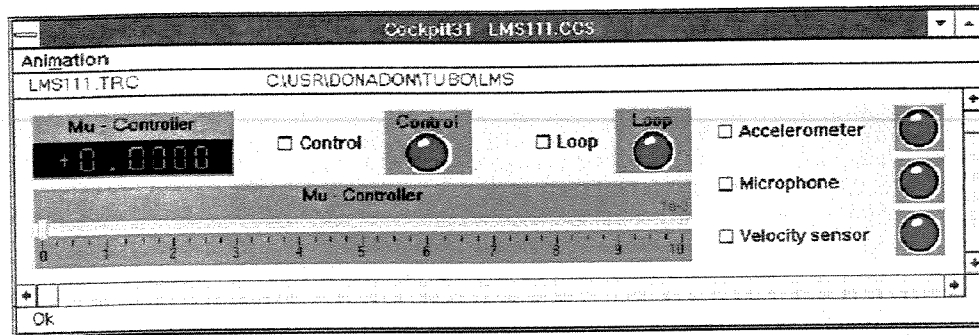


Figure B.4: Program "Cockpit" to control the real time implementation.

B.2 Filtered-X LMS Estimator

The block diagram for the filtered-X LMS as an estimator was implemented in the time domain, and the block diagrams are shown in Figure B.5 and Figure B.6. The program approximated the secondary source to a FIR (Finite Impulse Response).

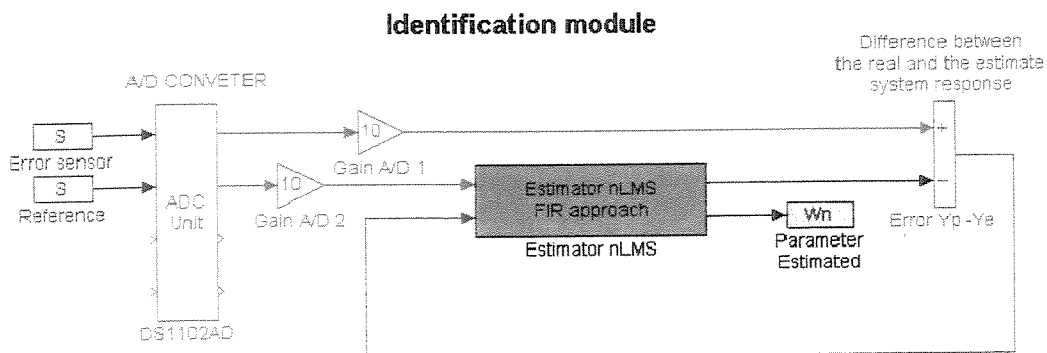


Figure B.5: Main block diagram to the Filtered-X LMS as an estimator.

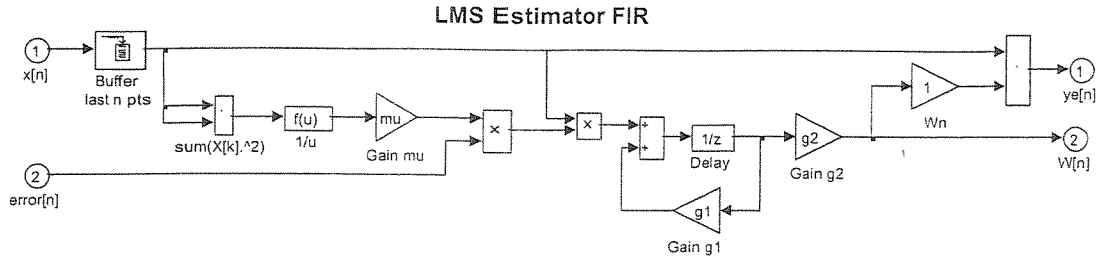


Figure B.6: Expansion of the block named Estimator nLMS in Figure B.5.

The gains “Gain g1” and “Gain g2” in Figure B.6 were introduced to make it possible to start and stop the estimation of the secondary source.

B.3 Frequency domain controllers

The control methods implemented in the frequency domain must have the signals changed from time domain to frequency domain using the Fast Fourier Transform (FFT), the methods calculate the control signal and an Inverse Fast Fourier Transform (IFFT) block to transform the signal to the time domain. These implementations are shown in Figure B.7, Figure B.8, and Figure B.9.

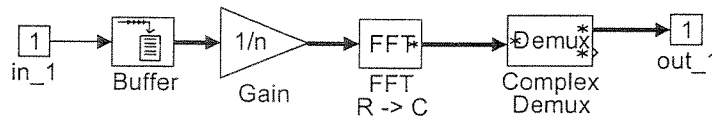


Figure B.7: Blocks to implement the FFT, expansion of the block “Time->Freq”.

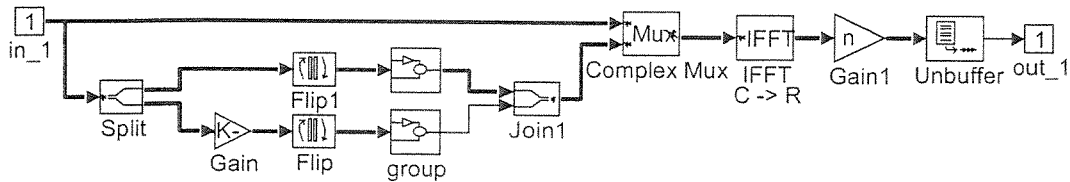


Figure B.8: Blocks to implement the IFFT, expansion of the block “Freq->Time”.

The block “group” in Figure B.9 must be implemented for each data length, i.e., this block implements the data mirroring that is necessary to the IFFT. So, its construction will depend on the number of the buffer length used, in Figure B.9 the data mirror was implemented for $N = 16$.

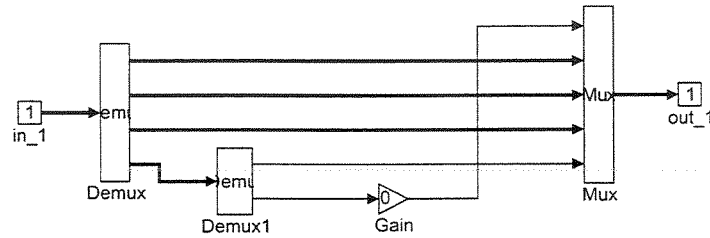


Figure B.9: Expansion of the block “group”

B.3.1 Filtered-X LMS in the frequency domain

The implementation of the filtered-X LMS in the frequency domain is shown in Figure B.10, Figure B.11, Figure B.12, and Figure B.13.

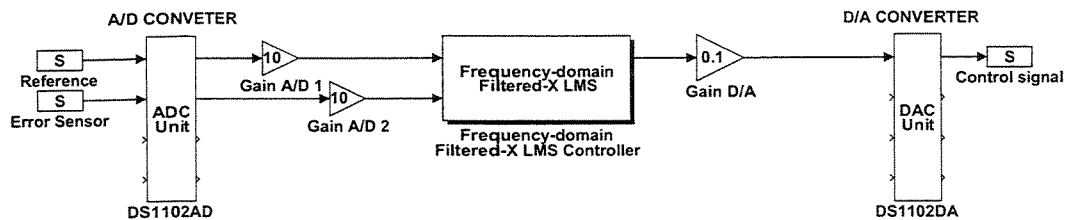


Figure B.10: Block diagram of the Filtered-X LMS in the frequency domain controller.

The gains “Gain A/D 1”, “Gain A/D 2”, and “Gain D/A 1” in Figure B.10 were introduced to make the signals compatible with the real signals, since the dSPACE 1102 control board divides the input signals by 10 and amplifies the output signal by 10.

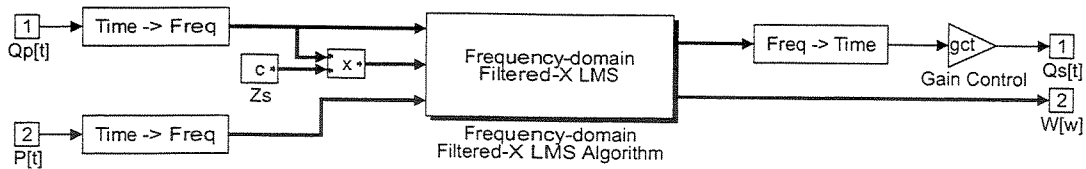


Figure B.11: Expansion of the block “Frequency-domain Filtered-X LMS Controller”.

In Figure B.11, the block “Zs” is the estimated secondary path, which can be implemented using the identified path directly. The blocks “Time->Freq” and “Freq->Time” were introduced to implement the transform of the signals to the frequency domain and to the time domain, respectively. The block “Gain Control” was introduced to turn the control on and off in the real time applications using the Cockpit 1.0 program.

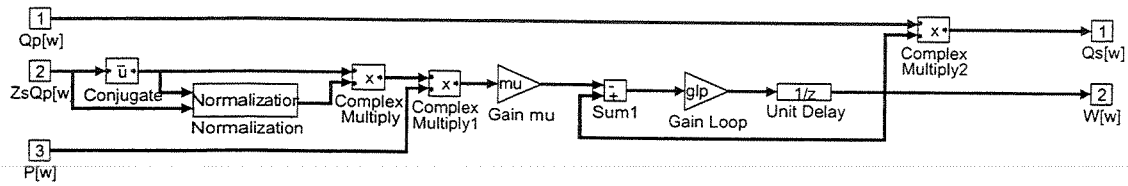


Figure B.12: Expansion of the block “Frequency-domain Filtered-X LMS Algorithm”.

In Figure B.12 the block “Gain Loop” was introduced to make it possible to control in real time the adaptation of the algorithm. In Figure B.12 and Figure B.13 the implementation of the normalization can be seen, and it is notorious that the normalization implies in an increase in the computational efforts.

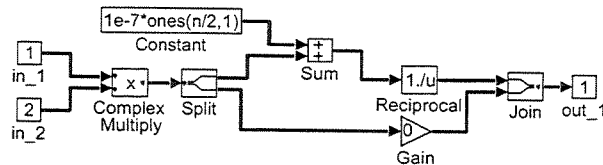


Figure B.13: Expansion of the block “normalization” to LMS.

B.3.2 ASIC using P-U approach

The implementation of the ASIC-PU controller is shown in Figure B.14, Figure B.15, Figure B.16, and Figure B.17. It is observed that the implementation is close to the filtered-X LMS in the frequency domain.

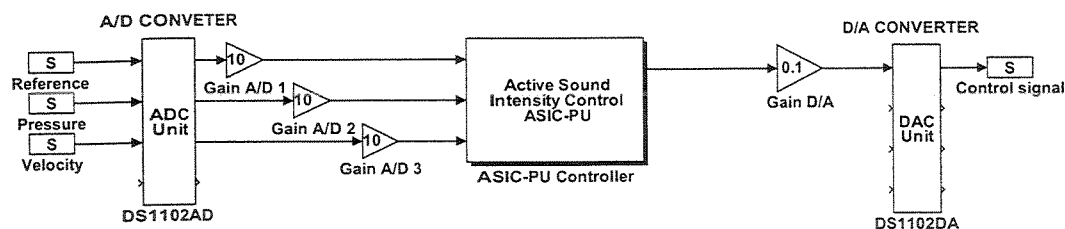


Figure B.14: Block diagram of the ASIC-PU controller.

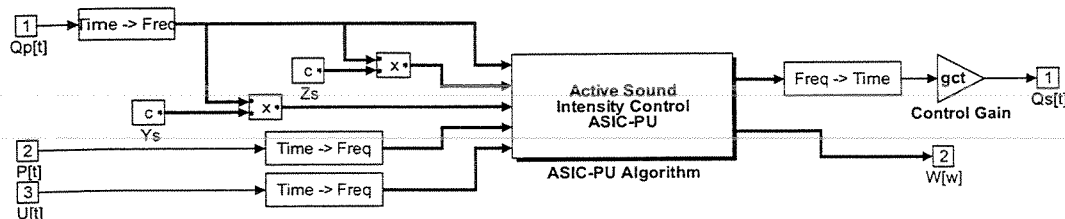


Figure B.15: Expansion of the block “ASIC-PU Controller”.

In Figure B.15 the blocks “Zs” and “Ys” are the secondary estimated path for pressure and particle velocity, respectively.

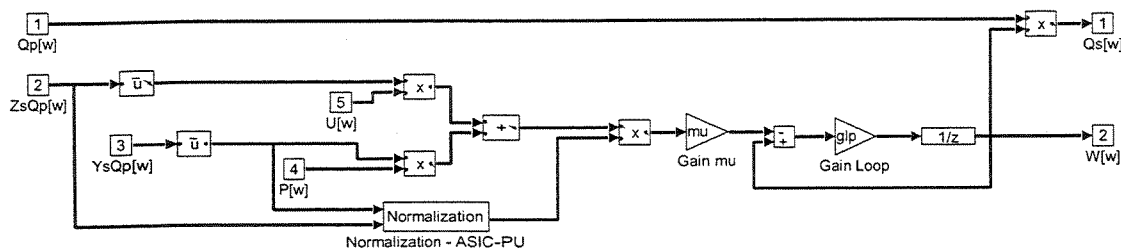


Figure B.16: Expansion of the block “ASIC-PU Algorithm”.

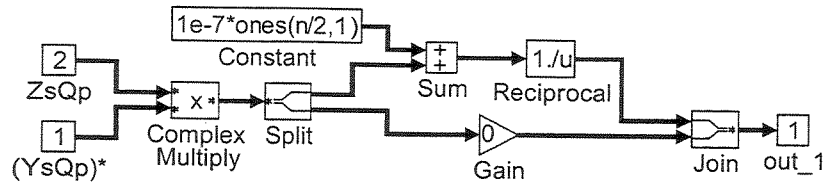


Figure B.17: Expansion of the block “normalization – ASIC-PU”.

B.3.3 ASIC using the P-P approach

The implementation of the ASIC-PP controller is shown in Figure B.18, Figure B.19, Figure B.20, and Figure B.21. It is observed that the implementation is nearly equal to the other control methods, filtered-X LMS and the ASIC-PU.

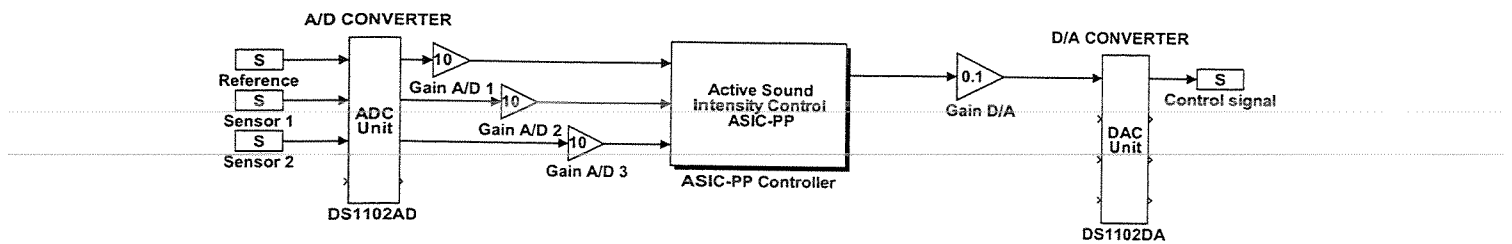


Figure B.18: Block diagram of the ASIC-PP controller.

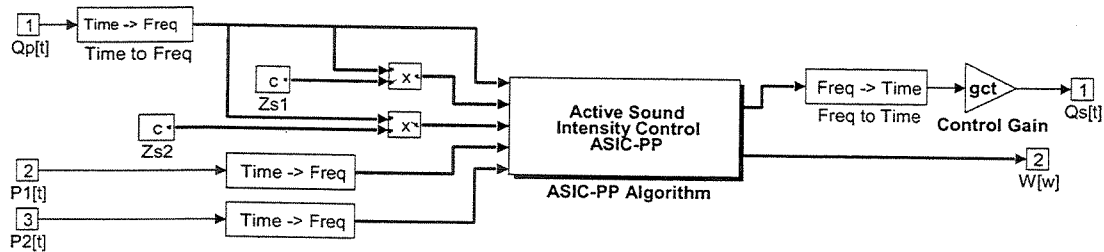


Figure B.19: Expansion of the block “ASIC-PP Controller”.

In Figure B.19 the blocks “Zs1” and “Zs2” are the secondary estimated path for the first and second error sensors, respectively.

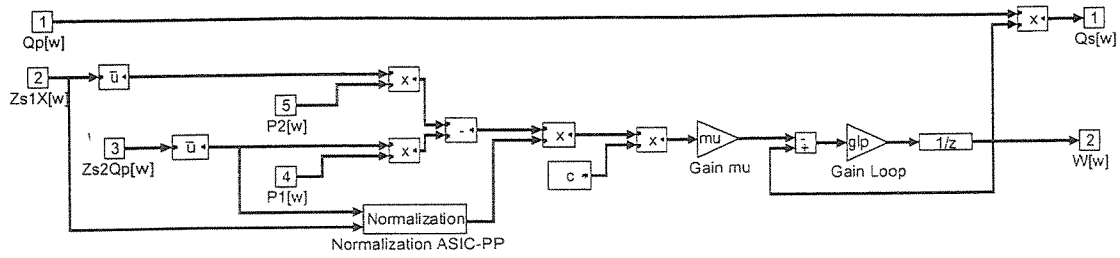


Figure B.20: Expansion of the block “ASIC-PP Algorithm”.

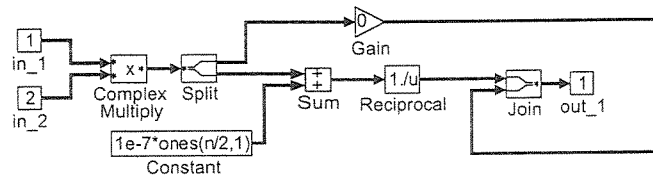


Figure B.21: Expansion of the block “normalization – ASIC-PP”.

B.3.4 Stating the real time implementation

Before starting the real time applications it is necessary to set some variables as presented in Figure B.22 for the ASIC-PP. The structures are the same for other control methods and, therefore, they will not shown here.

ASIC-PP Controller (Mask)

Block name: ASIC-PP Controller

Block type: ASIC-PP Controller (Mask)

Active Sound Intensity Control - ASIC-PP
Lázaro Valentim Donadon
DMQ/FEM/UNICAMP

Buffer length:
N

Step-size:
0

Sample Time:
ts

Control Gain:
0

Loop Gain:
0

Secondary Path:
Hs(-1 2)]

OK Cancel Help

Figure B.22: Initial data from the ASIC-PP.

In Figure B.22 “Hs” is the secondary path estimated in the frequency domain, the algorithm splits automatically the Hs to form Zs_1 and Zs_2 . The same procedure was developed for the other control methods.

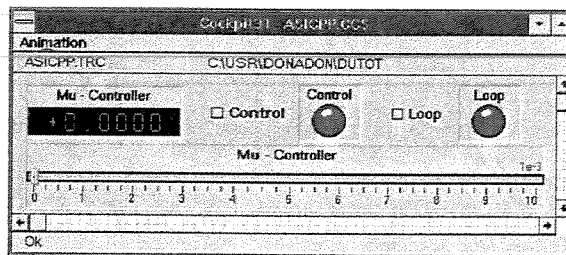


Figure B.23: Graphic interface developed in Cockpit 1.0 to drive the controllers in real time.

In Figure B.23 the graphic interface developed to drive the controller in real time is shown, the “Control” and the “Loop” are used to turn the controller and the loop on and off, respectively. The “Mu-Controller” is used to adjust on-line the step-size of the controller (the parameter μ).

B.3.5 Program to load the dSPACE 1102 control board

The program below illustrates how to choose correctly the implementation for the frequency domain controllers. The secondary paths were acquired with a sample frequency of

2048 Hz in the range of 0 to 512 Hz. The real time implementations were only possible for a sample time of 1.5 ms and $N = 16$ (buffer size). Therefore, the Nyquist frequency was 666.66 Hz, observed without leakage in 41.66, 83.33, 125, 166.66, 208.33 and 250 Hz. But the controllers were implemented for 41.66, 83.33, and 125 Hz, and the other frequencies were equal to zero. This procedure is done using the program below. The program extracts a vector of size equal to 16 for frequencies multiples of 41.66 Hz from the secondary path and makes the values different of 41.66, 83.33 and 125 Hz equal to zero.

```

%%%%%%%%%%%%%%%%%%%%%%%%%%%%%%%%%%%%%%%%%%%%%%%%%%%%%%%%%%%%%%%%%%%%%%%%
%
%   Program to load the dSPACE 1102 control board
%   with the data used in the control application
%
%%%%%%%%%%%%%%%%%%%%%%%%%%%%%%%%%%%%%%%%%%%%%%%%%%%%%%%%%%%%%%%%%%%%%%%%
clear all;close all;clc;pack
%=====
%           Loading the secondary path
%=====
% this path must be change to each control method
load DutoP % secondary path
%=====
%           Initial set up to the control application
%=====
ts=1.5e-3; % sample time
N=16; % buffer length
%=====
%   Adjusting the FRFS to match with the sample time
%=====
df=1/(N*ts); % sample frequency
fn=[0:df:(N/2-1)*df]; % possible frequencies to be controlled
fcon=fn(2:4); % controlled frequencies
% matching the frequencies to the FRFs
for k=1:length(fcon)
    indS(k)=find(fn==fcon(k));
end
% Interpolating the values
Hn=interp1(f,Zs,fn,'cubic');
% Creating the secondary path to the controller
Hs=zeros(N/2,size(Zs,4));
Hs(indS,:)=Hn(indS,:);
%=====END=====

```

B.4 Matlab Controllers

The programs to implement theoretically the controllers are listed below.

Program 1:

```
function [Y,W]=LMS_FD(Hp,Hs,X,mu,nint,Opt)

% LMS_FD      -> Multiple error Filtered-X LMS in frequency domain
%
%%%%%%%%%%%%%%%%%%%%%%%%%%%%%%%%%%%%%%%%%%%%%%%%%%%%%%%%%%%%%%%%%%%%%%%%
%%           [Y,W]=LMS_FD(Hp,Hs,X,mu,nint,Opt)
%%%%%%%%%%%%%%%%%%%%%%%%%%%%%%%%%%%%%%%%%%%%%%%%%%%%%%%%%%%%%%%%%%%%%%%%
%%
%%   The vectors must be columns in frequency domain
%%   without the mirror part
%%
%%   where
%%
%%       X -> reference
%%       W -> weight vector
%%       E -> error signal
%%
%%       Hp -> FRF from the passive path
%%       Hs -> FRF from the active path
%%
%%       nint -> Iteration number
%%       mu   -> step-size           0<=mu<=1
%%%%%%%%%%%%%%%%%%%%%%%%%%%%%%%%%%%%%%%%%%%%%%%%%%%%%%%%%%%%%%%%%%%%%%%%
%%
%%   Cost function      J(n) = E(n)E(n)*
%%%%%%%%%%%%%%%%%%%%%%%%%%%%%%%%%%%%%%%%%%%%%%%%%%%%%%%%%%%%%%%%%%%%%%%%
%%
%%   Adaptive Equation
%%%%%%%%%%%%%%%%%%%%%%%%%%%%%%%%%%%%%%%%%%%%%%%%%%%%%%%%%%%%%%%%%%%%%%%%
%%
%%
%%

$$W(n+1) = W(n) - \frac{\mu}{P_m(n)} (H_s X)^*(n) E(n)$$

%%
%%   Normalization      Pm(n) = |Hs X|^2
%%
%%   Error Equation : E = Hp X + Hs Y
%%%%%%%%%%%%%%%%%%%%%%%%%%%%%%%%%%%%%%%%%%%%%%%%%%%%%%%%%%%%%%%%%%%%%%%%
%%
%%   Author : Lázaró Valentim Donadon - 03/06/2000
%%%%%%%%%%%%%%%%%%%%%%%%%%%%%%%%%%%%%%%%%%%%%%%%%%%%%%%%%%%%%%%%%%%%%%%%
if size(Hp,2)~=size(Hs,2)
    disp('actuators and sensors INCORRECT')
elseif size(Hp,1)~=size(Hs,1)
    disp('sample frequency incorrect')
end
W = zeros(size(Hp,1),1);
for j=1:nint
    n=size(Hp,2);
    % Filter response
    Y=W.*X;
    % Error sensor responses
    E=Hp.*repmat(X,size(Hp))+Hs.*repmat(Y,1,size(Hs,2));
```

```

    % Estimate of the gradient
    grad=(conj(Hs.*repmat(X,size(Hs)))/(abs(Hs.*repmat(X,size(Hs))).^2)).*E;
    % ajuste dos pesos
    W=W-mu.*sum(grad,2);
end
%%%%%%%%%%%%%%%%%%%%%%%%%%%%%%%%%%%%%%%%%%%%%%%%%%%%%%%%%%%%%%%%%%%%%%%%

```

```

function [Y,W]=Asic_PU(Zp,Zs,Yp,Ys,X,mu,nint,f)

```

```

% Asic_PU    -> Active Intensity using P-U approach
%
%%%%%%%%%%%%%%%%%%%%%%%%%%%%%%%%%%%%%%%%%%%%%%%%%%%%%%%%%%%%%%%%%%%%%%%%
%%      [Y,W]=Asic_PU(Zp,Zs,Yp,Ys,X,mu,nint,f)
%%%%%%%%%%%%%%%%%%%%%%%%%%%%%%%%%%%%%%%%%%%%%%%%%%%%%%%%%%%%%%%%%%%%%%%%
%%
%%      The vectors must be columns in frequency domain
%%      without the mirror part
%%
%%      where
%%
%%          X -> reference
%%          W -> weight vector
%%          P -> Pressure
%%          u -> particle velocity
%%%%%%%%%%%%%%%%%%%%%%%%%%%%%%%%%%%%%%%%%%%%%%%%%%%%%%%%%%%%%%%%%%%%%%%%
%%      Zp -> FRF in impedance to the primary source
%%      Zs -> FRF in Impedance to the secondary source
%%      Yp -> FRF in particle velocity to the primary source
%%      Ys -> FRF in particle velocity to the secondary source
%%
%%      nint    -> Iteration number
%%      mu      -> step-size          0<=mu<=1
%%%%%%%%%%%%%%%%%%%%%%%%%%%%%%%%%%%%%%%%%%%%%%%%%%%%%%%%%%%%%%%%%%%%%%%%
%%
%%      Equations
%%
%%      Intensity      I = (1/2)Re{P*u}
%%
%%      Cost function   J(n) = I^2
%%
%%      Adaptive equation
%%
%%          W(n+1) = W(n) - mu *  $\frac{X^*}{|X|^2} - \frac{P Y_c^* + u Z_c^*}{Z_c Y_c^* + Y_c Z_c^*}$ 
%%
%%      Error : P = Zp X + Zs Y
%%              u = Yp X + Ys Y
%%%%%%%%%%%%%%%%%%%%%%%%%%%%%%%%%%%%%%%%%%%%%%%%%%%%%%%%%%%%%%%%%%%%%%%%
%%

```

```

%%      Author : Lázaro Valentim Donadon - 03/06/2000      %
%%                                                         %
%%%%%%%%%%%%%%%%%%%%%%%%%%%%%%%%%%%%%%%%%%%%%%%%%%%%%%%%%%%%%%%%%%%%%%%%

```

```

n = length(X);
W = zeros(n,1);
for j=1:nint
    % filter response
    Y=W.*X;
    % Error sensor responses
    P(:,j)=Zp.*X+Zs.*Y;
    u(:,j)=Yp.*X+Ys.*Y;
    % estimate of the gradient
    num=P(:,j).*conj(Ys)+u(:,j).*conj(Zs);
    den=(conj(X).*X).*real(Zs.*conj(Ys));
    grad=conj(X).*num./(10e-15+den);
    % adaptie equation
    W=W-mu.*grad;
end

```

```

%%%%%%%%%%%%%%%%%%%%%%%%%%%%%%%%%%%%%%%%%%%%%%%%%%%%%%%%%%%%%%%%%%%%%%%%

```

```

function [Y,W]=Asic_PP(Hp,Hs,X,mu,nint)

```

```

% Asic_PP      -> Active intensity using P-P approach
%

```

```

%%%%%%%%%%%%%%%%%%%%%%%%%%%%%%%%%%%%%%%%%%%%%%%%%%%%%%%%%%%%%%%%%%%%%%%%

```

```

function [Y,W]=Asic_PP(Hp,Hs,X,mu,nint)

```

```

%%%%%%%%%%%%%%%%%%%%%%%%%%%%%%%%%%%%%%%%%%%%%%%%%%%%%%%%%%%%%%%%%%%%%%%%

```

```

% The vectors must be columns in frequency domain
% without the mirror part

```

```

% where

```

```

% X -> reference
% W -> weight vector

```

```

% Hp -> FRF from the passive path
% Hs -> FRF from the active path

```

```

% nint -> Iteration number

```

```

% mu    -> step-size          0<=mu<=1

```

```

%%%%%%%%%%%%%%%%%%%%%%%%%%%%%%%%%%%%%%%%%%%%%%%%%%%%%%%%%%%%%%%%%%%%%%%%

```

```

% Basic Equations

```

```

% Intensity          I = 
$$\frac{1}{2 w \rho D x} \operatorname{Im}\{E_1(E_2)^*\}$$


```

```

% Cost function      J(n) = I^2

```

```

%% Adaptive equation
%%
%%      E2 (Hs1X)* - E1 (Hs1X)*
W(n+1) = W(n) - mu i -----
%%                               Im{Hc1X (Hc2X)*}
%%
%%      Error :  E1 = Hp1 X + Hc1 Y - sensor 1
%%               E2 = Hp2 X + Hc2 Y - sensor 2
%%
%%%%%%%%%%%%%%%%%%%%%%%%%%%%%%%%%%%%%%%%%%%%%%%%%%%%%%%%%%%%%%%%%%%%%%%%
%%
%%      Author : Lázaro Valentim Donadon - 03/06/2000
%%
%%%%%%%%%%%%%%%%%%%%%%%%%%%%%%%%%%%%%%%%%%%%%%%%%%%%%%%%%%%%%%%%%%%%%%%%
W = zeros(size(Hp,1),1);
for j=1:nint
    % Control law
    Y=W.*X;
    % sensor response
    E1=Hp(:,1).*X+Hs(:,1).*Y;
    E2=Hp(:,2).*X+Hs(:,2).*Y;
    % estimate gradient
    num=sqrt(-1)*(conj(Hs(:,1).*X).*E2-conj(Hs(:,2).*X).*E1);
    den=imag(Hs(:,1).*X.*conj(Hs(:,2).*X));
    grad=num./(2*den);
    % adaptive equation
    W=W-mu.*grad;
end

%=====

```

B.5 Implementation to the spectral element method to acoustic cases

```

function [Z,Y]=SEM_Duct_2D(Conect,Coord,x0,CondCon,S,K)

% SEM_Duct_2D.m      - FUNÇÃO para cálculo das FRFs teóricas de um elemento de
% Duto
%
% [Z,Y]=SEM_Duct_2D(Conect,Coord,x0,CondCon,S,K)
% FRFs para uma rede de dutos em 2D
%
% Z - Impedancia [Pa/velocidade de Volume]
% Y - Mobilidade [Velocidade de Volume/ velocidade de Volume]
% S - area do duto
% K - numero de onda
% x0 - no' da excitacao
% Conect - Matriz de conectividade [no' elem i elem j]
% Coord - Matriz das coordenadas dos elementos [elem comprimento angulo]
% CondCon - Matriz das condicoes de contorno [no' CC]
%
%      1 -> posicao da fonte
%      2 -> duto aberto
%      3 -> duto infinito

```

```

if nargin==0
    help SEM_Duct_2D
    break
end

[n m]=size(K);
if n<m
    K=K.';
end

%=====
%                               Acoustic Datas
%=====
im = sqrt(-1);           % imaginary number
rho = 1.21;              % air density [kg/m3]
c = 343;                 % sound speed [m/s]
%=====
%                               Frequency Range
%=====
f = c*K/(2*pi);
w = 2*pi*f;              % angular frequency [rad/s]
Np = length(f);          % número de pontos na frequência
Ne = size(Conect,1);      % número de elementos
Nn = max(max(Conect));    % número de nós
if length(S)==1 ; S=S*ones(1,Ne) ; end
%=====
%                               localizando condições de contorno
%=====
% posição da fonte
Q = zeros(Ne+1,1);
Q(x0)=1;
% posição de abertura Locin = 2
indA=CondCon(find(CondCon(:,2)==2)); % duto aberto
% posição de abertura Locin = 3
indI=CondCon(find(CondCon(:,2)==3)); % duto infinito
%=====
%                               Impedâncias Localizadas
%=====
% duto aberto
for n=1:Ne
    a=sqrt(S(n)/pi); % raio equivalente
    Zm(:,n)=rho*c*S(n)*((1/4)*(K*a).^2+im*0.6*K*a);
end
% duto infinito
Zinf=(rho*c);
%=====
% Matriz Global e Funções de Transferências em Impedância
%=====
for i=1:Np
    GlobMatr = zeros(Nn,Nn);
    for n=1:Ne
        % calculando a matriz elementar (L,S,K,rho,c)
        Elem = Elem_Duct(Coord(n,2),S(n),K(i),rho,c);
        % fazendo a transformação de coordenadas
        ElemT = Transform_2D(Elem,Coord(n,3));
        % montando a matriz global
    end
end

```

```

        GlobMatr (Conect (n,2:3),Conect (n,2:3))
GlobMatr (Conect (n,2:3),Conect (n,2:3)) + Elem;
end
% adicionando aberturas
if ~isempty(indA)
    for j=1:length(indA)
        GlobMatr(indA(j),indA(j))=GlobMatr(indA(j),indA(j))+(S(j)^2/Zm(i));
    end
end
% adicionando elemento infinito
if ~isempty(indI)
    for j=1:length(indI)
        GlobMatr(indI(j),indI(j))=GlobMatr(indI(j),indI(j))+S(j)/Zinf;
    end
end
end

```

```

% invertendo a matriz
HPl=GlobMatr\Q;
Z(i,:)=HPl.'; % função de resposta em frequência em Pressão
end

```

```

%=====
% Funções de Transferências em velocidade de partícula
%=====
for n=1:Ne
    for i=1:Np
        NGlobMatr=Elem_Duct (Coord(n,2),S(n),K(i),rho,c);
        Y(i,n:n+1)=(NGlobMatr*(Z(i,n:n+1).')).';
    end
end

```

```

Y(:,Nn)=-Y(:,Nn); % função de resposta em frequência em Velocidade
%%%%%%%%%%%%%%%%%%%%%%%%%%%%%%%%%%%%%%%%%%%%%%%%%%%%%%%%%%%%%%%%%%%%%%%%

```

```

%%%%%%%%%%%%%%%%%%%%%%%%%%%%%%%%%%%%%%%%%%%%%%%%%%%%%%%%%%%%%%%%%%%%%%%%
function Elem=Transform_2D(Elems,phi)
T=[cos(phi) sin(phi) ; -sin(phi) cos(phi)];
Elem=(T')*Elems*T;
%%%%%%%%%%%%%%%%%%%%%%%%%%%%%%%%%%%%%%%%%%%%%%%%%%%%%%%%%%%%%%%%%%%%%%%%

```

```

function K_Elem=Elem_Duct(L,S,K,rho,c)

% Elem_Duct.m - matriz de rigidez dinamica de um duto
%
% [K_Elem]=Elem_Duct(L,S,K,rho,c)
% Matriz elementar de duto
%
% L -> comprimento do elemento
% S -> área transversal
% K -> numero de onda
%
%%%%%%%%%%%%%%%%%%%%%%%%%%%%%%%%%%%%%%%%%%%%%%%%%%%%%%%%%%%%%%%%%%%%%%%%
%%
%% Equação elementar
%%
%% |U1| S 1 | 1+e^(2iKL) -2e^(iKL) ||P1|
%% | | = - ---- | | |
%%

```

```

%% |U2|          c rho    1 - e^(i2KL)    | -2e^(iKL)    1+e^(2iKL) ||P2| %
%%
%%%%%%%%%%%%%%%%%%%%%%%%%%%%%%%%%%%%%%%%%%%%%%%%%%%%%%%%%%%%%%%%%%%%%%%%
if nargin==0
    help Elem_Duct
    break
end

%=====
%                               constants
%=====

im=sqrt(-1);                % número imaginário

%=====
%                               Elementar Matrix      (1/Z)
%=====

gain=S/(c*rho);
delta=1-exp(im*2*K*L);

KD  = gain./delta.*(1+exp(im*2*K*L));
KDm = gain./delta.*(-2*exp(im*K*L));

K_Elem=-[KD  KDm ; KDm KD]; % matriz elemntar 1/Z

%%%%%%%%%%%%%%%%%%%%%%%%%%%%%%%%%%%%%%%%%%%%%%%%%%%%%%%%%%%%%%%%%%%%%%%%

```

Appendix C

Modal parameter identification and extraction from FRFs

In order to implement the controllers successfully, the secondary path must be identified, this identification can be performed “on-line” or “off-line”. The “on-line” system identification consists of implementing simultaneously the controller and the estimator, Kuo and Morgan (1996). The off-line system identification consists of identifying firstly the secondary path and then implementing the controller with the identification performed.

The system identification can be applied by recursive methods, such as Least Mean Square –LMS, Recursive Least Squares – RLS, and others, or by non-recursive methods such as Eigensystem Realization Algorithm – ERA, Least Squares Complex Experimental – LSCE, and others.

The advantages and disadvantages of each method can be summarized as:

The non-recursive identification methods, normally implemented off-line, use commonly a narrow band white noise in the frequency band of the primary source. These kinds of methods are robust and work well in the chosen frequency band. However, if there are variations in the acoustic path, as impedance alterations, changes in the position of the secondary source and the error sensors, the system identification should be performed again. On the other hand, it is important to remember that the adaptive algorithms can adapt to small changes; so, the user should judge on the necessity of identifying again the secondary path.

The recursive methods, which can be implemented on-line or off-line, are less robust than the non-recursive methods and the computational cost is high because the identification is performed continuously. On the other hand, they are able to adapt to possible variation in the secondary paths.

The main problems with the on-line system identification are the possible competition between the controller and the estimator. The estimator implemented should be faster than the controller. The computational cost is high because there are two adaptive algorithms working at the same time, and the difficulty caused by identifying a MISO system (Multiples Inputs and Single output) system.

The system identification methods are shown shortly, and one can obtain more information in the references given. In the first, part the LMS estimator is reviewed, Haykin (1996) and Kuo and Morgan (1996). In the second part, the method ERA, Juang and Pappa (1985) and Juang (1994), is reviewed. In the third part, the method ORTPOLY, Arruda et al. (1996) is reviewed.

C.1 Least Mean Square as Parameter Estimator

The first step when performing system identification is the choice of the model by which the unknown path is approximated, several models can be found in Ljung (1987). Here, the LMS as an estimator is shown in Figure C.1, where the “unknown path” is modeled by a Finite Impulse Response (FIR). The objective of the algorithm is to find out $S(z)$ in order to drive to zero the difference between the response from the unknown path and the response from the estimated path.

Observing Figure C.1, it can be seen that the error $e(n)$ is given by,

$$\begin{aligned} e(n) &= y(n) - y'(n) \\ &= y(n) - w^T(n)x(n) \end{aligned} \tag{C.1}$$

where $s(n)$ is the impulse response of $S(z)$ at time n , and $w(n)$ and $x(n)$ are given by,

$$\begin{aligned} \mathbf{x}(n) &= [x(n) \quad x(n-1) \quad \dots \quad x(n-L+1)]^T \\ \mathbf{w}(n) &= [w_0(n) \quad w_1(n) \quad \dots \quad w_{L-1}(n)]^T \end{aligned} \quad (\text{C.2})$$

where L is the order of the filter $w(n)$.

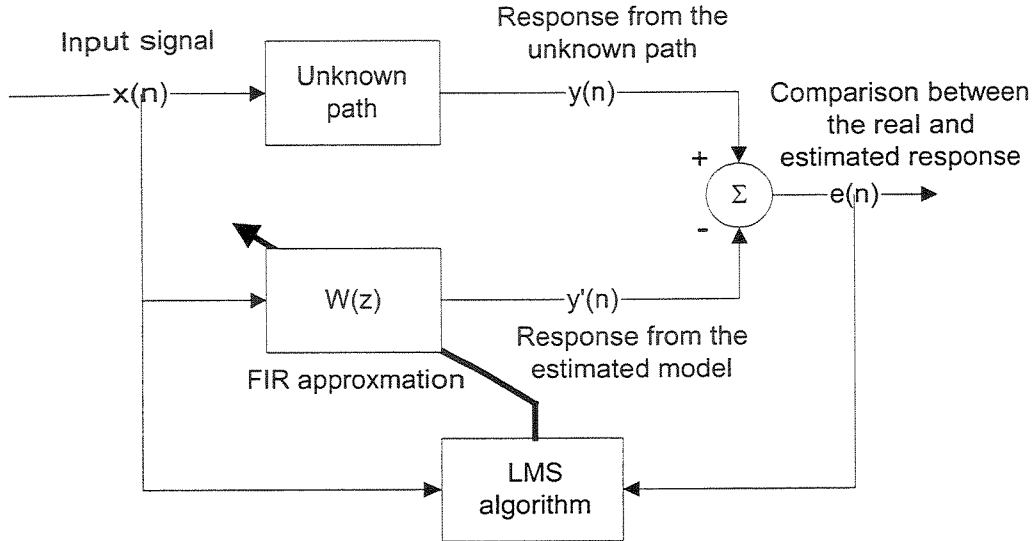


Figure C.1: Block diagram of the Least Mean Square algorithm as an estimator.

The adaptive law is developed using a self-orthogonalizing adaptive filtering algorithm as Haykin (1996) and Cowan (1987),

$$\mathbf{w}(n+1) = \mathbf{w}(n) - \mu \mathbf{R}^{-1} \nabla J(n) \quad (\text{C.3})$$

where n is the iteration time, μ is the step size defined between 0 and 1, \mathbf{R}^{-1} is the inverse of a correlation matrix \mathbf{R} , and $\nabla J(n)$ is the gradient of the cost function at iteration n .

The cost function $J(n)$ is defined as the instantaneous squared error, Widrow (1985),

$$J(n) = e^2(n) \quad (\text{C.4})$$

Taking the gradient of the cost function with respect to $\mathbf{W}(n)$,

$$\nabla J(n) = 2e(n) \frac{\partial e(n)}{\partial W(n)} = 2e(n) \begin{Bmatrix} \frac{\partial e(n)}{\partial w_0(n)} \\ \vdots \\ \frac{\partial e(n)}{\partial w_{L-1}(n)} \end{Bmatrix} = -2e(n)X(n) \quad (C.5)$$

The correlation matrix R can be found as in Widrow (1985), substituting (C.1) in (C.5),

$$-2(y(n) - x^T(n)w(n))x(n) = -2y(n)x(n) + X^T(n)w(n)x(n) \quad (C.6)$$

When applying the expected value, $W(n)$ is replaced by W_{opt} , so,

$$\nabla J = -2E[y(n)x(n)] + W_{opt}E[X^T(n)x(n)] \quad (C.7)$$

where $E[y(n)x(n)] = P$ and $E[x^T(n)x(n)] = R$ when the method converge at $n \rightarrow \infty$, so

$$\nabla J = -2P + W_{opt}R \quad (C.8)$$

Now, substituting the correlation matrix R and the gradient in the adaptive law, is found the LMS as an estimator,

$$w(n+1) = w(n) - \frac{\mu}{\alpha + |x(n)|^2} x(n)e(n) \quad (C.9)$$

where α is a small constant to avoid division by zero.

C.2 Eigensystem Realization Algorithm

The Eigensystem Realization Algorithm, ERA, consists of taking the time response of the system and extracting a state space model of minimal order. As the system identification is performed measuring the FRFs in the frequency domain, it is necessary transform the measured FRFs to the time domain first.

Considering a linear, discrete and time invariant system in the state space form as,

$$\begin{aligned} x(k+1) &= Ax(k) + Bu(k) \\ y(k) &= Cx(k) \end{aligned} \quad (C.10)$$

where A , B and C are the state space matrixes and x are the state variables at instant k .

The block controllability matrix $Q(k)$ of the system defined in Equation (C.10) is given by,

$$Q(k) = [B \quad AB \quad A^2B \quad \dots \quad A^{k-1}B] \quad (C.11)$$

The final state $x(k)$ of the system defined in Equation (C.10) can be written using the controllability matrix as,

$$x(k) = A^k x(0) + Q(k) [u(k-1) \quad u(k-2) \quad u(k-3) \quad \dots \quad u(0)]^T \quad (C.12)$$

The observability matrix $P(k)$ of the system defined in Equation (C.10) is given by,

$$P(k) = [C \quad CA \quad CA^2 \quad \dots \quad CA^{k-1}]^T \quad (C.13)$$

The final response to the system defined in Equation (C.10) can be written using the observability matrix as,

$$y(k) = P(k)x(0) \quad (C.14)$$

The impulse response of the system in Equation (C.10) using the Markov parameters is given by,

$$y_{ji}(k) = c_j A^{k-1} b_i \quad \begin{cases} i = 1, 2, \dots, m \\ j = 1, 2, \dots, p \\ k = 1, 2, \dots \end{cases} \quad (C.15)$$

where m is the number of inputs, p is the number of outputs, c_j is the row vector of the j^{th} output, and b_i is the column vector of the i^{th} input.

The problem of the minimal eigensystem realization is stated as:” Given a set of functions $y_{ji}(k)$, obtain a set of constant matrixes (A, B , and C) in terms of $y_{ji}(k)$ so that the identity in Equation (C.15) is true and the rank of A is minimum.

The response matrix $Y(k)$ can be expressed as,

$$Y(k) = \begin{bmatrix} y_{11}(k) & y_{12}(k) & \cdots & y_{1m}(k) \\ y_{21}(k) & y_{22}(k) & \cdots & y_{2m}(k) \\ \vdots & \vdots & \ddots & \vdots \\ y_{p1}(k) & y_{p2}(k) & \cdots & y_{pm}(k) \end{bmatrix} \quad (C.16)$$

The Block Hankel matrix, $H(k)$, is given by,

$$H(k-1) = \begin{bmatrix} Y(k) & Y(k+1) & \cdots & Y(k+s-1) \\ Y(k+1) & Y(k+2) & \cdots & Y(k+s) \\ \vdots & \vdots & \ddots & \vdots \\ Y(k+r-1) & Y(k+r) & \cdots & Y(k+s+r-2) \end{bmatrix} \quad (C.17)$$

which can be rewritten as,

$$H(k-1) = P(r)A^{k-1}Q(s) \quad (C.18)$$

Factoring the Hankel matrix, Equation (C.17), using Singular Value Decomposition (SVD) as,

$$H(0) = R_N \Sigma_N S_N^T \quad (C.19)$$

where R_N and S_N are orthonormal and Σ_N is a diagonal matrix with,

$$\Sigma_N = \text{diag}[d_1 \quad d_2 \quad \cdots \quad d_n \quad d_{n+1} \quad \cdots \quad d_N] \quad (C.20)$$

where

$$d_1 \geq d_2 \geq \cdots \geq d_n \geq d_{n+1} \geq \cdots \geq d_N \quad (C.21)$$

where n is the number of states in Equation (C.10).

Once determined the number n of states different from zero, R_N , Σ_N , and S_N are truncated to form,

$$\begin{aligned} R_n &= R_N(1:n, 1:n) \\ \Sigma_n &= \Sigma_N(1:n, 1:n) \\ S_n &= S_N(1:n, 1:n) \end{aligned} \quad (C.22)$$

Thus, the realization of low order with dimension n is reconstructed as,

$$\begin{aligned}
A &= \Sigma_n^{-1/2} R_n^T H(1) S_n \Sigma_n^{-1/2} \\
B &= \Sigma_n^{-1/2} S_n^T E_m \\
C &= E_p R_n \Sigma_n^{-1/2}
\end{aligned} \tag{C.23}$$

where $E_m = [I_m \quad 0]^T$ and $E_p = [I_p \quad 0]^T$, with I_m and I_p , the identify matrix of rank m and p , respectively.

C.3 Orthogonal Chebycheff Polynomials method

The method proposed here was explained by Arruda et al. (1996) and is based upon na unpublished manuscript by Vold (1990).

Among the available modal parameter extraction methods, the Orthogonal Chebycheff Polynomials method, ORTPOLY, seems to be the most appropriate in our case, as it is a frequency domain method which does not require equally-spaced frequency lines. Therefore, the user may choose the number and value of the frequencies where the response is measured, thus reducing the computational effort.

Assuming that the experimental FRF matrix $H(\omega)$, are measured for m inputs and p outputs, the dimension of the matrix $H(\omega)$ is $(p \times m)$. The modal parameter extraction method starts with the assumption that the FRF, matrix $H(\omega)$, can be expressed as a ratio of the matrix polynomials,

$$H(\omega) = \frac{\sum_{k=0}^r a_k \phi_k(i\omega)}{\sum_{k=0}^s b_k \phi_k(i\omega)} \tag{C.24}$$

where ϕ_k is the k^{th} Chebycheff polynomial, a_k is the k^{th} polynomial matrix coefficient (of same dimension as U) and b_k is the k^{th} denominator polynomial matrix coefficient, which is a scalar for single excitation and a matrix ($m \times m$) in the case of multiple excitation. Without loss of generality, making $b_s = I$ and rearranging Equation (C.24) as,

$$\sum_{k=0}^{s-1} H(\omega)^H \phi_k^* b_k^H - \sum_{k=0}^r \phi_k^* I a_k^H = -\phi_s^* H(\omega)^H \quad (C.25)$$

Arranging Equation (C.25) in matrix form for a varying ω , yields an overdetermined linear system of equations, which can be solved for a_k and b_k in a least-square sense. It is important to mention that the frequency ω should be normalized in order to improve the condition of the least-squares problems, Kelly (1967).

After the polynomial fit has been performed, Vold (1990) proposed to form a companion matrix problem in the orthogonal polynomial basis. The modified companion matrix can be formed by combining the characteristic equation, which in the case of multiple references is given by,

$$\left[\sum_{k=0}^{s-1} [b_k] \phi_k(i\omega) \right] \{V\} = \{0\} \quad (C.26)$$

The formula to generate the orthogonal Chebycheff polynomials is defined as,

$$\phi_k(i\omega) = 2i\omega\phi_{k-1}(i\omega) - \phi_{k-2}(i\omega) \quad (C.27)$$

Solving the combined eigenproblem formed in the usual way, a companion matrix is formed, and the eigenvalues s_r , $r=1, \dots, sm$ are obtained Vold (1990). The first m elements of the eigenvectors of the associated problem, V_r , are the so-called modal participation vectors L_r of the partial expression of $H(\omega)$, given by,

$$H(\omega) = \sum_{r=1}^{Nm} \psi_r \left(\frac{L_r^T}{i\omega - s_r} \right) + \psi_r^* \left(\frac{L_r^H}{i\omega - s_r^*} \right) \quad (C.28)$$

where $Nm = sm$ is the number of modes and ψ_r are the mode shapes.

Once the modal participation vectors and the eigenvalues are known, computing the mode shapes is straightforward. Equation (C.28) can be rearranged for each element of matrix H (corresponding to each degree of freedom) varying with frequency arranged in vector form to yield,

$$\tilde{H}_0 = \psi_0 B^T \quad (C.29)$$

where

$$B = \begin{bmatrix} LS_1 \\ LS_2 \\ \vdots \\ LS_{ns} \end{bmatrix}; \quad L = [L_1 \quad L_2 \quad \cdots \quad L_{Nm}] \quad (C.30)$$

$$S_i = \text{diag}[(i\omega_i - s_1)^{-1} \quad (i\omega_i - s_2)^{-1} \quad \cdots \quad (i\omega_i - s_{Nm})^{-1}] \quad (C.31)$$

where ω_i is the i^{th} frequency line, ns is the number of frequency lines and ψ_0 is a vector with components corresponding to the 0^{th} degree of freedom of all the identified mode shapes. Solving the linear system of equations in Equation (C.29) for each element of matrix $H(\omega)$ yields the mode shapes.

The final result of this procedure is to extract from the FRFs in matrix $H(\omega)$ the eigenfrequencies, $\omega_r = |s_r|, r = 1, \dots, sm$ and the eigenmodes $\psi_r, r = 1, \dots, sm$. Repeated eigenvalues with multiplicity up to m may be identified.

Appendix D

Least Mean Square Algorithm

In this appendix the Least Mean Square adaptive filtering algorithm (LMS) is shown briefly. More detail can be found in Widrow and Sterns (1985), Nelson and Elliott (1992), Kuo and Morgan (1996), and Hansen and Snyder (1997).

The LMS algorithm is an important member of the family of stochastic gradient algorithms. The term stochastic gradient is intended to distinguish the LMS from the method of steepest descent that uses a deterministic gradient in a recursive computation of the Wiener filter for stochastic inputs. (Haykin, 1996)

A significant feature of the LMS algorithm is its simplicity. Moreover, it does not require measurements of the pertinent correlation functions, nor does it require matrix inversion. Indeed, it is the simplicity of the LMS algorithm that has made it the standard against which other adaptive filtering algorithms are benchmarked. (Haykin, 1996).

D.1 Introduction to the adaptive filtering theory

The LMS linear adaptive filtering algorithm consists of two basic processes:

1. *A filtering process*, which involves the computation of the output of a transversal filter produced by a set of tap inputs, and the generation of an estimation error by comparing this output to a desired response.

2. *An adaptive process*, which involves the automatic adjustment of the tap weights of the filter in accordance with the estimation error.

Details of the transversal filter, which is an example of FIR (Finite Impulse Response), used in the filtering process is shown in Figure D.1. The tap-inputs or reference signal, $x(n)$, and the tap-weights, $w(n)$, are defined as,

$$\begin{aligned} x(n) &= [x(n) \quad x(n-1) \quad \dots \quad x(n-L+1)]^T \\ w(n) &= [w_0(n) \quad w_1(n) \quad \dots \quad w_{L-1}(n)]^T \end{aligned} \quad (D.1)$$

where the response of the filter is given by,

$$\begin{aligned} y(n) &= w^T(n)x(n) \\ &= x^T(n)w(n) \end{aligned} \quad (D.2)$$

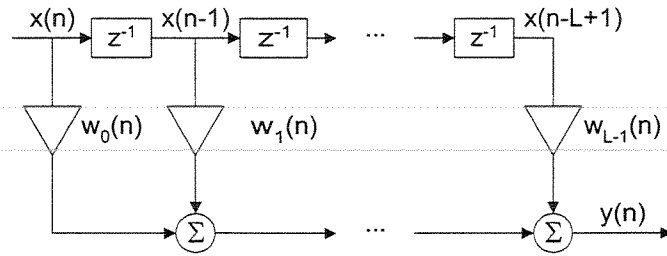


Figure D.1: Detailed structure of the transversal filter

The adaptive process is accomplished by comparing the output of the transversal filter, $y(n)$, with the desired response, $d(n)$, to obtain the estimated error signal, $e(n)$. Details of this process can be seen in Figure D.2. Thus,

$$e(n) = d(n) - y(n) = d(n) - w^T(n)x(n) = d(n) - x^T(n)w(n) \quad (D.3)$$

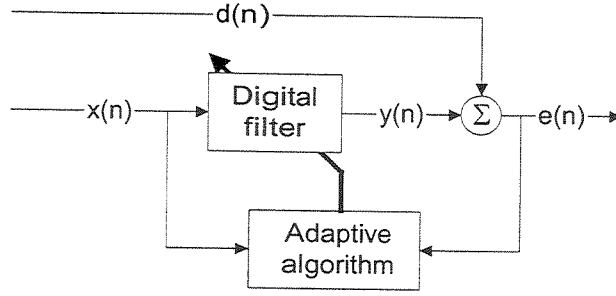


Figure D.2: Block diagram of the adaptive transversal filter

D.2 Mean-Square Error

The adaptive process is oriented toward minimizing the mean-square value, or the average power of the error signal. Defining the Mean-Square Error, ξ , as the expected value over the samples of the instantaneous squared error,

$$\xi = E[e^2(n)] \quad (D.4)$$

where $E[\cdot]$ represents the expected value.

Substituting (C.1) in (D.4),

$$\begin{aligned} \xi &= E[(d(n) - w^T(n)x(n))^2] \\ &= E[d^2(n) - d(n)(w^T(n)x(n)) + (w^T(n)x(n))(w^T(n)x(n))] \end{aligned} \quad (D.5)$$

Assuming that $e(n)$, $d(n)$ and $x(n)$ are statistically stationary, the MSE can be more conveniently expressed as,

$$\xi = E[d^2(n)] - 2P^T w(n) + w^T(n)Rw(n) \quad (D.6)$$

where P is a column vector of the cross correlation between the desired response and the tap-input vector defined as,

$$\begin{aligned} P &= E[d(n)x(n)] \\ &= [r_{dx}(0) \quad r_{dx}(1) \quad \cdots \quad r_{dx}(L-1)]^T \end{aligned} \quad (D.7)$$

with

$$r_{dx}(k) = E[d(n)x(n-k)] \quad (D.8)$$

and R is designed as the input correlation matrix and is given by,

$$\begin{aligned} R &= E[x(n)x^T(n)] \\ &= \begin{bmatrix} r_{xx}(0) & r_{xx}(1) & \cdots & r_{xx}(L-1) \\ r_{xx}(1) & r_{xx}(0) & \cdots & r_{xx}(L-2) \\ \vdots & \vdots & \ddots & \vdots \\ r_{xx}(L-1) & r_{xx}(L-2) & \cdots & r_{xx}(0) \end{bmatrix} \end{aligned} \quad (D.9)$$

with

$$r_{xx}(k) = E[x(n)x(n-k)] \quad (D.10)$$

Note that the expected value of any sum is the sum of expected values, but the expected value of a product is the product of expected values only when the variables are statistically independent.

The correlation matrix R has the following properties:

-
1. The correlation is symmetric;
 2. The correlation matrix is nonnegative definite;
 3. The eigenvalues are all real and nonnegative;

The correlation matrix R can be decomposed in,

$$R = Q\Lambda Q^{-1} = Q\Lambda Q^T \quad (D.11)$$

where Q are the eigenvector matrix and Λ is the diagonal eigenvalue matrix of R .

It is clear from (D.6) that the mean-square error is precisely a quadratic function of the components of the weight vector $w(n)$ when the input components and desired response input are stationary stochastic variables.

It is important to note that the MSE is a quadratic function in terms of $w(n)$ because the weights appear only to the first and second degrees. Besides, for each value of the filter

coefficient vector $w(n)$, there is a corresponding (scalar) value of MSE. Therefore, the MSE values associated with $w(n)$ form an $(L+1)$ -dimensional space (a hyperparaboloid), which is commonly called MSE surface, or the performance surface. This surface must be concave upward; otherwise, there would be weight settings that would result in a negative MSE, an impossible result with real, physical signals. For $L = 2$, this corresponds to an error surface in a three-dimensional space, Figure D.3, where the generic 3-D error surface for the case $L = 2$ is shown, with $w_{\text{opt}} = [w_0^0 \ w_1^0]$ is the optimal coefficient vector and ξ_{\min} is the minimum mean-square error.

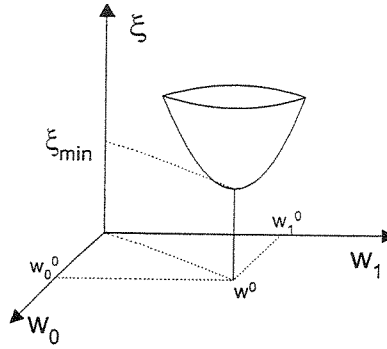


Figure D.3: Portion of a two-dimensional quadratic performance surface

One of the most important properties of the MSE surface is that it has only one global minimum point. At that minimum point, the tangents to the surface must be zero. Minimizing the MSE is the objective of many currently used adaptive methods such as the LMS algorithm.

The optimal solution to the coefficient filter w that minimizes the MSE cost function is found taking the gradient of (D.6) and equaling the result to zero. The gradient of the MSE is given by,

$$\nabla \xi = \frac{\partial \xi}{\partial w(n)} = \begin{Bmatrix} \frac{\partial \xi}{\partial w_0} \\ \frac{\partial \xi}{\partial w_1} \\ \vdots \\ \frac{\partial \xi}{\partial w_{L-1}} \end{Bmatrix} = -2P + R w(n) + R^T w(n) \quad (\text{D.12})$$

As the input correlation R is symmetric, and nonsingular, the optimal weight vector w_{opt} , sometimes called the Wiener weight vector, is given by,

$$\nabla \xi = \frac{\partial \xi}{\partial w} = -2P + 2Rw(n) = 0 \Rightarrow w_{\text{opt}} = R^{-1}P \quad (\text{D.13})$$

This equation is an expression of the Wiener-Hopf equation in matrix form. The minimum mean-square error associated with the optimal solution is now obtained substituting w_{opt} from (D.13) in (D.6),

$$\begin{aligned} \xi_{\min} &= E[d^2(n)] - 2P^T R^{-1}P + (R^{-1}P)^T R (R^{-1}P) \\ &= E[d^2(n)] - 2P^T R^{-1}P + (R^{-1}P)^T R R^{-1}P \\ &= E[d^2(n)] - 2P^T R^{-1}P + P^T R^{-1}P \\ &= E[d^2(n)] - P^T R^{-1}P \\ &= E[d^2(n)] - P^T w_{\text{opt}} \end{aligned} \quad (\text{D.14})$$

The MSE can be expressed using the minimum MSE combining (D.14) and (D.13) in (D.6), resulting in,

$$\begin{aligned} \xi(n) &= \xi_{\min} + P^T w_{\text{opt}} - 2P^T w(n) + w^T(n)Rw(n) \\ &= \xi_{\min} - P^T (2w(n) - w_{\text{opt}}) + w^T(n)Rw(n) \end{aligned} \quad (\text{D.15})$$

Substituting $P^T = w_{\text{opt}}^T R$,

$$\begin{aligned} \xi(n) &= \xi_{\min} - w_{\text{opt}}^T R (2w(n) - w_{\text{opt}}) + w^T(n)Rw(n) \\ &= \xi_{\min} - 2w_{\text{opt}}^T R w(n) + w_{\text{opt}}^T R w_{\text{opt}} + w^T(n)Rw(n) \\ &= \xi_{\min} + (w(n) - w_{\text{opt}})^T R (w(n) - w_{\text{opt}}) \end{aligned} \quad (\text{D.16})$$

resulting in,

$$\xi(n) = \xi_{\min} + v^T(n)Rv(n) \quad (\text{D.17})$$

where,

$$v(n) = w(n) - w_{\text{opt}} \quad (\text{D.18})$$

The weight misalignment vector $v(n)$ is the deviation of the weight vector from the Wiener optimal solution weight vector. Since R is positive semidefinite, the quadratic form on the right

side of (D.17) indicates that any departure of the weight vector $w(n)$ from the optimum w_{opt} would increase the error above its minimum value, or in other words, cause an excess mean-square error.

D.3 Method of Steepest Descent

The adaptation process consists of finding the minimum point of the cost function, which can be performed using simple search methods such as the steepest-descent method. The steepest-descent method is an iterative technique that is ideally suited to derive an adaptive algorithm since the related error surface is guaranteed to be quadratic with respect to the filter weights.

The steepest-descent method reaches the minimum by following the direction in which the performance surface has the greatest rate of decrease, i.e., an algorithm whose path follows the negative gradient of the performance surface. The concept of steepest descent can be implemented in the following algorithm,

$$w(n+1) = w(n) - \frac{\mu}{2} \nabla \xi \quad (\text{D.19})$$

where μ is a convergence factor (or step size) that controls stability and the rate of descent to the bottom of the cost function; the larger the value of μ , faster the speed of descent. The $\nabla \xi$ denotes the gradient of the error function with respect to $w(n)$ and the negative sign increments the adaptive weight vector in the negative gradient direction.

Substituting the gradient, Equation (C.5), in the steepest-descent method to form the adaptive search method,

$$\begin{aligned} w(n+1) &= w(n) - \frac{\mu}{2} (-2P^T + 2Rw(n)) \\ &= (1 - \mu R)w(n) - \mu P^T \end{aligned} \quad (\text{D.20})$$

However, the above equation is difficult to be implemented in practical applications, because it is necessary to compute the input correlation matrix R and the input cross-correlation P .

D.4 LMS algorithm

The LMS algorithm consists of using the instantaneous squared error to estimate the mean-square error,

$$\xi = E[e^2(n)] \Rightarrow \hat{\xi}(n) = e^2(n) \quad (D.21)$$

where $\hat{\xi}(n)$ is the estimate of the ξ at time n .

Thus, the gradient can be performed using the estimate of the MSE, in this case, the gradient is said to be the gradient estimate. Using this approach, the gradient estimate is given by,

$$\nabla \hat{\xi}(n) = \frac{\partial \hat{\xi}(n)}{\partial \mathbf{w}(n)} = \frac{\partial e^2(n)}{\partial \mathbf{w}(n)} = 2e(n) \frac{\partial e(n)}{\partial \mathbf{w}(n)} = -2e(n)\mathbf{x}(n) \quad (D.22)$$

Therefore, the adaptive method is performed substituting the estimate gradient in the steepest-descent method as,

$$\mathbf{w}(n+1) = \mathbf{w}(n) + \mu \mathbf{x}(n)e(n) \quad (D.23)$$

The above equation is the well-known LMS algorithm or stochastic gradient algorithm.

It is interesting to note that the estimate gradient is unbiased, which can be proved taking the expected value of both sides of (D.22),

$$E[\nabla \hat{\xi}(n)] = -2E[\mathbf{x}(n)e(n)] \quad (D.24)$$

Substituting the error, Equation (C.1), and assuming that $\mathbf{x}(n)$ e $\mathbf{w}(n)$ are statistically independent,

$$E[\nabla \hat{\xi}(n)] = -2E[\mathbf{x}(n)d(n)] - 2E[\mathbf{x}(n)\mathbf{x}^T(n)]E[\mathbf{w}(n)] \quad (D.25)$$

Substituting the input correlation matrixes \mathbf{P} and \mathbf{R} ,

$$E[\nabla \hat{\xi}(n)] = -2\mathbf{P} - 2\mathbf{R}E[\mathbf{w}(n)] = -2\mathbf{P} - 2\mathbf{R}\mathbf{w}_{\text{opt}} = \nabla \xi \quad (D.26)$$

proving that the gradient estimate is unbiased.

D.4.1 Performance analysis

The convergence analysis can be performed taking the expected value of (D.23),

$$E[w(n+1)] = E[w(n)] + E[\mu x(n)e(n)] \quad (D.27)$$

Substituting (C.1) in the above equation,

$$E[w(n+1)] = E[w(n)] + \mu(E[x(n)d(n)] + E[x(n)x^T(n)w(n)]) \quad (D.28)$$

Assuming that $x(n)$ and $w(n)$ are statistically independent, and substituting the input correlation matrixes P and R ,

$$\begin{aligned} E[w(n+1)] &= E[w(n)] + \mu(P + RE[w(n)]) \\ &= (I - \mu R)E[w(n)] + \mu P \end{aligned} \quad (D.29)$$

Substituting the optimal solution, Equation (D.13) in the form $P = R w_{\text{opt}}$ in the above equation,

$$E[w(n+1)] = (I - \mu R)E[w(n)] + \mu R w_{\text{opt}} \quad (D.30)$$

The axis translation, defined in (D.18), can be extrapolated to,

$$\begin{aligned} v(n) &= w(n) - w_{\text{opt}} \\ v(n+1) &= w(n+1) - w_{\text{opt}} \end{aligned} \Rightarrow \begin{aligned} E[v(n)] &= E[w(n)] - w_{\text{opt}} \\ E[v(n+1)] &= E[w(n+1)] - w_{\text{opt}} \end{aligned} \quad (D.31)$$

Substituting the above equations in (D.30),

$$E[v(n+1)] + w_{\text{opt}} = (I - \mu R)(E[v(n)] + w_{\text{opt}}) + \mu R w_{\text{opt}} \quad (D.32)$$

Rearranging the terms,

$$\begin{aligned} E[v(n+1)] &= (I - \mu R)E[v(n)] + \mu R w_{\text{opt}} - w_{\text{opt}} + (I - \mu R)w_{\text{opt}} \\ &= (I - \mu R)E[v(n)] \end{aligned} \quad (D.33)$$

Defining a axis rotation as $v = Qv'$, where Q is the eigenvalue matrix of the input correlation matrix R , and doing,

$$\begin{aligned} v(n) &= Qv'(n) \\ v(n+1) &= Qv'(n+1) \end{aligned} \Rightarrow \begin{aligned} E[v(n)] &= QE[v'(n)] \\ E[v(n+1)] &= QE[v'(n+1)] \end{aligned} \quad (D.34)$$

Substituting the above equation in (D.33),

$$QE[v'(n+1)] = (I - \mu R)QE[v'(n)] \quad (D.35)$$

Multiplying by Q^{-1} and substituting R by $Q\Lambda Q^{-1}$, as defined in (D.11),

$$Q^{-1}QE[v'(n+1)] = Q^{-1}(I - \mu Q\Lambda Q^{-1})QE[v'(n)] \quad (D.36)$$

Simplifying the above equation,

$$\begin{aligned} E[v'(n+1)] &= Q^{-1}(I - \mu Q\Lambda Q^{-1})QE[v'(n)] \\ &= (Q^{-1}Q - \mu Q^{-1}Q\Lambda Q^{-1}Q)E[v'(n)] \\ &= (I - \mu\Lambda)E[v'(n)] \end{aligned} \quad (D.37)$$

The above equation can be written in the following form,

$$E[v'(n)] = (I - \mu\Lambda)^n v'(0) \quad (D.38)$$

The convergence condition states that $w(n)$ converges from $w(0)$ until w_{opt} with $n \rightarrow \infty$ is equal to say that $E[v'(n)] = 0$ with $n \rightarrow \infty$. Thus, the term $\lim_{n \rightarrow \infty} (I - \mu\Lambda)^n$ must be zero, which means that $|I - \mu\Lambda|$ must be less than 1. Since Λ is the eigenvalue diagonal matrix of R , the inequality is obeyed if,

$$|1 - \mu\lambda_{\max}| < 1 \quad (D.39)$$

where λ_{\max} is the greatest eigenvalue of R .

Thus, $w(0)$ converges to w_{opt} if the step-size is given by,

$$0 < \mu < \frac{2}{\lambda_{\max}} \quad (D.40)$$

Since, λ_{\max} is less than the trace of Λ , and the trace of Λ is equal to the trace of R , the above condition can be interpreted as,

$$0 < \mu < \frac{2}{\text{tr}[R]} \quad (D.41)$$

It is important to remember that the trace of the R is the signal power of the input signal $x(n)$ plus filter length L , so,

$$0 < \mu < \frac{2}{(L + 1) \text{ input signal power}} \quad (\text{D.42})$$

D.4.2 Normalized LMS algorithm

As was shown before, the maximum step-size μ is inversely proportional to the filter order L and the power of reference signal $x(n)$. One important technique to optimize the speed of convergence while maintaining the desired steady-state performance, independent of the reference signal power, is known as normalized LMS algorithm.

The normalized LMS algorithm can be developed using a modified version of the steepest-descent method, that is the self-orthogonalizing adaptive filtering algorithm defined by,

$$w(n+1) = w(n) - \frac{\mu}{2} R^{-1} \nabla \xi(n) \quad (\text{D.43})$$

where R is the input correlation matrix, and can be approximated by its instantaneous value as,

$$\text{trace}[R] = \text{tr}[E[x(n)x^T(n)]] \Rightarrow \text{tr}[\hat{R}] = \|x\|^2 \quad (\text{D.44})$$

Thus, using the gradient estimate and the input correlation matrix estimate in the self-orthogonalizing adaptive filtering algorithm, the normalized LMS algorithm is found,

$$w(n+1) = w(n) - \frac{\mu}{\alpha + \|x(n)\|^2} x(n)e(n) \quad (\text{D.45})$$

where α is a small constant added to avoid division by zero.

The convergence analysis of (D.45) can be performed taking the expected value of both sides,

$$E[w(n+1)] = E[w(n)] - \frac{\mu}{E[\|x(n)\|^2]} E[x(n)e(n)] \quad (\text{D.46})$$

Substituting the error $e(n)$,

$$E[w(n+1)] = E[w(n)] - \frac{\mu}{E[\|x(n)\|^2]} (E[x(n)d(n)] - E[x(n)x^T(n)]E[w(n)]) \quad (D.47)$$

Substituting the input correlation matrixes P and R ,

$$\begin{aligned} E[w(n+1)] &= E[w(n)] - \mu R^{-1} (P - R E[w(n)]) \\ &= (1 - \mu) E[w(n)] - \mu R^{-1} P \end{aligned} \quad (D.48)$$

Using the axis translation defined in (D.18),

$$E[v(n+1)] + w_{\text{opt}} = (1 - \mu) (E[v(n)] + w_{\text{opt}}) + \mu R^{-1} P \quad (D.49)$$

Substituting the optimal solution, Equation (D.13),

$$E[v(n+1)] = (1 - \mu) E[v(n)] \quad (D.50)$$

Comparing (D.50) with (D.33) it is clear that the normalized LMS algorithm converges if the step-size μ is chosen as,

$$0 < \mu < 2 \quad (D.51)$$

D.5 Filtered-X LMS algorithm

In many applications of active noise control systems, Figure D.4, the structure shown in Figure D.2 for the LMS algorithm can not be applied successfully because there is a transfer function between the transversal filter response $y(n)$ and the estimate error $e(n)$. In this case, the transfer function $S(z)$ must be added in the method to form the Filtered-X LMS.

The error estimate or error signal $e(n)$ from Figure D.4 is given by,

$$\begin{aligned} e(n) &= d(n) - y'(n) \\ &= p(n) * x(n) - s(n) * y(n) \\ &= p(n) * x(n) - s(n) * (w^T(n)x(n)) \end{aligned} \quad (D.52)$$

where $*$ denotes linear convolution, $p(n)$ e $s(n)$ can be interpreted as the impulse response of the primary path $P(z)$ and the secondary path $S(z)$, respectively.

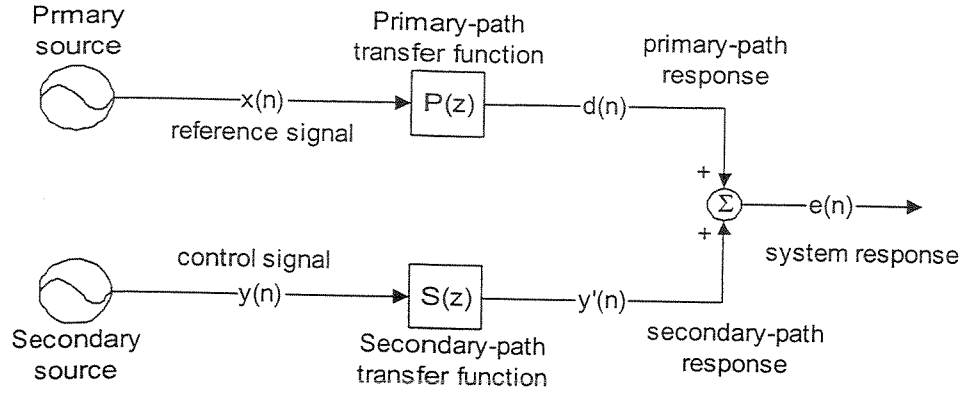


Figure D.4: Schematic representation of an active noise control system to 1-error sensor, 1-primary source and 1-secondary source.

Thus, the gradient of the cost function, Equation (D.22), reduces to,

$$\nabla \hat{\xi}(n) = 2e(n) \frac{\partial e(n)}{\partial w(n)} = 2e(n)(-s(n) * x(n)) = -2x'(n)e(n) \quad (D.53)$$

where $x'(n)$ represents the convolution of $s(n)$ with $x(n)$.

Substituting the estimate gradient in the steepest-descent method, the Filtered-X LMS algorithm is found as,

$$w(n+1) = w(n) + \mu x'(n)e(n) \quad (D.54)$$

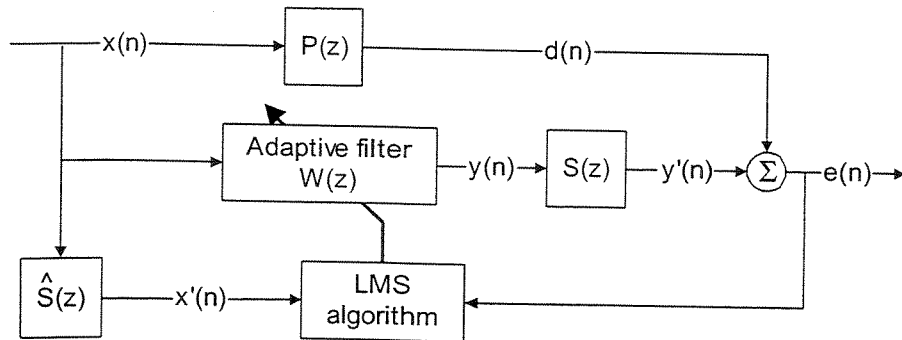


Figure D.5: Block diagram of the Filtered-X LMS algorithm applied to active noise control systems

The block diagram of the Filtered-X LMS algorithm applied to active noise control systems is shown in Figure D.5, where $\hat{S}(z)$ is a copy of $S(z)$. However in practical applications, $S(z)$ is unknown and must be estimated by an additional filter $\hat{S}(z)$. The filtered reference is generated by passing the reference signal through this estimate of the secondary path.

D.5.1 Convergence analysis

Assuming slow adaptation, $\hat{S}(z)$ matches exactly with $S(z)$, and comparing equation (D.54) with (D.23), it is obvious that the filtered-X LMS algorithm owns the same convergence constraint of the LMS algorithm, equation (D.40). However, the input correlation matrix R for the Filtered-X LMS is found taking the expected value from (D.53),

$$E[\nabla \hat{\xi}(n)] = -2[x'(n)e(n)] = -2E[x'(n)d(n)] + 2E[x'(n)(s(n) * (x^T(n)w(n)))] \quad (D.55)$$

Assuming that $x'(n)$ and $w(n)$ are statistically independent variables,

$$E[\nabla \hat{\xi}(n)] = -2E[x'(n)d(n)] + 2E[x'(n)(s(n) * x(n))]E[w(n)] \quad (D.56)$$

Defining,

$$\begin{aligned} P &= E[x'(n)d(n)] \\ R &= E[x'(n)(s(n) * x(n))] = E[(\hat{s}(n) * x(n))(s(n) * x(n))] \end{aligned} \quad (D.57)$$

It is easy to find,

$$\nabla \hat{\xi} = -2P + 2Rw(n) \quad (D.58)$$

That is the same solution found in (D.13). Thus, the Filtered-X LMS owns the same convergence condition of the LMS algorithm, but with the input correlation matrix defined in (D.57) rather than (D.9).

However, some estimation errors can occur since $\hat{s}(n)$ does not match exactly with $s(n)$ in (D.57), which means that the eigenvalues of R can assume any value (with real and imaginary part) and are not all real any more. Thus, the condition previously stated that $|I - \mu\Lambda| < 1$ is replaced by,

$$0 < \mu < \frac{2\Re\{\lambda_i\}}{|\lambda_i|^2} \quad (\text{D.59})$$

The condition stated above means that the method does not converge exponentially due to the imaginary part of the eigenvalue. However, if the real part of the eigenvalue is still positive, the method converges but with a longer time constant since it is necessary that the oscillating part of the eigenvalue goes to zero. (Kuo and Morgan, 1996).

In order to demonstrate the effects of the difference between $s(n)$ and $\hat{s}(n)$, it is introduced a phase error ϕ and an amplitude error α in $\hat{s}(n)$ in the following form,

$$\hat{s}(n) = (1 + \alpha)s(n)e^{i\phi} \quad (\text{D.60})$$

Substituting the above equation in the correlation matrix R , Equation (D.57),

$$\begin{aligned} R &= E[(1 + \alpha)e^{i\phi}(s(n) * x(n))(s(n) * x(n))] \\ &= (1 + \alpha)e^{i\phi} E[(s(n) * x(n))(s(n) * x(n))] \\ &= (1 + \alpha)e^{i\phi} Q\Lambda Q^T \end{aligned} \quad (\text{D.61})$$

where Q and Λ are the same matrixes defined in (D.11).

As the eigenvalues of R must have the real part positive to guarantee the convergence,

$$\Re\{(1 + \alpha)e^{i\phi}\} > 0 \Rightarrow (1 + \alpha)\cos\phi > 0 \quad (\text{D.62})$$

Thus, making the amplitude error equal to zero to simplify the analysis, it is found that the filtered-X LMS algorithm is stable if the phase error is given by,

$$-90^\circ < \phi < 90^\circ \quad (\text{D.63})$$

It is important to note that the maximum value of the step-size μ is dependent of the eigenvalue amplitude, see (D.40) for example. Thus, equation (D.61) means that the amplitude error α effects the maximum value of the step-size.

The optimal solution or the Wiener solution to the $w(n)$ is found assuming that when $n \rightarrow \infty$, $E[w(n)] = 0$, and $w(n) \rightarrow w_{\text{opt}}$, thus,

$$E[\nabla \hat{\xi}(n)] = 0 \Rightarrow w_{\text{opt}} = R^{-1}P \quad (\text{D.64})$$

Assuming for R and P the instantaneous value,

$$w_{\text{opt}} = \frac{x'(n)d(n)}{x'(n)(s(n) * x(n))} = \frac{p(n)}{s(n)} \quad (\text{D.65})$$

This shows that the optimal solution is independent of the difference between the $s(n)$ and $\hat{s}(n)$. Therefore, the error present in the estimated secondary path affects only the convergence time but not the optimal solution.

D.5.2 Normalization

The normalized filtered-X LMS algorithm is performed using (D.43) rather than the steepest-descent method,

$$w(n+1) = w(n) + \frac{\mu}{\alpha + \|x'(n)\|^2} x'(n)e(n) \quad (\text{D.66})$$

As the normalized LMS algorithm, the convergence of the normalized filtered-X LMS is guaranteed if the step-size is in between $0 < \mu < 2$ since estimation errors do not occur between $s(n)$ and $\hat{s}(n)$.

D.6 Normalized Filtered-X LMS algorithm in the frequency domain

The normalized Filtered-X LMS in the frequency domain is easily developed transforming the MSE (the cost function) to the frequency domain, giving,

$$\xi(\omega) = E[E^H(\omega)E(\omega)] \Rightarrow \hat{\xi}(\omega) = E^H(\omega)E(\omega) = |E(\omega)|^2 \quad (\text{D.67})$$

where H represents the conjugate transpose, $E(\omega)$ is the Fourier transform of $e(n)$, which is given by,

$$\begin{aligned} E(\omega) &= D(\omega) - Y'(\omega) \\ &= P(\omega)X(\omega) - S(\omega)Y(\omega) \\ &= P(\omega)X(\omega) - S(\omega)X(\omega)W(\omega) \end{aligned} \quad (\text{D.68})$$

The gradient of the cost function with respect to $W(\omega)$ is given by,

$$\nabla \hat{\xi}(\omega) = \frac{\partial \hat{\xi}(\omega)}{\partial W(\omega)} = -2X'^*(\omega)E(\omega) \quad (D.69)$$

where $*$ represents the conjugate, and the X' the product of the $X(\omega)$ with $W(\omega)$.

The optimal solution is given taking the gradient of the cost function and equaling the result to zero,

$$\nabla \hat{\xi}(\omega) = 0 \Rightarrow X'^*(\omega)E(\omega) = 0 \Rightarrow X'^*(\omega)(P(\omega)X(\omega) + S(\omega)W(\omega)X(\omega)) = 0 \quad (D.70)$$

Assuming that when the method converges, $W(\omega)$ is replaced by W_{opt} , defining the matrix P as,

$$P = X'^*(\omega)P(\omega)X(\omega) \quad (D.71)$$

and the matrix R as,

$$R = X'^*(\omega)S(\omega)X(\omega) = |S(\omega)X(\omega)|^2 \quad (D.72)$$

the optimal solution or the Wiener solution is given by,

$$W_{opr} = R^{-1}P = \frac{P(\omega)}{S(\omega)} \quad (D.73)$$

The adaptive law is the self-orthogonalizing adaptive filtering algorithm in the frequency domain, that is, the same form as presented in (D.43). Therefore, the normalized filtered-X LMS algorithm is given by,

$$W_{k+1}(\omega) = W_k(\omega) + \frac{\mu}{\alpha + |X'_k(\omega)|^2} X'_k(\omega)E_k(\omega) \quad (D.74)$$

where the subscript k is the iteration time.

The normalized filtered-X LMS in the frequency domain can be implemented efficiently transforming the signals from time domain to frequency domain using the FFT (Fast Fourier transform). Then, the algorithm can be computed taking only half of the signal length to avoid the

circularity problems or using the whole signal as suggested by Shynk (1992), where several forms to implement the LMS algorithm are shown.

The great advantage of computing the normalized filtered-X LMS in the frequency domain is the possibility of controlling each frequency bin independently because in this case the method uses only one weight $W(\omega)$ to each frequency.

Appendix E

List of the Equipment

In this appendix is given a list of the equipment used in the experiments.

E.1 Equipment used in the one-dimensional acoustic waveguide

Table E.1: Equipment used in the one-dimensional acoustic waveguide

Equipment	Function	model	Serial number	Trademark
Omnidirectional, 1/4", ICP, electret microphones Nominal sensitivity 25 mV/PA	Pressure sensors	Microphone type: 130A10 Preamplifier type: 130P10	4707	PCB
			5711	
			5703	
			5804	
Particle velocity sensor	Particle velocity sensor			Microflown
Loudspeakers	Acoustic sources	PWR 480	238.627	Novik
			311.408	
Control board	Control board	Ds 1102		DSPACE
Spectral analyzer 35650A	Data acquisition	35655A – 8 channel	2911A01216	Hewlett Packard
		35653A – source module		
		35651B – interface/signal processor		
Power supply ICP	Signal condition	482A05	1052	PCB
Power amplifier	Power amplifier	PA25E	509	LDS
			510	
Analog filter	Analog filter	900C/9L8B	790	Frequency Devices
			791	
Laser Doppler Vibrometer	Velocity sensor	OFV 3001SU – vibrometer controller	1 99 1225	Polytec
		OFV 303.8 – sensor head	1 99 1225	

E.2 Equipment used in the cylindrical shell

Table E 2 : Equipment used in the cylindrical shell

Equipment	Function	model	Serial number	Trademark
Omnidirectional, ¼", ICP, electret microphones, nominal sensitivity 25 mV/PA	Pressure sensors	Microphone type: 130A10 Preamplifier type: 130P10	4707	PCB
			5711	
			5703	
			5804	
			5644	
			5765	
			5763	
Particle velocity sensor	Particle velocity sensor			Microflown
Micro-accelerometers	Acceleration sensor	8614A500M1	C128255	Kistler
			C129195	
			C129189	
			C128256	
			C129193	
			C129191	
			C120486	
Driver	Acoustic source	D 405		
Force Transducer	Force transducer	208 A02	10496	PCB
Shaper	Structural source			LDS
PZT patches	Structural source	QP10N		LDS
Control board	Control board	Ds 1102		DSPACE
Spectral analyzer 35650A	Data acquisition	35655A – 8 channel	2911A01216	Hewlett Packard
		35653A – source module		
		35651B – interface/signal processor		
Power supply ICP	Signal condition	5134A1	C78384	Kistler
			C78385	
			C78386	
Power amplifier	Power amplifier	PA25E	510	LDS
	Quickpack power amplifier	EL 1224	US99K-338	Kistler
			US99J-332	
Analog filter	Analog filter	900C/9L8B	790	Frequency Devices
Laser Doppler Vibrometer	velocity sensor	OFV 3001SU – vibrometer controller	1 99 1225	Polytec
		OFV 303.8 – sensor head	1 99 1225	